qn v v nlq wrl n r u u wm rl l n
u r wm rwp rl r w r ln rwp oUrpq L
uu

wp L r

qn r kv r nm
l t u wm wr n r o nl q w u p
rwo uoruv nw o qn n r nv nw o qn mmp nn o
M l o qru yq qM

Mnl nv kn

lq u o wprwnn rwp

rv yn r q wLqnw

Abstract

Friction Stir Processing (FSP) is a solid-state processing technique which can be used to refine and modify as-cast microstructures for superior properties. The aim of the present research is to investigate the following fundamental aspects associated with FSP cast Al and Mg alloys: the quantitative relationships between processing speeds (rotation and linear speeds: ω and v) and the thermomechanical responses (tool torque–M, power–P, specific energy–E_s and material flow volumes–V_{flow}); the details of material flow/deformation and microstructural evolution during FSP of a cast Al-Si alloy; the mechanism governing the removal of β-$Mg_{17}Al_{12}$ particles during FSP of cast Mg-Al alloys.

Experimentally, FSP of A356 cast alloy were performed with wide ranges of ω and v. M was measured during each FSP experiment, and temperature (T) at various locations were monitored for selected experiments. Based on M, P and E_s were calculated. Stir zone areas (A_{flow}) were measured using the metallographic samples to estimate V_{flow} values. FSP experiments, using tool-pin-breaking technique, were conducted on A356 plates under two representative conditions. Macro-scale flow, micro-scale deformation, and microstructural evolution were studied by means of Electron Backscatter Diffraction technique. Pin-breaking FSP experiments were also conducted on AZ91/AM60 cast alloys during which T was monitored, based on which the thermomechanical and metallurgical explanations for the removal of β-$Mg_{17}Al_{12}$ particles were investigated.

The relationship between M and ω is found to be well described by an exponential decay function: $M = M_o + M_f\exp(-n\omega)$; while the influence of v on M can be described reasonably well by linearly relating M_o, M_f, and n to v. Together with the consideration of temperature data obtained, M is shown to intimately relate to material flow resistance to tool motion. Thus n and M_f can be adjusted for alloying effect in the low ω range, while such effect diminishes as ω increases. It is shown that tool shoulder flow volume generated per revolution ($V_{S-rev} = A_{shouder}v/\omega$) relates to M, which can be interpreted as energy input per revolution, in a form of $M = M_o + M_f[1 - \exp(-\gamma V_{S-rev})]$. The tool-pin flow volume does not require a proportional amount of energy input. The larger diameter of the shoulder

compared to the pin, coupled with higher material flow stress near shoulder region are the fundamental causes of this.

A new flow mechanism that explains the formation of the non-ring nugget during FSP A356 was identified. It is shown that regardless of the processing condition, the highly refined portion of the nugget zone clearly segregates from the less refined portion. How this macro-segregation relates to the difference in flow regime inside and outside thread spaces is demonstrated in detail. The deforming dendrites located ahead of the pin were traced and based on this the strain and strain rate during FSP were directly estimated.

The mechanism governing the recrystallization of α-Al dendrites was identified primarily as Geometrical Dynamic Recrystallization. Recrystallized α-Al grains around the pin displayed a dominating "A" shear texture, although the local "A" texture must undergo a degree of rotation to obtain the ideal "A" texture due to the local texture frame misaligned with the ideal texture frame. It was found that this misalignment is closely related to the direction of material flow at the location under consideration.

Finally, detailed evidences suggest that the major mechanism governing the removal of the eutectic β-$Mg_{17}Al_{12}$ particles is through a sequence of incipient melting of β-phase, Al rich liquid wetting recrystallized α-Mg grain boundaries thus leading to a significant increase in liquid/solid interface, transfer of Al solute from liquid to interiors of α-Mg and the growth of α-Mg into the liquid (resolidification).

Acknowledgement

The author would like to express sincere gratitude to supervisor Associate Professor Zhan Chen for his guidance, stimulating discussions, patience and expertise, which contributed significantly throughout this study. Professor Wei Gao (my secondary supervisor) and Dr Tianpin Zhu are greatly acknowledged for their valuable discussions. A notable acknowledge goes to Ross Reichardt, Mark Masterton, Bradley Scott and Yan Wang for their time and guidance during the experiments. Catherine Hobbis is thanked for her assistance with SEM and EBSD analysis.

Sincere acknowledge must be given to my family in China. Mum Xiuju Li, Dad Jianguo Cui, Grandpa Yue Cui, Grandma Fengying Yuan, and my girl friend Bing Li are thanked for their endurance, endless support and encouragement throughout my academic career.

Statement of Originality

I hereby declare that this submission is my own work and that, to the best of my knowledge and belief, it contains no material previously published or written by another person nor material which to a substantial extent has been accepted for the qualification of any other degree or diploma of a university or other institution of higher learning, except where due acknowledgement is made in the acknowledgements.

Name:

Date:

Table of Contents

List of Figures

Nomenclatures

Symbols	*Meaning*	*Units*
v	Tool linear speed	mm/s
ω	Tool rotation speed	rpm
θ	Tool tilt angle: angle between tool axis and vertical axis	°
H_{plunge}	Tool plunge depth in vertical direction	mm
t	Thickness of welding plates	mm
λ	Processing pitch	mm/rev
$A_{shoulder}$	Cross section area of shoulder flow zone	mm^2
A_{nugget}	Cross section area of nugget flow zone	mm^2
A_{RSM}	Cross section area of RSM flow zone	mm^2
A_{total}	Cross section area of total stir zone	mm^2
L_{pin}	Length of tool pin	mm
$V_{S\text{-}rev}$	Volume of shoulder flow zone per revolution	mm^3/rev
$V_{T\text{-}rev}$	Volume of total stir zone per revolution	mm^3/rev
R_{pin}	Outer radius of tool pin	mm
D_{pin}	Outer diameter of tool pin	mm
p	Pitch of threads machined on the tool pin	mm
d_{thread}	Depth of threads	mm
$R_{shoulder}$	Tool shoulder radius	mm
$D_{shoulder}$	Tool shoulder diameter	mm
Q_{fs}	Heat generation during friction stir	J
M	Torque acting on the tool	Nm
P	Power: total energy generated by tool per unit time	J/s
E_s	Specific energy: total energy input per unit length	J/mm
$T_{solidus}$	Solidus temperature of a material	°C
$T_{eutectic}$	Eutectic temperature of a material	°C
T_{pin}	Temperature at front-pin/material interface	°C
T_{nugget}	Temperature in nugget flow zone	°C
$T_{shoulder}$	Temperature in shoulder flow zone	°C
σ_{yield}	Yield stress of a material	MPa
τ_{yield}	Shear-yield stress of the material	MPa
τ_{shear}	Contact stress at tool material interface	MPa

$\tau_{friction}$	Friction shear stress between tool and material	MPa
σ_z	Vertical pressure between tool shoulder and material underneath	MPa
μ_f	Friction coefficient at tool material interface	1
δ	Tool material interface slip constant	1
ε	True strain of material deformation	1
$\acute{\varepsilon}$	Strain rate of material deformation	s^{-1}

Chapter 1. Introduction and Literature Review

1.1 Friction Stir Processing, Some General Comments

1.1.1 The General Features of Friction Stir Processing

Friction Stir Processing (FSP) originated from and shares the same thermomechanical principles with Friction Stir Welding (FSW), which is a mature joining technology. Thus, it is appropriate to first comment on FSW. FSW is a solid-state joining technology first invented by The Welding Institute (UK) in 1991. During FSW a non consumable rotating tool is inserted into the seam line between plates to be welded and traverses along the seam line (as shown in Figure 1-1 [1]). The tool contains two unique features, which include the shoulder and the pin (usually threaded). Advancing side refers to the side where tool rotational motion and transverse motion are in same direction, where retreating side is defined as the side where these two motions have opposite directions. Intensive heat is generated by contact friction between the tool and workpiece and the strength (i.e. flow stress) of the weld material reduces significantly as a result of the heat generated. Both forward and rotational motion of the tool will cause the softened (without melting) material to flow around the tool and deposit at the back of the pin during welding.

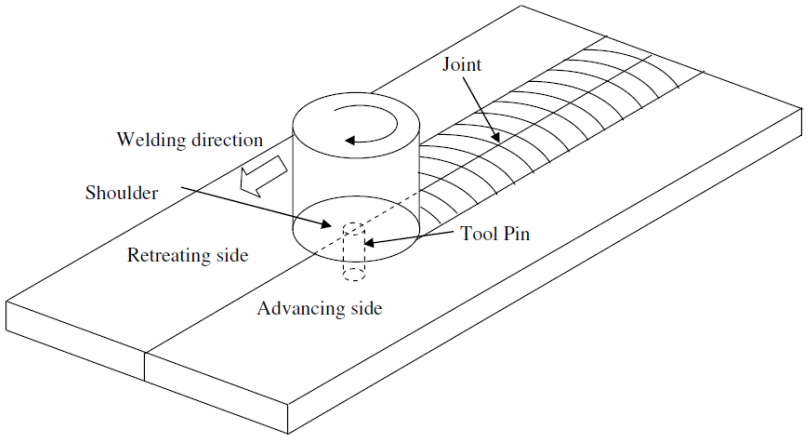

Figure 1-1. Schematic illustration of FSW [1], which indicates that a rotating tool is travelling along the joining line of two adjacent metal plates.

FSW has been increasingly researched and developed in recent years due to the many advantages it offers. The first advantage is that the material does not melt during the welding process, distortion can be minimized (under optimum welding conditions) and no porosities would exist as there is no resolidification of molten material. Furthermore, this solid-state nature implies that FSW fundamentally requires less energy compared to other traditional welding techniques. During FSW, significant frictional heating and intense plastic deformation is generated thereby resulting in the occurrence of dynamic recrystallization in the stirred zone, which leads to the formation of fully-recrystallized grains. The fine-grained weld structure yields superior mechanical properties compared to that of the traditional welding, such as higher UTS and creep resistance, and better corrosion resistance. FSW is also considered to be environmentally friendly because no gas or flux is need in the process. For those reasons, FSW becomes more and more attractive and it has already been successfully applied in a wide range of industries, such as the aerospace and automobile industries [1].

Based on the same thermomechanical principle, Friction Stir Processing (FSP) was developed by Mishra et al. [2] for localized microstructural modification and thus enhancing desired material properties. During FSP, a rotating tool with pin and shoulder is inserted in a single piece of material and traversed across the workpiece. A review on FSP was given by Ma [3]. FSP has been used on wrought aluminium alloys, e.g. the 7xxx wrought Al alloys, with the aim of generating ultra-fine grains thus attaining high-strain-rate superplasticity. Furthermore, FSP has been used for the fabrication of a surface composite on aluminium substrate, and the homogenization of powder metallurgy aluminium alloys and metal matrix composites [3]. However, the most important and potential application of FSP is to refine the microstructures of cast light alloys, such as Al, Mg, and Ti alloys, in order to improve the relatively poor as-cast mechanical properties.

Al-Si-Mg and Mg-Al-Mn alloys are widely used to cast high strength components in aerospace and automobile industries with the primary aim of reducing weight and fuel consumption. However, porosity, brittle eutectic/secondary particles (Si and $Mg_{17}Al_{12}$) along dendrite boundaries and coarse primary dendrites in these alloys

reduce the mechanical properties of the castings, in particular the ductility, toughness and fatigue strength [4].

The aforementioned disadvantages reduce the potentials of these cast alloys being used more extensively as structural components which are subject to critical loadings (both static and cyclic) [5, 6]. The use of FSP to achieve local/global refinement of the intrinsic coarse microstructures of cast alloys has been proven to be effective while economically advantageous compared to traditional heat treatments. For instance, conventionally, a solution treatment at ~ 415 °C for up to 40 hours followed by an aging is used to modify the morphology and distribution of the $Mg_{17}Al_{12}$-phase in Mg-Al cast alloys to enhance the mechanical properties. However, such a procedure is time consuming, resulting in not only increased material cost but also surface oxidation and grain coarsening.

Generally speaking, the major functions and benefits of FSP, for processing light cast alloys, are:

a. to break-up the coarse Si particles, and re-distribute them evenly within the matrix of Al alloys; while to significantly reduce the volume fractions of $Mg_{17}Al_{12}$ particles through mechanical breakage and solid state dissolution and thus homogenize the microstructure in Mg alloys [3, 4, 7, 8];

b. to refine the coarse aluminium/magnesium dendrites and resulting in recrystallized (equiaxed) grains. Furthermore, the grain size strengthening efficiency in Mg alloys is much higher than that in Al and other alloys, meaning that grain refinement in Mg alloys is more beneficial [9];

c. to break-up the coarse precipitates and dissolve part or most of them into the matrix;

d. to eliminate the casting porosity.

As FSW and FSP are thermomechanically the same process, we will use the term “FS” to represent the general friction stir technology.

1.1.2 Current Understanding: an Overview

Research associated with FSW was reviewed by Mishra et al. [1], Nandan et al. [10], and Threadgill et al. [11]; and a review on FSP (up to 2007) was given by Ma [3]. All researchers pointed out that, despite the extensive applications, the scientific research of the FS process is far from being complete.

Research topics associated with FSP cover an extremely wide range. Here, however, we try to use the following schematic (Figure 1-2) to summarize and divide the key quantities and features of FSP into four domains, which are the inputs domain, thermomechanics domain, transient microstructure domain and final microstructure and property domain respectively.

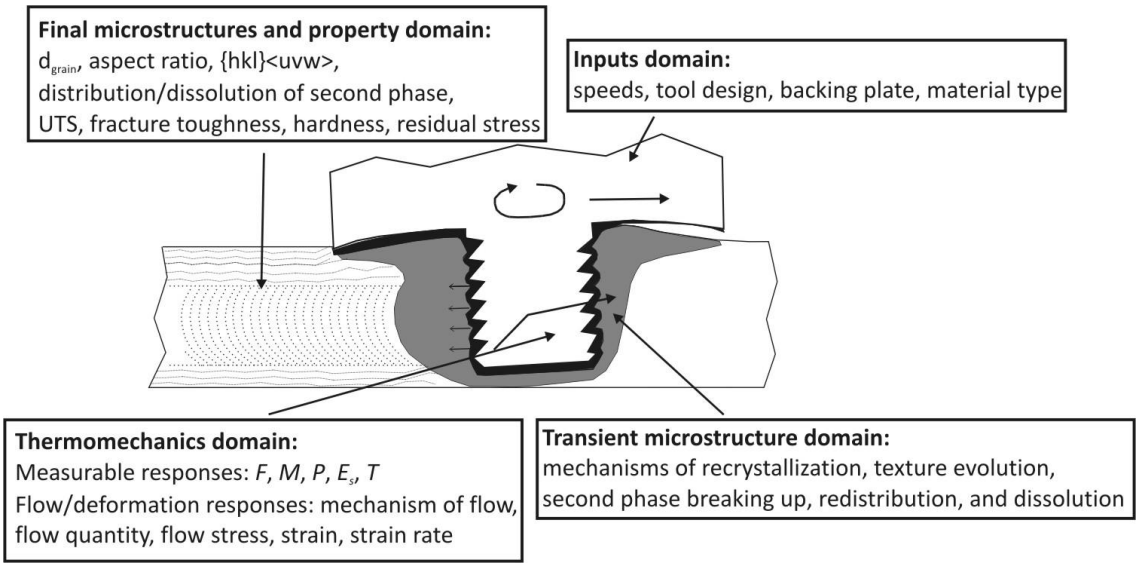

Figure 1-2. Schematic illustration of FSP. Physical quantities addressed in this thesis are summarised into five domains as illustrated.

The inputs domain refers to quantities which can be chosen independently, such as the processing speeds (v and ω), tool design, type of backing plate, and base materials. The final microstructure and property domain refers to the resultant material characters after FSP, such as grain size, aspect ratio, grain orientation, re-distribution and dissolution of secondary phase, strength (UTS), fracture toughness and hardness of the processed material.

The thermomechanical principle of FSP is that: external energy is input into the workpiece through the tool, which softens the material, and the latter is deformed

and transported by the tool. During FSP, the material which is in close contact with the tool is referred as the "stir zone". Work is done by the tool as it rotates and translates against the material, and therefore the energy input (per unit time and per unit length) by the tool (P and E_s) is directly related to the torque (M) and linear force (F_x) required by the rotation and translation of the tool. This energy input causes temperature of the stir zone (T) to rise. These quantities, as FSP reaches a steady-state condition, can be directly measured by using devices such as a strain gauge and thermocouple. Softened material in the stir zone is plastically deformed and transported by the tool. Therefore, the local strain (ε) and strain rate ($\dot{\varepsilon}$) experienced by the material as it is deformed, the paths of material flow, and the quantity of the flow are important flow/deformation responses to be considered. However, although some of these responses are quantifiable, they cannot be directly measured using standard instruments. Therefore, measurable responses, and flow/deformation responses together constitute the thermomechanics domain.

The initial microstructure (which belongs to the input domain of Figure 1-2) of the material which locates ahead of the tool starts to evolve as the tool induced deformation and material transportation become significant. Microstructural evolution is largely accomplished once the material deposits at the back of the tool, thus the final microstructure (i.e. the microstructure after FSP) is formed. We use the term transient microstructure to describe the evolving microstructure of the material while it is in contact with the tool. Thus, the transient microstructure domain includes the following key physical features: the mechanisms of material recrystallization, associated texture evolution, and for some cast alloys, the mechanisms of mechanical breakage, re-distribution and dissolution of the second phase particles. To observe the transient microstructure, tool-stop technique [12-15] is usually implemented which involves stopping the tool motion in a sudden manner to obtain tool/workpiece couple so that real-time tool/material interaction can be studied.

These Four domains combined together should cover the bulk of the physical quantities and features associated with FSP. That being said, it is important to note

that, in theory, all these quantities relate to one another in a direct or indirect way. Next, we will try to give a brief overview of the major knowledge gaps with regard to the thermomechanical responses and transient microstructure associated with FSP of cast Al-Si and Mg-Al alloys, which are the major focuses of this thesis.

From a process-control point of view, the relationships between input speeds (ω and v) and (steady-state) measurable responses ($F/M/P/E_s$) are of great importance. The general trends of how speeds can influence $F/M/P/E_s$ were reported in literature [16-24]. However satisfactory (physically meaningful) quantitative models, $F/M/P/E_s$ = f(ω, v), have not yet been developed. On the other hand, the general trends of how speeds affect material flow quantity (being an important quantifiable flow response) were also reported [25-32], despite the fact that flow quantity under various FSP speeds has never been precisely determined. Moreover, there have been few studies on the quantitative interrelationships between measurable responses and flow quantity, i.e. $F/M/P/E_s$ = f(flow quantity), although these relationships are generally important for the understanding of the thermomechanics of FSP.

The underlying mechanism of material flow during common FSW (of wrought Al alloys) was well studied by adopting various flow visualization techniques, such as the flow marker/sheet insert technique [33-36], pin stop and pin breaking technique [12, 14, 37-39]. These techniques will be illustrated more in Section 1.4. However, it can be shown that material flow during FSP (of a cast Al-Si alloy) could be significantly different from that of common FSW [40]. But this different flow mechanism has not been adequately investigated in literature. Thus, how various parts of the processed zone are formed (during FSP cast Al-Si alloys) must be studied in details as such knowledge is fundamental to the understanding of the overall thermomechanics of the FSP. In particular, this knowledge is crucial for controlling the material flow so that desirable microstructural formation can be achieved.

On a micro-scale, the details of deformation, such as the strain and strain rate, are important as they play a vital role in the subsequent microstructural evolution and thus directly affect the final microstructures and the quality of FSP. Strain and

strain rate were widely reported in literature for FSW wrought alloys [41-46], mostly based on 3D FS modelling. However, truly accurate FSW models have not yet been developed despite the fact that extensive effort has been made. This is primarily because the understanding of the underlying thermomechanics of FSW is still far from being complete. Therefore, experimental work is still required to accurately determine the strain and strain rate experienced by the material during FSP.

Now let us consider the transient microstructure (which occurs closely ahead of pin) during FSP. The mechanism governing the microstructural evolution is generally regarded as dynamic recrystallization. Furthermore, extensive grain orientation analysis suggested the final recrystallized microstructures (of FSW wrought Al alloys), all display strong shear textures. However, such studies have not been adequately extended to FSP cast Al-Si alloys. Considering that macro-scale material flow and micro-scale deformation during FSP Al-Si cast alloys could potentially differ from those of common FSW, it is necessary to clarify the mechanism by which recrystallization takes place during FSP Al-Si cast alloys. Moreover, how the Si particles are mechanically broken down, and evenly re-distributed among Al matrix are still not fully understood in current literature.

For cast Mg-Al alloys, FSP results in (near) complete removal of second phase particles ($Mg_{17}Al_{12}$). However, the exact mechanism by which these particles are removed is believed to be through mechanical breakage and solid-state diffusion [4, 47]. It was suggested that the diffusion rate must be significantly increased (up to 1000 times) [4] in order to fully dissolve the second phase within the time available during FSP. It must be pointed out that due to the lack of observation on the real-time tool/material interface, assumptions being made regarding to the increase in diffusion rate might not be realistic. Therefore, it is important to directly observe the initiation and the sequence of the removal of the second phase during FSP cast Mg alloys, in order to clarify the exact mechanism governing the removal of the second phase.

Following on the above brief comments on the major knowledge gaps associated with FSP, a detailed literature review on the (inter)relationships between speeds,

measurable and quantifiable thermomechanical responses will be given in Section 1.3. Detailed review on the mechanism of material flow and deformation (strain and strain rate) will be given in Section 1.4; following by detailed review on various aspects of the transient microstructure during FSP (Section 1.5), which includes mechanism of recrystallization, texture evolution, and the refinement and/or removal of secondary phase. However, an introduction on the microstructures of commonly used cast Al-Si and Mg-Al alloys will be given first in Section 1.2, this is because the initial microstructure inevitably influences the transient microstructure during FSP.

It is important to note that material flow and transient microstructure induced by the pin will be focused, rather than those induced by the shoulder. This is largely because under normal FSP conditions, the pin induced flow zone is much larger than the shoulder induced flow zone (see Figure 1-14). Furthermore, the threaded pin induces (in general) more complicated material flow, more intensive material deformation and thus more complete microstructural refinement. Following this detailed literature review, the aims and specific aspects, plus the sequence of this PhD research will be given.

1.2 Microstructures of Cast Al-Si and Mg-Al Alloys

The formation of the as-cast microstructures of Al-Si and Mg-Al alloys will be introduced in this section. The as-cast microstructure usually has two unique features: the primary dendrites and interdendritic eutectics. The solidification mechanisms (during commercial casting process) governing the formation of the dendrites will be illustrated in Section 1.2.1. How regular (in Al-Si alloys) and divorced (in Mg-Al alloys) eutectics form during casting will be given in Sections 1.2.2 and 1.2.3 respectively.

1.2.1 Dendrite Formation during Commercial Casting

During casting, the solidification of primary matrix material starts when equilibrium liquidus temperature ($T_{liquidus}$) is reached. Here we use the

solidification of A356 alloy as an example, α-Al will start to nucleate (i.e. solidify) as the temperature cools below 615 °C (indicated in Figure 1-3). Due to the existence of alloying elements, nucleation occurs at various locations in the liquid.

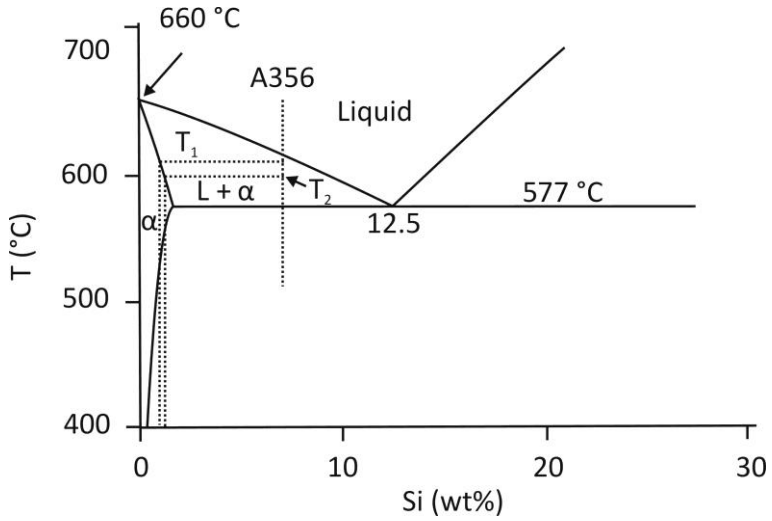

Figure 1-3. Al-Si phase diagram.

As the temperature reduces further, the nucleated α-Al grows while rejecting solute (Si for A356) to the liquid surrounding them. The solidified α-Al forms a dendritic structure. A schematic of the growth of multiple dendrites during casting of A356 alloy is given in Figure 1-4. On a primary dendrite trunk, multiple secondary dendrite arms can grow. The formation of dendrites is a common feature of commercial ingot casting, i.e. during casting Mg-Al alloys (e.g. AZ91), the solidified α-Mg will also display a dendritic morphology.

The formation of the dendritic structure is due to a well known phenomenon called "constitutional undercooling". The thermodynamics associated with this phenomenon will not be presented here however the detailed description is available in metallurgy textbooks [48] (Chapter 14.10–14.13).

For casting of metals with cubic unit cells (e.g. Al), the dendrites (both primary and secondary) grow in the crystallographic <100> directions, while for hexagonal close-packed metals (e.g. Mg) the growth direction is along $\langle 10\bar{1}0 \rangle$ direction [48] (page 446). During commercial casting, the direction of heat lost (as suggested in Figure 1-4) is perpendicular to the mould walls, and therefore the growth of the dendrites trunks/arms which approximately align with the heat lost direction is

favoured. For example, the primary trunks of three dendrites are marked by the dashed lines (Figure 1-4), and their growth is favoured because the trunks align well with the heat lost direction.

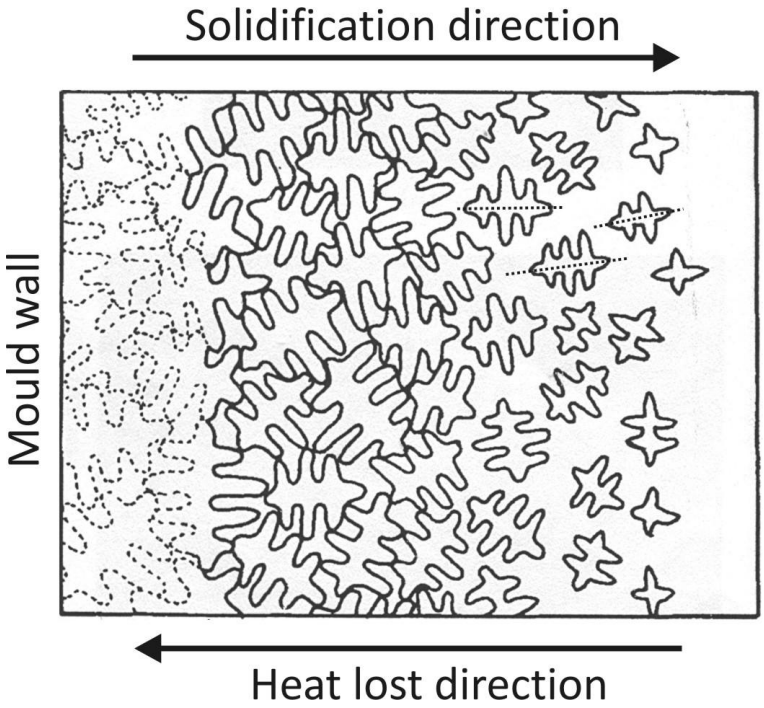

Figure 1-4. Schematic of the formation of dendrites during commercial ingot casting of A356 alloy [49]. The solidification and heat lost directions are indicated.

As the dendrites grow while the temperature continuously decreases during the casting process, the outer portion of the dendrites always has higher solute concentration than the inner portion. Let us use A356 as an example: referring back to Al-Si phase diagram (Figure 1-4), at a later stage during solidification, the outer portion of the dendrite solidifies at a lower temperature (say T_2), while the inner portion solidifies at a higher temperature (say T_1). This causes the Si solute concentration to be higher in outer portion of the dendrites than the inner portion. Such an effect is known as macro-segregation.

1.2.2 Formation of a Regular Eutectic

As the solidification proceeds, the temperature of the remaining liquid (A356) eventually reaches the eutectic temperature ($T_{eutectic}$ = 577 °C) of the alloy, while the solute concentration of the liquid reaches eutectic composition (12.5 wt% of

Si). At this stage, the solidified α-Al dendrites already occupy most of the ingot, the formation of the eutectic must occur between these dendrites.

As the temperature drops below the eutectic temperature, eutectic reaction will take place, during which a two phase structure "α + β" will be formed. During this transformation there must be a redistribution of the Al and Si components, to the extent that the Al and Si phases have different compositions neither of which is the same as that of the liquid (12.5 wt% of Si). This redistribution is accomplished by atomic diffusion. The microstructure of a regular eutectic consists of alternating layers of the Al and Si phases that form simultaneously during the eutectic reaction. A schematic of a regular Al-Si eutectic structure is represented in Figure 1-5.

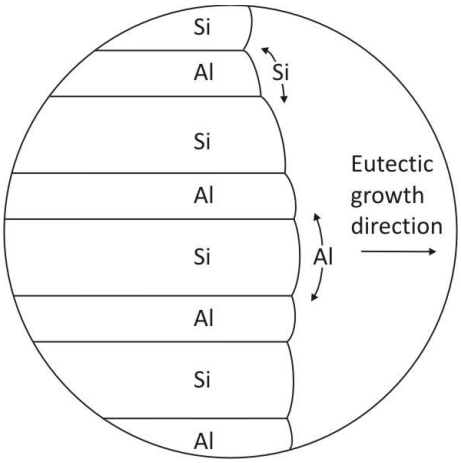

Figure 1-5. Schematic representation of the formation of the eutectic structure for the Al-Si system. Directions of diffusion of Al and Si atoms are indicated by arrows respectively.

A low and high magnification micrographs of as-cast A356 alloy are given in Figure 1-6a and b respectively. In these micrographs, both matrix and eutectic Al appears white, and the Si particles appear black. The dendritic structure of the matrix Al can be well recognized in Figure 1-6a. The rather regular Al-Si eutectic structure can be readily observed in Figure 1-6b.

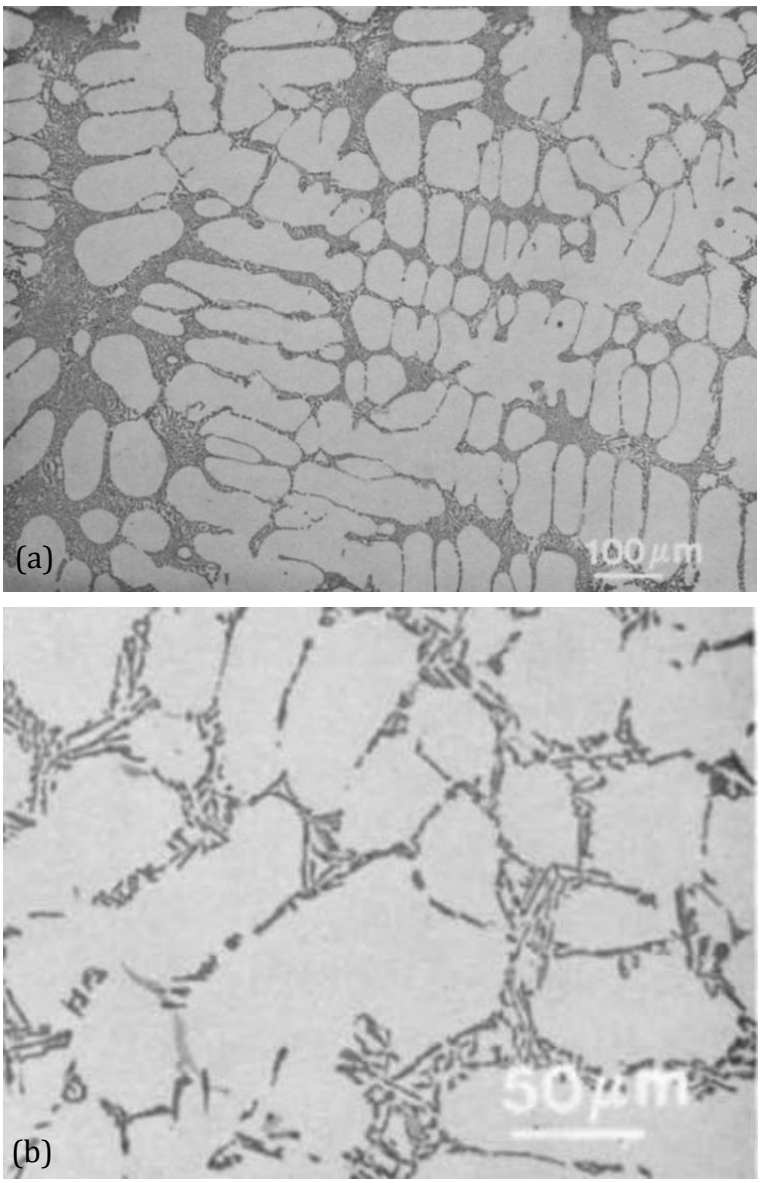

Figure 1-6. (a) A low magnification and (b) a high magnification micrographs of as-cast A356 alloy. Matrix and eutectic Al appears white, while Si particles black [50].

1.2.3 Formation of Divorced Eutectic

During commercial casting of Mg-Al alloys, the interdendritic eutectics display a divorced morphology, which is different to the normal eutectics observed in A356. The low magnification micrograph taken from a cast Mg-15Al plate is presented in Figure 1-7a, from which the dendritic structure of matrix Mg can be clearly identified. A fully divorced morphology refers to one within which the α and β phases are completely separated in the interdendritic regions. An example is marked by arrow "1" in Figure 1-7b, which was taken from an as-cast AZ91 plate

[51]. A partially divorced eutectic morphology is characterised by α-Mg "islands" within the β-particles, but the bulk of α-Mg is still outside the β-particles. An example is marked by arrow "2" in Figure 1-7b. After solidification, lamellar α + β can be formed by discontinuous precipitation, usually near large as-cast β-particles, which display a lamellar structure (α + β), as pointed by arrow "3". A high magnification on this two phase structure is given in Figure 1-7c.

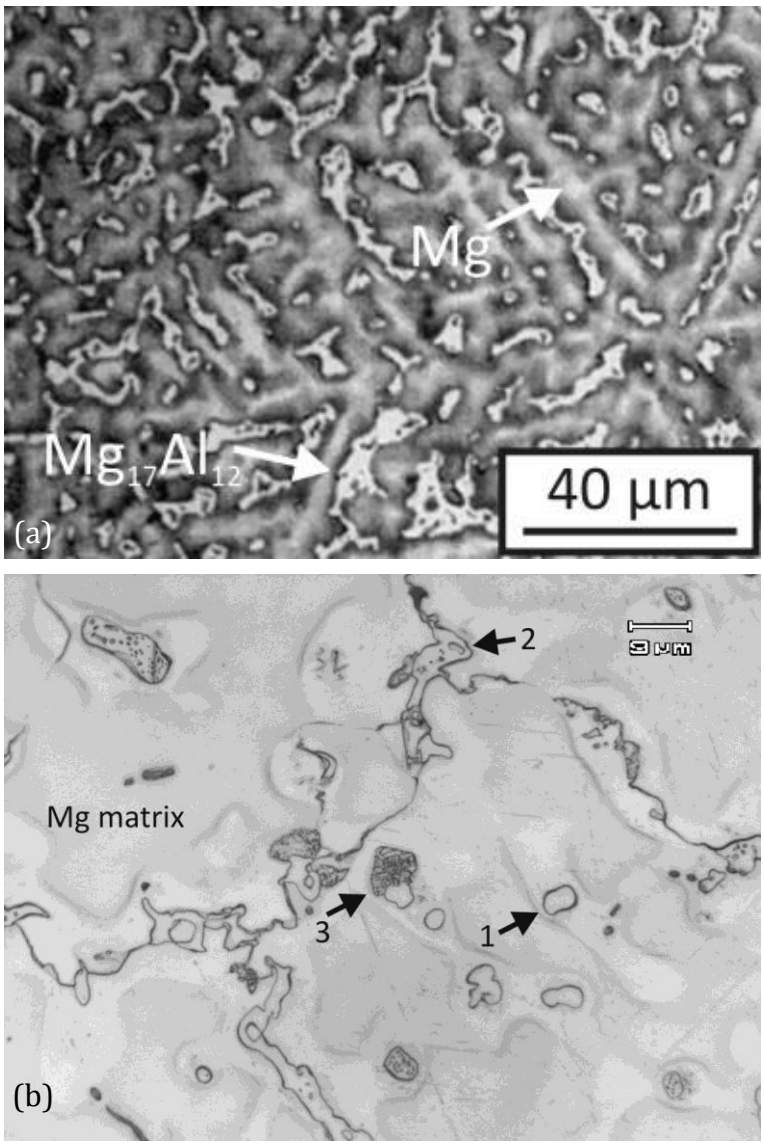

Figure 1-7. (a) A low magnification microstructure showing a well developed dendritic matrix in a Mg-15Al cast alloy [52]; (b) a high magnification microstructure showing fully and partially divorced β-particles in Mg-9Al alloy (AZ91) alloy [51]; (c) an enlarged view on the eutectic formed due to discontinuous precipitation. Matrix Mg appears white, $Mg_{17}Al_{12}$ particles light grey.

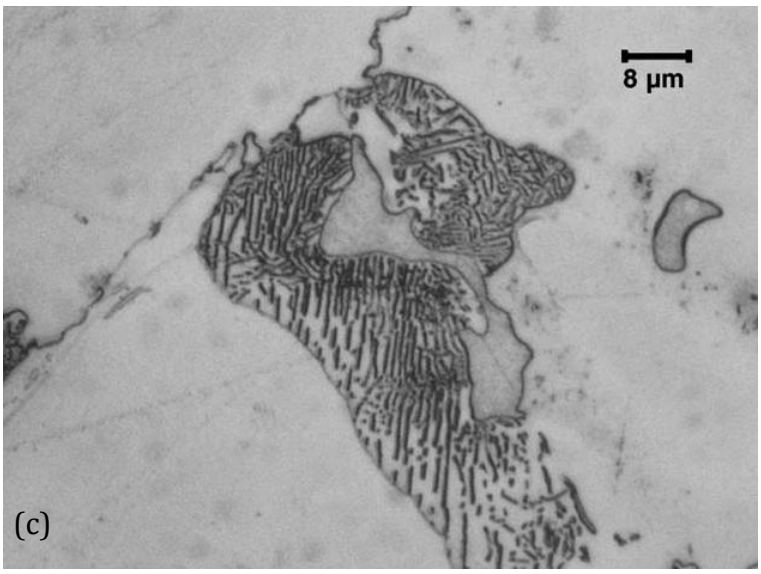

Figure 1-7. Continued.

The formation of fully divorced eutectic can be explained by using the following Mg-Al phase diagram (Figure 1-8). As explained by Dahle et al. [52], as the temperature drops below the liquidus temperature, the formation of α-dendrites will begin and the interdendritic liquid will be enriched in Al. As equilibrium eutectic temperature ($T_{eutectic}$) is reached, the remaining liquid should have reached the eutectic composition (33 wt% of Al). For the case of AZ91, the Al content is 9 wt%, which is far below the eutectic composition. This implies that by the time the eutectic composition is reached, the volume fractions of the solidified Mg dendrites are expected to be very high, while the liquid fraction is very low. This severely restricts eutectic solidification (of the remaining liquid) to small and isolated regions between Mg dendrites. Hence, nucleation of the β-particles is required at each individual region, which is very difficult to occur.

As a result, the formation of Mg dendrites continues, following the extension of the solidus line (marked as "1" in Figure 1-8), thus driving the remaining liquid undercooled with Al content passing beyond the eutectic composition (following curve "2"). Dahle et al. [52] suggested that the extended liquidus line passes the hypothetical couple zone. Within this zone, the eutectic solidification involves the simultaneous formation of α and β phases; while beyond this zone, the β-phase is the leading phase during eutectic solidification. As the undercooling intensifies, the extended liquidus line gradually approaches the hypothetical β-phase boundary

(curve “3”). Theoretically, this process eventually stops as curve “2” and “3” meet. Under this condition, the composition of the remaining liquid is very close to the composition of the (non-equilibrium) β-phase. Hence, the remaining liquid solidifies into β-phase only, resulting the β-phase being completely separated from the dendrites. Thus, fully divorced β-particles are only to be expected.

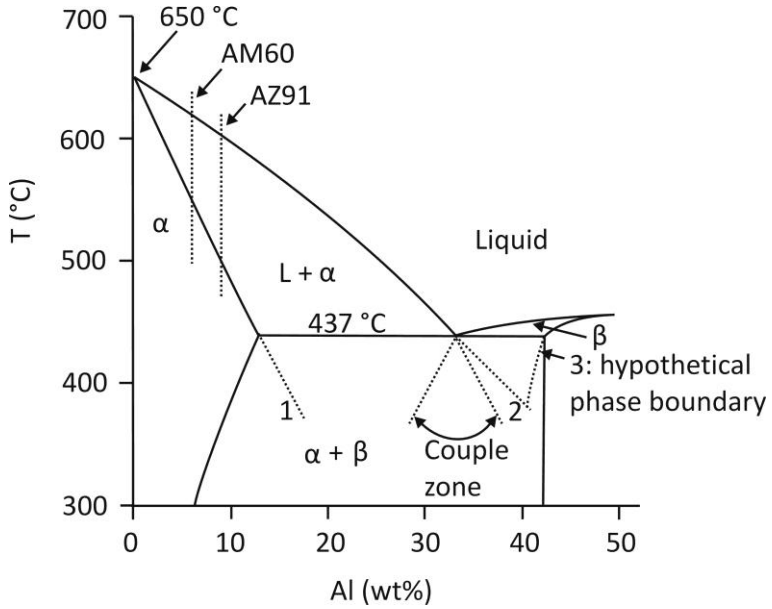

Figure 1-8. Mg-Al phase diagram [52]. Line 1, and 2 are the extended solidus and liquidus lines; while line 3 is the hypothetical phase boundary of the β-phase. Within the couple zone eutectic α and β should grow together; while to the right of the couple zone the β-phase is the leading phase during eutectic solidification.

Now let us consider the solidification sequence of the Mg-Al alloy (using AZ91 as an example) in more details so that the Al distribution in the alloy can be revealed. Zhu [51] used Figure 1-9 to schematically illustrate the microstructure (with fully divorced β-phase) and composition of a solidifying AZ91 alloy at various temperatures according to the binary Mg-Al phase diagram. $T_{initial}$ and T_{end} are the temperatures at which the formation of β-phase initiated and ended, respectively. $C_{initial}$ and C_{end} are the (Al) compositions of β-phase formed at $T_{initial}$ and T_{end}, respectively. At temperatures of T_1, $T_{eutectic}$, $T_{initial}$, T_2, and T_{end}, as marked in Figure 1-9a, Al distributions between two α-Mg dendrites are described by the solid lines in Figure 1-9b to Figure 1-9f. Mg dendrites, liquid, and β-phase are marked as white, squared, and grey respectively.

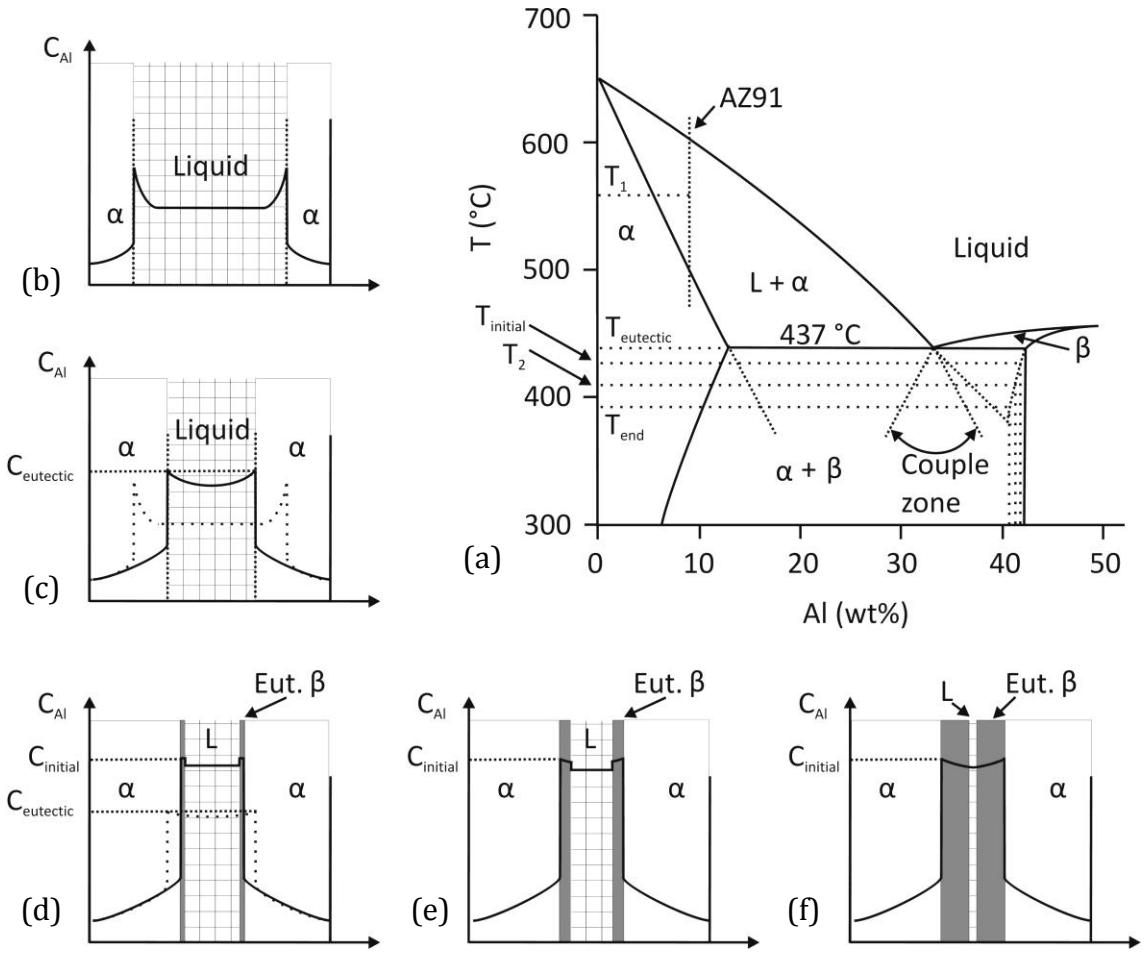

Figure 1-9. Schematic illustration of solidification sequence during the casting of AZ91 alloy [51]: (a) equilibrium Mg-Al phase diagram and extended solidus and liquidus representing non-equilibrium compositions of α, β and liquid phases, (b) Al rejected into liquid and build-up in liquid at T_1, (c) reaching eutectic composition in liquid at $T_{eutectic}$, (d) initial β-phase precipitation at interface of α and undercooled liquid in interdendritic regions at $T_{initial}$, (e) progress of β-phase precipitation during continuous cooling to T_2 between $T_{initial}$ and T_{end}, and (f) last liquid solidified in the middle of β-phase at T_{end}.

Zhu explained that as the temperature decreases from the liquidus temperature of AZ91 to T_1 (Figure 1-9b), the primary α-Mg dendrite keeps growing, and the Al content in the dendrite growth direction keeps increasing. Due to the growth of dendrites, Al is rejected into the interdendritic liquid and built up at solid/liquid interface. Cooling to $T_{eutectic}$, as shown in Figure 1-9c, the primary α-Mg has grown substantially, and the Al content in the liquid reaches the eutectic composition. Non-equilibrium solidification, with the difficulty of β-phase nucleation, results in the departure from the normal eutectic solidification (during which α and β growing together). Thus, as the temperature drops below $T_{eutectic}$, the α-Mg phase

continues to grow (following the extended solidus line), while driving the liquid undercooled with Al further accumulated in the liquid (following the extended liquids line).

The formation of β-phase with composition of $C_{initial}$ initiate at $T_{initial}$ when the liquid is sufficiently undercooled, as depicted in Figure 1-9d (assuming complete mixing in the interdendritic liquid at this stage). Since the composition of the undercooled liquid has passed beyond the couple zone, only the formation of the β-phase is expected, hence the Mg dendrites will not grow further.

Further cooling results in the growth of β-phase with reduced Al content following the non-equilibrium solidus line of β-phase (Figure 1-9e). The last liquid in the middle of β-phase solidifies at T_{end} with an Al content of C_{end}. The solidification (of a fully divorced β-phase), then, completes (see Figure 1-9f), forming β-phase particles with Al content decreasing from α/β interface to the middle of β-phase particle which corresponds to the different melting temperatures. For the clearness of illustration, $T_{initial}$ is not drawn to be much lower than $T_{eutectic}$. However, as previously illustrated, the formation of fully divorced β-phase is promoted by a large undercooling, i.e. $T_{initial}$ should be significantly lower than $T_{eutectic}$.

1.3 Thermomechanical Reponses of FSP

Referring back to Figure 1-2, thermomechanical responses of FSP can be subdivided into measurable responses and flow/deformation responses, and they interrelate to one another in a direct or indirect way. In this section, detailed review on the interrelationships between speeds (being the most important input parameters), measurable responses ($F/M/P/E_s$), and a quantifiable flow response (flow quantity) will be given.

We will first present how speeds qualitatively influence $F/M/P/E_s$ and flow quantity. Then, the current understanding on the interrelationships among speeds, $F/M/P/E_s$ and flow/deformation responses will be given. Lastly, analytical FS

thermomechanical models, based on the current understanding of these interrelationships, will be briefly addressed.

1.3.1 Relationships between Speeds and Measurable Responses

As previously illustrated, energy is generated as the tool is rotating and translating against the workpiece, therefore torque (M) and linear force (F_x) required by the tool to overcome the material resistance are related to energy input during FSP. Energy input per unit time (P), and per unit length travelled (E_s) are calculated as:

$$P = M\omega + F_x v \approx M\omega \qquad \textit{Equation 1-1}$$

$$E_s = \frac{P}{v} \approx M\frac{\omega}{v} \qquad \textit{Equation 1-2}$$

F_x and M can be directly monitored by using strain gauges (placed on the tool). The term associated with the forward force ($F_x v$) is normally < 1% of the total tool energy and thus can be ignored [22]. P has a unit of J/s while E_s has a unit of J/mm.

The rise of temperature is a consequence of energy input (P and E_s). It is generally understood [18, 19, 53, 54] that the temperature (T) histories of the workpiece during FSP can be described by the Rosenthal solution for temperature distribution during welding [55]. The measured P was used as the heat input in the Rosenthal model [18, 19, 54]. However, heat loss through the backing plate and through the tool also needs to be considered [20]. This consideration of heat partition depends on the degree of sophistication used in estimating the temperature distribution and P (and thus M) remains essential for such estimation.

Experimental investigations on the direct relationships between speeds and measurable responses ($M/P/E_s/T$) have been widely addressed in literature [16-24, 56, 57]. Generally speaking, ω was treated as the primary variable while v was the secondary one. In any of these studies, experimental torque data was relatively limited. To be specific, there is very little data available at low and high ω range (< 300 rpm and > 1000 rpm); while v was commonly varied within a narrow range (100–300 mm/min). Nonetheless, some common trends (regardless of workpiece material and tool geometry) can be summarised as below, and these trends are also illustrated in Figure 1-10.

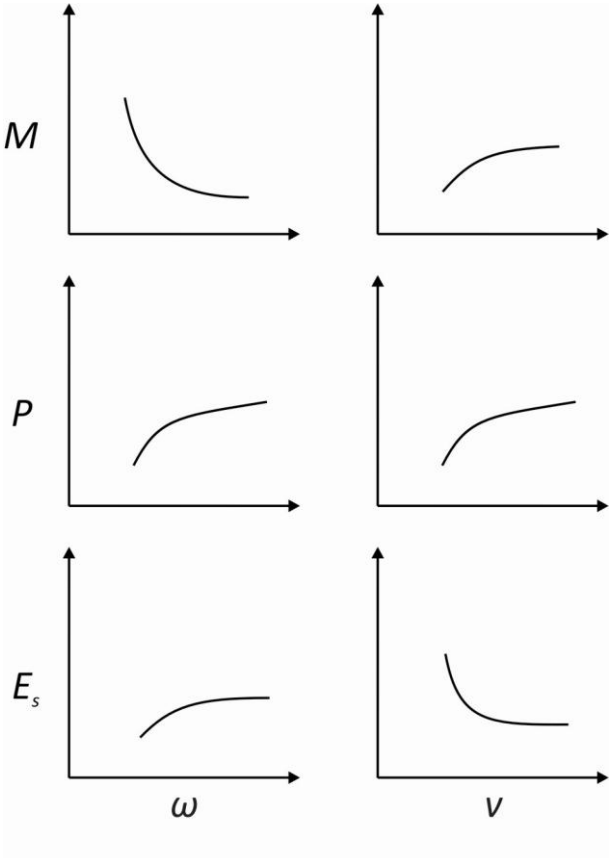

Figure 1-10. Schematic illustration of the effects of speeds on the measurable responses ($M/P/E_s$). Drawing is based on data available in literature.

It can be seen from Figure 1-10 that M is negatively related to ω while positively related to v. Furthermore, a strong and weak dependence of M on ω and v, respectively, were suggested [20, 56]. The effects of speeds on P are approximately the opposite of these on M [18, 23, 57]. P only moderately increases with the increases in ω and v. The relationships between E_s and speeds are scaled by a factor of $1/v$ from those between P and speeds. As a result, E_s has a weak positive relationship with ω, and a strong negative relationship with v.

Although M is primarily responsible for energy input during FSP, a model which directly relates M to varying speeds (M = f(ω, v)) has not been well developed, despite the fact that general trends between M and range of speeds were widely reported. A model:

$$M = K\frac{v^{\alpha}}{\omega^{\beta}} \qquad \textit{Equation 1-3}$$

where both α and β are positive values, was used in literature to describe the experimental data of M (measured using a strain gage attached to the machine spindle) verse ω and v [19]. M was measured with ω varying from 964 to 2000 rpm, which can be considered as a high range, while keeping v at 254 mm/min. This model can describe the observed trends as long as ω is not too low or too high. If M values for a wide range of ω are considered, Equation 1-3 becomes invalid. The equation implies that as $\omega \to 0$, $M \to \infty$, which is not physically reasonable and that as $\omega \to \infty$, $M = 0$, which is also unrealistic.

Alternative empirical models that describe M = f(ω, v) was also reported, expressed in polynomial forms derived from regression analysis of experimental M data and FSP parameters [22]. Torque data was recorded by varying ω and v between 200 and 800 rpm, and 51 and 279 mm/min respectively, both of which can be considered as a low-intermediate range. It can be shown that the torque model extrapolates poorly outside the experimental ω range. For example, for FSP conducted on 5.5 mm thick AA7075 plate with a linear speed of 279 mm/min, the torque model (Equation 1-4), where t represents thickness, predicts a value of 225 Nm at 200 rpm; while –183 Nm at 1400 rpm (which is not an unusual condition), which is obviously a wrong prediction.

$$M = -636.4 + 0.2584v + 159.5t + 0.5171\omega - 0.2013t\omega + 8.488 \times 10^{-4}\omega^2 - 4.860 \times 10^{-7}\omega^3 \quad \textit{Equation 1-4}$$

From the review given above, it is clear that there has not been a satisfactory quantitative torque model M = f(ω, v) in literature. Although ω has been treated as a more important variable compared to v, a detailed quantitative study on the sensitivity of $M/P/E_s$ to ω and v cannot, and has not been conducted due to lack of a reasonable torque model. Nonetheless, a physically meaningful torque model is generally important for the field of FS, and it is especially important for FS processing control and optimization.

1.3.2 Relationships between Speeds and Flow Quantity

The shoulder and pin generate a shoulder flow zone and nugget flow zone respectively. The geometry of each flow zone, under a normal FSP condition, can be observed in Figure 1-14 (page 28). In general, the shoulder flow zone (locating above) is much wider than the nugget zone (locating below); while the nugget zone usually displays an "onion-ring" structure (which is apparent in Figure 1-14). The mechanism governing the formation of the flow zones will be discussed in Section 1.4, and only the quantity of the flow zone will be considered in the current section.

Flow quantity is an important quantifiable flow response (refer to Figure 1-2) and how it (qualitatively) relates to input speeds has been widely reported in literature [23, 25-27, 30-32, 56, 58]. A series of FS experiments were performed on a wrought Al alloy with ω varying between 200 rpm and 542 rpm, by Arbegast [25], and the associated cross section macrographs are given in Figure 1-11a. Zones I and II represent the advancing and retreating side of the nugget zone (caused by pin), zone III represents the flow zone induced by shoulder drag, material from zone II may flow downward thus reaching below the pin, forming zone IV. The division between adjacent flow zones was based on the difference in flow direction. However how the flow direction was determined has not been well illustrated by the author. It was pointed out that the area of shoulder induced flow ($A_{shoulder}$, represented by zone III) increases as ω increases (as shown in Figure 1-11a). The author suggested this is due to the excessive heating (softening effect) causing the shoulder-material interface reaching a sticking dominant condition. The thickening of the shoulder zone inevitably causes the nugget zone (Zone I and II) to compress, thus reducing its volume. However, it must be pointed out that the precise contact condition at the shoulder/workpiece interface, i.e. whether slip or stick dominant, has never been clearly determined in current literature. Hence, it is reasonable to state that their suggestion is only conceptual in nature.

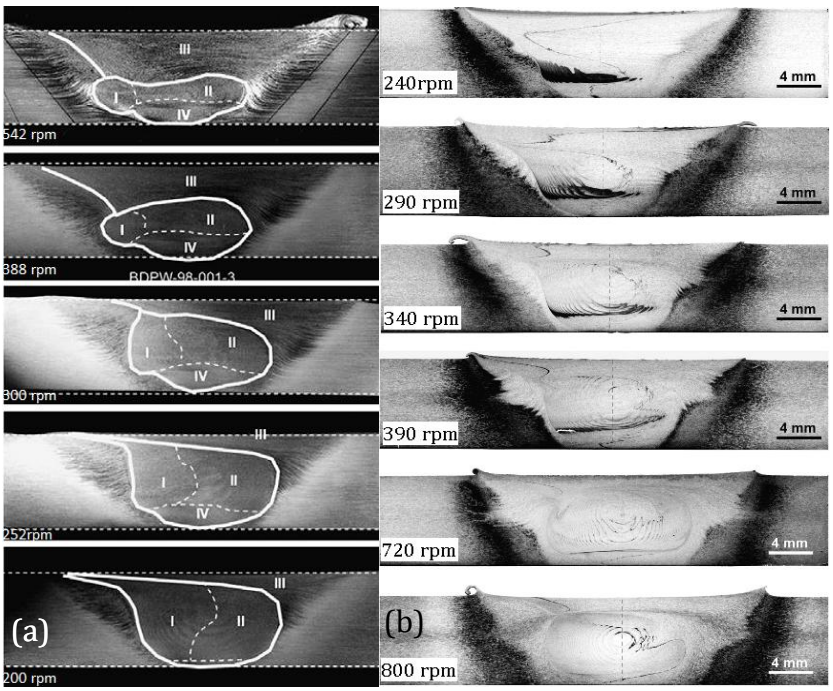

Figure 1-11. Cross section views during FSW, (a) reported by Arbegast [25] and (b) reported by Xu et al. [26]. Opposite effects of increasing ω on the flow zone formation can be observed: a higher ω results in a larger shoulder flow zone in (a) and a smaller shoulder flow zone in (b).

In general, Arbegast's observation is in contradictory to the common observation reported in literature. It is commonly observed that either increasing ω or decreasing v results in a smaller $A_{shoulder}$ and a larger nugget flow zone (A_{nugget}). This can be demonstrated by comparing the cross sections of FS conducted on AA6061 alloy by varying ω from 240 to 800 rpm while keeping v at 142 mm/min, as given in Figure 1-11b. Furthermore, it has been experimentally and numerically demonstrated that a higher ω or a lower v would result in an overall larger stir zone ($A_{total} = A_{shoulder} + A_{nugget}$) [23, 56]. Beside the aforementioned general observations, the material flow quantities of individual and combined flow zones under various FSP conditions have never been precisely determined in current literature.

1.3.3 An Overview on the Interrelationships among Thermomechanical Responses

As discussed previously, input parameters and all thermomechanical responses interrelate to one another in a direct or indirect way. How measurable responses ($M/P/E_s/T$) relate to quantifiable flow response (e.g. flow quantity) is generally

important for the field of FSP. This is because from a processing control point of view, state-of-art processing inputs can be developed which yield both large amount of refined material, while not requiring excessive amount of force/torque and energy inputs.

Now let us review the current literature on interrelationships between flow quantity and measurable responses. Based on comparing CFD (computer fluid dynamics) modelled material flow lines to experimental macrographs (as indicated in Figure 1-12, where ω increases from 400 rpm to 1600 rpm), Colegrove et al. [58] suggested that the reduction in shoulder flow area ($A_{shoulder}$) is fundamentally related to the rise in temperature in the shoulder zone ($T_{shoulder}$). The increase in $T_{shoulder}$ (as ω increases) leads to significant material softening effect (i.e. lower σ_{flow}). Strengthening of σ_{flow} due to the increase in strain rate (caused by greater surface velocity as a result of increasing ω) is not significant enough to compensate the decrease in σ_{flow}. To be specific, flow stress is related to temperature and strain rate through the well known Zener-Hollomon relationship:

$$Z = \dot{\varepsilon} exp\left(-\frac{Q}{RT}\right) = A\left(\sinh \alpha\sigma_{flow}\right)^{n} \qquad \textit{Equation 1-5}$$

Therefore, the author suggested that a greater softening effect, which occurs under a higher ω (and thus a higher $T_{shoulder}$) condition, causes less material to stick with the rotating shoulder (thus a smaller $A_{shoulder}$).

In another study, Mishra [1] showed that a higher energy input corresponds to a larger nugget zone (A_{nugget}). The author used a pseudo-heat index (ω^2/v) to represent the energy input, instead of the more commonly used P and E_s. From the review given above, it seems that energy input (and temperature rise) relates to the material flow quantity.

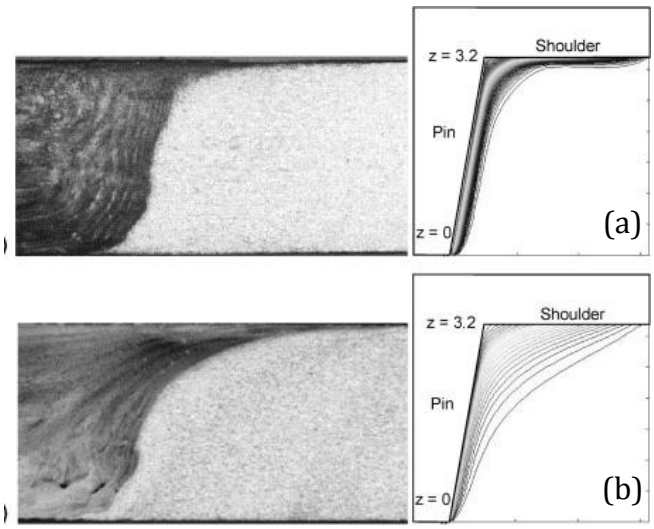

Figure 1-12. Comparison between macrographs (ω = 1600 rpm at the top and ω = 400 rpm at the bottom) and the shapes of predicted velocity fields during FSW AA2124 [58].

However, despite the attempts of interrelating flow quantities to various measurable responses, there has not been a clear and quantitative understanding of this interrelationship. One crucial reason for this lack of understanding is that material flow (under various FSP speeds) has not been systematically quantified, and thus the (possible) quantitative relationship between flow quantity and measurable responses cannot be investigated.

1.3.4 "Self-limiting" Effect and Temperature

Since the thermomechanical responses interrelate to, and thus constrain, one another, an important effect results, which is known as the "self-limiting" effect of FSP. The net result is that (bulk of) the workpiece does not melt regardless of the input parameters. This is because as stir zone temperature (T) approaches the melting temperature of the workpiece, the material flow stress (σ_{flow}) will be very low, thus the workpiece in contact with the tool can no longer resist tool rotation and translation. Hence, no further energy (P) will be input by the rotating and translating tool. As a result, it is a general understanding that the maximum attainable temperature (T_{max}) should be (approximately) governed by the lowest melting temperature of the workpiece. For well homogenized wrought Al alloys and cast alloys, the lowest melting temperature should be the solidus temperature ($T_{solidus}$) and eutectic temperature ($T_{eutectic}$) respectively.

From the review above, it is clear that T relates to measurable responses and flow/deformation responses together because it significantly influences material flow stress, and inevitably material flow and torque. Furthermore, T directly affects the (transient) microstructural evolution during FSP. For example, the final grain size is related to the Zener-Hollomon parameter (Z) [42, 46, 59], which is further related to T (refer to Equation 1-4). Moreover, T is also an important factor which controls the removal of second phase particles during FSP Mg alloys, as it is believed that the mechanism governing the removal is solid-state dissolution [47] (see Section 1.5.6 for details). In the following paragraphs, experimental measurements of T at various locations (close-to-tool) during FS experiments will be addressed, in order to reveal the thermal condition in the stir zone.

The temperature experienced by the material will increase as the tool approaches and will reach the highest level once it is in contact with the tool. Nonetheless, it is experimentally difficult to measure the temperatures at locations very close to the tool because the intensive material flow induced by the tool will displace the thermocouples away from their original locations. Perhaps the most reliable way to estimate the temperatures at tool/pin interface is by placing thermocouples within tools, while keeping the distance between thermocouple tip and tool surface as small as possible [18, 59-62]. Thermocouple locations and tool dimensions used in these investigations are given in Figure 1-13.

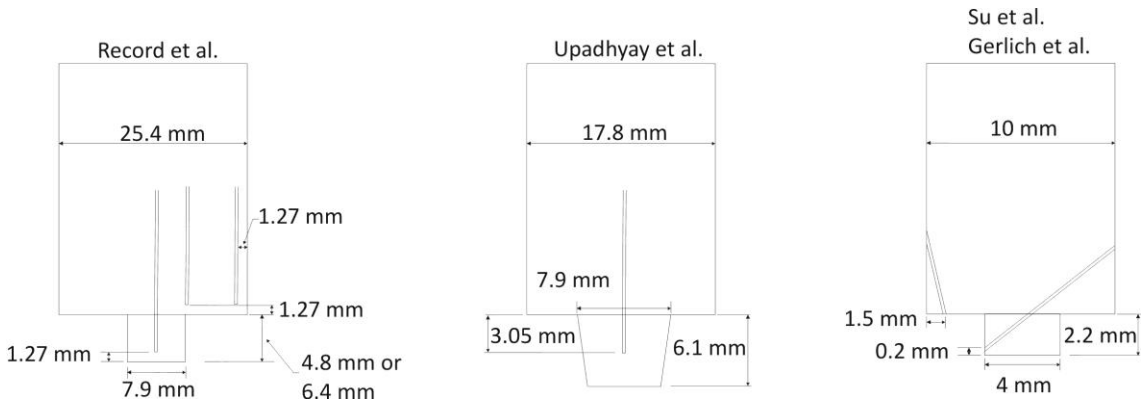

Figure 1-13. Thermocouple locations, and tool dimensions used by Record et al. [61], Upadhyay et al. [18], Su et al. [60] and Gerlich et al. [59, 62].

Upadhyay et al. [18] performed FSW experiments on AA7050 alloy (with $T_{solidus\text{-}7050}$ = 488 °C), using a tool with normal dimensions. At ω = 1000 rpm and v = 612

mm/min, temperature at centre of the pin (T_{pin}, indicated in Figure 1-13) has almost reached $T_{solidus\text{-}7050}$.

Gerlich et al. [59, 62] and Su et al. [60] conducted FS spot welding on wrought Al alloys (AA2024, 5754, 6061 and 7075) and AZ91D alloy respectively. During FS spot welding, the tool only rotates but not translates against the material. However, it is generally believed the "self-limiting" effect is valid for FS spot welding. For FS spot welding on wrought alloys (ω = 3000 rpm), T_{pin} was measured as 495, 565, 541 and 524 °C, for AA2024, 5754, 6061 and 7075 respectively. These measurements correspond to approximately $0.95T_{solidus}$ of each alloy. On the other hand, under ω = 3000 rpm (FS spot welding of AZ91D), maximum temperature at pin/material interface (T_{pin}, indicated in Figure 1-13) was measured as 453, 454 and 460 °C, with plunging speed equals to 2.5, 5 and 25 mm/s respectively. It is clear that T_{pin} has exceeded the eutectic temperature of Al-Mg alloys ($T_{eutectic}$ = 437 °C).

From the review given above, it can be concluded that the "self-limiting" effect of FS, as a generally accepted phenomenon, was well observed in FS wrought alloys. However, under some conditions, T_{pin} exceeded $T_{eutectic}$ during FS spot welding of cast Mg-Al alloy (e.g. AZ91D).

Furthermore, it was consistently proven that temperature at shoulder region is lower than that at pin region, regardless of material type and tool design. Record et al. [61] measured temperatures at three locations: 1.27 mm from pin bottom (T_{pin}), 1.27 mm from pin/shoulder interception (T_{root}), and 1.27 mm from shoulder rim ($T_{shoulder}$) during FS AA7075 alloy plates, conducted under different speeds. It was shown that T_{pin} is consistently higher than T_{root}, which is consistently higher than $T_{shoulder}$.

1.4 Material Flow during FS

Referring back to Figure 1-2, the macro-scale material flow and micro-scale material deformation (strain and strain rate) are important thermomechanical

responses of FS, although they are not directly measurable. Material flow and subsequent formation of the stir zone have been extensively studied particularly for FS wrought Al alloys. Under the commonly used conditions, the stir zone displays the so called “Onion Rings” structure. The flow mechanism leading to the formation of the “Onion Rings” structure is now quite well understood. However, there are conditions where “Non Ring” and “Partial Ring” structures are found but the corresponding forming mechanism has been rarely studied. We will describe the general features of the “Onion Rings” structure and discuss the material flow leading to this structure. Then, the features of “Non Ring” and “Partial Ring” structures will be illustrated. Lastly, the current understanding on the strain and strain rate of the deforming material during FS will be reviewed.

1.4.1 General Flow Features

A typical cross section of a FS 7075Al sample produced using a standard tool is shown in Figure 1-14 [1]. Based on microstructural characterization of grains and precipitates, three distinct zones: total stir zone (SZ), thermomechanically affected zone (TMAZ), and heat affected zone (HAZ) can be identified. The total stir zone contains shoulder flow zone and nugget flow zone which are induced by the shoulder and pin respectively. Intensive high temperature deformation results in recrystallized fine-grained microstructure within the stir zone. Unique to the FS process is the formation of a transition zone – TMAZ between HAZ and SZ. The TMAZ also experiences high temperature deformation, however not as intensive as in the stir zone so that generally no recrystallization occurs. On the other hand, dissolution of some precipitates can occur, and grains in TMAZ usually contain a high density of sub-boundaries. Beyond the TMAZ there is a HAZ, which experiences a thermal cycle but does not undergo any plastic deformation. The HAZ retains the same grain structure as the parent material. However, coarsening of precipitates and the widening of precipitate free zone (PFZ) can occur.

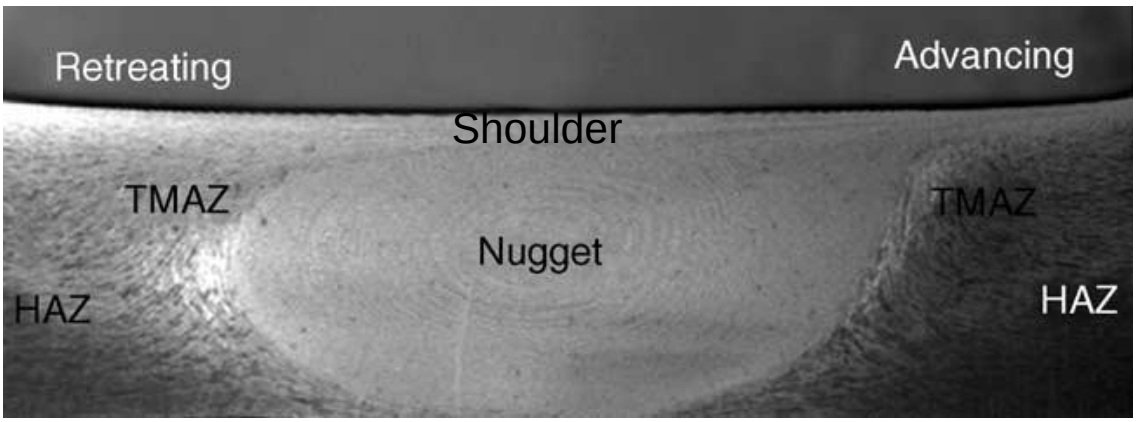

Figure 1-14. A typical macrograph showing various microstructural zones in FS 7075Al-T651. A standard tool was used, and ω = 400 rpm, and v = 51 mm/min [1].

1.4.2 Formation of "Onion Rings" Structure

Under normal FS conditions, the nugget zone usually occupies a very large portion of the stir zone, as is obvious in Figure 1-14. Furthermore, the cross section view of the nugget zone often displays the well known "Onion Rings" structure, if a standard tool with a simple threaded pin is used. Such a structure can be seen (Figure 1-15) very clearly in a FS AA2195 sample (top, appears dark) and AA6061 sample (bottom, appears light grey). Early studies [63, 64] have well demonstrated that the formation of "Onion Rings" is not symmetrical: stronger appearance can be found on the advancing side as opposed to the retreating side of the workpiece. On the plane section, the "Onion Rings" appear as the "banded" structure (Figure 1-16), which contains periodic flow layers, with thickness (λ) equals to tool travel distance per revolution (v/ω).

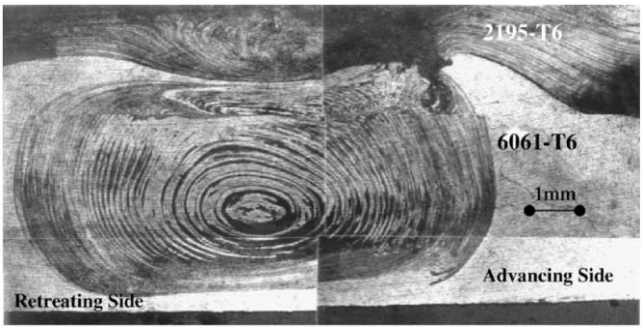

Figure 1-15. "Onion Rings" observed in FS performed on 2195 (on top) and 6061 (on bottom) alloys, with ω = 1000 rpm and v = 180 mm/min [64].

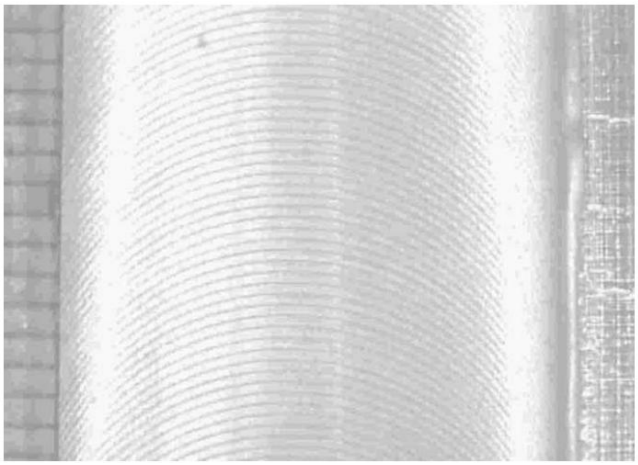

Figure 1-16. Plane section view of a FS performed on 6061Al plates, with v = 288 mm/min, and ω = 800 rpm [65]. The thickness of the bands is measured as 0.33 mm, which correlates well to v/ω, which is 0.36 mm.

Early studies [34, 63, 64] have suggested that the formation of "Onion Rings" is related to the combination of extrusion flow (primary) and vertical flow (secondary) induced by the threaded pin. In a later study, Krishnan [65] suggested that the formation of the flow layers can be considered as extruding the materials, with periodicity equalling to the time for one rotation, around the pin so that a set of semi-cylinders would form as the pin moves ahead. A clay model was constructed to demonstrate the "extrusion" theory. The model involved pressing a few semi-cylinders, with two different colours, together, as shown in Figure 1-17a. The model was then cross sectioned, and both parts clearly displayed the "Onion Rings" structure.

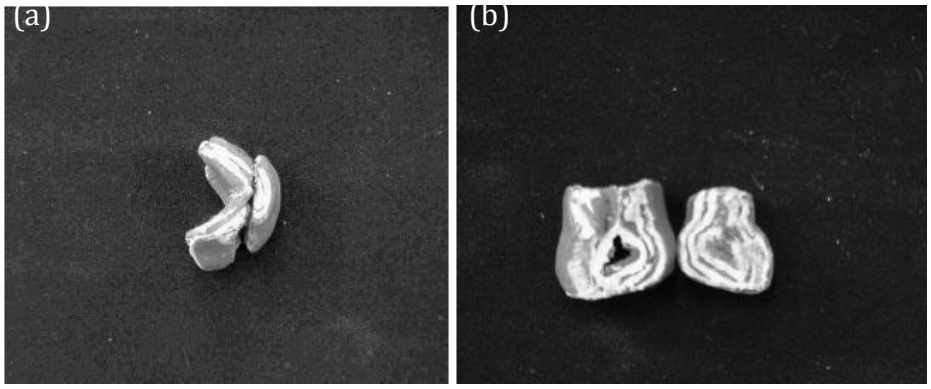

Figure 1-17. A clay model is shown in (a), by pressing semi-cylinders with two different colours together; in (b) the model was cross sectioned, clearly showing the "Onion Rings" structure [65].

However, the aforementioned literature has not clearly explained how exactly these extrusion layers are formed. This is largely due to the fact that it is experimentally difficult to examine the instantaneous interactions between the pin and surrounding workpiece. Chen et al. [37, 38] used the so called "pin-breaking" technique, which involved machining a sharp corner at the pin-shoulder interception area to assist pin to break during FS, to obtain pin-material couple so that material flow/deformation around the frozen pin can be directly analyzed. Tools were usually heat treated to a high hardness (~ 52 HRc) in order to minimize the time of breaking. Furthermore, a relatively small shoulder, coupled with a zero tilt angle, were used to severely reduce the amount of material flow at the shoulder region, i.e. a channel occurred at the upper portion of the weld, therefore enabled a direct (3D) observation on the pin-material interaction. Examples of 2D and 3D views of the instantaneous layer-to-layer formation at the back of the pin are given in Figure 1-18 and Figure 1-20a respectively.

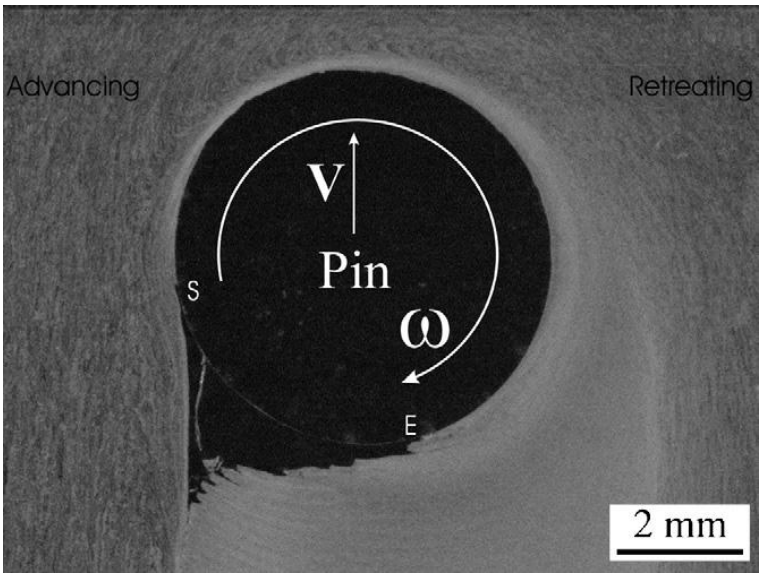

Figure 1-18. Mid-plane sections of frozen pin-material couples obtained during FS AA5083 alloy at v = 120 mm/min and ω = 760 rpm [37]. The formation of the bands can be clearly identified, and λ = v/ω.

The micrograph taken at the mid-thickness plane of a FS performed on AA5083 alloy with v = 120 mm/min and ω = 760 rpm is shown in Figure 1-18 [37]. It is clearly shown that the extruded/sheared flow layers exist around the pin and detach at the back. Based on this observation, Chen et al. suggested one complete layer will be formed and detached from the pin in one revolution. Chen's model can

be better illustrated by a schematic diagram given in Figure 1-19. P0 and P1 represent the positions of the pin at one particular moment and one revolution after this respectively. As the pin moves from P0 to P1, the cavity at the back of pin naturally grows larger, due to the fact that the pin does not act a force on the workpiece material (at that region); meanwhile, in the front part of the pin, the continuous shearing effect tends to shear new material into the cavity, i.e. creating a new shear layer. The enlargement in cavity is cancelled out by the introduction of newly formed layers and thus the cavity is stable and moves with the pin.

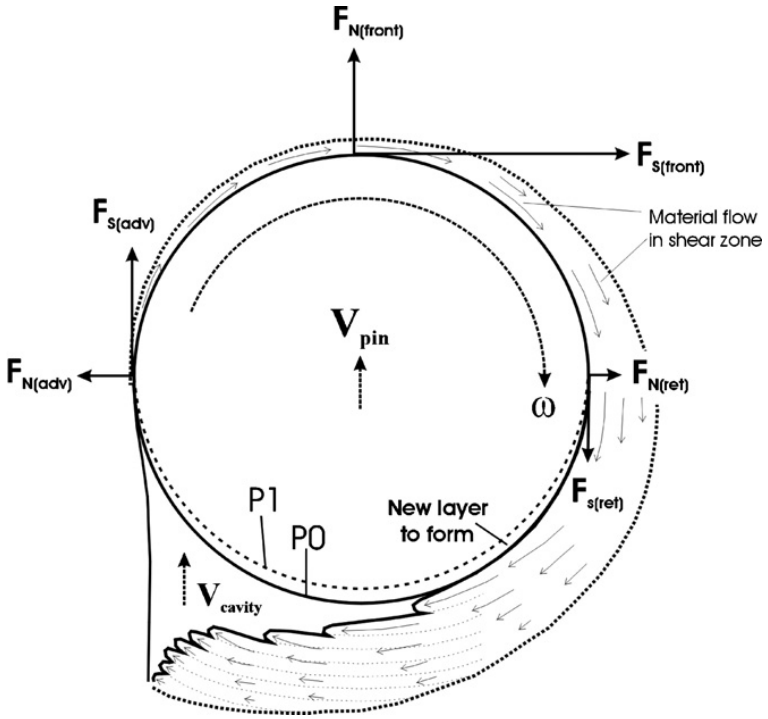

Figure 1-19. Schematic illustration of material flow in the shear zone around the pin. P0 represents the current pin location and P1 is a location of the pin after one revolution. Forces acting on the material are suggested [37].

Now let us consider the deposition of the flow layers in a 3D sense. A high magnification SEM image of the pin-workpiece couple (shown in Figure 1-20a) are given in Figure 1-20b. Four shear layers (L1 to L4) at the back of the broken pin can be clearly identified from Figure 1-20a. Layers being formed (L1 to L3) extend further and reaching the advancing side (left) of the weld as the pin rotates and moves ahead. The sample was further sectioned through the line–A1, so that L2 and L3 can be studied in more details (shown in Figure 1-20b). It can be seen that both L2 and L3 originate from the root of the thread, and the interface between the

threads and the layers appears to be very clean. The observation suggests that as the tool rotates for another revolution, L2 is extended downwards and towards the advancing side, becoming L3. Following this logic, L1 becomes L2, and L3 becomes L4. L4, which already reaches the advancing side of the weld, detaches away from the threads thus forming a complete shear layer at the wake of the weld.

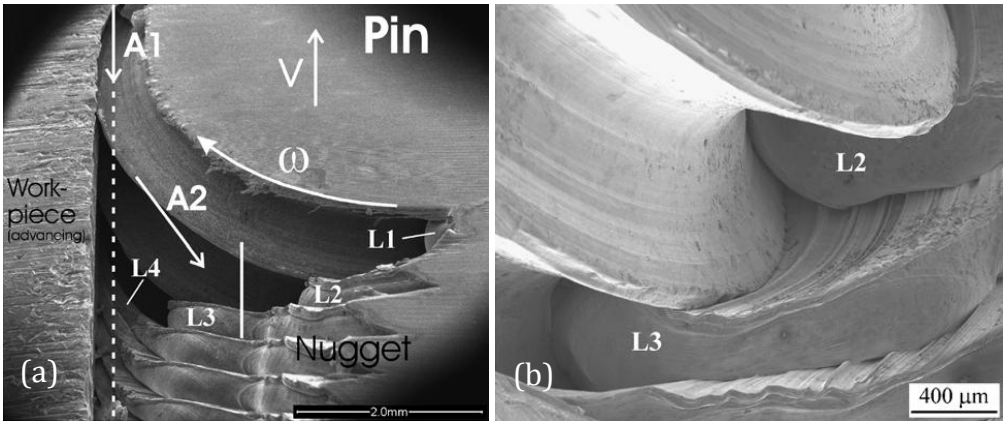

Figure 1-20. SEM images of a pin-workpiece couple sampled from a FS performed on AA5083 using v = 315 mm/min, ω = 710 rpm (thus λ = 440 μm) [38]. (a) A low magnification view and four layers (L1 to L4) can be identified; (b) enlarged view of L2 and L3 by further sectioning the sample through A1.

1.4.3 Formation of the Non-Ring Structure

Although the "Onion Rings" pattern was recognized as the most typical feature of FS, it may not occur under some conditions. Figure 1-21 shows the cross section of a FS performed on A356 alloy [40], using a normal tool and under a normal condition (800 rpm and 180 mm/min). It can be seen that the stir zone differs significantly with that of FS wrought Al alloys (such as shown in Figure 1-14 and Figure 1-15). Firstly, the commonly seen "onion-ring" structure cannot be identified. Secondly, the nugget zone in FSP A356 can be divided into two distinct flow zones (as outlined), depending on the characters of material deformation. Close to the advancing side (left), the workpiece is heavily deformed so that the original dendritic structure cannot be identified. This portion extends but tails off toward the retreating side in the mid-to-lower region (but not the bottom) of the nugget zone. On the middle-retreating side, the workpiece is deformed much less intensively, therefore the as-cast structure is still apparent.

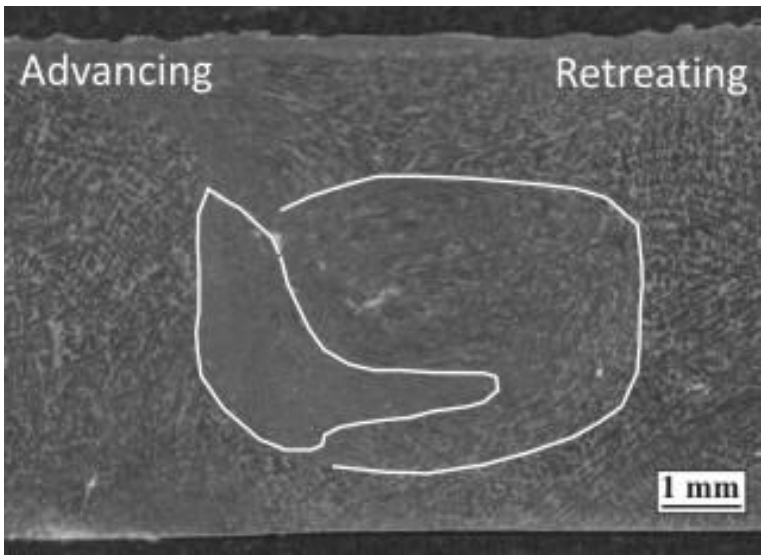

Figure 1-21. Cross section (advancing side on the left) of A356 cast alloy FS sample made using v = 180 mm/min, ω = 800 rpm and θ = 2°, showing the absence of clear "Onion Rings" in the nugget zone (outlined) and a heavily deformed RSM region (also outlined) within that zone [40].

When either low ω or low ω/v were used, the formation of a nugget zone without the "Onion Rings" structure was repeatedly reported in literature, especially for FSP conducted on cast Al alloys [66-73], and Mg alloys [74-77]. Cross sections of FSP conducted on A356 alloys and a magnesium (Mg-Zn-Y-Zr) alloy are given in Figure 1-22a to c respectively, all of which clearly display a "Non Ring" structure. More specifically, in Figure 1-22a and b, less deformed A356 material can be identified on the lower-retreating (left) side, while highly refined material occupies the rest of the nugget. This deformation segregation is in common to that observed in Figure 1-21.

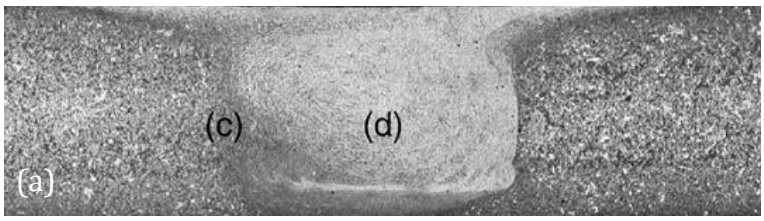

Figure 1-22. FS performed on (a) A356, with v = 500 mm/min, ω = 1250 rpm [71], (b) A356, with v = 30 mm/min, ω = 1200 rpm [69] and (c) a Mg-Zn-Y-Zr alloy, with v = 100 mm/min, ω = 800 rpm [75].

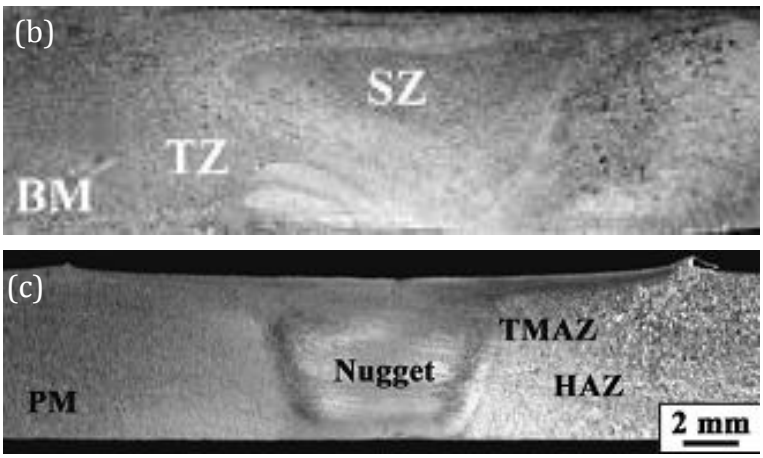

Figure 1-22. Continued.

"Partial Ring" structures were observed for FS on A356 [78], [79] AZ31 [80], and ZK60 [81] respectively. Furthermore, it was well demonstrated by Ma et al. [66] that during FS A356, the increase in ω causes the "Non Ring" structure gradually transitioning into the "Onion Rings" structure, which is illustrated in Figure 1-23. It can be seen "Onion Rings" structure dominates the stir zone at high rotation speed condition (g and h), i.e. 900 rpm. At intermediate speed range, i.e. 500–700 rpm, the "Onion Rings" structure can be observed primarily on the advancing side (right) of the stir zone (c to f). At relatively low rotation speed (300 rpm), the "Onion Rings" structure can be barely observed (a and b).

It is thus apparent that macro-scale material flow of FS conducted on cast Al-Si and Mg-Al alloys (under low ω or ω/v conditions) can be significantly different to that of FS on wrought Al alloys. However, the detailed (macro-scale) flow mechanism which leads to the formation of the "Non Ring" structure, and the deformation and deposition segregation have not been adequately investigated in literature. Furthermore, how the material flow is influenced by the increase in rotation speed, thus causing the "Onion Rings" structure to occur, is also unclear. As FSP becomes a more popular way to modify the as-cast microstructures of Al and Mg alloys, the knowledge on the detailed (macro-scale) flow mechanism needs to be further explored.

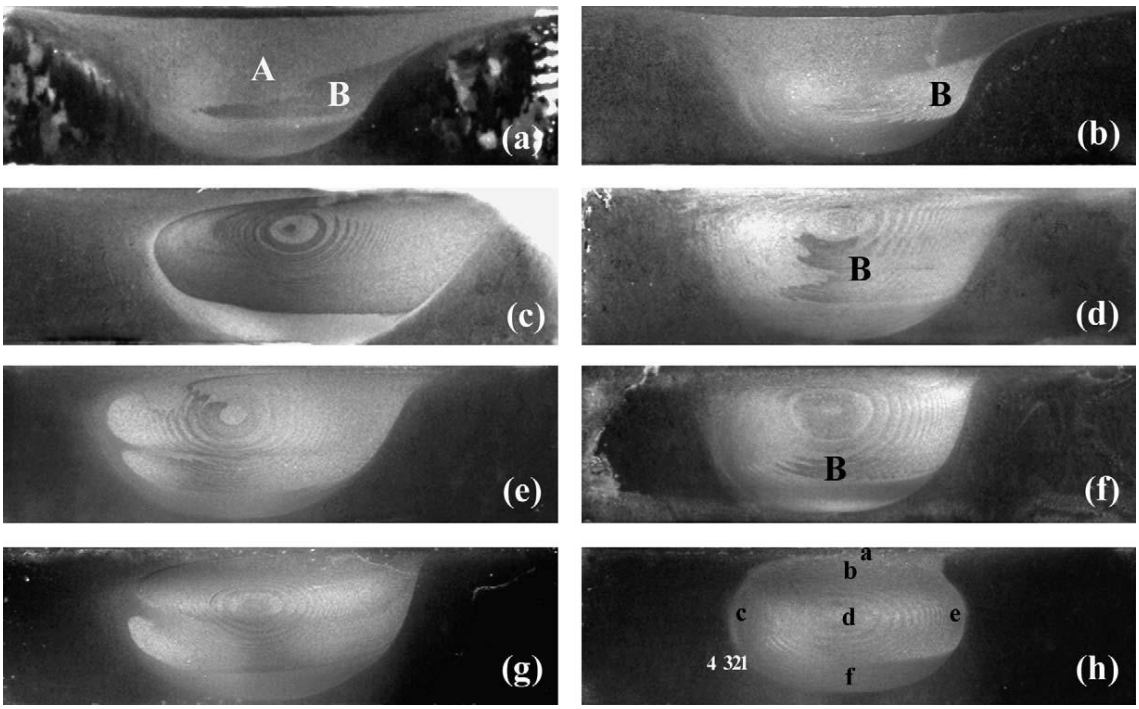

Figure 1-23. Macrographs showing variation in the processed zone in FSP A356 samples with processing parameter combinations of (a) 300 rpm, 51 mm/min; (b) 300 rpm, 102 mm/min; (c) 500 rpm, 51 mm/min; (d) 500 rpm, 102 mm/min; (e) 700 rpm, 102 mm/min; (f) 700 rpm, 203 mm/min; (g) 900 rpm, 102 mm/min; (h) 900 rpm, 203 mm/min. The advancing side of the nugget is on the right in all macrographs.

1.4.4 Strain and Strain Rate

The macro-scale material flow (forming the stir zone) during FS was reviewed in the previous section. In this section, the details of micro-scale material deformation (strain and strain rate) will be reviewed. Strain (ε) and strain rate ($\acute{\varepsilon}$) experienced by the workpiece during FS has been an important area of research [82] because its understanding is critical to reveal the details of material microstructural evolution from a quantitative perspective. For example, it was shown that, material (which locates ahead of the pin) does not recrystallize unless the strain experienced by the material becomes large enough [14, 39], this will be illustrated in Section 1.5.2. On the other hand, the strain rate experienced by the material significantly influences the final grain size (illustrated later in this section), thus the mechanical property of the material after FS. Furthermore, referring back to Equation 1-5 (page 23), material flow stress is a function of strain

rate, and the former can severely influence the torque (M) and power generation (P and E_s).

In order to study the strain and strain rate in a direct way, it is necessary to know how the material is deformed at close-to-pin region. In the absence of reliable method of direct measurement, Reynolds [45] recently proposed a simple geometrical method for estimating strain. Material flow lines around the pin are given in Figure 1-24, assuming that the material ahead of the pin is extruded, following tool rotation direction, to the back without causing any movement in lateral direction. Furthermore, material was assumed to travel less than one revolution. Following this logic, if the tool has rotated for one revolution, a piece of material (with length of λ) locating on the advancing side of the pin will be stretched to length equals to pin periphery as it being extruded around the pin. At the back of the pin, this extruded piece will be compressed back to the original length (λ). Similarly, the equivalent piece of material which locates ahead of the pin centre will be stretched to length equals to half the pin periphery then compressed after deposition. The strain, due to both stretching and compressing, can be calculated as:

$$\varepsilon = \ln\left(\frac{l}{\lambda}\right) + \left|\ln\left(\frac{\lambda}{l}\right)\right| \qquad \textit{Equation 1-6}$$

where l is the extruded length, which equals to $2\pi R_p$ for material locating on advancing side, and πR_p for material locating at pin centre. For λ = 0.5 mm, and R_p = 5 mm, the strains experienced by material on advancing side, pin centre, and retreating side are ~ 8, ~ 6.5 and 0 respectively.

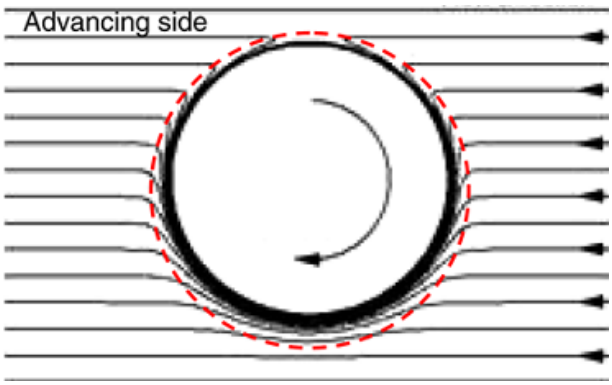

Figure 1-24. Assumed material flow lines around the pin [45].

The above calculation, although based on (overly) simplified material flow and deformation during real FS, still provides some guidelines for estimating strain by considering possible solid-state deformation experienced by the workpiece.

In a more recent study, Mukherjee et al. [41] estimated strain and strain rate during FS by tracing the deformation pattern of the tracer material. A slice of 0.29 mm thick marker (AA5457 alloy) was placed in AA5083 workpiece, perpendicular to the tool travelling direction. After FS conducted at 1500 rpm and 50.8 mm/min, the deformed marker material, which locates on the retreating side of the pin and 1 mm below tool shoulder, was examined, as illustrated in Figure 1-25. The thickness of the marker material at various locations was measured, and the minimum thickness of the tip of the deformed marker was measured as 3 μm. By assuming the thinning of the marker was merely due to pin shearing effect and no material lost occurred, the shear strain experienced by the material was estimated as:

$$\varepsilon = \ln\left(\frac{D_0}{D}\right) \qquad \textit{Equation 1-7}$$

where D_0 is the undeformed marker thickess where D is the deformed marker thickenss. The maximum strain experienced by the material located just outside the pin periphery on the retreating side, was estimated to be ~ 4.6. Strain rate was further estimated using modelling. In the model, a uniform tangential material velocity along the pin/workpiece interface was assigned and the workpiece velocity was set as 10% of the pin rotating velocity. Maximum strain rate experienced by the material at the pin interface was estimated as ~ 87 s^{-1}. It is important to point out that the strain rate estimition was based on an arbituarily chosen workpeice velocity. The assumed workpeice velocity might not be reasonable considering that the true workpeice velocity near the pin region was not clearly understood. Hence, the accuracy of the estimated strain rate is still unclear.

It is important to note that the strain and strain rate estimation conducted in this thesis [83] is similar to (however earilier than) Mukherjee's work in the sense that

the estimation is based on tracing the real-time deformation pattern of the material. The detailed results will be presented in Section 5.3.

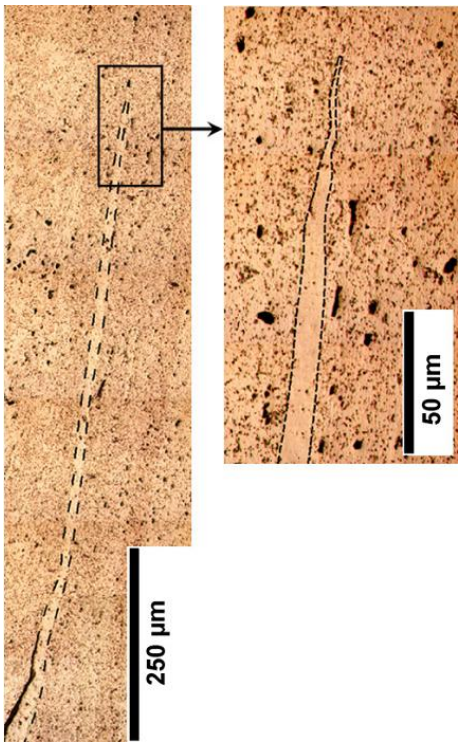

Figure 1-25. Deformed AA5457 marker on the retreating side of pin, obtained from a FS conducted on AA5083 workpiece, at 1500 rpm and 50.8 mm/min [41].

During dynamic recrystallization (which is believed to be the major recrystallization mechanism during FS), strain rate can be estimated by relating the grain size (d) to the Zener-Hollomon parameter through the following relationship [42, 46, 59]:

$$d^{-1} = a + b\log(Z) = a + b\log\left(\dot{\varepsilon}\exp\left(\frac{Q}{RT}\right)\right) \qquad \textit{Equation 1-8}$$

where a, b are constitutive constants of the workpiece, and Q, R and T have the usual meanings. Therefore, knowing the (average) grain size and the temperature at a particular location in the stir zone, the average strain rate experienced by the material can be estimated. The (average) grain size can be determined from the microstructure after FS; while the temperature at a particular location of the nugget zone can be measured by using a thermocouple.

Based on this method, Frigaard et al. [42] estimated the strain rate near the nugget centre to be between 1.6 and 17.3 s^{-1}, during FS conducted on AA6082 and AA7108 alloy at a rotation rate of 1500 rpm and linear speed between 300 and 720 mm/min. Gerlich et al. [46, 59] conducted FS spot welding with a rotation rate between 1000 rpm and 3000 rpm. The estimated strain rates near the nugget centre were between 20 and 650 s^{-1} for AA7075 alloy, 180 and 497 s^{-1} for AA5754 alloy, and 55 and 395 s^{-1} for AA6061 alloy respectively.

Using the same principle indicated by Equation 1-8, Masaki et al. [43] estimated the strain rate by simulating the deformation condition during FS using a plane compression test, during which the strain rate was controlled by adjusting the stroke speed. Strain rates used in the compression tests were 1, 3.2, 10 and 32 s^{-1}. After the tests, grain size was measured. FS experiments were conducted on AA1050 alloy with rotation speed varying between 600 and 1200 rpm and a constant linear speed of 100 mm/min. Stir zone temperatures were recorded for each weld and the compression tests were performed at the measured temperatures.

Since grain size test is affected by temperature and strain rate, as indicated by Equation 1-8, the grain size after FS and compression experiments were compared with one another, so that the corresponding strain rate during FS could be estimated. The relationship between strain rate and grain size after compression is given in Figure 1-26. Grain size after actual FS was measured as 9.5, 13.4 and 15.2 μm at 600, 1000 and 1200 rpm respectively; which corresponded to the strain rate between 1.7 and 2.7 s^{-1}. These values are substantially lower than those reported by Frigaard et al. [42] and Gerlich et al [46, 59].

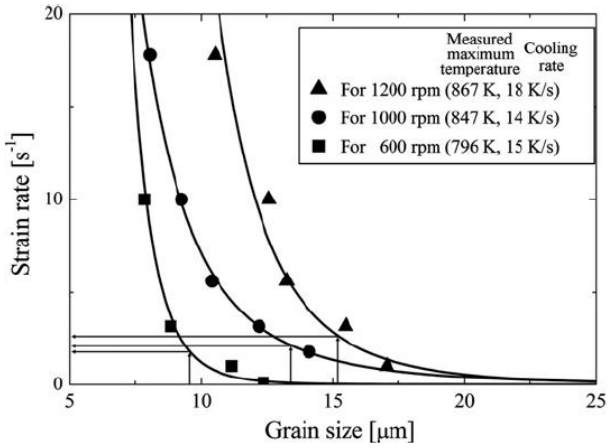

Figure 1-26. Relationship between residual grain size and effective strain rate after compression tests [43]. Equivalent rotation speed was given.

It is important to note that the strain rate experienced by the material during FS starts from zero when the deformation just begins and gradually increases as the deformation intensifies. This strain rate history of the deformation cannot be estimated based on the Zener-Hollomon parameter (Equation 1-8). By using the Zener-Hollomon parameter only the average strain rate can be estimated. More importantly, during Geometrical Dynamic Recrystallization, which is one of the major mechanisms governing the recrystallization of the workpiece during FS, the grain size after recrystallization is not affected by the strain rate (Section 1.5.1 and 1.5.2). Hence, Equation 1-8 is not valid in these cases.

Strain and strain rate were also extensively estimated by using FS numerical models. These results were well summarized by Nandan et al. [10]. However, truly accurate FS models have not yet been developed as the underlying thermomechanical principles have not been completely understood. Therefore, over-simplified assumptions must be made in current FS models. For instance, current FS models are unable to take the pin threads, being the most fundamental feature of FS, into consideration. As a result, the modelled strain and strain rate cannot be viewed as correct. For example, it was reported that the maximum strain can be up to 40 [84], which implies that original material with a unit length will extended by $e^{40} = 2.35 \times 10^{17}$ times. Such an extraordinary deformation is beyond comprehension. Therefore, strain and strain rate based on FS modelling are not reviewed in this thesis.

After the review given above, it may be appropriate to conclude that despite extensive studies having been conducted, reliable estimation of strain and strain rate experienced by the workpiece has not been achieved so far. However, tracing the deformation pattern (as shown in Figure 1-25) of marker material seems to be a promising way to accomplish this task. However, studies of strain and strain rate based on marker tracing technique were very limited in current literature, and such studies have not been yet extended to FSP of Al-Si alloys. Such knowledge is important as the final microstructure (and thus processing quality) is intrinsically related to the level of the deformation generated by the tool.

1.5 Microstructural Evolution during FSP

In this section, current literature on the transient microstructure (ahead of pin) during FS will be reviewed. Firstly, mechanisms of dynamic recrystallization, and subsequent texture evolution during FS on wrought Al alloys, will be reviewed. This is because wrought Al alloys were the most widely used alloys in current literatures on recrystallization and texture evolution. Furthermore, reviews on microstructural evolution phenomena which are unique for FSP as-cast Al and Mg alloys will be separately given. To be specific, how the microstructural evolution is affected by the large and non-dissolvable second phase Si particles in cast Al-Si alloys and by the dissolvable $Mg_{17}Al_{12}$ particles in Mg-Al alloys will be addressed.

1.5.1 Basics of Recovery and Recrystallization

The gradients in strain, strain rate, and temperature are inherent in the thermomechanical cycles of the FS process [85]. Microstructure transformations and restoration process in the presence of such gradients have only recently begun to be understood [14, 15, 85-90].

Before reviewing this literature, the basics of recrystallization will be introduced. During deformation of alloys, energy is stored mainly in the form of dislocations. This energy is released in three main processes, those of recovery, recrystallization and grain coarsening. The usual definition of recrystallization is the formation and

migration of high angle grain boundaries (HAGBs) driven by the stored energy. HAGBs are those with greater than 10–15° misorientation. On this definition recovery includes all processes releasing stored energy that do not require the movement of a HAGB.

The dislocation motion (such as dislocation climb, glide, and cross-slip) is relatively easy in metallic material with a high stacking fault energy (such as aluminium). Under this circumstance, the annihilation and rearrangement of dislocations can readily occur, which promote the formation of grain boundaries with low misorientation angle (LAGBs) and subgrains. This process is regarded as recovery. As recovery proceeds, the misorientation of LAGBs will gradually increase (which is equivalent to subgrain rotation), which lowers the stored energy per dislocation.

Recovery and recrystallization may occur during deformation at high temperatures. These phenomena are classified as dynamic recrystallization; which distinguish them from the static annealing processes which occur during post-deformation stage.

In metals in which recovery processes are slow, such as those with a low or medium stacking fault energy (copper, nickel), dynamic recrystallization may take place when a critical deformation condition is reached. A simplified description of the phenomenon is as follows. New grains originate (nucleate) at the old grain boundaries. But, as the material continues to deform, the dislocation density of the new grains increases, thus reducing the driving force for their further growth, and the recrystallized grains eventually cease to grow. This type of dynamic recrystallization is known as the discontinuous dynamic recrystallization (DDRX).

If the dynamic recovery is efficient, a microstructure of HAGBs may evolve in ways other than the nucleation and growth of grains at pre-existing boundaries, as for the case of DDRX.

Grain boundaries develop serrations during dynamic recovery (Figure 1-27), and the wavelength of these serrations is similar to subgrain size. If the material is subject to a large reduction in cross section, for example by hot rolling or hot

compression, then, as the original grains become flattened, the size of these serrations will become comparable with the grain thickness as shown in Figure 1-27. Interpenetration of the scalloped boundaries will occur, resulting in a microstructure of what appear to be small equiaxed grains. This phenomenon is described as geometric dynamic recrystallization (GDRX) [91].

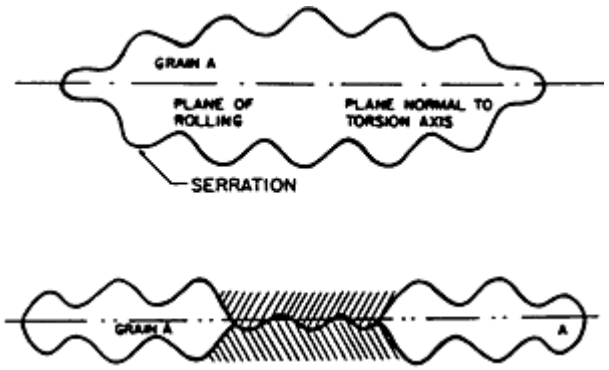

Figure 1-27. When the grains are elongated and thinned extremely, they pinch off where opposite serrations meet [92].

There is considerable evidence that in certain materials, new grains with HAGBs may be formed, by the progressive rotation of subgrains with little accompanying boundary migration. This is a strain-induced phenomenon which should not be confused with the subgrain rotation which has been postulated to occur during static recovery. This phenomenon is denoted as Continuous Dynamic Recrystallization (CDRX). The phenomenon involves subgrains adjacent to pre-existing grain boundaries being progressively rotated as the material is strained. The old grains develop a gradient of misorientation from centre to edge. In the centre of the old grain, subgrains may not be well developed or may have very low misorientations (LAGBs). Towards the grain boundary, dislocations produced by strain hardening accumulate progressively in LAGBs, leading to the increase of their misorientation angle and the formation of HAGBs, when a critical value of misorientation angle is reached. The microstructure is thus intermediate between a subgrain and a grain structure: while grains and subgrains are entirely delimited by HAGBs and LAGBs, respectively [93]. Figure 1-28 shows the microstructure of an Al-5%Mg alloy in which well developed subgrains have formed along the original grain boundary.

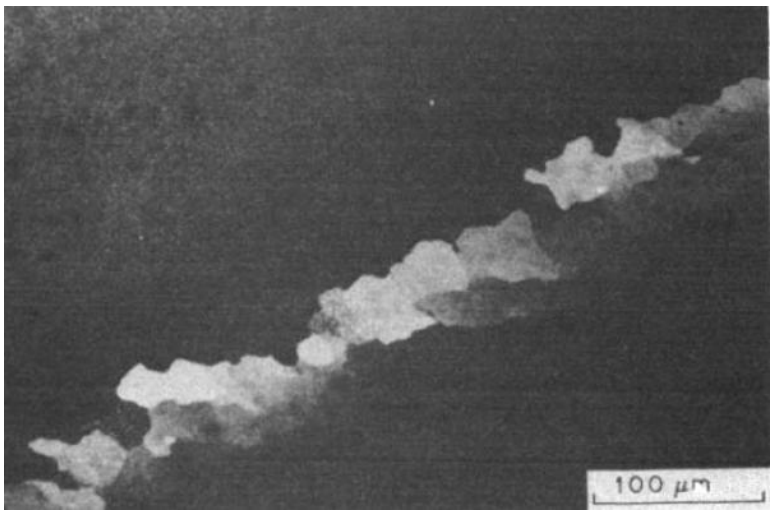

Figure 1-28. Development of misorientations by lattice rotation adjacent to the grain boundary during deformation of Al-5%Mg [94].

1.5.2 Dynamic Recrystallization during FS

The microstructure of the nugget zone of FS is characterized by fine and fully-recrystallized grains. The exact forming mechanism of this unique microstructure has been extensively debated in literature [12, 14, 15, 39, 87, 95-97]. To understand the details of microstructural evolution during FS, it is important to observe the real-time material deformation around the tool pin. Such observation can be obtained by using the stop-action technique. High resolution Electron Backscatter Diffraction (EBSD) studies on the material around the frozen-pin provide insight of the mechanisms of recrystallization [12-15], and the associated texture evolution during FS. Materials used in these studies include AA2195 and AA6016 Al alloys. The AA2195 alloy in the referred study contains large grains and it is resistant to recrystallization; the original microstructure of AA6016 has fine fully recrystallized grains with HAGBs.

The locations of the EBSD maps obtained in these studies with reference to the pin are shown in Figure 1-29. The EBSD scans are given in Figure 1-30 to Figure 1-32. HAGBs are marked by solid black lines while LAGBs are marked by white/grey lines. Statistics of grain boundary misorientation at a few locations ahead of the pin are given in Figure 1-33 and Figure 1-34 for FS AA2195 and AA6016 respectively. In Figure 1-34, the specific grain boundary area, which is defined as length of grain

boundary over the area under examination, was considered rather than the number of grains.

During FS, recovery/recrystallization and plastic deformation occur simultaneously at elevated temperature, and therefore dynamic recovery/recrystallization play a major role in the grain refinement process. It is important to bear in mind that recovery occurs very fast during the deformation of Al alloys due to their high stacking fault energy. Hence, the recrystallization is inevitably delayed due to the reduced accumulation of dislocations by the fast recovery process.

The grain refinement process experienced by the material in nugget region, regardless of material type and FS conditions, has common features which are summarized as below.

a. Grain subdivision:

   During FS AA2195, due to the existence of macroscopic shear induced by the pin, the large grains exist in AA2195 alloy subdivide into coarse deformation bands (Figure 1-30a (i)), commonly seen in aluminium alloys below 300 °C at strains > 0.5 ~ 2 [14]. This occurs in grains of orientations that are unstable within the imposed strain field and hence different sets of slip systems will be activated to accommodate the shear deformation. Due to the same reason, the large deformation bands rotate and/or elongate differently, ultimately developing subgrain boundaries between them (Figure 1-30a (ii)). The arrows in Figure 1-31 indicate that a single grain at the left of this image changes orientation as it approaches the tool and develops elongated, parallel subgrains. Subdivision of the original grains during FS AA6016 can also be readily observed, as indicated by the arrows in Figure 1-32a. This subdivision process can be well reflected by the significant increase in number and specific area of LAGBs, as shown in Figure 1-33 (400–700 μm) and Figure 1-34 (Region 1).

b. Geometrical thinning:

As the pin approaches, the grains and subgrains elongate due to the increase in shear strain, resulting in fibrous grains and subgrains with high aspect ratio (Figure 1-30b, Figure 1-31 and Figure 1-32c). The HAGBs at fibrous grain/subgrain boundaries become wavy as the thermal energy increases (due to the increase in temperature) and boundary migration starts to occur. As the strain further increases, closely spaced parallel HAGBs become even more elongated and reduce their width. Once the width approaches one subgrain wide, adjacent wavy grain boundaries may impinge with each other, forming fine equiaxed grains. Such a grain refinement process, as previously illustrated (Figure 1-27), is called Geometrical Dynamic Recrystallization (GDRX). Grains formed due to GDRX can be found in Figure 1-30b location (iii), and Figure 1-32c. Finally, a reasonably uniformly refined nugget-like microstructure is formed comprised of low aspect ratio fine grains (Figure 1-30c and Figure 1-32d). Thus, it can be suggested that GDRX plays an important role in the microstructure evolution during FS.

Furthermore, the bulges along the original grain boundaries (indicated by arrows in Figure 1-32d) can eventually transform into fine grains. These fine grains are typically surrounded by HAGBs, and have little substructure. Thus, their development fits the definition of discontinuous recrystallization.

At a region very close to the pin, the grain boundary misorientation shows a drastic increase in the number of HAGBs and a significant decrease in the number of LAGBs. Such a phenomenon can be clearly observed by comparing the misorientation distribution of 0–100 μm to that of 100–200 μm in Figure 1-33; and also by comparing Region 4 to Region 3 in Figure 1-34. This observation strongly indicates that much of the LAGBs have transformed into HAGBs in a sudden manner, which is consistent to the nature of GDRX.

c. Continuous subgrains rotation:

It is evident that some of the fine grains form preferentially along existing grain boundaries, such as indicated by the arrows in Figure 1-31 and by circles in Figure 1-32d. These grains develop the misorientation continuously and gradually with proximity to the tool. Throughout their development, the subgrains remain similar in both size and shape to the more pronounced subgrains and grains observed close to the tool. The continuous development of subgrain while maintaining a stable size and shape is consistent with a continuous dynamic recrystallization mechanism (CDRX).

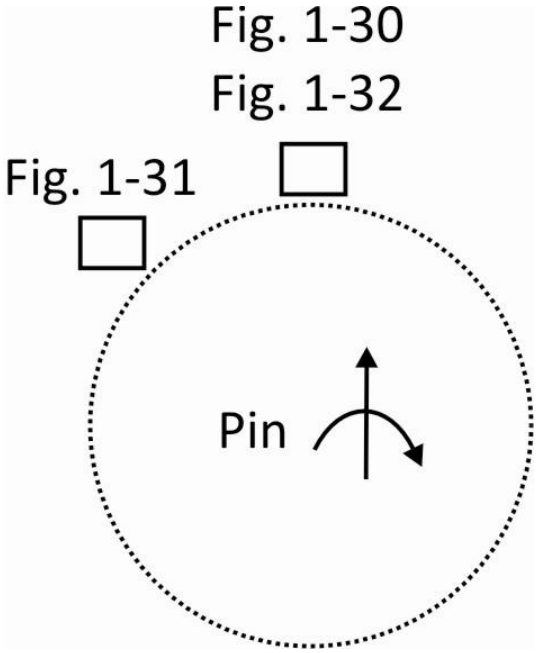

Figure 1-29. The locations of EBSD scans shown in Figure 1-30 to Figure 1-32 with reference to the pin.

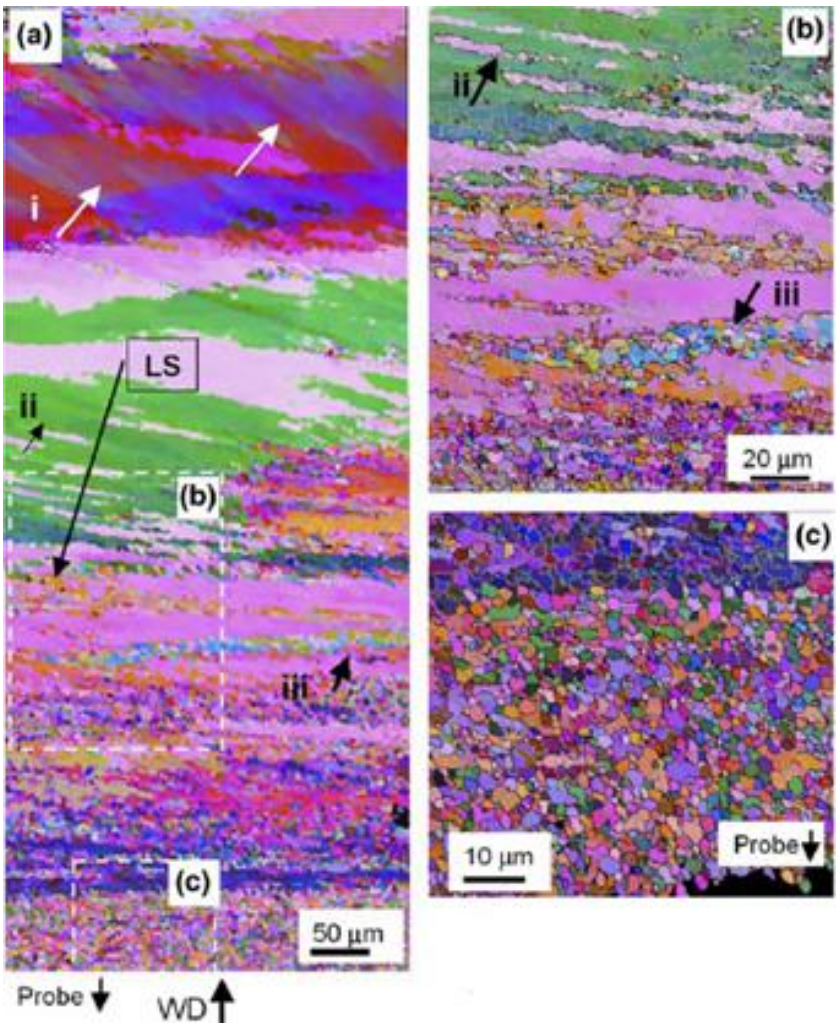

Figure 1-30. EBSD map ahead of the pin, reported by Prangnell et al. [14]. (a) Directly ahead of the pin; (b) enlarged view of thinning parallel subgrains and (c) fully recrystallized grains next to the pin.

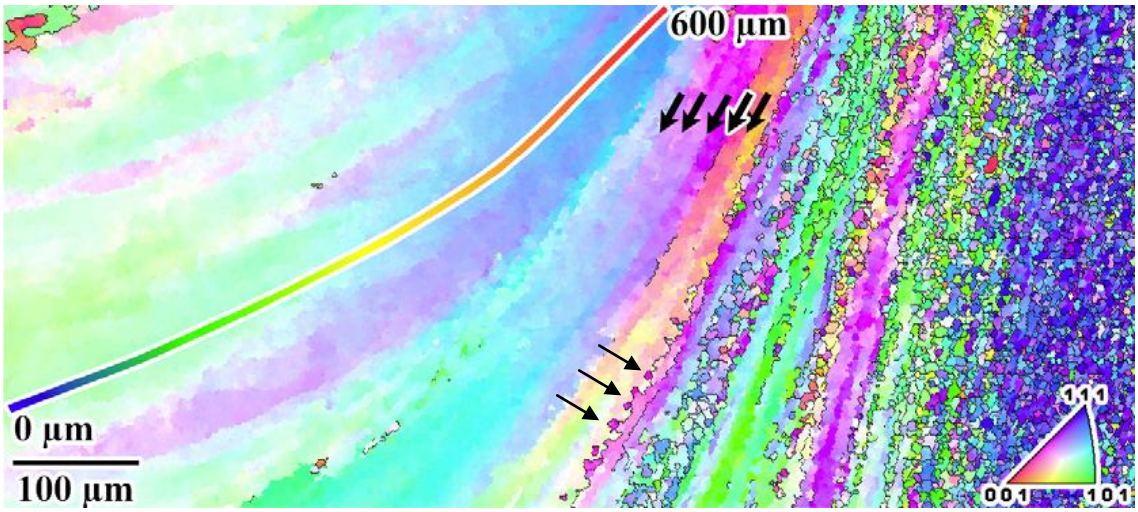

Figure 1-31. Crystal orientation map of a region locating on the advancing side of the tool during FS AA2195 alloy [15].

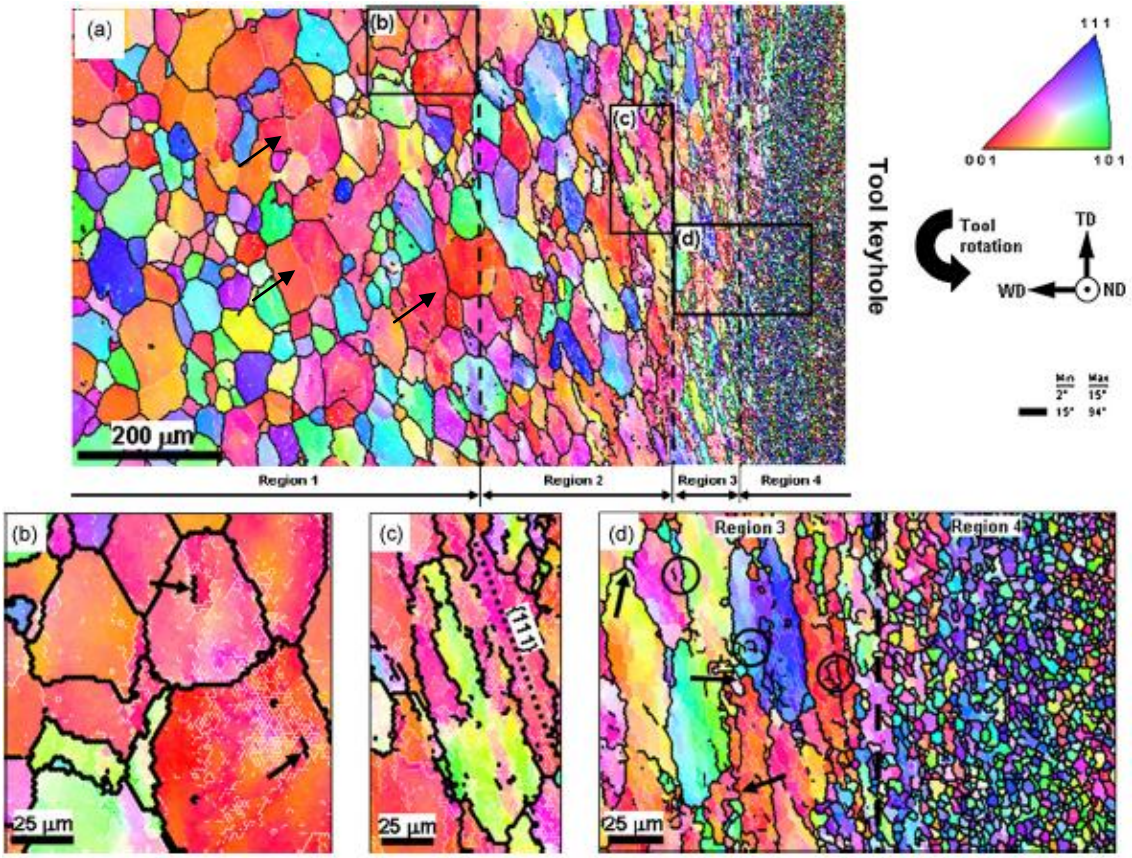

Figure 1-32. (a) EBSD map taken ahead the tool keyhole. (b–d) with selected areas shown at higher magnifications [39].

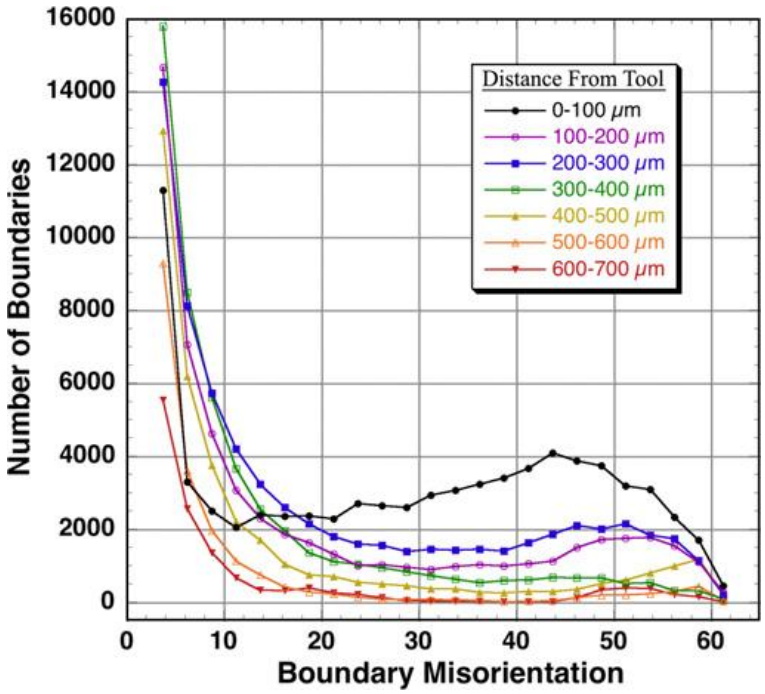

Figure 1-33. Graph of interpixel misorientations for 100 µm wide regions ahead of tool showing evolution from the initial large grains to the refined grains near tool (0 µm) [15].

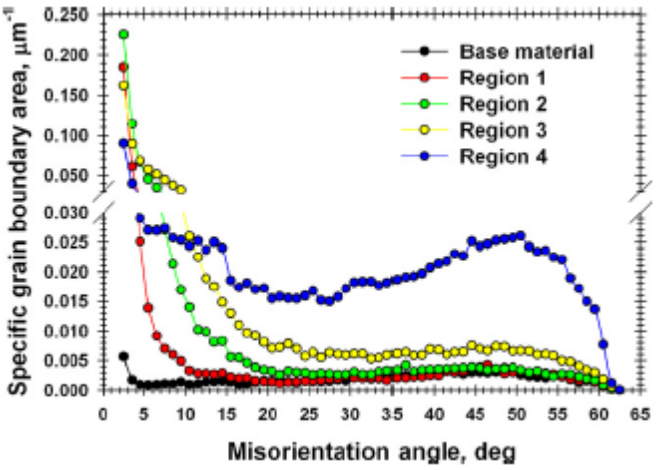

Figure 1-34. Evolution of specific grain boundary area statistics from base material to Region 4 (Figure 1-32d) [39].

From the above review on grain recrystallization mechanisms, it may be reasonable to state that recrystallization due to thinning and elongation of grains/subgrains (GDRX) plays a major role in the grain refinement process in FS. However, CDRX and discontinuous recrystallization also contribute, although to a much less extent, on the grain refinement process. It is important to note that few studies so far have considered the mechanism of recrystallization during FSP cast Al alloys (such as A356), despite the fact that the quality of FSP (of A356) can be intrinsically related to how is the coarse as-cast structure (Figure 1-6) recrystallized, i.e. refined, with the presence of a high portion of non-deformable second phase.

1.5.3 Textures of Aluminium Alloys

Preferred orientations, i.e. textures, may exist after alloys have undergone deformation induced recrystallization (e.g. torsion and FSP), and directional solidification. The formation of ideal textures after recrystallization is commonly studied using standard torsion testing. Torsion test and FSP are similar in the sense that the deformation which is experienced by the material is primarily shear deformation. Therefore, the textures developed during torsion testing will be addressed first, which will serve as a base for analyzing the textures after FSP.

The shear frame (r, θ, Z) of the torsion test [98] is given in Figure 1-35a: the dashed circle represents a particular shear plane (rθ), the shear direction (θ) at a

particular point on the shear plane is tangential to the dashed circle, and shear plane normal (Z) is perpendicular to the shear plane. The simplified shear frame (r, θ, Z) of FSP is illustrated in Figure 1-35b, which is slightly different to that of torsion testing. It has been previously explained that during FSP, material at close-to-pin region experiences a 3D flow (Figure 1-20). Here, we use the word "simplified" to indicate that only the horizontal shear flow induced by the pin is considered in the present case. To be specific, the "simplified" shear plane (rθ) of FSP, which is represented by the small rectangular box, is tangential to the pin column, whereas in torsion testing it is parallel to the horizontal plane. The "simplified" shear direction (θ) during FSP is tangential to the pin periphery, i.e. in line with the horizontal pin shearing velocity. In reality, the shear direction (θ) might not be on the horizontal plane, if the vertical flow motion induced by the pin is taken into consideration.

The ("simplified") shear frame (r, θ, Z) during FSP is location dependent because the shear direction (θ) is always parallel to the pin periphery. On the other hand, the sample frame (ND, TD, RD) is constant, with ND, TD, and RD represents normal direction, transverse direction and rolling direction respectively. RD is equivalent to the tool feed direction during FSP.

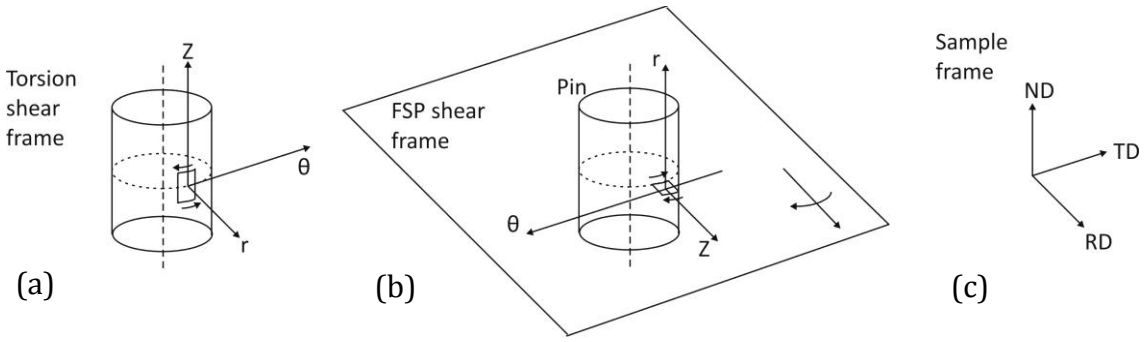

Figure 1-35. (a) Schematic illustration of shear frames (r, θ, Z) in torsion testing [98] and (b) in FSP. The small rectangles represent the shear planes, while the short arrows represent the shearing effects on those planes. The sample frame of FS (ND, TD, RD) is given in (c).

It is common to represent the texture in the format of {hkl}<uvw>, where hu + kv + lw = 0, so that direction <uvw> is on plane {hkl}. {hkl} is a simple crystallographic plane near (not necessarily parallel to) the macroscopic shear plane (rθ) and <uvw> is a simple crystallographic direction (usually a close-packed direction)

near the macroscopic shear direction θ. For example, if a piece of material after a torsion test displays a $(\bar{1}11)[110]$ texture, it implies that the material orientates in such a way that the $(\bar{1}11)$ planes are parallel to the shear plane, and [110] directions are parallel to the shearing direction θ.

It is well established that four ideal textures, could occur during torsion of aluminium [98-100]. Furthermore, "Cubic" texture is seen in directionally solidified Al castings [101] or in some fully recrystallized cube alloys [102, 103]. Strictly speaking, directionally solidified material does not have shear direction or shear plane. However, it is convenient to assign solidification direction of the crystal and the crystal planes which are perpendicular to the solidification direction as the equivalent shear direction and shear plane respectively. Furthermore, "Goss" texture was reported for Al alloys after rolling [104]. The equivalent shear plane and shear direction of these textures are summarized as:

Table 1-1. Summary of ideal shear orientations, and common deformation textures.

Texture	*Equivalent shear plane and direction*
A	$(1\bar{1}\bar{1})[110]$ and $(\bar{1}11)[\bar{1}\bar{1}0]$
A*	$(\bar{1}\bar{1}1)[112]$ and $(11\bar{1})[\bar{1}\bar{1}\bar{2}]$
B	$(\bar{1}12)[110]$ and $(1\bar{1}\bar{2})[\bar{1}\bar{1}0]$
C	$(001)[110]$
Cubic	$(001)[100]$
Goss	$(110)[001]$

Each of the "A", "A*" and "B" textures consists of two crystallographically equivalent parts. For example, the two parts of "A" texture are $(1\bar{1}\bar{1})[110]$ and $(\bar{1}11)[\bar{1}\bar{1}0]$ respectively.

Textures are usually presented in the form of pole figures (PF), and the {111} PFs of the previously listed textures are given in Figure 1-36. For "A", "A*" and "B" textures, the two crystallography parts are represented by upward and downward triangles respectively. A more detailed introduction on how PFs of textures are obtained will be given in Section 2.4.1.

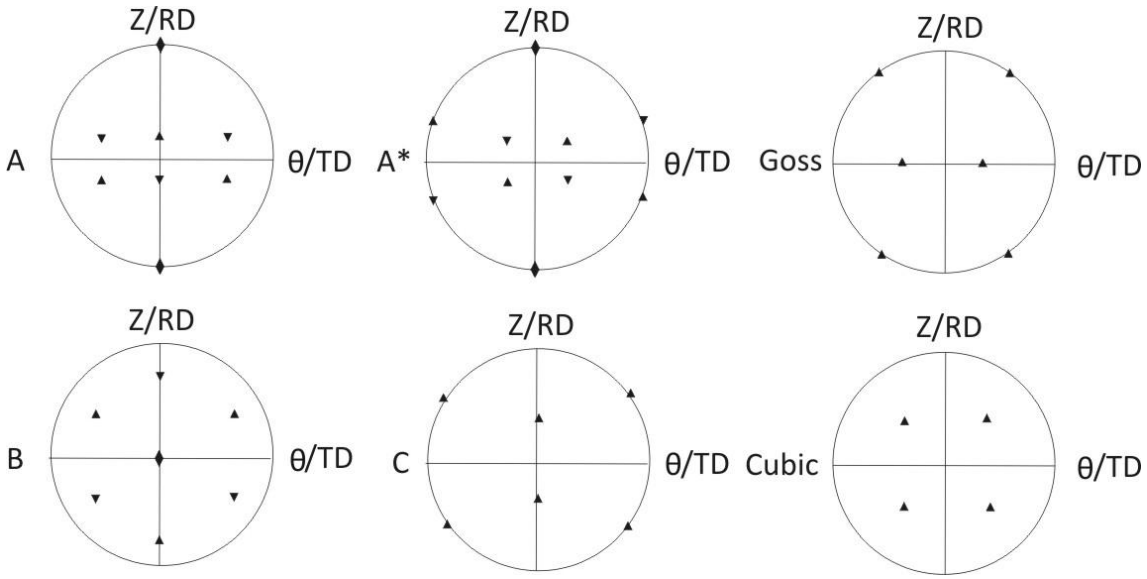

Figure 1-36. Ideal shear and recrystallization textures observed for FCC alloys. Each triangle represents a {111} pole, the up-pointing triangles and down-pointing triangles represent the {111} poles of each of the pair of the slipping system.

Common observation on the texture development during the torsion tests of FCC metals can be summarized as below [98-100, 105, 106]:

a. At low deformation temperature (20 °C) and small strain rate (7×10^{-3} s^{-1}), the "A" orientation is present at $\varepsilon = 0.62$, and vanishes at $\varepsilon = 4.98$, whereas the "C" component becomes stronger with increasing ε. The $(1\bar{1}\bar{1})[112]$ part of the "A*" component can also be detected at $\varepsilon = 4.98$.

b. As the temperature and ε are further increased (from 5 to 20), the "C" component is systematically replaced by the "B" component.

c. There are no absolutely stable textures during the torsion tests. As deformation begins, the crystals rotate towards the macroscopic shear. Furthermore, the first developed preferred textures tend to have (not always) the smallest lattice rotations from the initial texture.

1.5.4 Texture Evolution during FS

The nugget zone usually displays a strong shear texture after FS. The existence of the "B" shear texture in the nugget zone has been widely reported in literature [12, 14, 39, 87, 96, 107-110]. Materials used in these studies include: AA1050, AA2195, and AA6xxx.

However, other shear textures were identified in the nugget zone, but much less extensively. At the wake of the nugget, periodic occurrence of “C” texture was observed by Fonda et al. and [87] and Ahmed et al. [110], although both authors indicated “B” shear texture as the dominant texture. The periodicity is well correlated to the tool advance per revolution. Fonda el al. attributed the texture variation to the variation in (micro-scale) deformation condition. It was suggested that the high temperature (> 400 °C) and high strain level (>> 3) experienced by the material seemed to promote the formation of “B” texture [98].

Textures of the shoulder zone can be significantly different from those of the nugget zone. Kang et al. [109] and Sato et al. [97] observed Goss-texture ({110}<001>) and “Cubic” and “A” textures in the shoulder zone of FS 6xxx alloys respectively. On the other hand, a mixture of {110}<001> and {114}<221>, and a strong “B” texture was observed in the nugget zone. By analyzing the texture of a sample obtained from using the “stop-action” technique [111], the nugget zone immediately behind the pin displays a strong “B” texture. However, at a location further behind the pin where the material experiences an additional flow induced by the shoulder, the “B” texture is replaced by the “Cubic” texture, which is the original texture of the base metal. The above studies clearly demonstrate that the differences between (macro-scale) shoulder-flow and nugget-flow could potentially induce significant influences in texture formation.

As introduced in the previous section, the shear frame (r, θ, Z) during FS is location dependent, while the sample frame (ND, TD, RD) is always constant. Therefore, depending on the location, the obtained textures of FS must undergo some rotations (with respect to the FSP frame) to become the standard textures (which are given in Figure 1-36). The relationship between the frame of textures (Z, θ and r) and the frame of FSP samples (ND, TD and WD) was investigated by Ahmed et al. [110]. It was found the standard textures can be obtained by rotating the frame of texture about ND by angle α and about TD by angle β, respectively. It was assumed that the direction of shear (θ) at a particular location on the tool pin was determined by the instantaneous linear velocity (due to pin rotation) at that location. The authors only considered the horizontal pin shearing direction, and

the potential vertical flow direction was ignored. At pin front, the shearing direction (θ) should be perpendicular to WD whereas on the extreme advancing and retreating sides the shearing direction (θ) is parallel to WD (Figure 1-37).

The angle between TD and the horizontal shearing direction (θ) is described by angle α, and it is related to the location on the pin. Therefore, the local textures must be rotated around ND by angle α to obtain standard textures. Furthermore, due to the tapering of the pin, which is 20°, the shear plane (rθ in Figure 1-35), regardless of the location on the pin, should always be tilted by 20° with respect to the pin vertical direction. Hence the obtained textures must also be rotated by angle β (with a constant value of 20°) in order to compensate the tapering of the probe. Ideal shearing textures were obtained after the aforementioned rotations.

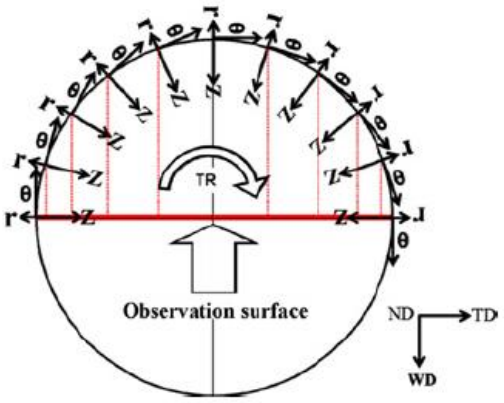

Figure 1-37. Schematic diagram showing the shear-frame (θ, Z, r) around tool pin, with respect to the FS frame (ND, TD, WD) [110].

From the review given above, it can be stated "B" texture, is the dominant texture formed in the nugget zone during FSP (wrought) Al alloys (1xxx, 2xxx and 6xxx series), regardless of the tool geometry and FS speeds. Furthermore, the variation in macro-scale material flow and micro-scale deformation could result in different texture formation. However, from all those quoted studies, it is still unclear why a predominantly "B" texture is formed; or how exactly is texture formation influenced by material flow and deformation. Moreover, the rotation required to transfer the resulting (local) texture to the standard texture is clearly related to the misalignment between the frame of texture (which is further dependent on material flow direction) and that of the sample. However, how the vertical flow

induced by the pin could influence the texture rotation has not been considered so far and thus remains unclear.

It is important to recall that the mechanisms of material flow in the nugget zone could differ significantly from one another during FSP wrought and cast alloys (e.g. A356). However, as stated in Section 1.5.2, that few studies in literature have considered the recrystallization mechanism, thus inevitably the texture after recrystallization, of FSP cast Al-Si alloys. Therefore, it is of scientific importance to investigate the texture evolution of FSP cast Al-Si alloys; and to further study how the texture formation and rotation are affected by macro-scale material flow and micro-scale deformation.

1.5.5 Deformation of α-Al Dendrites and Al-Si Eutectic

FSP of cast Al-Si alloys can result in fine recrystallized Al matrix, and broken-down Si particles evenly embedded within the matrix. The micrographs of as-cast A356 and nugget zone after FSP (using a normal tool with ω = 900 rpm and v = 203 mm/min) are given in Figure 1-38a and b respectively [1]. The as-cast A356 is characterized by coarse acicular Si particles with an aspect ratio of up to 25, coarse primary aluminium dendrites with an average size of 100 μm, and porosity of 50 μm diameter (Figure 1-38a). The acicular Si particles are preferentially distributed along the boundaries (interdendritic regions) of the primary aluminium dendrites. As can be seen from Figure 1-38b, FSP results in a significant breakup and uniform redistribution of the acicular Si particles (2–3 μm and an average aspect ratio of ~ 2.0); and also highly refined aluminium grains (5–8 μm). Furthermore, FSP leads to complete removal of the casting porosities. It has been reported [4] that at higher tool rotation rates, the size and aspect ratio of the Si particles tend to decrease due to the more intense stirring effect.

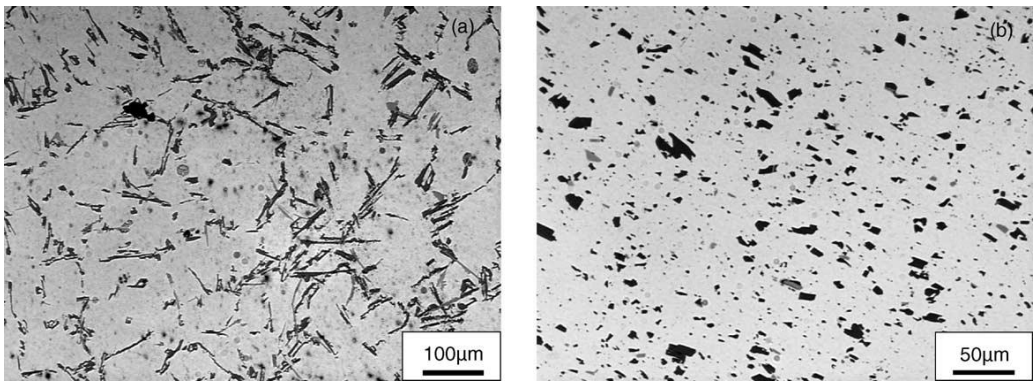

Figure 1-38. Optical micrographs showing the microstructure of as-cast and nugget of FSP A356 (standard threaded pin, 900 rpm and 203 mm/min) [1].

Current understanding on the microstructural evolution during FSP A356 is largely based on the comparison between the microstructures of the as-cast and after-FS materials. The transient microstructure during FSP A356, i.e. the microstructure closely ahead of pin, has not been well studied due to the lack of direct observation of the real-time interaction between pin and workpiece. Hence, how are the Si particles broken down, and re-distributed within Al matrix during FSP have not been clarified in current literature, despite these effects are the major objectives of FSP of Al-Si cast alloys.

Taking one step further, it is well established that there is a strain incompatibility effect between the soft α-Al matrix and the hard Si particles during thermomechanical processing of A356, such as Equal Channel Angular Processing (ECAP) [112]. This inevitably leads to inhomogeneity in deformation, i.e. the deformation of the Al matrix is much more severe near non-deformable Si particles than in adjacent dendritic region. Hence, recrystallization of the Al matrix is more intensive near Si particles. Bearing that in mind, it is important to investigate how the (local) deformations of dendrites and Al-Si eutectic region differ with each other.

1.5.6 Mechanism of β-$Mg_{17}Al_{12}$ Dissolution

Microstructures of as-cast AZ91 and after FSP (400 rpm and 100 mm/min) are given in Figure 1-39a and b respectively. The as-cast structure is characterized by coarse α-Mg dendrites (appear white) and a network-like eutectic β-$Mg_{17}Al_{12}$ phase (bright particles within grey eutectic region) along grain boundaries.

Referring back to Section 1.2.3, the as-cast β-$Mg_{17}Al_{12}$ particles clearly display a fully/partially divorced morphology. Single pass FSP results in fully recrystallized α-Mg grains (mostly 5–10 μm) and significant reduction of the β-particles, unlike in FSP A356 where Si particles do not dissolve. Moreover, identifiable banded structures can be identified in the stir zone on the cross section Figure 1-39b. This visible banded structure can be attributed to left over β-particle bands and non-uniform grain regions occur periodically, which are further due to the FS strain rate/strain and temperature conditions.

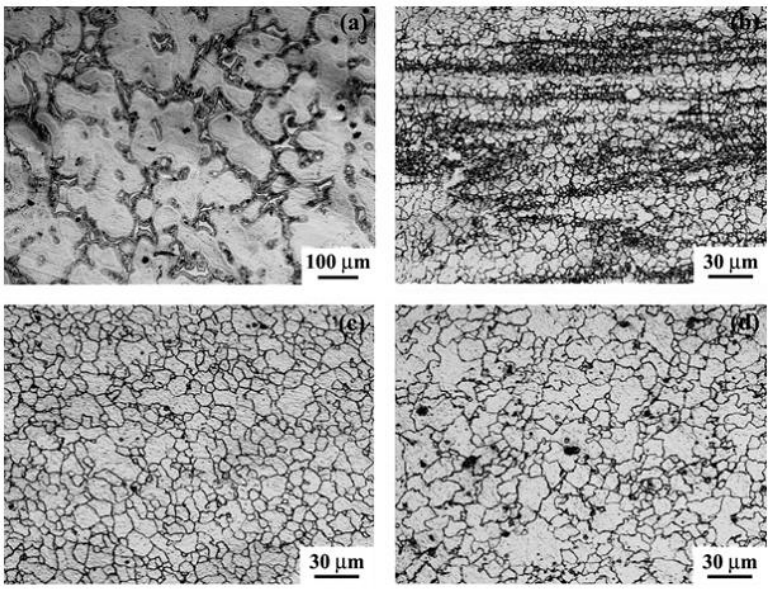

Figure 1-39. Optical microstructure of AZ91 magnesium alloy: (a) as-cast, (b) single-pass FSP, (c) single-pass FSP with a pre-ST and (d) two-pass FSP (400 rpm and 100 mm/min for all samples) [4].

Pre-FSP solution treatment (ST) can also result in enhanced reduction of β-phase. The microstructure of the nugget zone obtained with a 16 h at 415 °C pre-ST is given in Figure 1-37c. As can be clearly seen, most of the β-phase is removed. Alternatively, multiple-pass FSP with a 100% overlap is an effective approach to achieve the microstructural refinement and homogeneity. A two-pass FSP at 400 rpm produce a fine and uniform microstructure in as-cast AZ91 (Figure 1-37d), with 89% of the β-phase having been dissolved [7].

It was proposed (speculated) that the removal (i.e. reduction in volume fraction) of β-phase can be attributed to solid state dissolution/diffusion. For Mg-Al alloys, the inter-diffusion coefficient $\widetilde{D}$ can be expressed by [47]:

$$\widetilde{D} = 3.39 \times 10^{-4} m^2 s^{-1} exp\left(\frac{-135KJ/mol}{RT}\right)$$ *Equation 1-9,*

where R is the gas constant and T is the absolute temperature. The time needed for a diffusion distance d can be estimated by the relationship $t = d^2D^{-1}$ [47]. For ingot-cast AZ91 and AZ80 alloys, the typical grain size is ~ 100–200 μm (Figure 1-39a). Supposing that the diffusion distance for aluminium is 50 μm (half of the dendrite size), it will take ~ 37 h to complete the diffusion at 415 °C (which is in the typical temperature range of FSP [113]). It is clear that the diffusion distance and/or the diffusion coefficient must be significantly shortened/enhanced in order for complete dissolution of β-phase to occur within the time frame of a normal FSP.

It is assumed material in the stir zone experiences severe plastic deformation, resulting in intense mechanical break-up of β-phase and subsequent mixing of α-Mg and β-phase [4], despite this there has been no direct evidence to support such an assumption. Nonetheless, following this assumption, the diffusion distance for aluminium solute can be significantly shortened. If the diffusion distance of aluminium solute is 0.5 μm during FSP (assuming recrystallized grain size is 1 μm), then it takes only ~ 13 s to complete the diffusion at 415 °C. This overly simplified consideration, however, may still be inadequate to account for the significant reduction in β-phase. For instance, the temperature experienced by the material at a particular location does not stay at the maximum level for very long (i.e. likely to be much less than the required 13 s due to sharp temperature gradient surrounding the tool). Furthermore, fully recrystallized grains can only be formed very close to the pin (Figure 1-30 to Figure 1-32), which indicates that very limited time is available for the acceleration of diffusion (due to reduction in diffusion distance) to occur.

On the other hand, it was suggested that the high dislocation density is introduced by severe plastic deformation during FSP [114] might allow the occurrence of pipe diffusion. It was stated that the diffusion coefficient for the case of pipe diffusion can be at least 1000 times higher than the bulk one for magnesium [4]. Thus, if the diffusion distance remains the same (half the dendrite width), the time needed for complete dissolution is shortened by at least 1000 times. However, this

consideration is speculative in nature and no evidence seems to support that a huge increase in diffusion coefficient has occurred under deformation environments of FSP.

After the aforementioned reviews, it is reasonable to state that there is no evidence to suggest intensive mechanical breakage of β-phase (thus reducing diffusion distance) and/or a significant increase in diffusion rate, which are believed to be responsible for the removal of β-phase during FSP Mg-Al cast alloys. Hence, the real mechanism governing the removal of β-phase remains totally unclear.

1.6 The Scope of the Present Research

It is clear from the above literature review that a number of fundamental aspects of FSP, of Al-Si and Mg-Al cast alloys, remain unclear and the understanding of these is important for the field of FSP.

Regarding the measurable and quantifiable thermomechanical quantities, how tool torque, which is an important response governing the energy input, quantitatively relates to speeds, being the most fundamental input parameters, is unclear. Furthermore, there is insufficient understanding and total lack of a quantitative relationship established describing how flow quantity, which is also an important thermomechanical response, relates to speeds, and torque/power/specific energy.

Regarding macro-scale material flow and micro-scale deformation of FSP cast Al-Si alloy, the mechanism governing the formation of a "Non Ring" nugget, within which highly refined material clearly segregates from less refined material, during FSP (A356) is still unclear. Furthermore, the details of deformation, strain and strain rate, experienced by the material during FSP (A356) in the transient zone (closely ahead of pin) remained controversial despite its importance to FSP science.

Regarding the transient microstructure during FSP A356, the mechanisms governing the recrystallization of Al matrix, the breakage and re-distribution of Si particles are not sufficiently understood. Subsequent texture evolution and how it

is related to macro-scale material flow is unclear. For FSP Mg-Al alloys, how the β-phase is removed during FSP has been theoretically highly speculative and experimentally has not been verified.

Thus, the objectives of the present research are:

a. A torque model, M = f(ω, v) will be developed. This model should be sensible to the whole ranges of ω and v within which the processing can be characterised as FSP. Using this model, a detailed evaluation of the sensitivity of M to changes in ω and v will be made. The physical meanings of the model parameters will also be evaluated. The torque model will also be extended to tool power and specific energy. (Chapter 3).

b. The quantitative effects of ω and v on the individual and combined FSP flow quantity will be determined. The flow quantity will also be quantitatively related to $M/P/E_s$ and the explanation, based on measured thermal data and based on theoretical consideration of flow resistance, will be made. (Chapter 4).

c. The macro-scale material flow during FSP A356 leading to the formation of a "Non Ring" nugget zone will be investigated and indentified. On the micro-scale, an attempt will be made to determine the strain and strain rate experienced by the workpiece in the transient zone (closely ahead of pin) during FSP. (Chapter 5).

d. The mechanisms governing the recrystallization of Al matrix, and the breakage and redistribution of Si particles during FSP A356 will be investigated and revealed. The subsequent texture evolution, and its relationship to macro-scale material flow, will be investigated. (Chapter 6).

e. The thermomechanical and metallurgical reasons for the evolution of β-phase leading to its removal during FSP Mg-Al alloys will be determined based on studying the transient microstructure obtained through FSP "freezing" experiments. (Chapter 7).

Chapter 2. Experimental Design

In this chapter, the experimental procedures of the current PhD study will be illustrated in detail. Firstly, an overview on the experiments designed to investigate each of the subjects (as summarized in Section 1.6) will be outlined in Section 2.1. Then, machine setup, FSP experimental conditions, metallurgical examinations, and other quantitative analysis will be detailed in Section 2.2–2.5 respectively.

2.1 Experimental Series

Three series of experiments were designed in the present study, which are:

A series of FSP experiments on an Al-Si cast alloy (A356), with v and ω varying over a wide range, were conducted. For each FSP pass made, M was monitored. The amount of material flow of these experiments was quantified. Some of these experiments were repeated, so that temperatures at various locations were monitored. This series of experiments focus on developing a torque model (M = f(ω, v)), and also on developing the interrelationships among speeds, measurable responses ($M/P/E_s$) and material flow quantities.

Pin-breaking FSP experiments on A356 using selected FSP conditions were conducted. The tool was designed so that the pin would easily break off during FSP experiments, thus real time metallurgical events occurring in the transient zone (ahead of the pin) can be frozen for analysis. Pin/material couples were examined under an optical microscope, to investigate the detailed macro-scale material flow and micro-scale material deformation (strain and strain rate). The same samples were examined using SEM and EBSD in order to study the microstructural evolution in the transient flow zone, including the mechanism governing the recrystallization, and subsequent texture evolution.

Pin-breaking FSP experiments, under selected (commonly used) conditions, were performed on two representative Mg-Al alloys, which included AZ91 and AM60

ingot castings respectively. These experiments were repeated, using a normal tool, under the same FSP conditions, also the temperature was monitored at various locations for these experiments. These series of experiments aim to investigate the transient microstructural evolution ahead of pin, with a focus on the thermomechanics and metallurgy governing the removal of the second phase particles during FSP Mg-Al cast alloys. It is important to point out that the aforementioned investigation on FSP AZ91 will be focused as the volume fraction of the second phase in AZ91 is significantly higher than that of AM60 alloy (this will be shown in Section 2.2.3). Hence, a clearer observation on the second phase can be achieved in FSP AZ91 compared to that in FSP AM60. Nonetheless, whether or not the mechanism governing the removal of second phase during FSP AZ91 is common in FSP Mg-Al alloys can be determined by investigating the microstructural evolution during FSP AM60.

2.2 FSP Machines, Workpiece and Monitoring Systems

2.2.1 FSP Machine and Clamping System

All FSP experiments were performed by using a Lagun milling machine, which has step-control feed speed and rotation speed. For series 1 and 2 of the experiments, bolted clamping system (as indicated in Figure 2-1) was implemented to restrain the thermal expanding bulging behaviour of the plates which would otherwise be encountered during normal FSP conditions. The distance between two bolts was kept at 30 mm, and standard M6 bolts was used. For series 3 experiments, normal jaw clamping was used: AM60/AZ91 plates were clamped at both ends. The large thickness of the ingot casting plates, approximately 40 mm, significantly reduces the tendency of bulging (due to thermal expansion). Therefore, jaw clamping is sufficient.

Figure 2-1. A modified milling machine, with step-change linear and rotation speeds control. A LowStir device has been installed on the milling machine for monitoring forces/torque during experiments.

2.2.2 Tools Preparation and Pin Breaking Technique

In the present study, all tools were CNC machined from H13 too steel bars (30 mm in diameter). Three types of tools were used in this study, and the dimensions have been summarized in Table 2-1. Heat treatment of the tools involved:

a. austenitizing at 1050 °C for one hour and then water quenched;

b. tempering at 600 °C for one hour, and then air cooled.

The hardness of the tools after heat treatment was approximately 48 HRc. For pin breaking experiments, step b was abandoned in order to further increase the hardness of the tools (up to ~ 53 HRc) while reducing the facture toughness, which would enable the pin to break off in a sudden manner.

Various tool designs were used for each series of experiments, and the key dimension parameters are summarized in Table 2-1. In series 1 experiments, a rather standard tool was used. In series 2 experiments, a smaller shoulder and a slightly longer pin were used in order to generate less heat and increasing the contact area between pin and material, which can improve the chances of breaking the pin during FSP. In series 3 experiments, the overall size of the tools was increased in accordance with the thicker plates used during the experiments.

Table 2-1. Summary of dimensions of tools used in the present study. All threads are left-handed.

Series	*Purpose*	D_{pin} *(mm)*	L_{pin} *(mm)*	$D_{shoulder}$ *(mm)*	*Shoulder type*	p *(mm)*	d_{thread} *(mm)*
1	FSP A356 M/T measurements	6	5	18	8° cone	1.2	0.8
2	FSP A356 pin-breaking	5.5–6	5.5–6	16	flat	1.2	0.8
3	FSP AM60/AZ91 T measurements and pin-breaking	8	8	18	flat	1.25	0.7

Pin-breaking technique was used to facilitate sudden pin-breaking during FSP experiments in order to obtain pin/material couple. A sharp corner was machined at the pin/workpiece interception area, as indicated in Figure 2-2. The sharp corner was machined with different depths, ranging from 1–1.5 mm. Furthermore, a zero tilt angle and a featureless shoulder were used in order to reduce the effect of shoulder acting on the pin after breaking off.

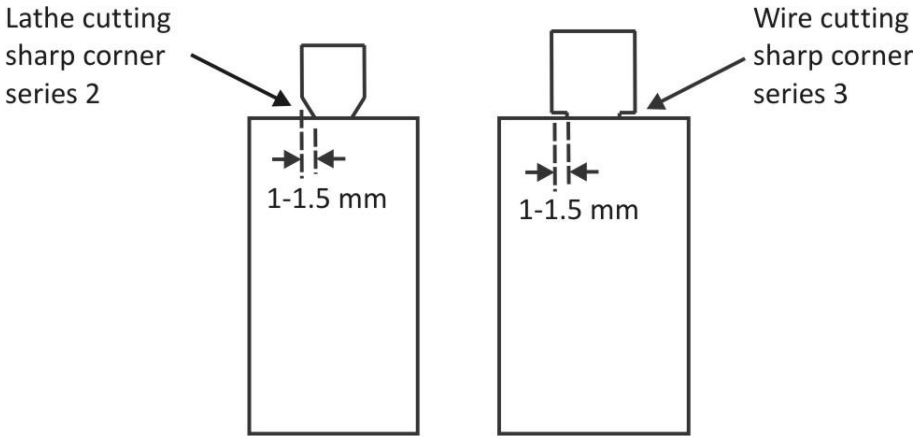

Figure 2-2. Sharp corner at the shoulder/pin interception made by lathe cutting and wire cutting, used in experiment series 2 and 3 respectively.

For series 2 and 3, where the pin breaks could not be independently controlled. In some cases, the pins broke off as soon as the tool started moving ahead, and in other cases, the pin did not break even after several FSP passes. Therefore, obtaining a broken pin sample is a time consuming process which requires large amount of patience. During the FSP AZ91 pin-breaking experiments, water quenching was immediately engaged after the pin has broken, in order to freeze

the instantaneous metallurgical events occurred ahead of pin while reducing the effects of post-FSP static annealing. However, water quenching was not performed for FSP AM60 experiments, as well as in series 2 experiments (pin-breaking during FSP A356).

2.2.3 Plates Preparation

For series 1–2, A356 plates were sectioned from cast ingots, and joined together by FSW, and then machined down to the desired dimension (290 mm by 85 mm by 6.35 mm, and 150–200 mm by 100 mm by 7–8 mm respectively). As illustrated in Figure 2-3, a plate was sectioned from the cast ingot along A–A and A'–A'. For series 3 experiments, large AM91/AZ60 casting ingots were machined down to a constant dimension: 600 mm by 110 mm by 40 mm.

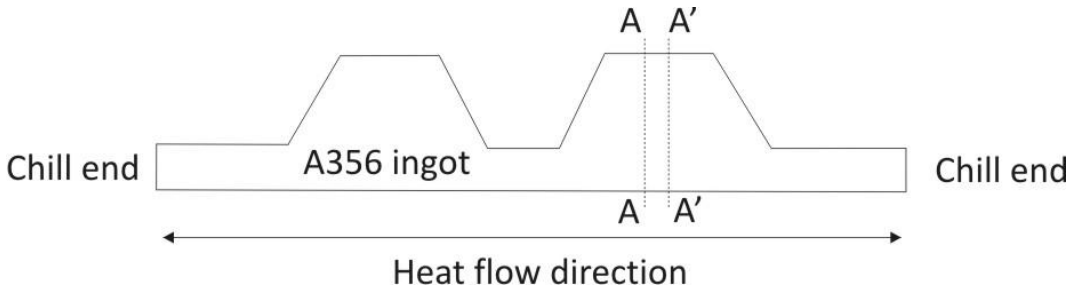

Figure 2-3. Schematic illustration showing how plates are cut from as-cast A356 ingots. A plate has been cut along A–A and A'–A'.

Chemical compositions of the materials used are summarized in Table 2-2.

Table 2-2. Nominal chemical composition of A356, AM60 and AZ91 alloys.

Series	*Material*	*Al*	*Mg*	*Cu*	*Mn*	*Si*	*Fe*	*Zn*
1, 2	A356	Bal.	0.25–0.45	0.20	0.10	6.5–7.5	0.20	0.10
3	AM60	5.5–6.5	Bal.	0.35	0.13	0.5	-	0.22
3	AZ91	8.3–9.7	Bal.	0.1	0.13	0.5	-	0.35–1.0

The microstructures of A356, AZ91 and AM60 plates used in this study are given in Figure 2-4a to d respectively. The as-cast dendrites (appear white) of A356 can be observed very clearly from Figure 2-4a. A rather regular eutectic structure (Al + Si) is given in a higher magnification micrograph in Figure 2-4b. The as-cast structures of AZ91 and AM60 ingots are given in Figure 2-4c and d, from which the (mainly)

fully divorced β-$Mg_{17}Al_{12}$ particles (appear light grey) can be clearly observed. These particles completely separate from the Mg dendrites (appear white). In AM60, both quantity and size of the β-$Mg_{17}Al_{12}$ are significantly smaller than those in AZ91. Furthermore, the Mn containing particles in AZ91 and AM60 (Al_8Mn_5, and Al_4Mn) appear black.

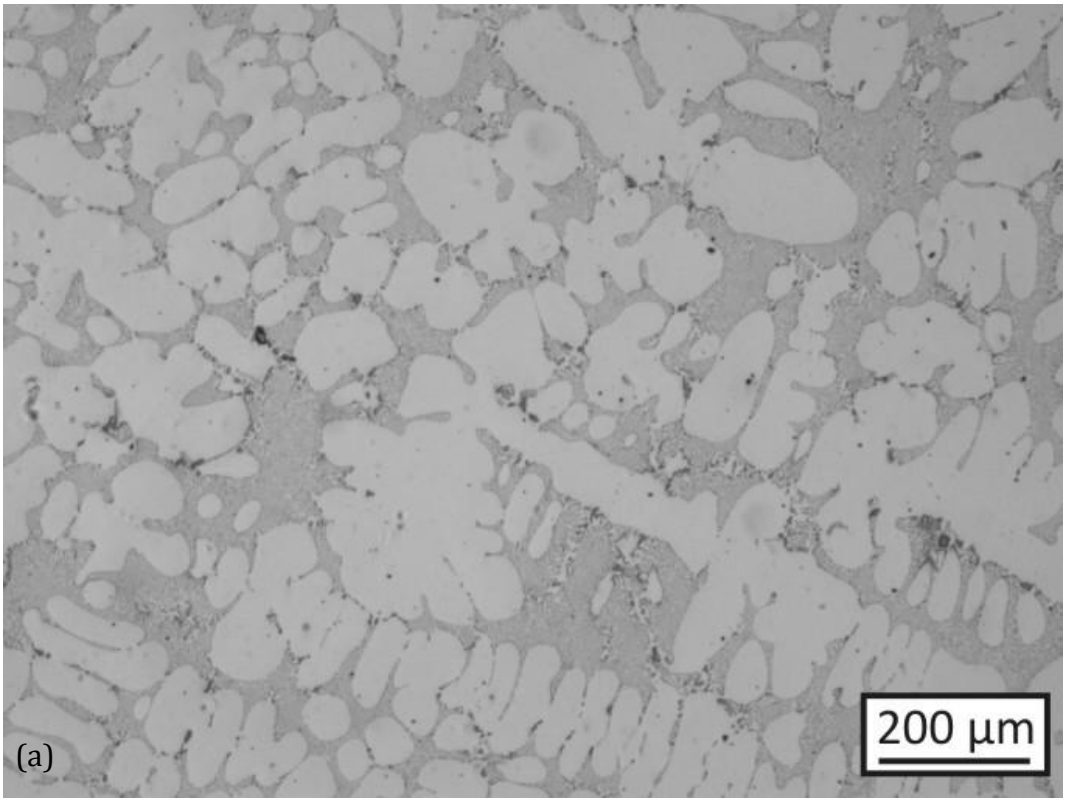

Figure 2-4. (a) Low magnification micrograph of as-cast A356 alloy. Matrix and eutectic Al appears white, while Si particles black. (b) High magnification micrograph of A356 showing the eutectic structure. (c) and (d) micrographs of AZ91 and AM60 ingots. Matrix Mg appears white, $Mg_{17}Al_{12}$ particles light grey and Al_8Mn_5 and Al_4Mn particles black. The morphology of Al_8Mn_5 is very equiaxed, while Al_4Mn has a rather high aspect ratio.

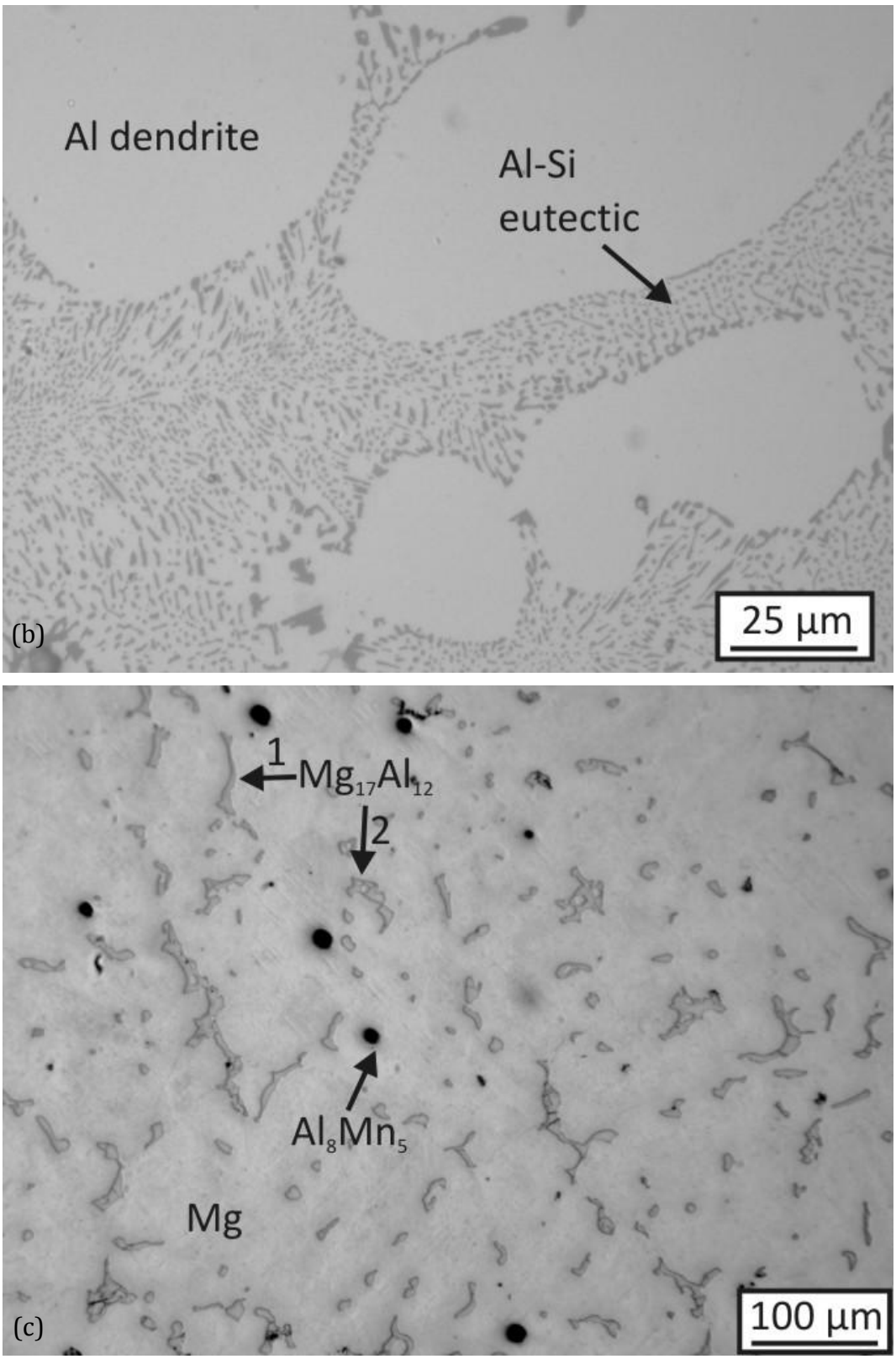

Figure 2-4. Continued.

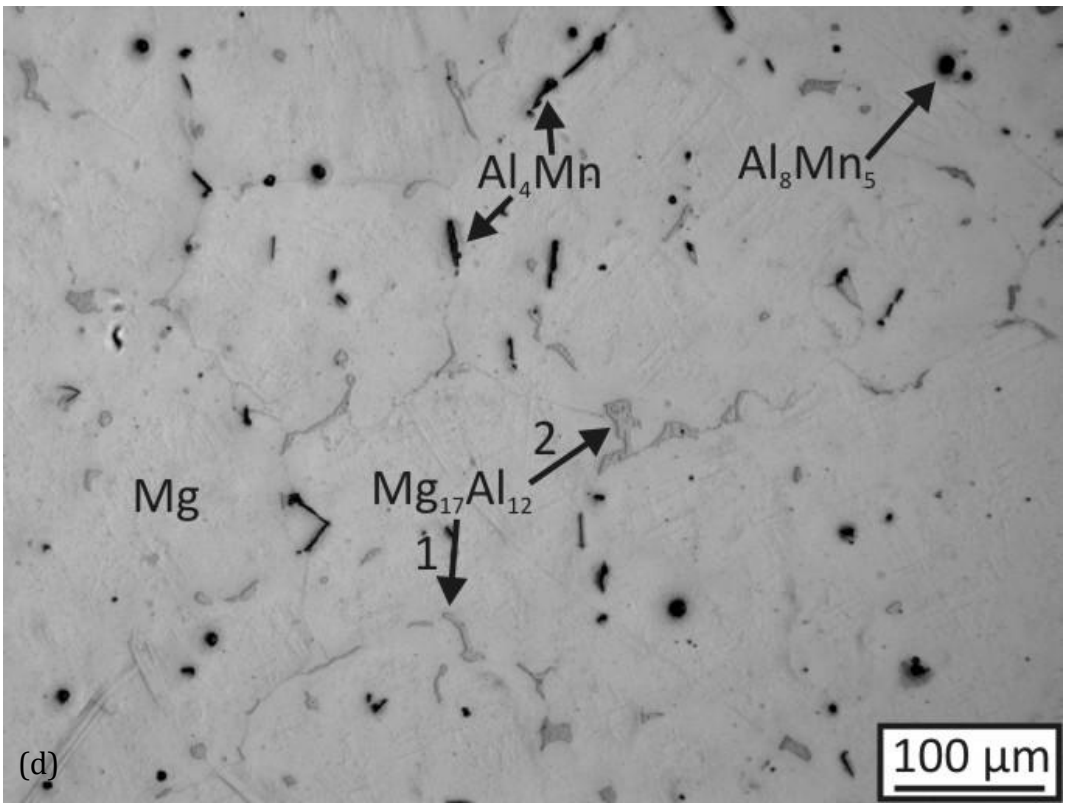

Figure 2-4. Continued.

The experiment layouts, from series 1 to series 3, are given in Figure 2-5. In series 1, four FSP experiments were conducted on one plate, as indicated in Figure 2-5. FSPs 1–2 were performed first, and then the plate was rotated by 180° so that FSPs 3–4 could be performed exactly the same way as FSPs 1–2. In all experiments, a minimum gap of 5 mm was kept between two adjacent FSPs.

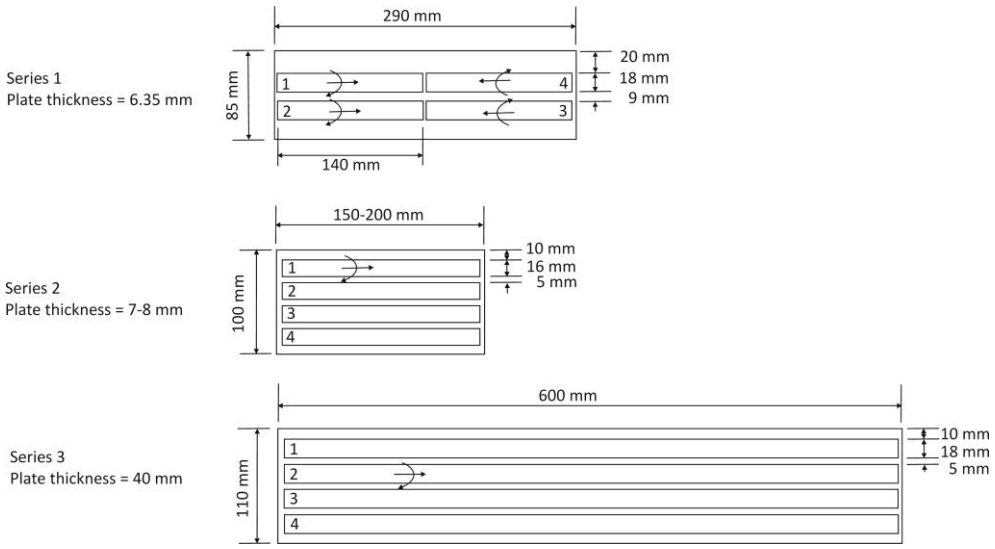

Figure 2-5. Schematic illustration of FSP experiments (series 1–3) layouts.

2.2.4 Temperature, Force and Torque Monitoring

As can be seen from Figure 2-1, a *LowStir™* device, manufactured by Sigmapie System (UK), was used to monitor the torque (M) during FSP experiments. Strain gauges are built within the device which is able to monitor down-force, horizontal force, and torque during FSP. The strain data captured by the *LowStir™* is transmitted to a Signal Processing Module (SPM), which converts the data into digital format which can be displayed on the computer, and saved as Microsoft Excel file.

The measuring frequency was kept constant at 300Hz, i.e. five sets of measurements per second. The M measurements during a FSP experiment performed under a normal condition (v = 224 mm/min, ω = 500 rpm, θ = 2.5°) are given in Figure 2-6. Tool plunging started from ~ 11 s and finished at ~ 40 s. After the (rotating) tool was fully immersed into the plate, Figure 2-6 Indicates M experiences a drop. The tool travelling started from ~ 47 s and finished at ~ 78 s. Stable M establishes from ~ 50 s onwards. It is important to note that torque value is always above zero throughout the entire FSP experiment, and it is how the *LowStir™* device functions. The initial M is 3.2 Nm; while after withdrawing the tool, the M does not fall back to zero: the remaining torque is 7.5 Nm. Obviously, there has been an upward drift of the torque (4.3 Nm) during the experiment, and when exactly this drift occurred cannot be determined. However, both the initial and the remaining torques are relatively insignificant compared to the stabilized M, which is 58.2 Nm (taken as the average of the 20 data before 78 s). Therefore, M during FSP is the difference between measured M and remaining M, which is 50.7 Nm in the current case. Torque in other FSP experiments was calculated using aforementioned method.

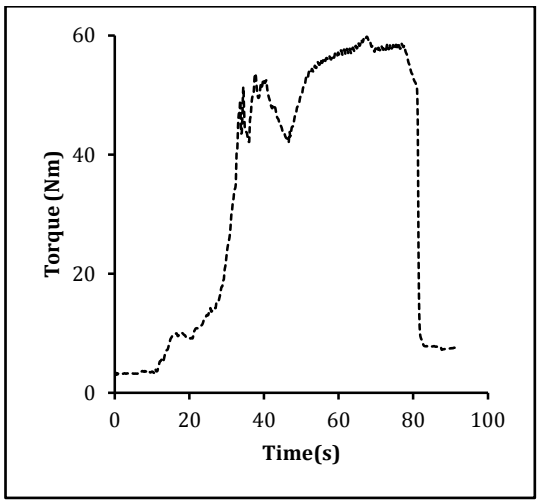

Figure 2-6. Forces/torque measured by using the LowStir device.

K type thermal couples, manufactured by ECEfast NZ Ltd., were used in the current study for all temperature measuring experiments. The thermocouples can measure temperatures up to 1200 °C. The length of thermal couple probe is either 15 mm or 30 mm, and the diameter of the probe is 1 mm. The probe has an Inconel (austenitic nickel-chromium-based alloy) shield.

An IOtech Personal Daq/55 temperature measuring system was used for all temperature measurement experiments. The system is able to interpret both analog and digital data inputs, and the former was used in the current study. For FSP A356 plates, the measuring frequency was 170 Hz; for FSP thick cast AM60/AZ91 plates, the frequencies were 1300 Hz (for measuring pin centre temperature) and 400 Hz (for measuring shoulder temperature).

A schematic illustration of the thermocouple placements is given in Figure 2-7. As can be seen, in series 1, temperatures were measured at three positions:

a. 2 mm below plate surface, 3 mm away from the pin threads (representing shoulder region temperature).

b. 3 mm below plate surface, at pin centre (representing pin centre temperature).

c. 4 mm below plate surface, 1 mm away from pin threads (representing nugget temperature).

In series 3, temperature was measured at three positions:

a. 4.5 mm below plate surface, at pin centre.

b. 4.5 mm below plate surface, 1 mm away from pin threads.

c. 4.5 mm below plate surface, 5 mm away from pin threads.

The thermocouples which were placed at the pin centre can be used only once, because the forward motion of the tool bent the thermocouple probes towards the advancing side hence they could not be extracted after experiments. Thermal conducting paste was inserted into the holes in order to enhance the contact between plates and thermocouple probes.

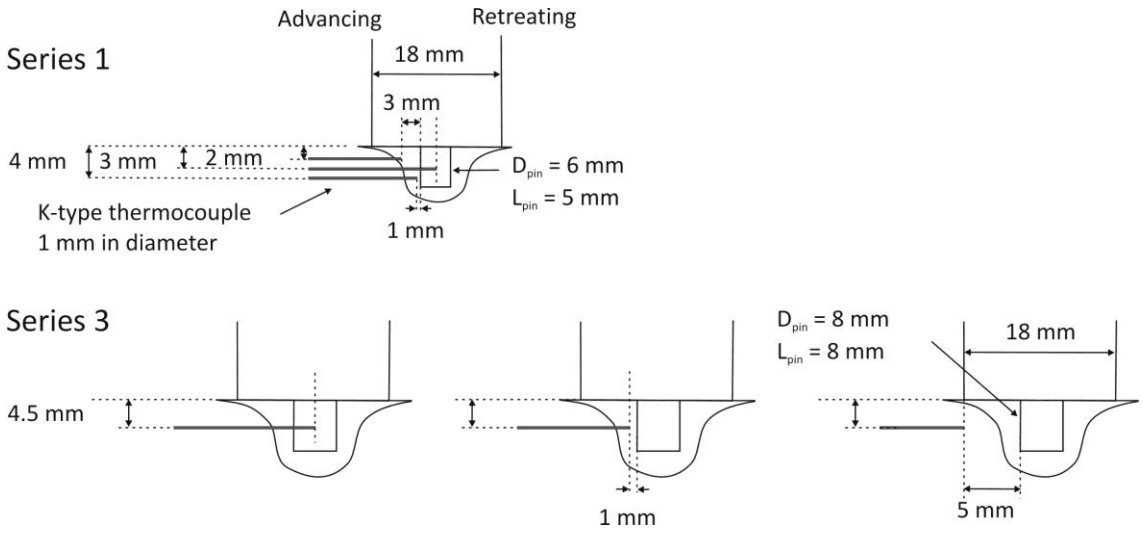

Figure 2-7. Schematic illustration of thermocouple placements during series 1 and 3 of the FSP experiments. Drawing is only illustrative and not to scale.

Furthermore, as introduced previously, once the pin broke off during FSP AZ91 experiments (series 3), machining coolant was immediately engaged to minimize after-FSP static annealing effect. Therefore, during the temperature measuring experiments conducted on AZ91, once the pin touched the thermocouple, cold machining coolant was engaged to imitate the thermal history experienced during pin breaking experiments.

2.3 Experimental Conditions

2.3.1 Tool Positioning

All experiments were conducted with tool vertical position control mechanism, which involved maintaining the vertical position of the tool during the entire FSP experiment. Let us consider the FSP experiments on A356 plates (conducted using tool with pin length of 5 mm), three steps were involved during the plunge stage:

a. Tool was positioned in a way that the pin tip just touched the surface of the A356 plate (Figure 2-8), and hence the vertical control handle of the FSP machine was assigned "zero". Furthermore, the distance between a reference point on the FSP spindle (in this case a stationary bolt) and the machine bed was measured by using a height gauge (with the smallest division of 0.02 mm). This distance is denoted as d_1 in Figure 2-8.

b. Then the tool was moved downward for 5.2–5.3 mm, the movement of the vertical control handle was controlled with an accuracy of ±0.05 mm (the smallest division of the vertical dial is 0.1 mm). Also, the distance between the reference point and the machine bed was measured again (as d_2).

c. The actual distance by which the pin immersed into the plate (d_{plunge}) was calculated as the difference between d_1 and d_2. It was found that plunge depth indicated by the vertical dial was ~ 5% larger than the actual plunge depth: e.g. if the dial of the vertical handle indicates the tool is moved downward by 5.3 mm, the actual distance moved is approximately 5.1 mm, i.e. the root of the pin (as indicated in Figure 2-8) is immersed 0.1 mm beneath the surface.

In all experiments, the root of the pin was immersed around 0.1 mm beneath the top surface of the plate, in order to make sure that sufficient flow at the shoulder region would be generated.

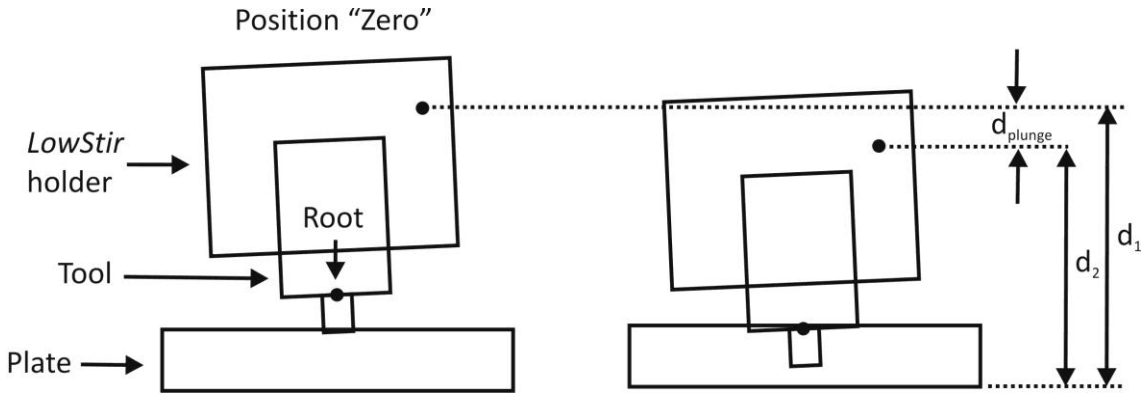

Figure 2-8. Schematic illustration of tool plunge during a normal FSP experiment. Position zero is set when the pin tip touches the plate surface. The actual depth of plunge is denoted as d_{plunge}.

2.3.2 Selection of a Systematic Range of Forward/Rotation Speeds

As introduced previously, series 1 of the experiments involve performing FSP experiments on A356 plates under various welding conditions in order to determine the effects of speeds on material flow quantity and measurable responses ($M/P/E_s$). Therefore, this series of experiments were conducted under a wide processing window. As for series 2, experiments were performed under a few selected conditions (ω = 710 rpm, v = 112 and 160 mm/min). It will be shown later (Section 4.2) that the FSP structures obtained under these selected conditions can represent the structures obtained under all conditions used in current study. Similarly, for series 3 experiments, only two representative conditions were used. All FSP conditions are summarised below:

Table 2-3. Summary of FSP experimental conditions.

Series	No	v (mm/min)	ω (rpm)	Series	No	v (mm/min)	ω (rpm)
1	1	28	63	1	15	224	250
	2	28	125		16	224	500
	3	28	250		17	224	710
	4	28	500		18	224	1000
	5	28	710		19	224	1400
	6	28	1000		20	315	500
	7	56	250		21	315	710
	8	56	710		22	450	500

9	56	1400		23	450	710
10	112	250		24	450	1000
11	112	500	2	1	112	710
12	112	710		2	160	710
13	112	1000	3	1	112	1000
14	112	1400		2	160	1000

Except in series 1, where a constant tilt angle of 2.5° was kept, a zero tilt angle was used for the rest of the FSP experiments. In series 3, experiment No.1 has been conducted on AM60 thick cast ingot, while No.2 was conducted on AZ91.

2.4 Metallurgical Examinations

2.4.1 Optical and Electronic Microscopes

Nikon optical microscope (FX–35A) and Olympus stereomicroscope (SZX9) were used for macro/microstructure observations for low magnification range (up to 100 times).

Scanning Electron Microscope used in this study is a FEI Quanta 200F Environmental Scanning Electron Microscope (ESEM). This SEM is also equipped with a TSL EBSD system and an EDAX Genesis EDS system. The standard accelerated voltage was chosen as 20 kV.

Fundamentals of EBSD

EBSD is a technique by which an SEM can be used to evaluate the microstructure of a sample based on crystallographic analysis. It is an ideal technique for analyzing grain orientation, texture, and grain boundary characteristics. The principle components of an EBSD system are given in Figure 2-9.

EBSD operates by arranging a flat, finely polished sample at a small angle (10°) to the incident electron beam (illustrated in Figure 2-9). The SEM stage tilts the plane of the sample to this shallow angle. With moderate to high electron beam accelerating voltages (10 to 30 kV), the electron beam is diffracted by the crystal lattice of the sample at the point where incident beam strikes on the sample

surface. With the beam stationary, an electron backscatter diffraction pattern (EBSP) emanates spherically from this point in all directions. If an EBSP detector is placed close to the incident beam point, it intersects a portion of this diffraction pattern. The detector is in fact similar to a digital camera which is contained within a vacuum compatible and retractable body. The camera's CCD (Charge-Coupled Device) chip is illuminated by the phosphor screen that intersects the spherical diffraction pattern. The phosphor converts the diffracted electrons into light suitable for the CCD camera to record.

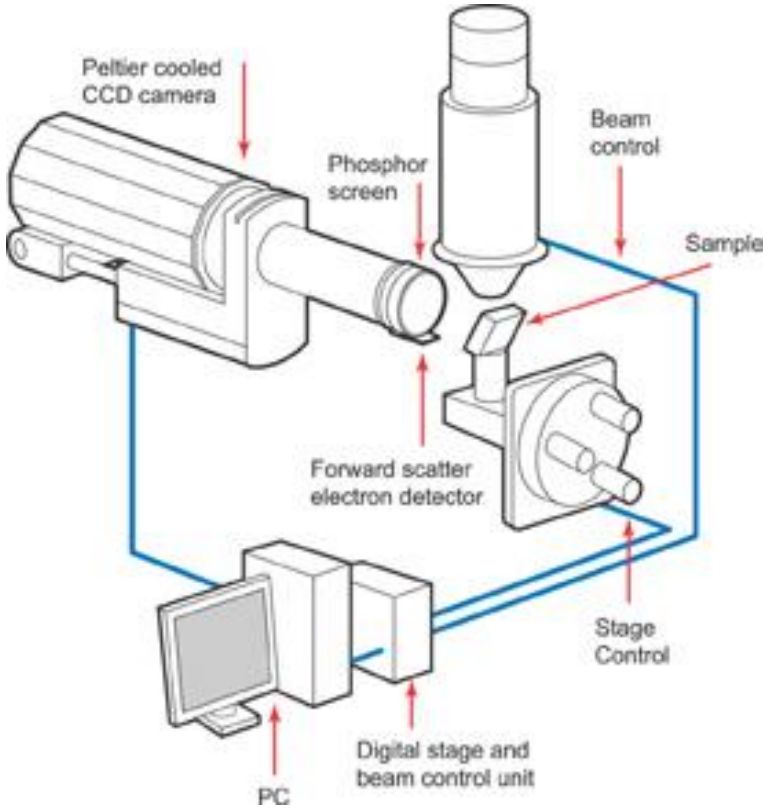

Figure 2-9. Diagram of the principle components of an EBSD system [115].

With a stationary beam on a point of the sample surface, the EBSP is analysed and stored. The EBSP is uniquely defined by the lattice parameters of the particular crystal under the beam, and by its orientation in space. By selecting the expected crystal phases from a phase database, all possible identities and orientations of the crystal under the beam are matched to the EBSP until the best fit is found. The pattern is then considered indexed, and the best-fit orientation and phase is reported as the orientation and phase of the point on the sample.

As the speed of pattern analysis has increased, it has become practical to scan the beam over multiple points on the sample to create an orientation map (OM). This is a common method for a microstructural investigation with EBSD. When the beam is scanned in a grid across a polycrystalline sample and the crystal structure and orientation are analysed at each point, the resulting map will reveal the constituent grain morphology, orientations, and boundaries.

Crystal Orientation Representation

Crystal orientation (texture) is usually presented in the form of Pole Figure (PF). A crystallographic direction, or the normal to a crystal plane, can be described as a point on the reference sphere. For example, the directions perpendicular to {100} planes of a cubic cell intercepting with the reference sphere is shown in Figure 2-10a, thus creating six <100> poles. Three <100> directions locating on the positive sphere are marked by solid lines; while the other three <100> directions locating on the negative sphere are marked by dashed lines. If the reference sphere is attached to an external frame (ND, TD, RD), the position of the pole on the sphere provides information on the crystallographic orientation of the crystal with respect to this frame.

In order to represent the 3D orientation of the poles on a 2D plane, one requires projecting the poles on reference sphere onto a projection plane. This projection is shown in Figure 2-10b. The point of projection is at “B”. For example, the reference sphere is represented by the basic circle on the projection plane. Hypothetically, if point P represents one of the <100> poles on the reference sphere, the projection of P onto the plane is represented by point P’. By projecting the three <100> poles (locating on the positive sphere) onto the plane, the <100> PF can thus be obtained. Similarly, <111> PF is obtained by projecting the interceptions of <111> poles with the reference sphere onto the projection plane. Therefore, the crystal orientation with respect to the external reference frame (ND, TD, RD) can be represented by PFs.

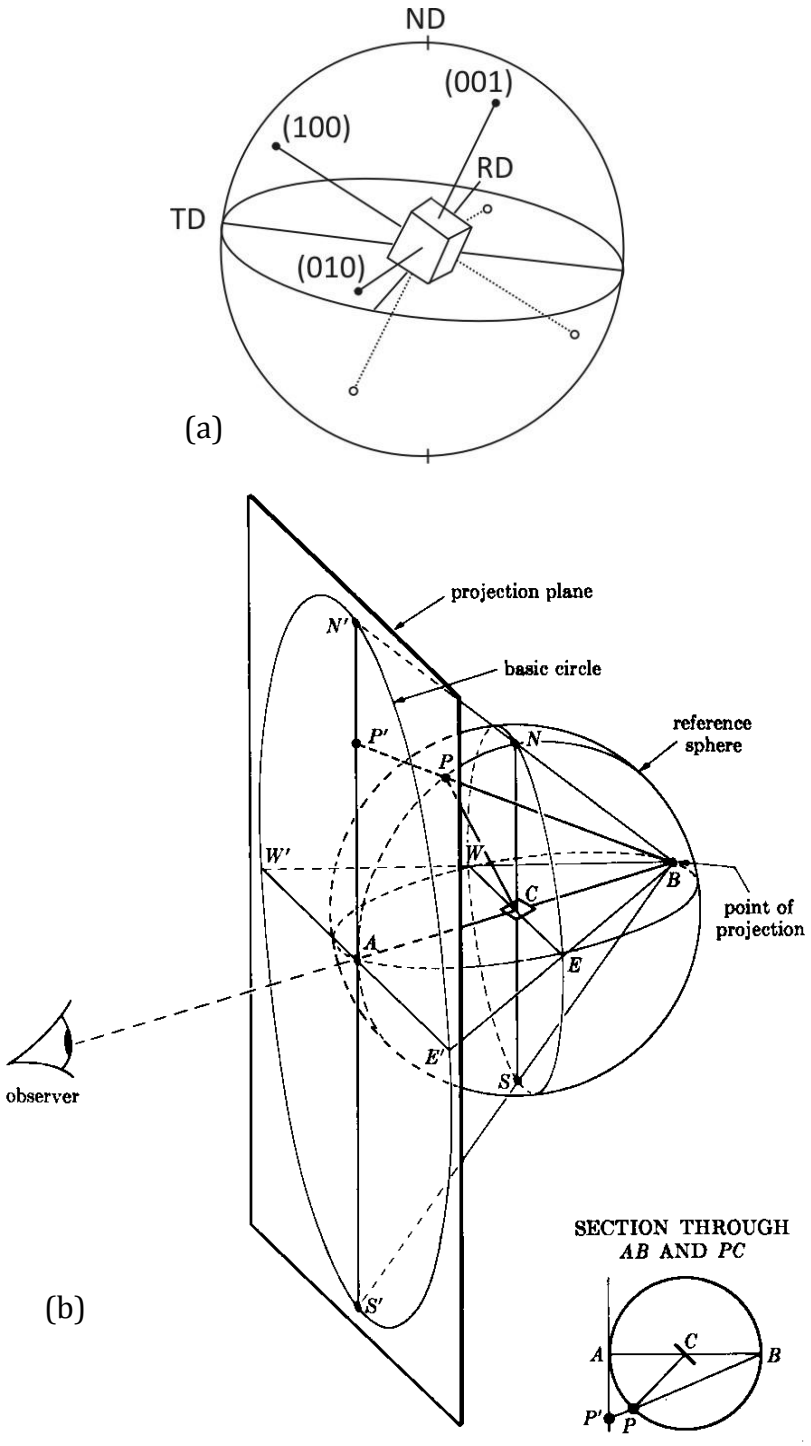

Figure 2-10. (a) Presentation of the {100} poles of a cubic crystal intercepting with the reference sphere. (b) Schematic illustration of stereographic projection of a pole figure [116].

Let us refer to Figure 1-35b and c, where the FSP reference frame (ND, TD, RD) is defined. If the crystal orientation of the material is such that the $(1\bar{1}\bar{1})$ plane is parallel to the shear plane (represented by the rectangle) while [110] direction is

parallel to the shear direction (indicated by short arrows), the <111> pole figure of such an orientation, observed along ND, is thus the "A" texture given in Figure 1-36.

In Inverse Pole Figure (IPF), we focus on a specific sample frame direction, and find which crystal direction, of the point being scanned, is parallel to this specific direction. This specific sample frame direction is also the observation direction. Therefore, for an ordinary mounted sample, the specific direction is perpendicular to the polished surface. A specific colour can be assigned to the point being scanned according to its orientation. In current EBSD system, red, blue or green will be assigned to a point if the <100>, <111> or <110> crystal direction is parallel to the observation direction. Hence, an EBSD orientation map (OM) of an area can be constructed by scanning, and thus colour coding every point within the area being scanned.

For example, let us consider an OM (Figure 2-11) taken from an area ahead of pin, from a pin-breaking sample obtained during FSP A356 plate. No Si particles are contained in this OM. As will be described, the top half of the pin will be removed so that the observation can be made on the pin mid-thickness plane. Therefore, the observation direction is parallel to the pin axis, and thus parallel to ND of the sample (refer to Figure 1-35c). Hence, the OM will show which crystal direction is parallel to ND. In the current case, the overall colour is red. As indicated on the top-right corner, the red colour indicates the <100> axis is parallel to ND. Similarly, the blue colour represents the <111> axis is parallel to ND.

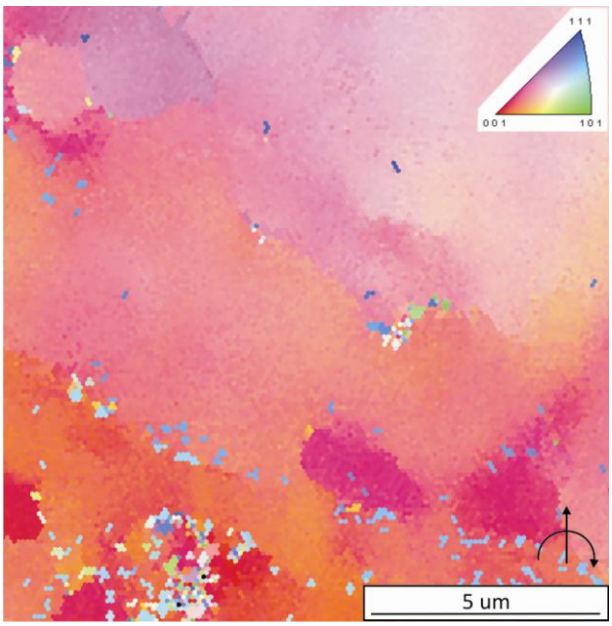

Figure 2-11. EBSD map taken ahead of the pin from a pin-breaking sample conducted on A356 plate. The observation direction is parallel to tool axis (ND), and the tool in this case is moving upward in this page.

EBSD Operations Inputs

The scanning step used in the current study varied between 0.1 μm to 1 μm, depending on the size of the scanned area. The scan speed was ~ 6 points per second. The most important inputs of the EBSD operation are the crystallographic parameters of the expected phases contained by the sample being studied. EBSD studies were only performed on pin-breaking samples obtained from FSP A356. The overwhelming phases existing in A356 alloy is α-Al and Si. The crystallographic parameters of Al and Si are summarised as below:

Table 2-4. Summary of crystallographic parameters of the major phases in A356 alloy.

Phases	*Crystal system*	*Lattice parameter (Å)*	*Point group*	*Space group*
Al	FCC	4.05	$m\bar{3}m$	$Fm\bar{3}m$
Si	FCC (diamond cubic)	5.43	$m\bar{3}m$	$Fd\bar{3}m$

Si Particles Identification

Normally, EBSD analysis software (in this case the TSL software) contains a function which can be used to distinguish different phases included in the EBSD

scans. Unfortunately, this function cannot be used in the current study. The available version can only describe the different crystal point groups but not the space groups. Therefore, satisfactory phase discrimination between Al and Si phases cannot be achieved.

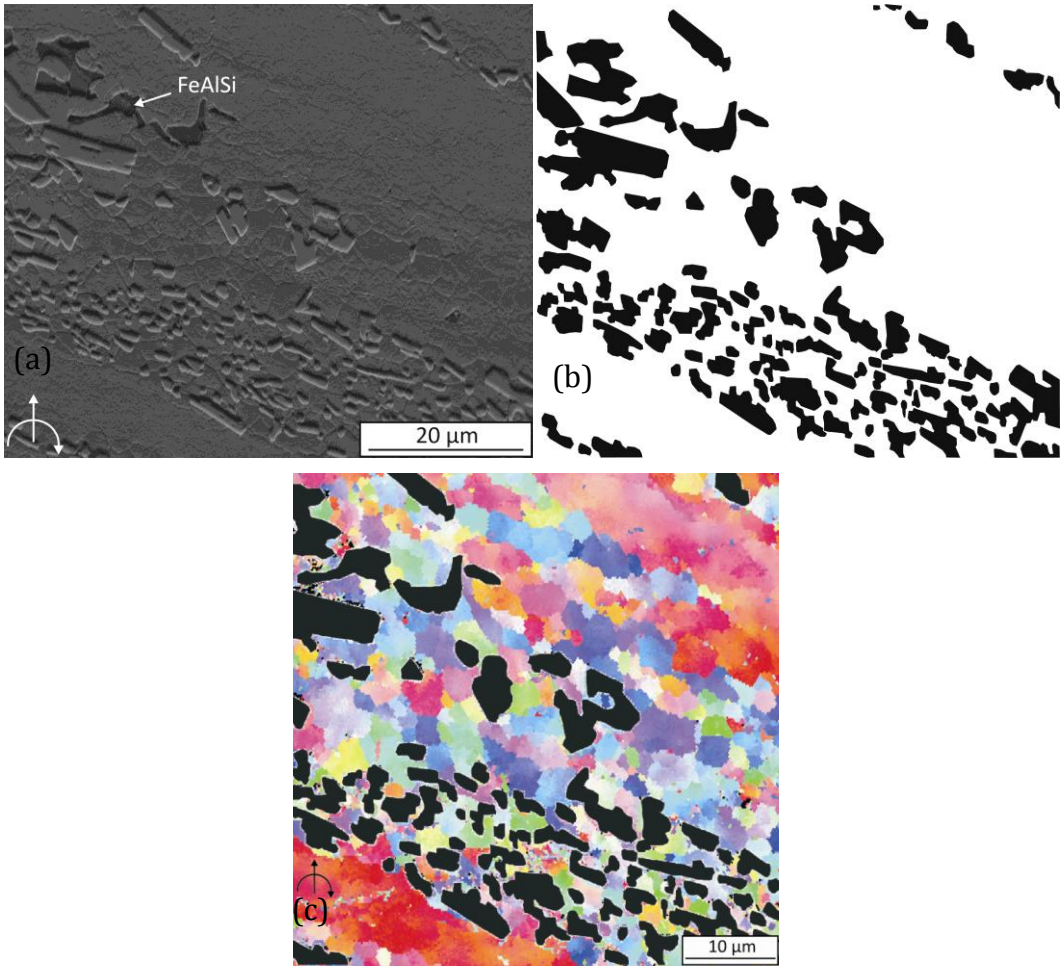

Figure 2-12. (a) SEM taken at a location ahead of the pin during FSP A356, (b) the Si particles are marked black using Coreldraw, and (c) EBSD scan taken from the same location with Si-identification superimposed onto it. FSP conditions are: 112 mm/min, 710 rpm, and 0 tilt angle.

Thus, a different methodology needed to be used in order to make the phase distinctions in current EBSD scans. An example of how this is done is given in Figure 2-12. A SEM image taken ahead of the broken pin obtained from FSP A356 is shown in Figure 2-12a. Si particles, and some α-FeAlSi particles (as indicated) can be easily identified, and they can be marked black (shown in Figure 2-12b) by using standard drawing software (Coreldraw). This particles-identification can be

superimposed onto the EBSD taken from the same location, as indicated in Figure 2-12c.

2.4.2 Sample Preparation

Mounting and polishing machines used in the current study are LaboPress–3 and TegraPol–25 provided by Struers. For sample mounting, phenolic hot mounting resin was used. Resin and sample were heated up 150 °C for 6 minutes in the LaboPress–3 machine with downward pressing force about 25 kN. Then samples were cooled by room temperature water for 6 minutes. Mounted samples then went through two grinding step: manually grinding using SiC papers with grit up to 300; and automatic grinding on TegraPol–25 using MDMol grinding pad with DiaPro–Allegro Largo suspension (9 μm abrasive size) for 4 minute. Fine polishing of the samples included: using MDLargo polishing pad with DiaPro–Mol suspension (3 μm abrasive size) for 3 minutes; using MDChem polishing pad with OP–S suspension (0.04 μm abrasive size) for 1 minute. Polished samples were cleaned with AR ethanol using an ultrasonic cleaning machine for 30 s.

In addition, broken-pin/material couples must be carefully grounded, to the desired thickness, using SiC (180 grit) grounding paper before conducting normal grinding and polishing procedures. For example, a broken-pin sample obtained from series 2 contains a 6 mm long steel pin (Figure 2-13). A line was marked 2.5 mm below the top surface of the sample, and then the sample was grinded until the marked line was reached. By performing the aforementioned normal grinding and polishing procedures, approximately another 0.5 mm (the top 3 mm of the pin in total) was removed, hence the mid-thickness plane could be observed.

Chemical etching procedures varied depending on the samples. In series 2, broken pin samples (in A356 plates) were etched with 0.5% HF (0.5 mL saturated HF, and 100 mL water) for up to 3 minutes. In series 3, AM60/AZ91 normal and pin-breaking samples etching for optical microscopy was performed for 30 s in 10 mL saturated nitric acid, 90 mL ethanol followed by 20 s in 6 g picric acid, 100 mL ethanol, 5 mL saturated acetic acid. For SEM observation, AM60/AZ91 pin-breaking samples were electro-polished right after normal mechanical polishing.

The etchant contained 30 mL of phosphoric acid and 50 mL of ethanol, both cooled to 2 °C. The polishing took 20 s at 3 V and 1 V respectively. After electro-polishing, samples were stored in ethanol (98%) below 4 °C.

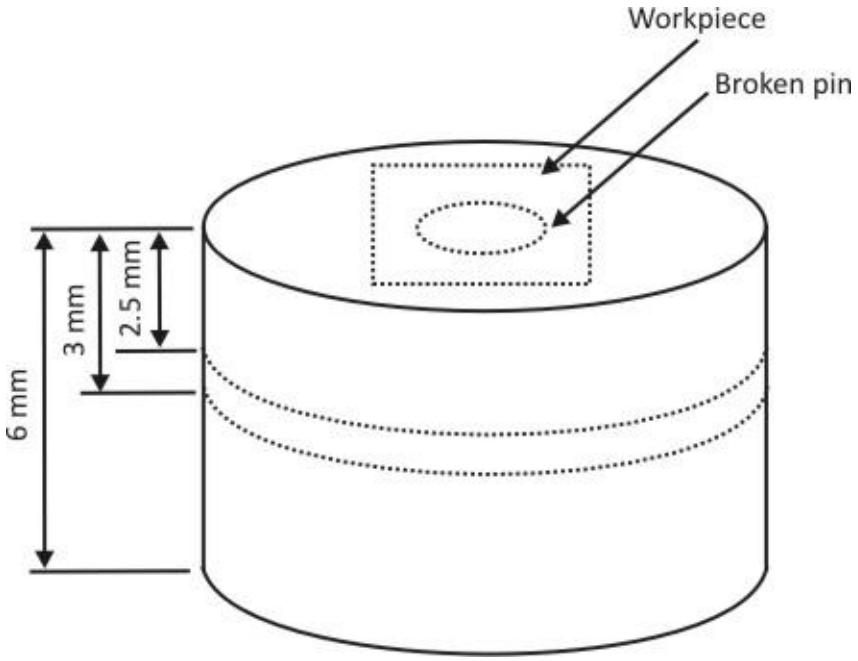

Figure 2-13. Schematic illustration of how broken-pin samples are sectioned.

2.5 Quantitative Analysis

2.5.1 Quantifying Flow Volumes

As described earlier, series 1 experiments was designed to study the interrelationships among speeds, measurable responses ($M/P/E_s$), and flow quantity. Hence, material flow (forming various processed zones) during FSP A356 needed to be precisely quantified. The relatively large dendrites and Si particles of the as-cast state A356 were used as natural flow markers.

For example, the cross section macrograph of FSP conducted using v = 28 mm/min, ω = 710 rpm is given in Figure 2-14a to illustrate. This macrograph was taken using a stereo-microscope. The Al dendrites appear black while the Al-Si eutectic appears light grey. As can be seen, the total stir zone, which includes material that has gone through noticeable deformation, is outlined by the dashed curve. The solid curve divides the total stir zone into shoulder flow zone (induced by the

shoulder) and nugget flow zone (induced by the pin). The division curve was determined by closely examining the deformation directions in the upper-retreating region of the cross section (the enlarged view is shown in Figure 2-14b). As pointed by the arrows, dendrites locate at the upper region are deformed downward while dendrites locate at the lower region are deformed upward. Therefore, the partition curve must locate where the flows converge together.

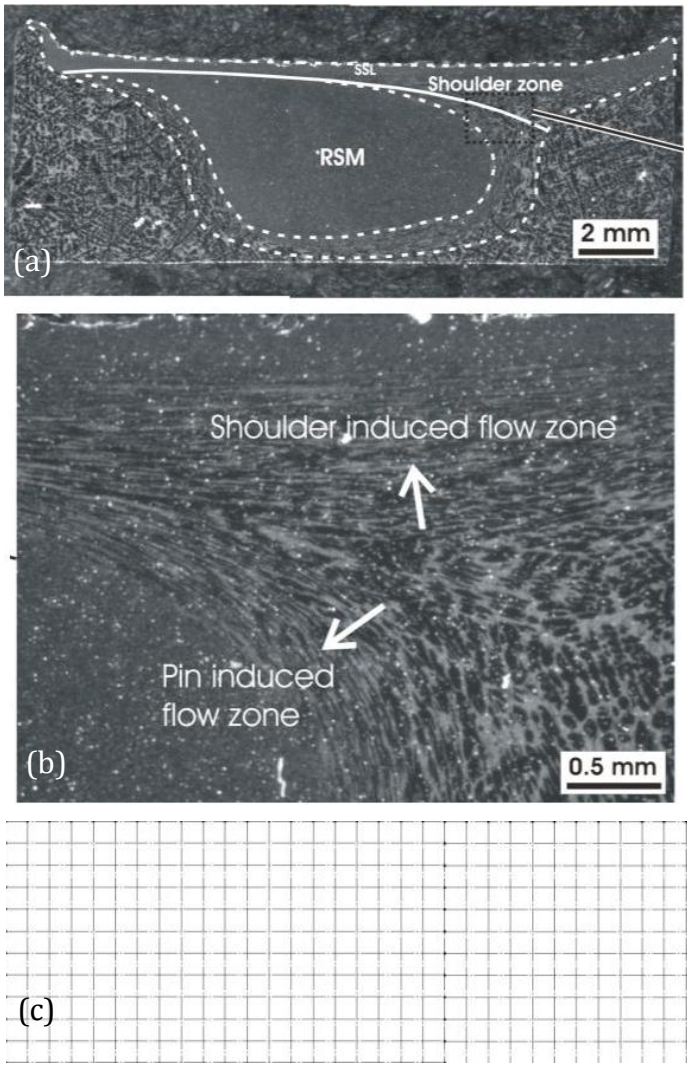

Figure 2-14. (a): cross section (advancing side on the left) of FSP sample made using v = 28 mm/min, ω = 710 rpm, and θ = 2.5°. The solid line marks the division of shoulder flow zone and nugget flow zone. (b): an enlarged view on the upper retreating side. (c) mesh grid with a unit area representing 0.25 mm by 0.25 mm.

To quantify the area of each flow ($A_{shoulder}$, A_{nugget} and A_{total}), a fine mesh grid (as indicated in Figure 2-14c) was superimposed onto the macrographs, and hence flow areas could be manually counted.

However, the flow area (A_{flow}) only measures the flow quantity in a 2D manner. Flow volume generated per revolution ($V_{flow\text{-}rev} = A_{flow}v/\omega$) was used to describe the flow quantity for a 3D consideration. The first graph in Figure 2-15 illustrates an ideal situation that the tool has rotated for one revolution and hence travelled ahead for $\lambda = v/\omega$. By assuming that a steady FSP condition has been established, the cross section macrograph thus would remain the same.

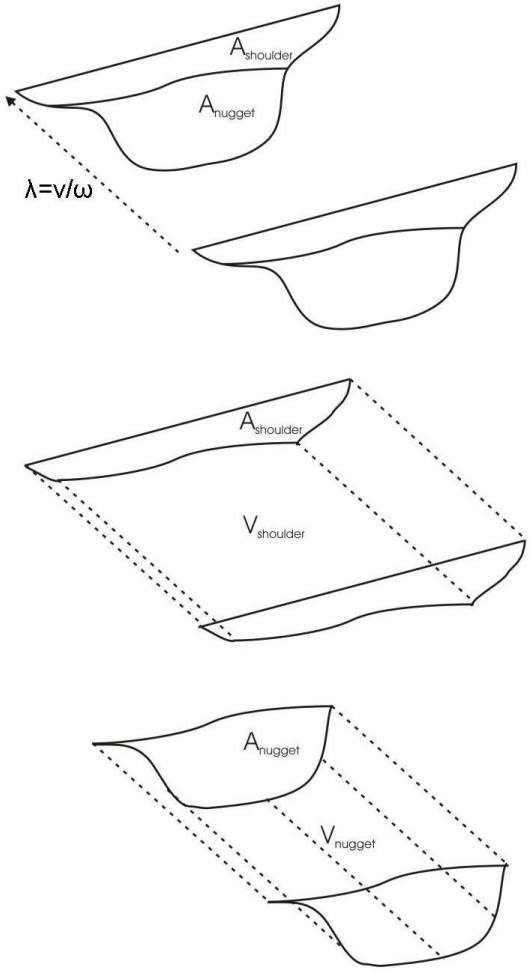

Figure 2-15. Schematic illustration of the shoulder and pin flow volumes generated within one revolution of tool rotation.

Within this distance ($\lambda = v/\omega$), the amount of shoulder flow ($V_{S\text{-}rev}$) and the amount of nugget flow ($V_{N\text{-}rev}$) would be:

$$V_{S-rev} = A_{shoulder}\frac{v}{\omega} \qquad \textit{Equation 2-1a}$$

$$V_{N-rev} = A_{nugget}\frac{v}{\omega} \qquad \textit{Equation 2-1b}$$

Furthermore, the total area (A_{total}) and total flow volume per revolution ($V_{T\text{-}rev}$) can be determined as:

$$A_{total} = A_{shoulder} + A_{nugget} \qquad \textit{Equation 2-2a}$$

$$V_{T-rev} = V_{S-rev} + V_{N-rev} \qquad \textit{Equation 2-2b}$$

2.5.2 Analyzing Particles using ImageJ

As summarised in Section 1.6, how the volume fraction of the β-phase changes ahead of the pin during FSP Mg castings will be studied in this thesis. Thus the volume fraction of β-phase must be quantified first. An example of how β-phase was identified is given in Figure 2-16. A micrograph taken from a location 1446 μm ahead of the pin during FSP AZ91 is given in Figure 2-16a. As-cast β-phase (bright), partially melted β-phase (black), and equiaxed Al_8Mn_5 particles (light grey) are indicated by arrows. In general the β-particles have much higher aspect ratio compared to the Al_8Mn_5 particles.

The primary task is to differentiate as-cast and partially melted β-phase from the rest of the material which is the α-Mg. As can be seen from Figure 2-16a, both partially melted β-phase and Al_8Mn_5 particles have darker colours; while as-cast β-phase and Mg phase have lighter colours. Particle identification using ImageJ requires the particles to have a rather different colour with the matrix material (Mg phase). Hence, the partially melted β-phase can be easily identified from the matrix; while the as-cast β-phase cannot be accurately identified. Therefore, as-cast β-phase was manually marked black using standard drawing software (Coreldraw), this is shown in Figure 2-16b. On the other hand, the existence of dark Al_8Mn_5 can confuse the identification of β-phase. Hence, these particles were marked white using Coreldraw, as indicated in Figure 2-16b.

By using the "Threshold" function in ImageJ, substances with darker colours, i.e. the partially melted and original β-particles were highlighted by red colour. On the other hand, substances with light colour, i.e. α-Mg and Al_8Mn_5 particles, were ignored. The upper and lower levels of "threshold" were 10 and 200 respectively. This standardization was required so that the identification of the β-phase was

consistent at various locations ahead of the pin. By comparing Figure 2-16a and c, it can be seen that the areas occupied by β-phase are well recognized by using ImageJ.

The volume fraction of the outlined β-particles was then determined by ImageJ using the "Analyze Particles" function.

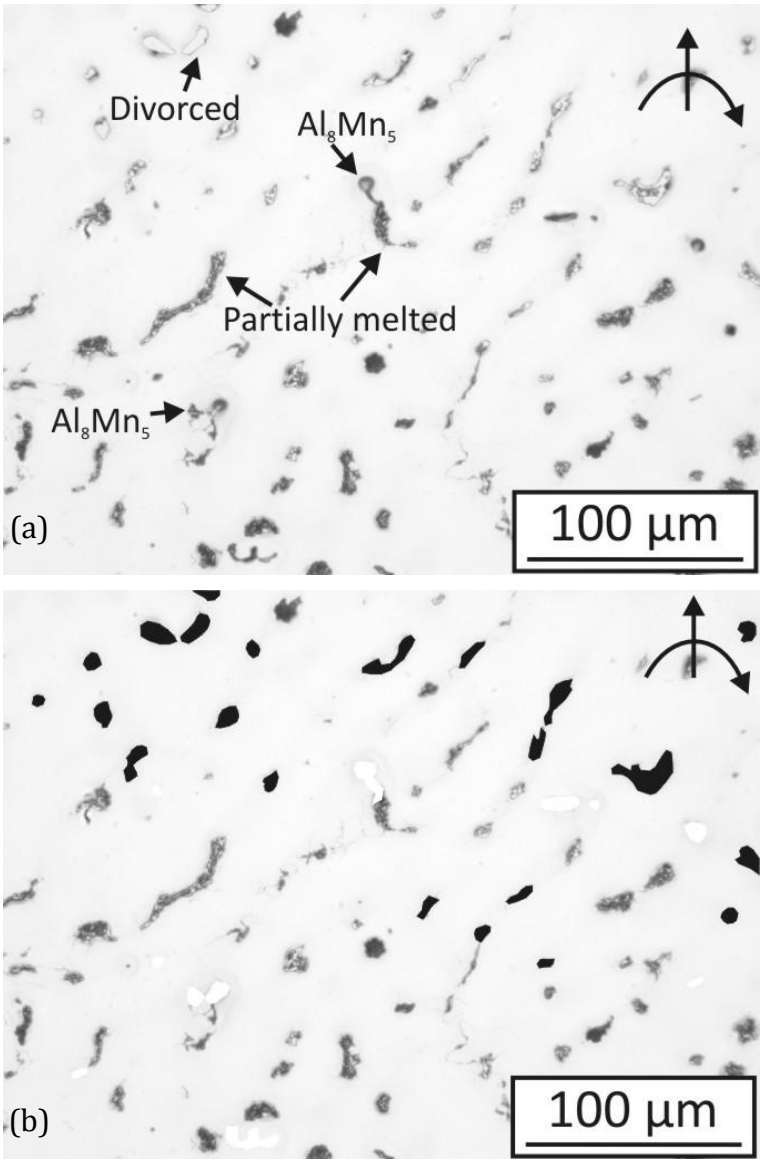

Figure 2-16. Micrograph taken from a location 1446 µm ahead of the pin during FSP AZ91 (a), with original β-particles appear bright, partially melted β-particles appear black, and equiaxed Al_8Mn_5 particles appear light grey. In (b), original β-particles are marked black while Al_8Mn_5 particles are marked white. In (c), both the original and partially melted β-particles are identified by using ImageJ software.

Figure 2-16. Continued.

Chapter 3. Models Relating Torque to Speeds

As discussed in Section 1.3.1, it is clear that there has not yet been a model relating M to ω and v in literature, despite of its importance. In this chapter, the extensive series of experimental results on M during FS over a wide range of ω and v are presented. Based on the data, a $M = f(\omega, v)$ model is described. The model will then be extended to P and E_s relating ω and v. Using this model, important trends between FS variables observed in this work and in literature are also studied and presented in this chapter.

3.1 Model Relating M to ω

As has already been reviewed, M is more strongly influenced by ω than by v. Thus, M values are first presented and plotted as a function of ω, in Figure 3-1. Observing these data, a clear trend can be established: M decreases and $dM/d\omega$ also decreases as ω increases. It is also clear in Figure 3-1 that in general an increase in v causes an increase in M. These are in agreement with the general trends observed in literature, as has been briefly reviewed before, although the present experiments and data are extensive covering wide ranges of ω and v. Importantly, the trend of these data suggests that M should not be infinitely large and rather there should be a definite M value when $\omega \to 0$. The trend of the data also indicates a non-zero M value when $\omega \to \infty$.

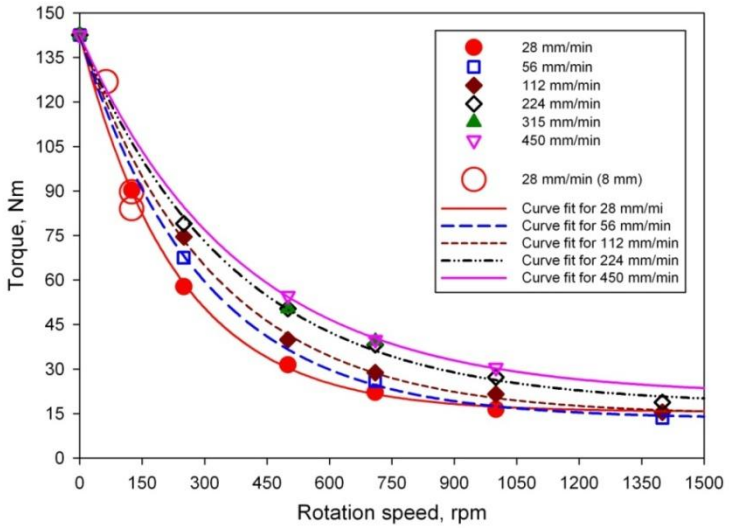

Figure 3-1. Torque (M) as a function of rotation speed (ω) with forward speed (v) constant during FSP A356.

A decay function, describing the decrease of M from a maximum value when $\omega = 0$, should be more reasonable for describing the data obtained. Fitting of the data using a decay model started with the case of v = 28 mm/min. This is because, using this low v value, FSP experiments could be conducted using very low ω values without resulting in internal voids in the stir zone. As shown in Figure 3-1, an exponential decay function can be seen to fit very well the experimental data of M as a function of ω. This function is in the form:

$$M = M_o + M_f e^{-n\omega} \qquad \textit{Equation 3-1}$$

where M_o is the minimum torque parameter, M_f the pre-exponential parameter and n the decay parameter. The parameter M_o ($M_o > 0$) eliminates the unreasonable behaviour of Equation 1-3 as $\omega \to \infty$. Value n implies the rate of decay and a more quantitative evaluation of $dM/d\omega$ will be made in the following section. For the case of v = 28 mm/min, M_o = 15.6 Nm, M_f = 127.1 Nm and n = 0.0043 rpm^{-1} in Equation 3-1. By using these values, one can obtain $M_{\omega=0} = M_o + M_f$ = 142.7 Nm. This extrapolated, not measured, value is also plotted in Figure 3-1.

We now examine the possible maximum M value that the strength of the workpiece provides during FS. Theoretically, in a fully stick situation (i.e. material adjacent to the tool rotates with the tool) [117]:

$$M = M_{shoulder} + M_{pin\ bottom} + M_{pin\ surface}$$
$$= \frac{\int_{r_i}^{r_o} r\tau 2\pi r dr}{2} + \int_0^{r_i} r\tau 2\pi r dr + r_i \tau 2\pi r_i h \qquad \textit{Equation 3-2a}$$

Take $\tau = \frac{\sigma}{\sqrt{3}}$, then:

$$M = \frac{2\pi\sigma}{\sqrt{3}} A_{M-Tool} = \frac{2\pi\sigma}{\sqrt{3}} \left[\frac{\int_{r_i}^{r_o} r^2 dr}{2} + \int_0^{r_i} r^2 dr + {r_i}^2 \times h \right] \qquad \textit{Equation 3-2b}$$

Using the dimensions of the tool used, we obtain:

$$M = \frac{2\pi\sigma}{\sqrt{3}} \left[\frac{\int_{0.003\mathrm{m}}^{0.009\mathrm{m}} r^2 dr}{2} + \int_0^{0.003\mathrm{m}} r^2 dr + (0.003\mathrm{m})^2 \times \right.$$
$$0.006\mathrm{m} = 2\pi\sigma 31.17\times 10-7+9\times 10-9+5.4\times 10-8 \qquad \textit{Equation 3-2c}$$
$$\mathrm{m}^3 = 6.5 \times 10^{-7} \sigma\ \mathrm{m}$$

If σ = 210 MPa (which is approximately the UTS of the A356 alloy) for room temperature flow stress, we have:

$$M = 6.5 \times 10^{-7} \times 210 \times 10^6 \frac{\mathrm{N}}{\mathrm{m}^2}\ \mathrm{m}^3 = 137\ \mathrm{Nm} \qquad \textit{Equation 3-2d}$$

This M value is comparable to the experimentally extrapolated value ($M_{\omega=0}$ = 142.7 Nm). This is reasonable as when $\omega \rightarrow 0$ and little heat is generated to soften the workpiece, M has to reach the value to overcome the room temperature strength (or M) value. Thus, the trend of M when $\omega \rightarrow 0$, which is not possible to be experimentally determined in the current experimental environment, is to reach a maximum value that depends on the alloy strength at room temperature.

The good predictive capability of the decay model can be further seen by examining the data and the fitted curve for the case of v = 28 mm/min. The curve was obtained based on data for $\omega \geq 128$ rpm using 6.4 mm thick plate. Later, experiments were repeated using 8 mm thick plate. The measured M values (for $\omega \leq 128$ rpm) are seen to lie very close to the predicted curve, although the use of the very low ω value at 63 rpm resulted in the M value outside the device calibrated range. These data, obtained even in the rapid decay and low ω region, show that the change in plate thickness does not have an effect on M. This supports the

supposition that as $\omega \rightarrow 0$, M is limited by the room temperature strength, so using the same tool plate thickness should be insignificant.

3.2 Model relating *M* to *v*

At low ω, increasing v results in insufficient material flow during FS leaving behind a cavity in the stir zone. For example, a visible void in the cross section of the FS sample made using 112 mm/min at 250 rpm can be observed under a stereomicroscope (as will be shown in Section 4.2.1). Thus low ω values (< 250 rpm) were only used for the low v (= 28 mm/min) value experiments. For higher v value M data, using Equation 3-1 to fit the data and extrapolate M to $\omega \rightarrow 0$ can also be done but the uncertainty is higher due to the lack of data for the low ω (< 250 rpm) value region where M increases rapidly when $\omega \rightarrow 0$. However, observing all the data in Figure 3-1 suggests that, as $\omega \rightarrow 0$, M appears to be moving to a relatively narrow region of values.

Although presently it is not experimentally possible to verify, the reason of room temperature strength determining the M value when $\omega \rightarrow 0$ may apply to all the cases using various v values. This approximation means that, within the range of v values used, little frictional heat is generated when $\omega \rightarrow 0$. For this reason, $M_{\omega=0}$ = 142.7 Nm for the case of v = 28 mm/min is used for all other cases using different v values. Thus, Equation 3-1 was used to fit each individual v value experimental data together with the $M_{\omega=0}$ value (shown in Figure 3-1). This means that each curve starts with $M_{\omega=0}$ = 142.7 Nm. It can be seen in Figure 3-1, for various sets of experiments with different v values, the decay function fits all the data well.

In Figure 3-1, a fitted curve differs from others slightly in M_o, M_f & n values of Equation 3-1. This means that M_o, M_f and n values are slightly v dependent, as can be seen by plotting them in Figure 3-2.

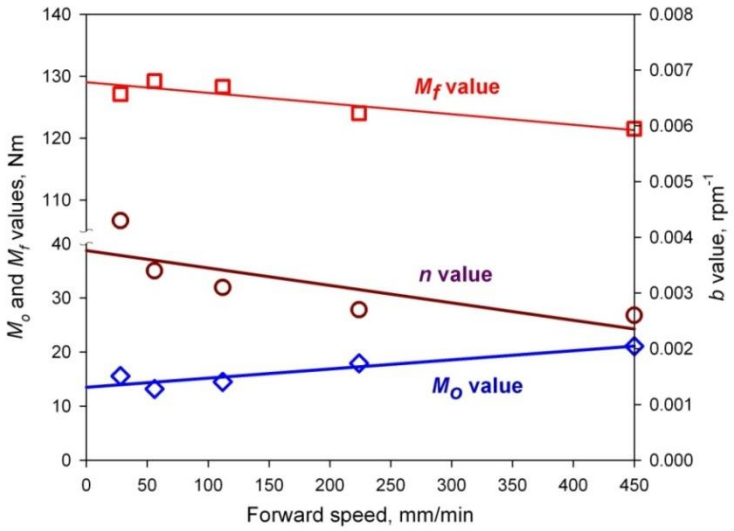

Figure 3-2. M_o M_f, and n values of Equation 3-1 vs. v.

As is indirectly shown in Figure 3-1 and will be shown clearer later, M increases as v increases but the rate, $\mathrm{d}M/\mathrm{d}v$, is in fact not high. In this present work the dependence of M on v is evaluated approximately by linearly relating M_o, M_f & n to v, although the linearity for n value may be regarded poor:

$$M_o = A + Bv = 13.5 + 0.017v \qquad \textit{Equation 3-3a}$$

$$M_f = C + Dv = 129.0 - 0.017v \qquad \textit{Equation 3-3b}$$

$$n = a + bv = 0.00377 - 3.13 \times 10^{-6}v \qquad \textit{Equation 3-3c}$$

Then:

$$M = A + Bv + (C + Dv)e^{-(a+bv)\omega} \qquad \textit{Equation 3-4}$$

In Figure 3-3, calculated M values (curves) are plotted verse v using Equation 3-4, with a constant ω value for each curve. The experimentally measured M values are also plotted in the same figure. The calculated curves describe the measured data well, showing the usefulness of Equation 3-4. Although Equation 3-4 is not a linear function but the A, B, C, D, a and b values determined and used in Equation 3-4 in the present case have resulted in M relating to v in a form that can approximately be described as linear. This is clear in Figure 3-3.

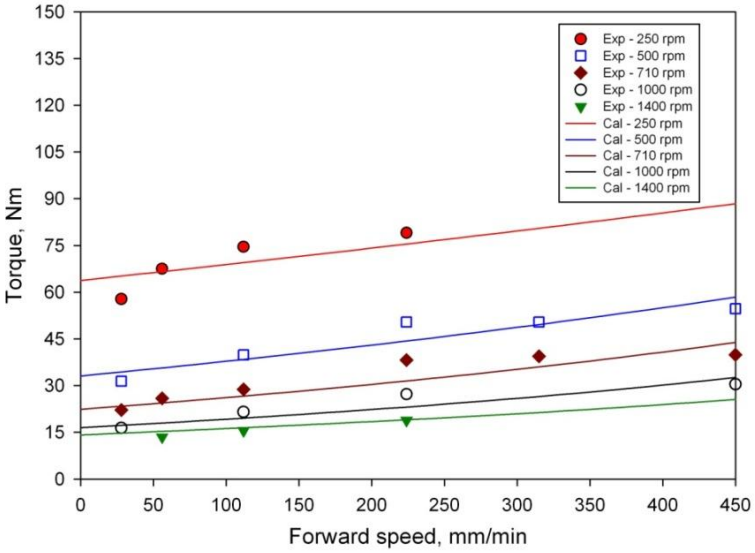

Figure 3-3. Curves of M as a function of v with various (constant) ω values, calculated using Equation 3-4.

3.3 Significance of *v* on *M*

With Equation 3-4 that reasonably describes the experimental data, the dependence of M on v can be better evaluated. Differentiating M with respect to v, Equation 3-4 becomes:

$$\frac{dM}{dv} = B + [D - b\omega(C + Dv)]e^{-(a+bv)\omega} \qquad \textit{Equation 3-5}$$

dM/dv for each v value is in turn plotted as a function of ω in Figure 3-4, displaying a number of features. Firstly, for very small and very large ω values, dM/dv is not v dependent. As predicted by Equation 3-5 and shown in Figure 3-4, $dM/dv = 0$ when $\omega = 0$, as $B = -D$ (see Equation 3-3a and Equation 3-3a). This relates to $M_{\omega=0}$ equalling to a constant, as already described. Secondly, Equation 3-5 predicts that $dM/dv = B$, when $\omega \to \infty$, and as is also evident in Figure 3-4 that all curves tail off to that single value (0.017 Nm/mm/min). Thirdly, there is a $(dM/dv)_{max}$ at $\omega \sim 300$ rpm or at a slightly higher ω value for a higher v value. Fourthly, increasing v can be seen to inflate the curve of dM/dv verse ω, keeping $dM/dv = 0$ when $\omega = 0$ and $dM/dv = B$, when $\omega \to \infty$.

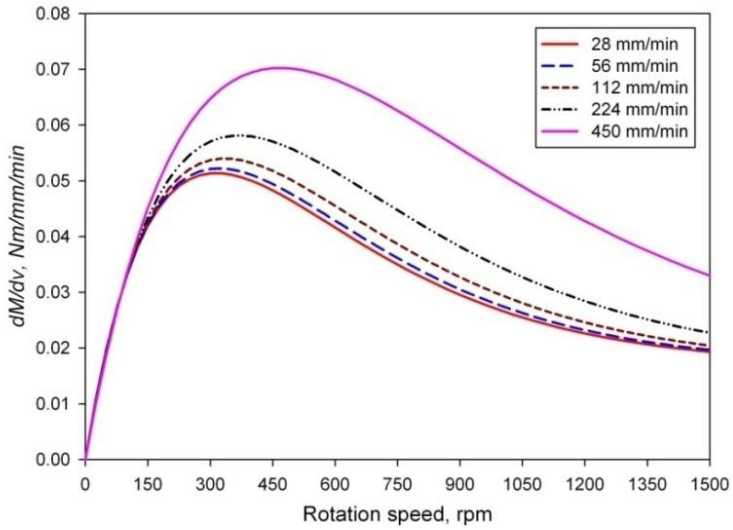

Figure 3-4. dM/dv plotted as a function of ω for various v values, based on Equation 3-5.

However, Figure 3-4 shows that dM/dv values are overall low, meaning a generally weak dependence of M on v. This weak dependence can be illustrated by examining the $(\mathrm{d}M/\mathrm{d}v)_{\max}$ value which is ~ 0.06 Nm per mm/min (at ~ 350 rpm) for a medium v value of 224 mm/min. This means that for an increase of 100 mm/min, which may be seen as a significant increase in v value in FS practice, M increases by 6 Nm. This is, for a reference, regarded as a moderate increase. However, for the same amount of increase in v, an increase in M is only 2.6 Nm at 1400 rpm. This diminishing effect of v on M (reducing dM/dv) as ω (> 350 rpm) increases is clear not only in Figure 3-4 but also in Figure 3-1.

As already reviewed, Equation 1-3 has been used twice in literature [2,3], although no detailed evaluation on the dependence of M on v was conducted. Different tool size and workpiece thicknesses were used in these studies and therefore direct comparison using Equation 1-3 on M is not valid. However, the use of $(\mathrm{d}M/\mathrm{d}v)/M$ may provide a comparison base, in the case of using Equation 1-3. It can be shown that:

$$\frac{dM/dv}{M} = \frac{\alpha}{v} \qquad \textit{Equation 3-6}$$

In Kalya et al's study [19] α = 0.165, and thus a relatively weak dependence of M on v, and in Colegrove and Shercliff's case [17], α = 0.5, and a significantly stronger dependence of M on v can thus be suggested. This may not be surprising

considering that in Colegrove and Shercliff's experiments ω < 500 rpm and in Kalya et al's study ω ranged from 964 to 2000 rpm. The latter is in the range of ω that the effect of v on M has significantly diminished, as has been shown in this study (Figure 3-4).

It is also worthwhile to examine the M data recently published by Upadhyay and Reynolds [18]. Two sets of data of M verse ω in a reasonably wide range (150–1000 rpm) were reported, although v values of these data were not constant. One set was for experiments conducted in ambient environment and the other underwater. Their two sets of data display the same general trend but $\Delta M = M_W - M_A > 0$ at the same ω, where M_W and M_A represent torque measured underwater and in ambient respectively. Both sets of data could be fitted well with Equation 3-1 giving the n value being higher for the case of ambient environment. Their data also clearly show that there is a $(\Delta M)_{\max}$ value at 300–350 rpm, with ΔM being smaller at lower ω and diminishing as ω increases when ω > 350 rpm. These features are the same as those just shown for the effect of v on M in this work (Figure 3-4). The effect of FS underwater is to increase heat loss, compared to FS in ambient condition. This is equivalent to increasing v during FS in ambient condition. Thus the change in M, due to underwater FS or increasing in v, is the biggest at the same ω range.

3.4 Significance of ω on M

Firstly, we will quantitatively evaluate how strong the dependence of M is on ω. Differentiating M with respect to ω in Equation 3-4 gives:

$$\frac{dM}{d\omega} = -(a + bv)(C + Dv)e^{-(a+bv)\omega} \qquad \textit{Equation 3-7}$$

Curves of $dM/d\omega$ plotted as a function of ω for various v values are given in Figure 3-5, showing quantitatively a strong dependence in low ω range and the dependence diminishing as ω increases. Take for an example ω = 700 rpm which may be regarded as a medium value for FS and also take $\Delta\omega$ = 300 rpm which may be seen as a significant increase. Then, from Figure 3-5, it can be seen $dM/d\omega \approx$ –

0.05 Nm/rpm, and thus $\Delta M \approx -15$ Nm. This decrease in M value, as compared to the reference value of 6 Nm arbitrarily set as a moderate value of change before, may be regarded large. Thus, in general, it could be felt that ω influences M more than v. Hence, the present model as, described by Equation 3-1 to Equation 3-7, can provide a base for a complete and quantitative evaluation on the influences of speeds (in any range) on torque.

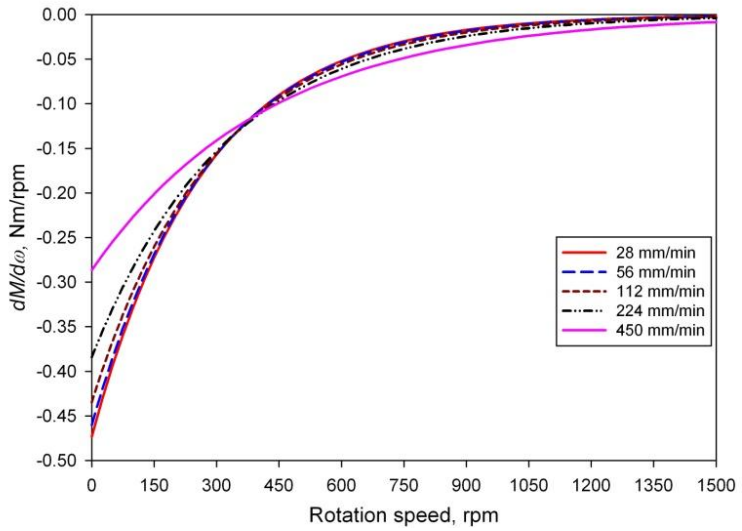

Figure 3-5. dM/dω plotted as a function of ω for various v values, based on Equation 3-7.

It is worthwhile to more directly compare M data from this work to those available in literature, to examine the usefulness of Equation 3-1 in order to ascertain whether it can be applied more widely. Examining the available data in literature, surprisingly, M data obtained in a reasonable wide range of ω and v is actually not very extensive. There may only be three studies [18, 20, 23] that are suited for a comparative examination and the torque data from these studies are plotted in Figure 3-6, together with an exponential decay curve that fits the 112 mm/min data from this work. In the three quoted studies and our work, the tool sizes are only slightly different. It can be seen in Figure 3-6, in general, Equation 3-1 seems to be suitable for all the experimental data from the quoted sources.

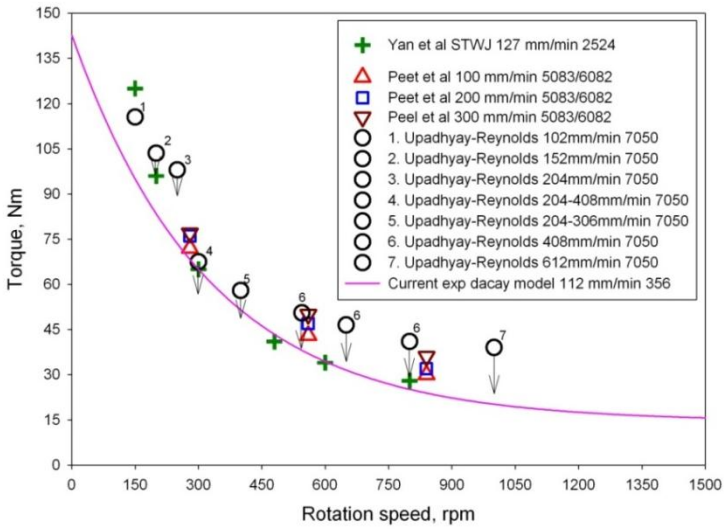

Figure 3-6. Torque data from literature, Upadhyay and Reyonds [18], Peel et al. [20] and Yan et al. [23], together with a decay curve from the present work.

We now examine Figure 3-6 more closely. The features of the slight increase in M as v increases from 100 to 300 mm/min (Peet et al.'s data) are almost the same as for the present work if the same range of ω is considered. In Figure 3-6, Peel et al.'s three M data of v = 100 mm/min locate very close to the decay curve from this work. Yan et al's data, using a similar v value (127 mm/min, compared to 112 mm/min in our case), can be well described with the use of the present decay curve plotted in Figure 3-6 for $\omega \geq 300$ rpm. For $\omega < 300$ rpm, Yan et al's M deviates and is higher than M predicted from the present decay curve. This deviation in M increases as ω decreases.

A comparison to Upadhyay and Reynolds' data cannot be made directly as they did not use a constant v value. However, a correction may be attempted, taking into account the effect of v on M as demonstrated in this work. An arrow has been drawn in each of their data (Figure 3-6), except the one for 100 mm/min. The data had been suggested to move downward roughly to a point as if that point was obtained using the same v value (100 mm/min). With the correction, if a fitted curve was made for Upadhyay and Reynolds' data, the curve should be very close to the decay curve (using the similar v value) from the present work for $\omega \geq 300$ rpm, similar to that described for Yan et al's data. The feature at $\omega < 300$ rpm is also the same as that already described for Yan et al's data.

The above comparisons and discussion suggest that, using the same FS condition and a similar tool, M values should be almost the same for most common aluminium alloys when $\omega \geq 300$ rpm. The differences in M for lower ω values would be due to the differences in $M_{\omega=0}$ and thus also in the n values. This is reasonable as a different alloy has a different room temperature strength and thus a different $M_{\omega=0}$ value. It may be suggested that with the increase of ω to 300 rpm, sufficient heat must have been generated and the major alloy pre-strengthening mechanisms, either work hardening or age hardening, do not operate any more. Thus most aluminium alloys behave similarly when $\omega \geq 300$ rpm.

To understand this further it is useful to investigate how flow stress (σ) varies as ω increases for a range of aluminium alloys. There is no simple relationship between ω and σ due to the complex coupled (thermal and mechanical) nature of FS. However, there is a clear link between these parameters; as ω is increased, P and thus stir zone temperature (T_{sz}) are increased, and σ decreases. This, in turn, reduces the ability of the material to generate heat by viscous dissipation, which provides the "self limiting" mechanism widely noted for FS. The relationship between T, strain rate ($\dot{\varepsilon}$), and σ is widely represented in terms of the Zener-Hollomon parameter (Z) and a constitutive law is given Equation 1-5 (page 23). Constants (Q, R, A, n) used in Equation 1-5, for some common Al alloys, are given by Colegrove et al. [118].

Using Equation 1-5, σ is plotted for a wide range of aluminium alloys as a function of T for two $\dot{\varepsilon}$ values (1 and 10 s^{-1}), as given in Figure 3-7. These aluminium alloys have static room temperature 0.2% proof stress values ranging from 140 to 600 MPa (over 4 times different). It can be seen that as T increases, σ values of the alloys begin to converge. For example, once the temperature has reached 400 °C, the ratio between σ values of the strongest to weakest alloy has reduced to ~ 1.5. This is because the alloys that are strongest at room T are also those with microstructures that are most unstable to an increase in T.

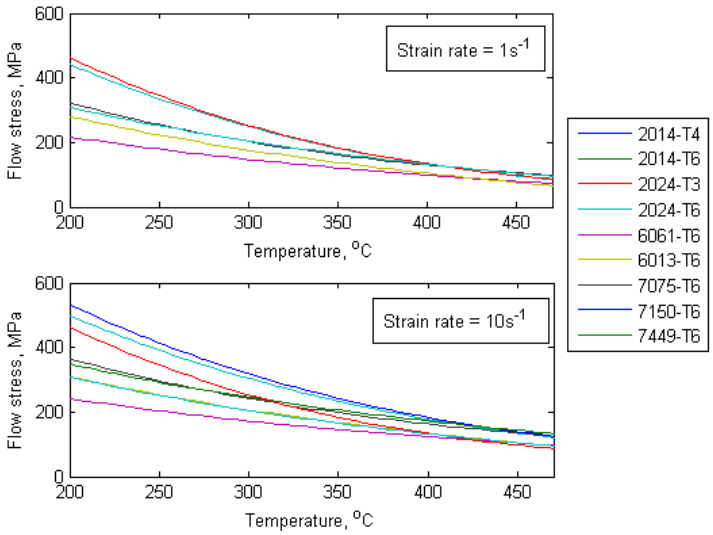

Figure 3-7. Calculated flow stress (σ) as a function of temperature (T) for a range of aluminium alloys at two strain rates ($\dot{\varepsilon}$ = 1 and 10 s^{-1}).

For example, as is clear in Figure 3-7, the alloy with the greatest room temperature σ is AA7449–T6. It achieves this through intense precipitation of nano-scale strengthening precipitates. These precipitates are thermally unstable, and will coarsen and dissolve on heating. At T encountered in the nugget during FS, the strengthening precipitates in most aluminium alloys will be either dissolved or massively coarsened, and make little contribution to strength. The dependence on the temper state of the alloy will also be reduced, since the differences in the precipitate populations developed by the different tempers will be destroyed by the heat and deformation during FS. Persistent small differences in σ as T increases will then be due largely to differences in solute content.

Since torque is intimately related to the material flow stress, the convergence of flow stress values as T increases is ultimately responsible for the convergence of torque curves. It can also be seen from Figure 3-7 that the dependence of σ on T is much stronger than its dependence on $\dot{\varepsilon}$. The effect of increasing ω on σ is therefore largely governed by the increase in T (reducing σ) with changes in $\dot{\varepsilon}$ having a second order effect.

3.5 Models of Power and Specific Energy

Combining Equation 1-1 (page 18) and Equation 3-4, P is expressed as:

$$P = M_o\omega + M_f e^{-n\omega}\omega = A\omega + Bv\omega + (C\omega + Dv\omega)e^{-(a-bv)\cdot\omega} \qquad \textit{Equation 3-8}$$

The calculated curves of P, each for an individual v value, are plotted in Figure 3-8 showing that they in general agreement with the experimentally determined values which are also plotted in the same graph. Equation 3-8, predicts that $P \to 0$ as $\omega \to 0$. This is supported by the available experimentally determined data.

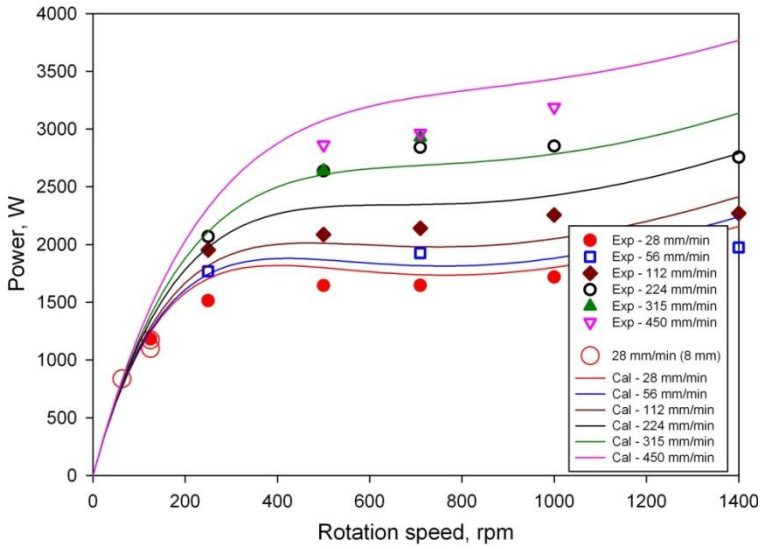

Figure 3-8. Curves of P as a function of ω with constant v values, calculated using Equation 3-8.

In Equation 3-8 differentiating P with respect to ω yields:

$$\frac{dP}{d\omega} = M_o + M_f e^{-n\omega}(1 - n\omega) \qquad \textit{Equation 3-9}$$

For ω = 0, $dP/d\omega = M_o + M_f = M_{\omega=0}$ meaning room temperature alloy strength dependent. For $\omega \to \infty$, $dP/d\omega = M_o$ which should be the same for all aluminium alloys. In the range of medium ω values of 500–1000 rpm which are used commonly, the prediction by Equation 3-9 and experimental data plotted in Figure 3-8 show that $dP/d\omega \approx 0$, meaning P is little affected by ω in this range of ω values. The small but almost linearly increase in P as v increases is shown in Figure 3-9.

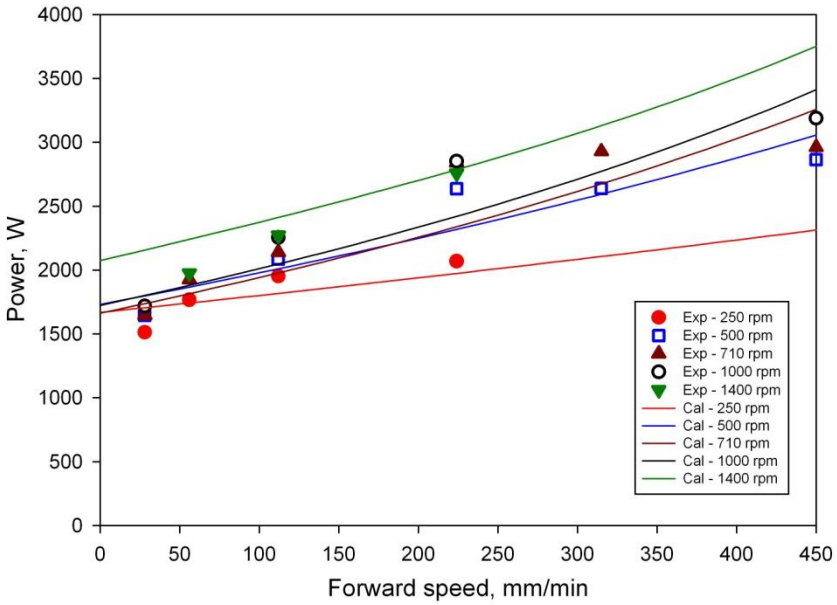

Figure 3-9. Curves of P as a function of v with constant ω values, calculated using Equation 3-8.

Calculation of specific energy can be done by combining Equation 1-2 (page 18) and Equation 3-4. Then:

$$E_s = \left[M_o + M_f e^{-n\omega}\right]\frac{\omega}{v} = \left[A + Bv + (C + Dv\,)e^{-(a+bv)\omega}\right]\frac{\omega}{v} \qquad \textit{Equation 3-10}$$

The properties of this equation are similar to those discussed for Equation 3-8, with a scaling factor of $1/v$. Thus the shape, not the magnitude, of each curve in Figure 3-10 with E_s plotted as a function of ω is similar to P verse ω in Figure 3-8.

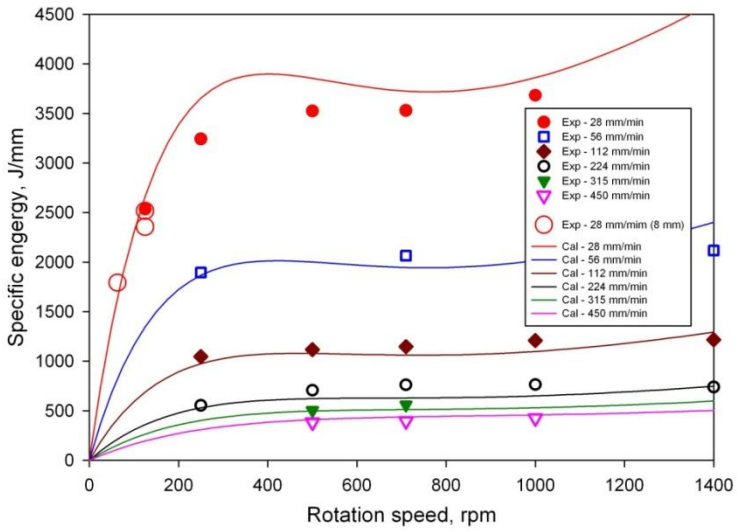

Figure 3-10. Curves of E_S as a function of ω with constant v values, calculated using Equation 3-10.

In the wider ω range (500–1400 rpm), E_s is affected little by ω. This feature of little effect of ω on E_s is better seen in Figure 3-11, plotting E_s as a function of v. Thus, E_s as a function of v only, by taking a medium ω value (ω_m), can be obtained:

$$E_s \approx \left[M_o + M_f e^{-n\omega_m}\right]\frac{\omega_m}{v} = \frac{A'}{v} + B' + \left(\frac{C'}{v} + D'\right)e^{-(a'+b'v)} \qquad \textit{Equation 3-11}$$

where $A' = A\omega_m$, etc. and this equation can closely predict E_s, regardless what the real ω value is within that wide range of ω.

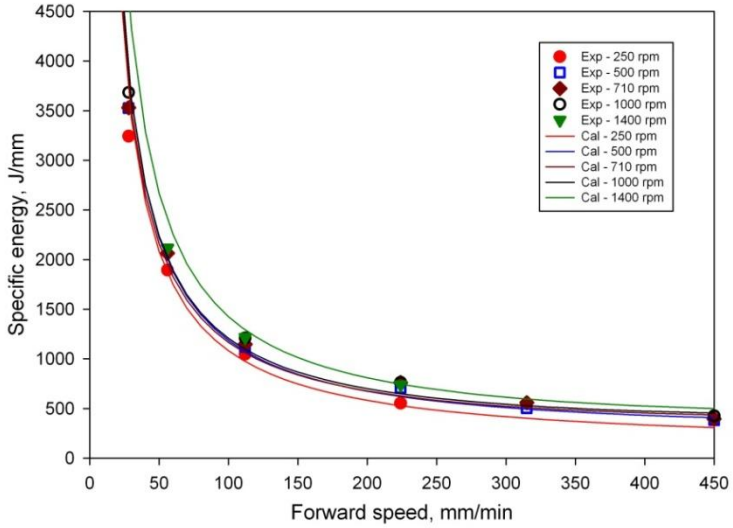

Figure 3-11. Curves of E_s as a function of ω with constant v values, calculated using Equation 3-10.

Chapter 4. Relationships among Flow, Speeds, and Torque

As has also between explained in Chapter 1, there have been few attempts to relate speeds and measureable responses ($M/P/E_s$) to flow quantity, which is an important thermomechanical response of FSP. These quantitative relationships are and discussed in this chapter.

4.1 Characterization of the Stir Zone

In Figure 4-1a, a cross section of a FS sample made using the normal tool with a normal FS condition (ω = 710 rpm and v = 224 mm/min) is presented. In the image taken using a stereo microscope (low magnification), α-Al dendrites appear dark and eutectic regions light grey. In images taken using a normal microscope (for a higher magnification), α-Al phase appears bright and Si particles are dark. The total stir zone was marked by the outmost dashed line within which the material has undergone noticeable deformation. The boundary between the stir zone and the undeformed workpiece is clearer on the advancing side (left) than on the retreating side (right). Within the total stir zone, the shoulder flow zone and the nugget flow zone, induced by the shoulder and pin respectively, are divided by a solid line. How this is done has been given in Section 2.5.

In Figure 4-1a, the microstructure in as-cast state (outside the stir zone) is a coarse one comprising α-Al dendrites and Al-Si eutectic in the interdendritic regions. The nugget zone (Figure 4-1a) shows that a clear "Onion Rings" structure cannot be identified in the present case. The nugget displays a region of rotation shear material (RSM) on the advancing side (left) of the nugget and this RSM region extends but tails off toward the retreating side (right) in the mid-to-lower region (but not the bottom) of the nugget zone. In this RSM region of heavily deformed material, the originally concentrated Si particles in the interdendritic regions in as-cast state have become quite evenly distributed in α-Al matrix. The rest of the nugget is the material that has been deformed but much less extensively, particularly more toward the retreating side, and thus the originally dendritic

feature of segregation of silicon particles is still apparent. Thus, a division between the RSM zone and the rest of the nugget zone can be drawn. The aforementioned deformation features can also be observed in Figure 1-21, where a FSP was performed on A356 using similar speeds. The forming mechanism of the individual flow zones will be investigated in more detail in Section 5.1.

Reducing *v* from 224 to 28 mm/min results in an increase in the portion of RSM region in the nugget (Figure 4-1b). RSM extends to the retreating side, occupying almost fully the nugget. Comparing Figure 4-1b to Figure 4-1a, it is also clear that reducing *v* also results in an increase in the size of the total stir zone. How speeds affect the areas of individual and combined flow zones will be systematically examined in the following section. How the area of flow zone (A_{flow}) is quantified is illustrated in Section 2.5.1.

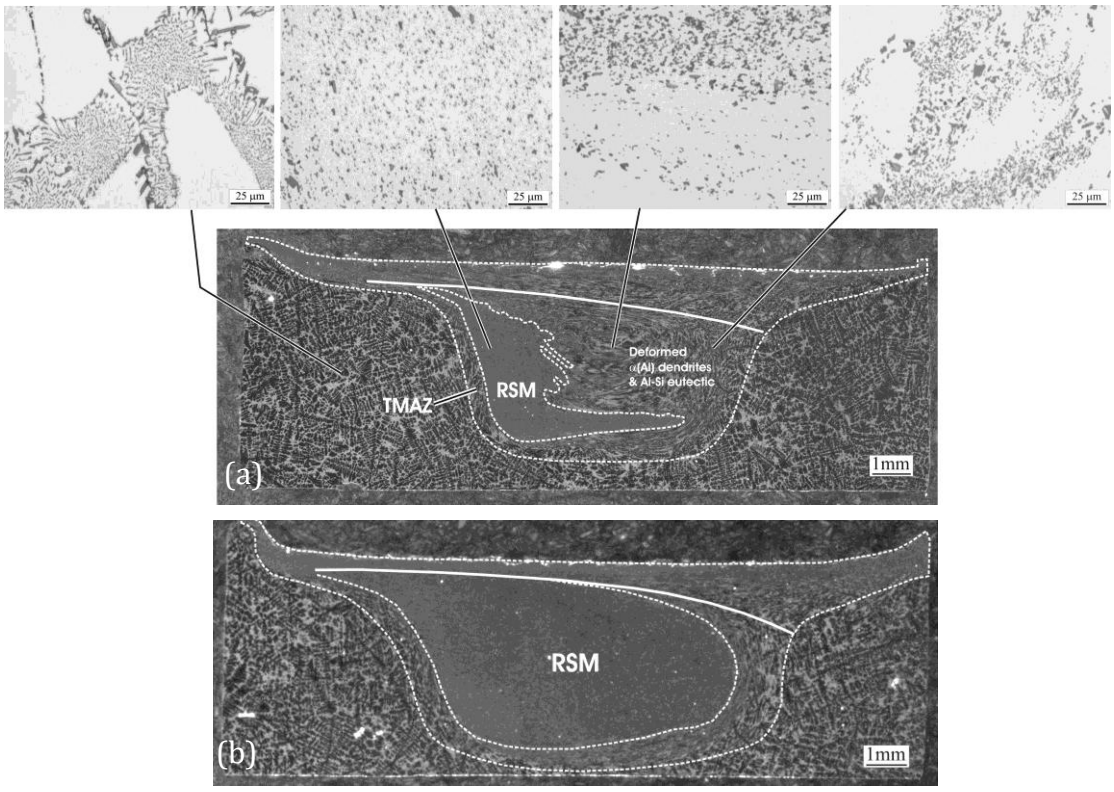

Figure 4-1. Cross sections (advancing side on the left) of A356 cast alloy FSP samples made using θ = 2.5°, ω = 710 rpm and (a) v = 224 mm/min and (b) v = 28 mm/min. The total stir zone has been outlined. The solid line marks the division of shoulder induced (above) zone and pin induced (below) flow zone. RSM denotes rotational shear material in the nugget.

4.2 Areas of Flow Zones Relating to Speeds

4.2.1 Effects of Speeds: Microscopic Analysis

Cross sections of FS performed with a constant v (224 mm/min, which can be considered as a commonly used v) while ω varying from 250 to 1400 rpm are given in Figure 4-2a to e respectively. Cross sections with a constant ω (710 rpm, which also can be considered as a commonly used ω) while v varying from 28 to 450 mm/min are given in Figure 4-3a to d respectively.

FS with no internal voids were made under most conditions, except when ω was very low (250 rpm). As can be seen in Figure 4-2a, the formation of voids indicates insufficient material flow is generated at low ω range. As can be seen from Figure 4-2a to e, the increase in ω clearly induces a significant increase in the area of nugget flow (A_{nugget}) and RSM flow zone (A_{RSM}); while a large decrease in area of shoulder flow zone ($A_{shoulder}$). However, the increase in A_{nugget} outweighs the decrease in $A_{shoulder}$ so that the area of total stir zone ($A_{total} = A_{nugget} + A_{shoulder}$) increases. As shown in Figure 4-3, a decrease in v induces similar effects, however less obvious, on individual and combined flow zones.

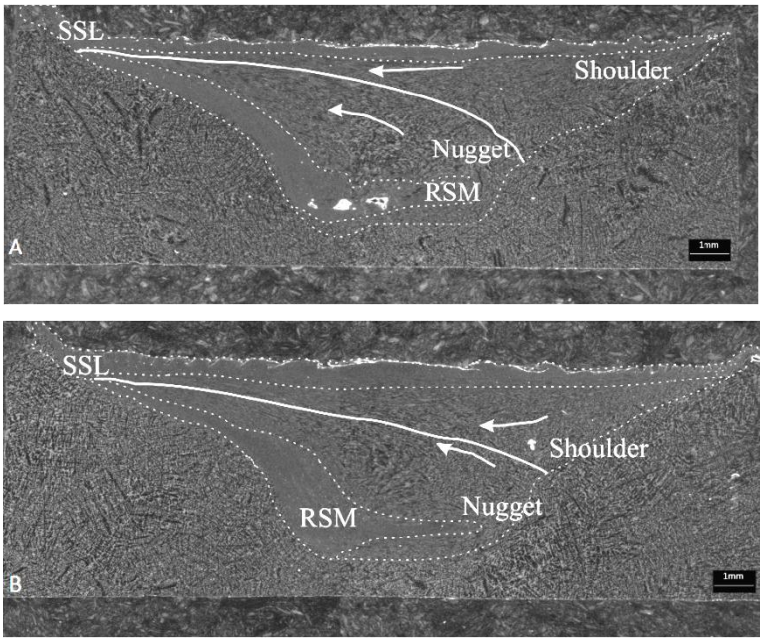

Figure 4-2. Cross sections (advancing side on the left) of FS A356 cast alloy made using v = 224 mm/min and (a) ω = 250 rpm, (b) ω = 500 rpm, (c) ω = 710 rpm, (d) ω = 1000 rpm and (e) ω = 1400 rpm.

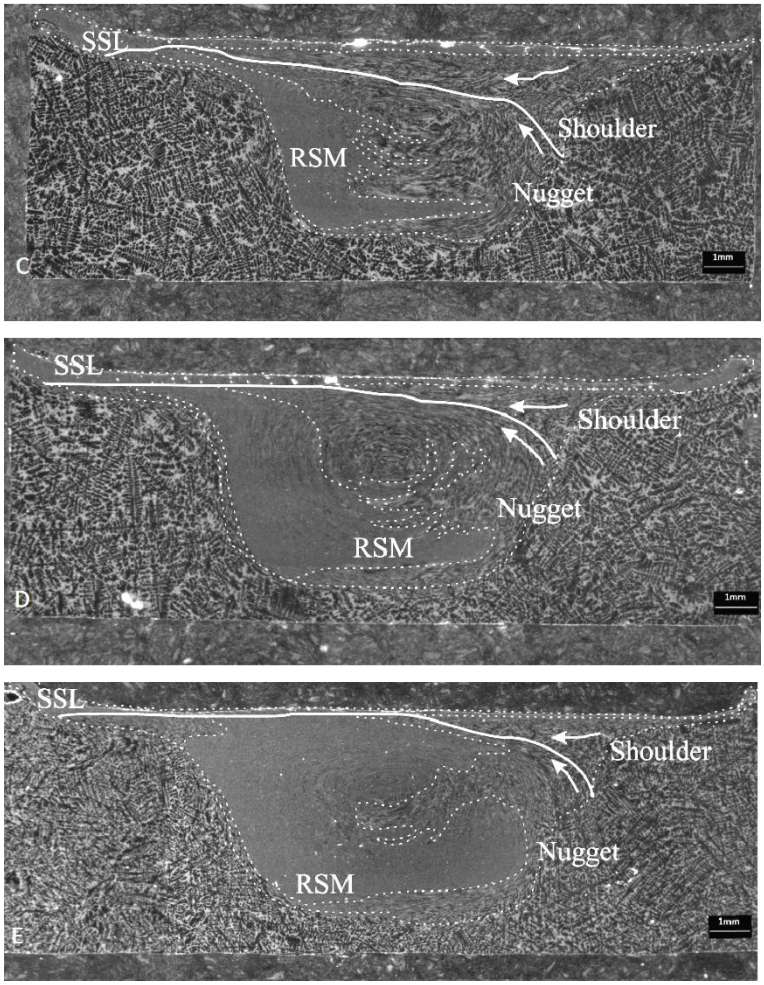

Figure 4-2. Continued.

The increase in A_{RSM} plays a major role in the increase in A_{nugget}. As can be seen from Figure 4-2a and Figure 4-3d, RSM preferentially deposits on the lower-advancing side of the stir zone, which is consistent with the observation from a FS sample made with similar speeds (Figure 1-21). Either increasing ω or decreasing v causes RSM zone to gradually expand towards the upper-retreating side (Figure 4-2e and Figure 4-3a), occupying increasingly larger portion of the nugget zone. Regardless of the significant changes in A_{RSM} and A_{nugget}, the segregation between RSM and the rest of the nugget zone exists throughout the whole experiment range. Hence, there is no evidence suggesting that the variations in speeds (with ω and v increased by more than 5 and 16 times respectively) have induced a change in flow mechanism during FS A356 alloy using the current experimental setup.

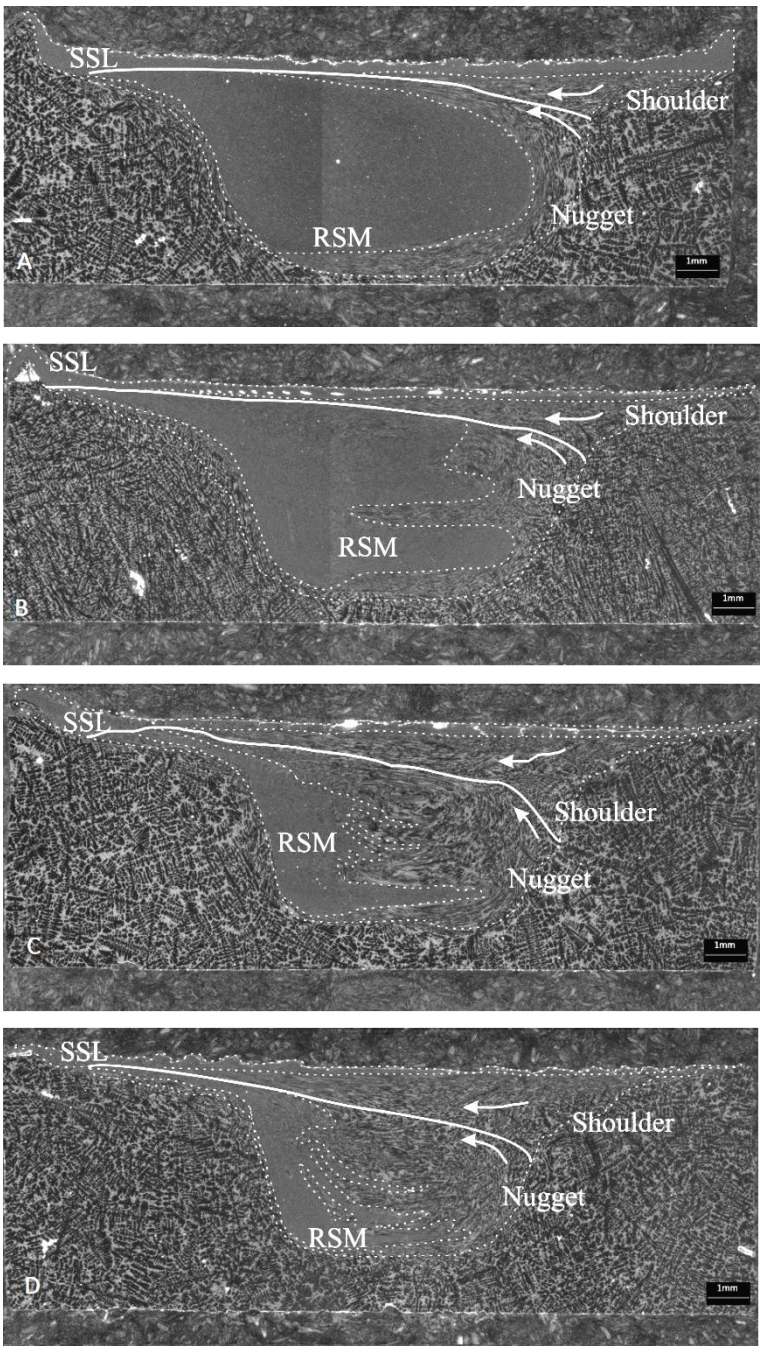

Figure 4-3. Cross sections (advancing side on the left) of FS A356 cast alloy made using machine settings ω = 710 rpm and (a) v = 28 mm/min, (b) v = 112 mm/min, (c) v = 224 mm/min, (d) v = 450 mm/min.

Regardless of the area, the RSM flow zone does not display a strong periodical flow features (such as "Onion Rings" and flow bands), indicating the deposition of the RSM zone is fundamentally different to that of FS wrought Al alloys (as given in Figure 1-20). The lack of periodical flow features also strongly suggests the material deformation and mixing leading to the formation of RSM zone is very

homogeneous, i.e. the periodic variations in grain size and grain orientation do not exist in RSM zone. At higher ω range (Figure 4-2d and e), very weak periodical flow features can be identified just outside the RSM zone, suggesting inhomogeneous material deformation and mixing. The deformation of material in RSM zone and the rest of the nugget zone will be discussed in more details in Section 5.3.

4.2.2 Effects of Speeds: a Quantitative Analysis

The quantitative effects of ω and v on the individual and combined flow zones are shown in Figure 4-4a and b respectively, showing a number of features. Firstly, the increases in A_{nugget} and A_{RSM}, caused by either increasing ω or decreasing v, can be fit by linear equations. Moreover, the difference between nugget and RSM zones, $A_{nugget} - A_{RSM}$, is almost always the same.

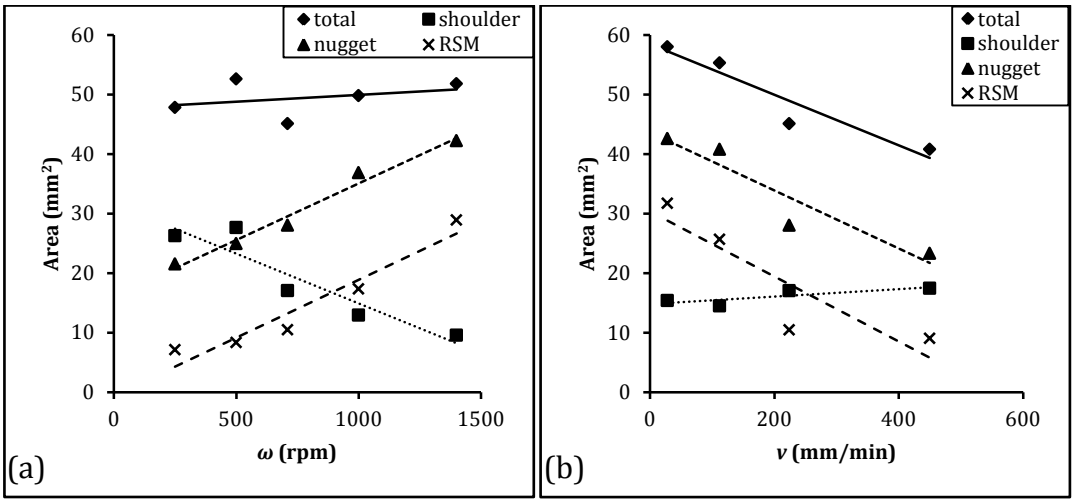

Figure 4-4. The effects of ω and v on A_{nugget}, $A_{shoulder}$, A_{RSM}, and A_{total}, at (a) v = 224 mm/min, (b) ω = 710 rpm, and linear fitting lines have been applied for both cases. The effects of λ on A_{nugget} is shown in (c).

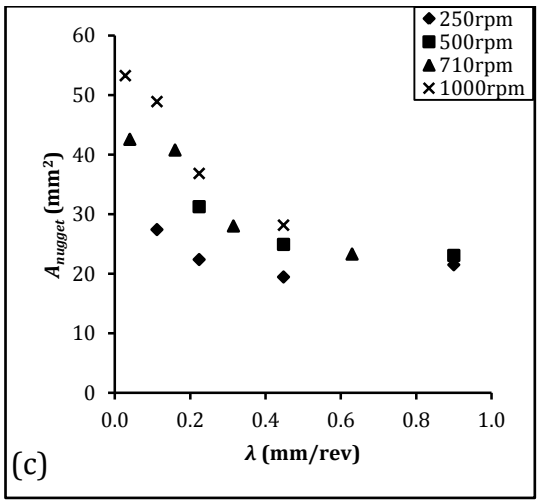

Figure 4-4. Continued.

Secondly, the effects of λ (= v/ω) on A_{nugget}, at constant v and ω, are shown in Figure 4-4c. The maximum attainable A_{nugget}, ($A_{nugget\text{-}max}$) is ~ 53 mm^2 and the minimum A_{nugget}, ($A_{nugget\text{-}min}$) is ~ 20 mm^2. The later is approximately 67% of the pin sectional area ($L_{pin} \times D_{pin}$ = 5 mm × 6 mm). In general, a smaller λ (which represents more tool rotation per mm travelled) corresponds to a larger A_{nugget}, due to more intensive shearing and softening effects. However, at a constant λ (e.g. 0.2 mm/rev), a combination of a larger v and a larger ω would result in a larger A_{nugget}, compared to the combination of a smaller v and a smaller ω. Furthermore, it can be seen from Figure 4-4c that the values of A_{nugget} at a higher ω (e.g. 1000 rpm) are consistently larger than those at lower ω values.

Combining these observations, it is reasonable to conclude that parameter λ is not the only factor that determines A_{nugget}, and ω has a more significant effect on A_{nugget} compared to v. This is not surprising as that ω has a more significant effect than v on temperature rise in the nugget zone (Section 1.3), thus on the decrease in flow stress (which will be investigated further in Section 4.4). In general, softer material would be sheared/displaced more easily which would result in a larger nugget flow zone. Hence, even if ω and v have increased by the same percentage, i.e. keeping λ unchanged, a larger A_{nugget} will be generated due to the overall decrease in flow stress. By examining the data of A_{nugget} at very low λ, it seems that there is a finite maximum value of $A_{nugget\text{-}max}$ (being ~ 55 mm^2) as λ approaches 0 (or $\omega \rightarrow \infty$). Such observation is most likely due to the self limiting effect of FS process, i.e. the

ever increase in ω does not result in continuously reduced flow stress. Hence, the generation of A_{nugget} will reach a saturation point no matter how much ω is further increased.

Thirdly, as shown in Figure 4-4a and b, increasing ω and decreasing v decreases $A_{shoulder}$. This is not surprising because the nugget zone always forms before the shoulder zone. This is illustrated back in Figure 2-8, which indicates that the pin is in contact with the material first following by the rear portion of the shoulder. And in a confined space (cross section of the plate being constant), a larger nugget zone would geometrically requires a smaller shoulder zone. However, the decrease in $A_{shoulder}$ is more sensitive to the increase in ω than to the decrease in v. To be more specific, as ω decreases from 1400 to 250 rpm (at 224 mm/min), the decrease in A_{nugget} ($\sim$ 20 mm^2) is readily compensated for by the increase in $A_{shoulder}$ ($\sim$ 17 mm^2); as v increases from 28 to 450 mm/min (at 710 rpm), the decrease in A_{nugget} ($\sim$ 18 mm^2) is far larger than the increase in $A_{shoulder}$ ($\sim$ 4 mm^2). The exact reason for this non-proportionality is unclear. However, it is likely that the amount of flash is significantly increased by the increase in ω, due to severe softening effect on the shoulder zone.

Fourthly, as is also clearly shown in Figure 4-4a and b, A_{total} is affected little by ω but relatively strongly by v. This is because at constant v, the increase in A_{nugget} (due to increase in ω) is largely cancelled by the decrease in $A_{shoulder}$ and hence only a small change of (increase in) A_{total} is resulted. However, at constant ω, the significant decrease in A_{nugget} (due to increase in v) cannot be compensated for by the rather small increase in $A_{shoulder}$, and therefore a relatively larger reduction decrease in A_{total} is resulted.

4.3 Volumes of Flow Zones Relating to Torque

In traditional welding, a larger power input (voltage × current) always results in a larger melting zone and thus a larger welding cross section. For the case of FSP, $M/P/E_s$ cannot be independently controlled, and in contrast, they are dependent on input speeds, tool design, backing plate thermal properties. Therefore, the

interrelationships among $M/P/E_s$ and flow volumes during FSP are more complex than those for traditional fusion welding. Nonetheless, E_s represents total energy input per unit travel distance (J/mm), and by using Equation 1-2 (page 18), M should have an alternative unit of (J/rev), as $M = E_s\, v/\omega$, i.e. M indicates the energy input per tool revolution. Intuitively, there seems to be an underlying connection between M and total stir zone volume generated per revolution (V_{T-rev}, mm^3/rev), i.e. a larger total flow volume would naturally require a larger M to accomplish. V_{T-rev} can be expressed as:

$$V_{T-rev} = A_{Total}\frac{v}{\omega} = A_{Total} \cdot \lambda \qquad \textit{Equation 4-1}$$

The relationship between V_{T-rev} and M is presented in Figure 4-5a. By examining the data points, it can be seen that a larger V_{T-rev} corresponds to a larger M, but the rate of increase (dM/dV_{T-rev}) decreases as V_{T-rev} increases. An exponential rise function seems to describe the relationship between V_{T-rev} and M well. Equation 3-4 (page 93) can be extended to develop this relationship.

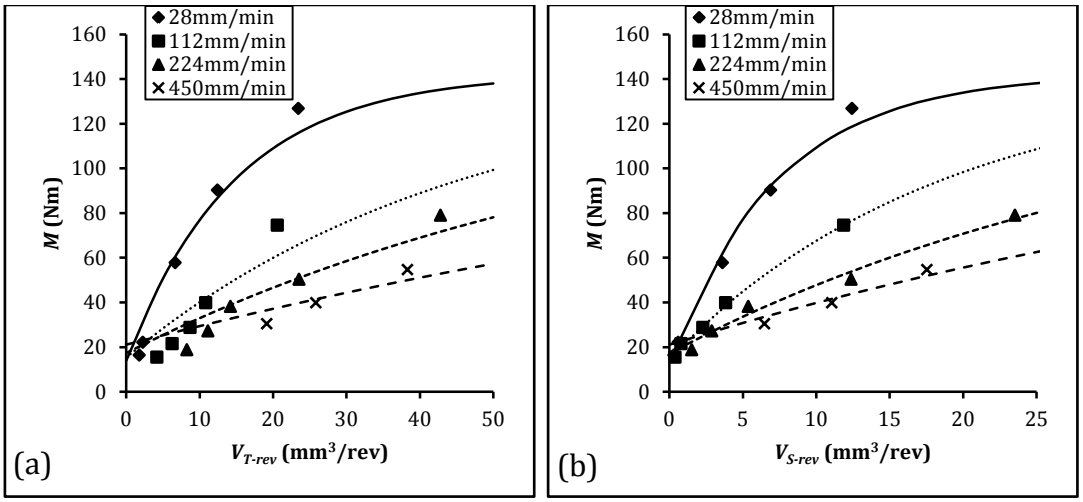

Figure 4-5. The relationships (at constant v) between (a) total flow volume per revolution (V_{T-rev}) and M (b) shoulder flow volume per revolution (V_{S-rev}) and M. Exponential curve fittings have been applied to all cases by using Equation 4-2a and Equation 4-3.

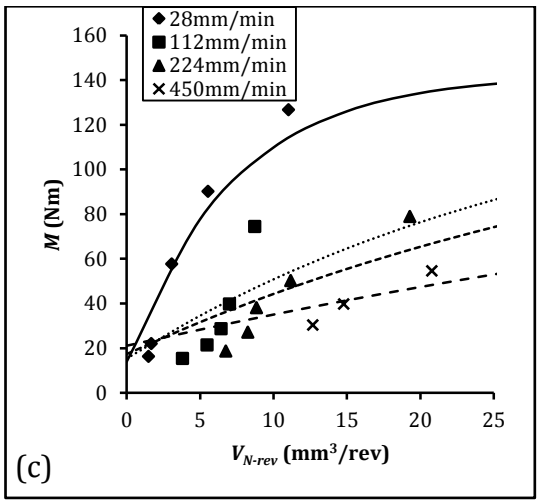

Figure 4-5. Continued.

Using v = 28 mm/min as an example, Equation 3-4 indicates that as $\omega \to 0$ $M_{\omega\to 0}$ = 142.5 Nm, and $\omega \to \infty$ $M_{\omega\to\infty}$ = 14.0 Nm. Meanwhile, Equation 4-1 indicates that $V_{T\text{-}rev} \to \infty$ if $\omega \to 0$ and $V_{T\text{-}rev} \to 0$ if $\omega \to \infty$. Thus, an exponential rise function, bounded by $M_{\omega\to 0}$ and $M_{\omega\to\infty}$, has been applied to describe the relationship between $V_{T\text{-}rev}$ and M:

$$M = M_{\omega=\infty} + (M_{\omega=0} - M_{\omega=\infty})\left[1 - e^{(-\gamma V_{T-rev})}\right]$$
$$= M_o + M_f\left[1 - e^{(-\gamma V_{T-rev})}\right] \qquad \textit{Equation 4-2a}$$
$$= 13.5 + 0.017v + (129.0 - 0.017v)\left[1 - e^{(-\gamma V_{T-rev})}\right]$$

where γ is a positive fitting constant, and for the case of v = 28 mm/min, Equation 4-2 can be written as:

$$M = 14.0 + 128.5\left[1 - e^{(-0.1354 V_{T-rev})}\right] \qquad \textit{Equation 4-2b}$$

the value of γ is estimated to be –0.1345 mm^{-3}. However, as can be seen from Figure 4-5a, Equation 4-2a does not seem to describe the relationship between $V_{T\text{-}rev}$ and M well. To be specific, at low $V_{T\text{-}rev}$ range (i.e. high ω range), Equation 4-2a over predicts M required. It has been suggested by Schmidt et al. [117] that the torque resulted from the shoulder could be greater than 80% of the total torque generated, partially due to the fact that the shoulder diameter is much larger than the pin diameter. Bearing that in mind, shoulder flow volume per revolution ($V_{S\text{-}}$

$_{rev}$) against M was plotted in Figure 4-5b, and Equation 4-3 was used to fit all the data:

$$M = M_{\omega=\infty} + (M_{\omega=0} - M_{\omega=\infty})\left[1 - e^{(-\gamma V_{S-rev})}\right]$$
$$= M_o + M_f\left[1 - e^{(-\gamma V_{S-rev})}\right] \qquad \textit{Equation 4-3}$$
$$= 13.5 + 0.017v + (129.0 - 0.017v)\left[1 - e^{(-\gamma V_{S-rev})}\right]$$

It can be seen that V_{S-rev} and M are much better related to each other, indicating that the amount of M is determined largely by the amount (mm^3/rev) of the shoulder flow. This suggests that the portion of M required for nugget flow (volume) is consistently small, although the nugget flow (volume) is sometimes large. Such suggestion is justified by the fact that similar exponential rise function does not seem to correlate V_{N-rev} (nugget flow volume per revolution) to M well (Figure 4-5c). The thermomechanical reasons will be discussed in the following section.

4.4 Geometrical and Thermal Effects

Now let us examine why shoulder flow contributes much more significantly compared to nugget flow to the total torque generation. First of all, one major reason could be that the shoulder flow zone (regardless of its flow volume), is fundamentally larger in diameter compared to nugget zone (on the cross section), which is because the tool shoulder diameter (18 mm) is three times as large as the pin diameter (6 mm). As such, shoulder flow would intuitively require larger torque (which is the product of force and radius). Let us re-consider the theoretical calculation of M using Equation 3-2a (page 91). The theoretical ratio ($r_{s/p}$) between shoulder generated torque and pin (on both surface and bottom) generated torque can be calculated as:

$$r_{s/p} = M_{shoulder} / \left(M_{pin\ bottom} + M_{pin\ surface}\right)$$
$$= \left(\frac{\int_{r_i}^{r_o} r\tau 2\pi r dr}{2}\right) \Big/ \left(\int_0^{r_i} r\tau 2\pi r dr + r_i \tau 2\pi r_i h\right) \qquad \textit{Equation 4-4a}$$

$$= \left[\tau_{shoulder}\left(\frac{\int_{r_i}^{r_o} r^2 dr}{2}\right)\right] \Big/ \left[\tau_{nugget}\left(\int_0^{r_i} r^2 dr + {r_i}^2 h\right)\right]$$

Using the current tool dimensions, the ratio becomes:

$$r_{s/p} = \frac{\tau_{shoulder}}{\tau_{nugget}}\left[\frac{\int_{0.003\mathrm{m}}^{0.009\mathrm{m}} r^2 dr}{2} \Big/ \left(\int_0^{0.003\mathrm{m}} r^2 dr + 0.003\mathrm{m}2 \times 0.006\mathrm{m} = 1.86 \times \tau_{shoulder}/\tau_{nugget}\right)\right. \quad \textit{Equation 4-4b}$$

Thus, without considering the effect of flow stress, there is an intrinsic geometrical factor (1.86 times) that causes torque acting on the shoulder greater than the torque acting on the pin.

Secondly, Equation 4-4b suggests that the difference in the average material flow stress between shoulder and nugget zone is also responsible for the difference in torque generation. The lower material flow stress (due to higher temperature) in the nugget zone (compared to shoulder zone) could reduce the torque requirement. However, it is important to point out that accurate flow stress distribution, which is a function of temperature and strain rate distribution, in the total stir zone cannot be determined based on current experimental setup. Nevertheless, how the temperature difference (between shoulder and nugget zones) could potentially affect required M has been estimated in this study. Temperature was measured at three selected positions (shown in Figure 2-7), which are:

a. 2 mm below plate surface, 3 mm away from the pin threads (representing shoulder region temperature).

b. 3 mm below plate surface, at pin centre (representing pin centre temperature).

c. 4 mm below plate surface, 1 mm away from pin threads (representing nugget temperature).

Three sets of measurements were obtained under different FSP conditions: v = 28 mm/min, ω = 63 rpm; v = 224 mm/min, ω = 250 rpm; and v = 450 mm/min, ω =

710 rpm. This is because under these conditions, $V_{S\text{-}rev}$ is approximately the same (Figure 4-5b). Pin centre temperature was also measured for v = 112 mm/min, ω = 710rpm. Details of the temperature measurements are given in section 2.2.4. The highest detected temperatures are summarized as below:

Table 4-1. Summary of highest detected temperatures under three FSP conditions.

v (mm/min), ω (rpm)	$T_{shoulder}$ (°C)	T_{nugget} (°C)	T_{pin} (°C)
28, 63	243.5	244.6	289.5
224, 250	349.7	353.3	414.1
450, 710	410.2	458.7	511.5
112, 710	-	-	534.0

As can be seen, $T_{shoulder}$ is lower than T_{nugget} and T_{pin} under all conditions, and such observation is consistent with literature [61]. The difference between these quantities tends to be larger at higher ω. Material flow stress (σ) is strongly affected by temperature (T) and strain rate ($\dot{\varepsilon}$), they relate to one another through the Zener-Hollomon equation (Equation 1-5, page 23). By rearranging this equation, σ can be solved:

$$\sigma = \alpha^{-1} \sinh^{-1}\left\{[A^{-1}\dot{\varepsilon} exp(Q/RT)]^{1/n}\right\} \qquad \textit{Equation 4-5b}$$

Material constants used in this equation for A356 alloy have been reported by a few researchers [119-121], that A = 4.38 × 10^{19} s^{-1}, Q = 271.84 kJ/kgK, R = 8.314 kJ/mol, n = 5.616, and α = 0.025. Flow stresses (σ) with strain rates equal to 1 s^{-1}, 10 s^{-1}, and 100 s^{-1} were calculated for temperature ranging from 240 to 580 °C (equilibrium solidus temperature of A356 is 577 °C), which are shown in Figure 4-6.

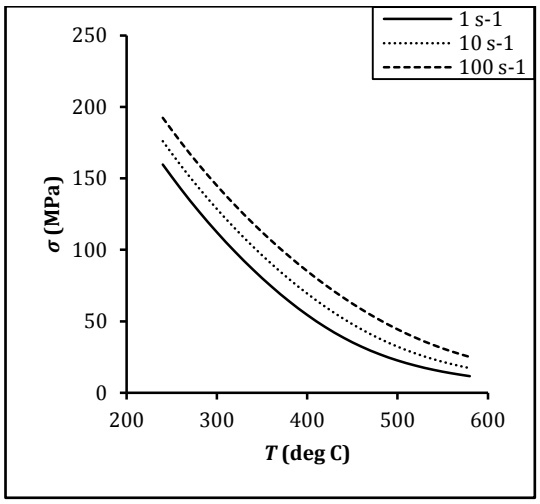

Figure 4-6. σ plotted against T, calculated by using Equation 4-5b.

As can be seen from Figure 4-6, T plays an overall more important role than $\dot{\varepsilon}$, in determining the flow stress (σ). At v = 450 mm/min and ω = 710 rpm, the difference between $T_{shoulder}$ and T_{nugget} is 48.5 °C, and that between $T_{shoulder}$ and T_{pin} is 101.3 °C. The estimated flow stresses at shoulder, nugget and pin centre regions are 64.5, 44.8, and 29.3 MPa respectively, with $\dot{\varepsilon}$ arbitrarily chosen to be 10 s^{-1}. Therefore, at a moderate ω, the representative flow stress at shoulder region should be significantly larger than that closely ahead pin centre (120% larger). Thus, to shear the same amount of material, the torque acting on the shoulder is expected to be much larger than that acting on the pin. The combined geometrical and thermal effects can thus explain why shoulder flow volume (V_{S-rev}) correlates better to the total torque generation; while the nugget flow volume (V_{N-rev}), although being large, does not contribute proportionally to the torque generation.

At v = 28 mm/min and ω = 63 rpm, the difference between $T_{shoulder}$ and T_{nugget} is only 1.1 °C, while the difference between $T_{shoulder}$ and T_{pin} is 46 °C. Therefore, the difference between the flow stress of shoulder and nugget regions is likely to be very small. If the strain rate is chosen as 10 s^{-1}, the representative flow stresses of shoulder, nugget and pin are 172.9, 171.9, 136.1 MPa respectively. The flow stress at shoulder is only 27% larger than that at the pin. Therefore, to shear a unit volume of material, the shoulder should not require much larger torque than the pin, as far as flow stress is concerned. In other words, the nugget flow volume (V_{N-rev}) should have contributed to the total torque by a fairly significant amount. This

may explain why the data point (M = 126.8 Nm) at v = 28 mm/min, and ω = 63 rpm, is larger than what has been predicted by the model (which does not include the effect of V_{N-rev}).

Figure 4-5b shows that with approximately the same V_{S-rev}, the M required at v = 28 mm/min ω = 63 rpm, v = 224 mm/min and ω = 250 rpm, and v = 450 mm/min ω = 710 rpm are 126.8 Nm, 79.0 Nm, and 39.9 Nm respectively. Under these conditions, the measured $T_{shoulder}$ is 243.5 °C, 349.7 °C and 410.2 °C respectively, and corresponding estimated σ value is 172.9, 96.3 and 64.5 MPa, respectively. The representative flow stress at 63 rpm is 2.7 times the flow stress at 710 rpm, while the corresponding torque ratio is 3.2. Thus, the difference in flow stress could satisfactorily, although not fully, justify the difference in torque required.

4.5 Energy, Temperature and Flow Stress

We now try to describe the interrelationships among energy inputs ($M/P/E_s$), temperature, and flow stress all together. $M/P/E_s$ can be used as indicators of energy input by the tool during FSP, which describes energy input per revolution, per unit time, and per unit length travelled respectively (as explained previously in Section 4.3). On the other hand, localized temperature rise and overall temperature rise are intrinsically related to energy input during FSP ($M/P/E_s$). The temperature experienced by the centre of the pin (T_{pin}) is arguably, the most crucial temperature variable in FS. The relationship between T_{pin} and ω can be described by exponential rise to maximum function, as described below.

It may be appropriate to quote Upadhyay and Reynolds's recent study again [18]. Their data shows that, T_{pin} is inversely related to M, and rises exponentially with ω. This means, as is also suggested strongly by examining their graph of T data verse ω, a function of exponential rise:

$$T_{pin} = T_o + T_f(1 - e^{-q\omega}) \qquad \textit{Equation 4-6}$$

can be used to model their T_{pin}–ω data well. Then, as T_{pin} is a function of ω that can be described by Equation 4-6, but E_s, and to a less extend P, is almost not a function

of ω (Figure 3-8 and Figure 3-10), at least within a reasonable wide range of ω, T_{pin} should not simply relate well to E_s or P. This latter prediction is consistent with the observation made by Peel et al. [20] that E_s and P do not correlate well with T_{sz} (stir zone temperature) during FSP.

In summary: the partition between RSM zone (highly refined) and the rest of nugget zone (much less refined) is a common feature during FSP A356 under all conditions; the increase in ω and/or decrease in v, result in an increase in the area of nugget zone (A_{nugget}), due to a stronger shearing effect; and hence a smaller shoulder zone ($A_{shoulder}$) is required geometrically; energy input per revolution (represented by M) relates well to shoulder flow volume generated per revolution (V_{S-rev}), rather than total flow volume (V_{T-rev}); and this is a combined result of geometrical effect (shoulder being wider than pin) and thermal effect (flow stress near the shoulder is high than that near the pin).

Chapter 5. Material Flow and Deformation

The thermomechanical aspects of FS were studied in details in the previous two chapters. This chapter will focus on the macro-scale material flow, and micro-scale deformation (strain and strain rate), in close-to-pin region during FSP A356. As introduced in literature review (Section 1.1.2), to study these issues, it is vital to examine the real-time microstructure of the close-to-pin region.

5.1 Rotation Shear Materials and Nugget Zone formation

Referring back to Figure 4-1, a flow segregation, between Rotation Shear Material (RSM) and the rest of the nugget, can be clearly observed in FSP on A356. This segregation is common in all the samples although the relative portions vary as FS speeds change. Since high level of microstructural refinement was achieved in RSM, its formation mechanism is important to be understood and thus was studied using the "pin-breaking" technique for two FS conditions that are commonly used. Detailed FS procedures associated with this technique have been given in Section 2.2.2.

Figure 5-1a to c illustrate the cross section, mid-thickness plane section, and mid-thickness longitudinal section of FS A356 plate (6 mm thick), samples produced using v = 160 mm/min, and ω = 710 rpm. Tilt angle was kept at zero, so that the tool shoulder would have as little effect on the broken pin as possible. If a tilted tool was used, the broken pin would be pushed slightly by the rear portion of the shoulder.

As can be seen from Figure 5-1a, the use of a zero tilt angle results in a less shoulder flow, which causes an insufficient joint between the nugget zone and the shoulder zone. Three features, which are essentially the same as those observed in Figure 4-1a, and thus quite representative of the typical features of a FSP (of A356) conducted using a normal condition, are observed in Figure 5-1a:

a. absence of a ring structure in the nugget,

b. a heavily deformed RSM region on the advancing side and tailing off to the retreating side in the lower part of the nugget,

c. the rest of the nugget formed by material that has been deformed but still displays some dendritic features.

The RSM region and the non-RSM region of a nugget represent regions of material experiencing different amounts of deformation. Thus the flow path of material arriving and deposited in each region is likely to be different from one to the other. The detailed analysis on this is given below.

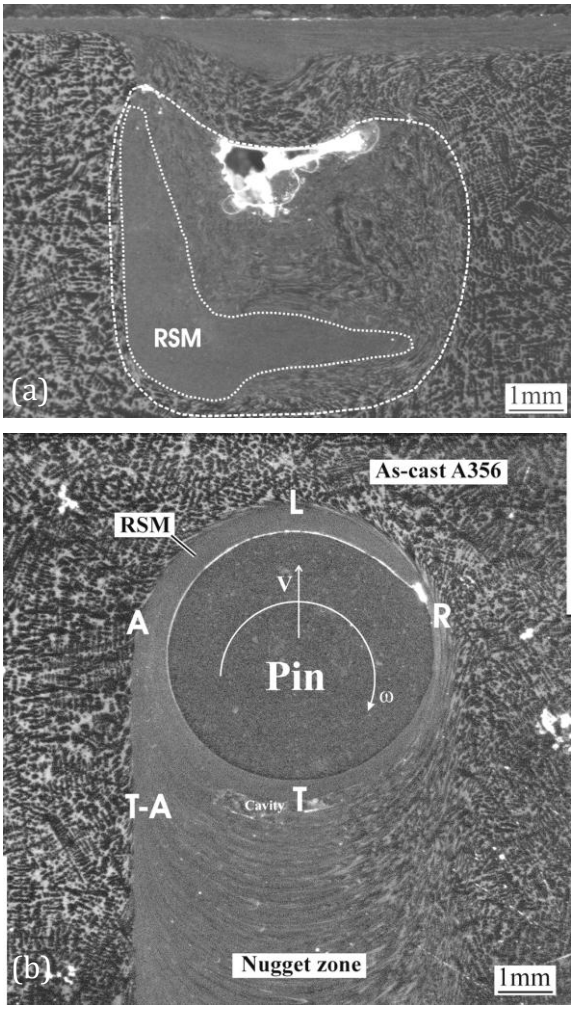

Figure 5-1. Cross sections of FS samples made using θ = 0 °, v = 160 mm/min and ω = 710 rpm: (a) a nugget zone and the RSM region inside the zone as outlined, (b) a broken pin embedded sectioned longitudinally along the plane ~ 4 mm from the surface; (c) a broken pin embedded sectioned longitudinally along the mid-section of the pin (normal to surface). L signifies leading, R retreating, T trailing and A advancing sides of the pin.

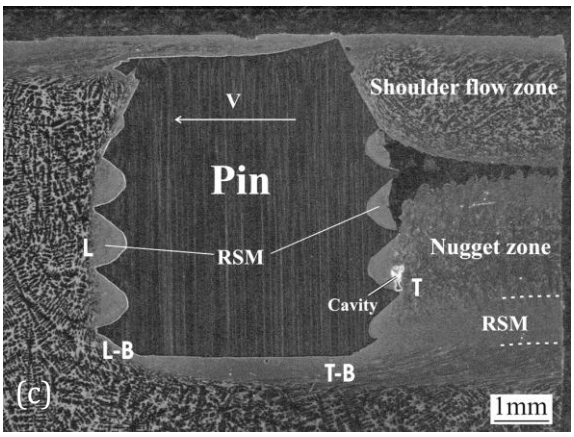

Figure 5-1. Continued.

Figure 5-1b and Figure 5-1c are low magnification micrographs of the workpiece material around the tool pins, broken and embedded in workpieces during FS experiments. The nomenclature is: A, L, R, T, and B denote the advancing, leading, retreating, trailing and bottom locations of a pin/workpiece couple. Heavily deformed material is clearly present in thread spaces around the pin, implying that this shear material rotates with the pin during FS (although not necessarily at the same speed), and thus is named rotational shear material (RSM), referred to as rotation [35] zone in the literature of FS welding. This RSM is also present below the pin (Figure 5-1c). Outside the pin/RSM and nugget zone, the as-cast dendritic microstructure is clearly displayed.

During FS, as the rotating tool moves forward, a portion of the workpiece material in the front is forced (sheared) into thread spaces and then becomes RSM. The further movement of this RSM in thread space is referred to as RSM flow. In the trailing half, for mass balance, RSM needs to detach from thread spaces. For a better illustration, the pin-workpiece couple in Figure 5-1b is schematically represented in Figure 5-2. In this figure, forces and features of material flow are suggested. Each pair of forces (normal force F_N and shear force F_S) represents the forces acting on the edge of the RSM from outside material. Take F_{S-R} for example, material outside RSM resists its flow. Therefore, there will be an opposite (reactive) force of F'_{S-R} which shears the material outside RSM towards the wake of the tool. This reactive force within regions L to R generally shears the workpiece

material outside RSM to R–T regions. This shear flow is referred to as rounding flow.

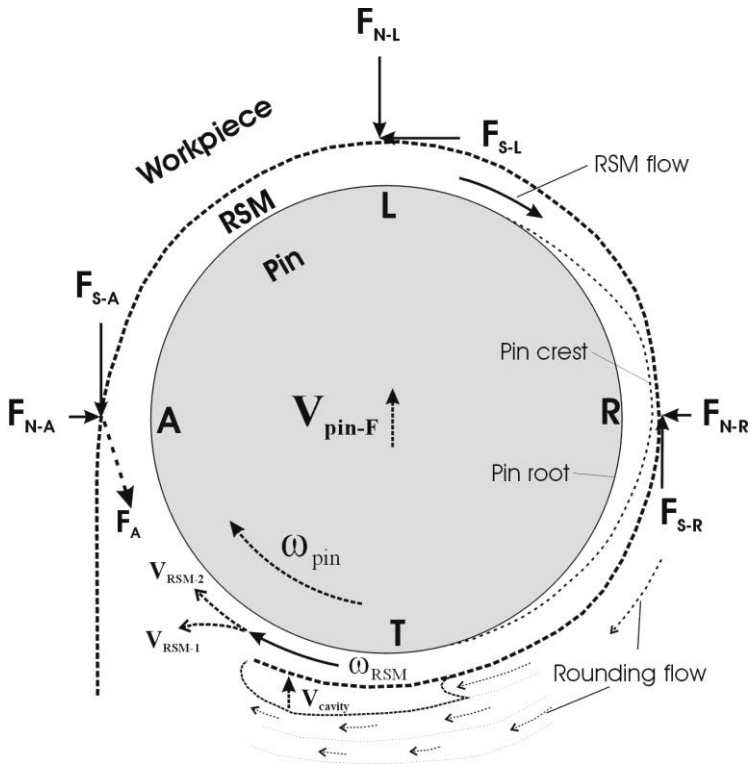

Figure 5-2. Schematic illustration of RSM around the pin, forces acting on the periphery of RSM, and various material flow directions. For generality, RSM has been drawn continuously around the pin with the pin crest in a particular location is also indicated.

The rounding flow forms part of the nugget with the original dendrites having gone through increasing amounts of deformation and thus decreasing clarity of dendritic appearance towards the central region of the nugget (Figure 5-1b). A cavity forms as a result of the rounding flow separating from RSM in region T, due probably to the region being under tension as the pin keeps moving forward and away. The newly separated portion of the rounding flow will continue to flow towards the advancing side, pushed by the rounding flow behind. The cavity is stable and moves forward with the pin, as the cavity grows due to flow separation on one hand and is subsequently filled by the continued rounding flow.

Referring to RSM flow within thread spaces, after region T (Figure 5-1b and Figure 5-2), the flow should gradually enter into the zone whereby pressure should increase towards region A, as the leading half is a compressive zone. The

compressive zone during FS is the result of the pin moving forward and compressing the workpiece material ahead. Therefore the continuation of a full RSM flow through region A to the leading half becomes increasingly unlikely. The result of this is the detachment of RSM from thread spaces in region T–A, as represented by flow V_{RSM-1} in Figure 5-2. This provides a reasonable explanation of the observed RSM region on the advancing side of the nugget, as shown in Figure 4-1a and Figure 5-1b.

The evidence that thread spaces are continuously and almost completely filled by RSM (Figure 5-1b and Figure 5-1c) suggests that RSM may not completely detach in location T–A. A portion, indicated as V_{RSM-2} in Figure 5-2, may continue to rotate through point A and to mix with the newly entered RSM. RSM residing in thread spaces should also flow downward pushed or sheared by the flanks of the rotating thread. This shearing down effect is quite dominant during FSP wrought Al alloys (Figure 1-20). Thus, a portion of RSM, particularly that which resides in lower thread spaces, should detach from the bottom of the pin. This is seen to be the case when a vertical section is examined, as shown in Figure 5-1c. The combined sideward and downward flows (detachments of RSM) should then result in forming an L–shaped RSM region in the nugget zone, as is clear in Figure 4-1a and Figure 5-1b.

Now let us re-consider the areas of RSM flow and nugget flow (A_{RSM} and A_{nugget}). As observed from Figure 4-4a and b, that the difference between A_{nugget} and A_{RSM}, which is the area of rounding flow ($A_{rounding}$), is almost nearly constant regardless of speeds used, i.e. $A_{nugget} - A_{RSM} = A_{rounding}$ = constant. As discussed, the pin shearing effect plays a primary role in the formation of RSM flow. The rounding flow is to assist the formation of the rest of the nugget, and this flow zone is not in direct contact with the moving and rotating pin. Therefore, it is not unreasonable to assume that the volume and area of this rounding flow are not sensitive to the speeds.

5.2 Features of Deformation and Flow Induced by Pin

Micro-features of deformation can be better illustrated in a higher magnification as in Figure 5-3 and Figure 5-4. The as-cast structure of α(Al) dendrites and interdendritic Al-Si eutectic are clearly seen to have transformed (deformed) into RSM where Si particles are reasonably evenly distributed. Dendritic features are clearly unaltered in a short distance (the width of a transitional zone) outside the RSM. A transitional zone is where the as-cast microstructure transits (shears) into a heavily deformed structure. Careful observation indicates that the transitional zone is 200–250 μm wide in region A (Figure 5-3d), 350–400 μm in region L (Figure 5-3a) and 450–500 μm in region R (Figure 5-3b). In the region (between) T–R, material outside the RSM is seen sheared by the rotating RSM forming the rounding flow. Separation of the two occurs in region T due to slippage between them (Figure 5-3c).

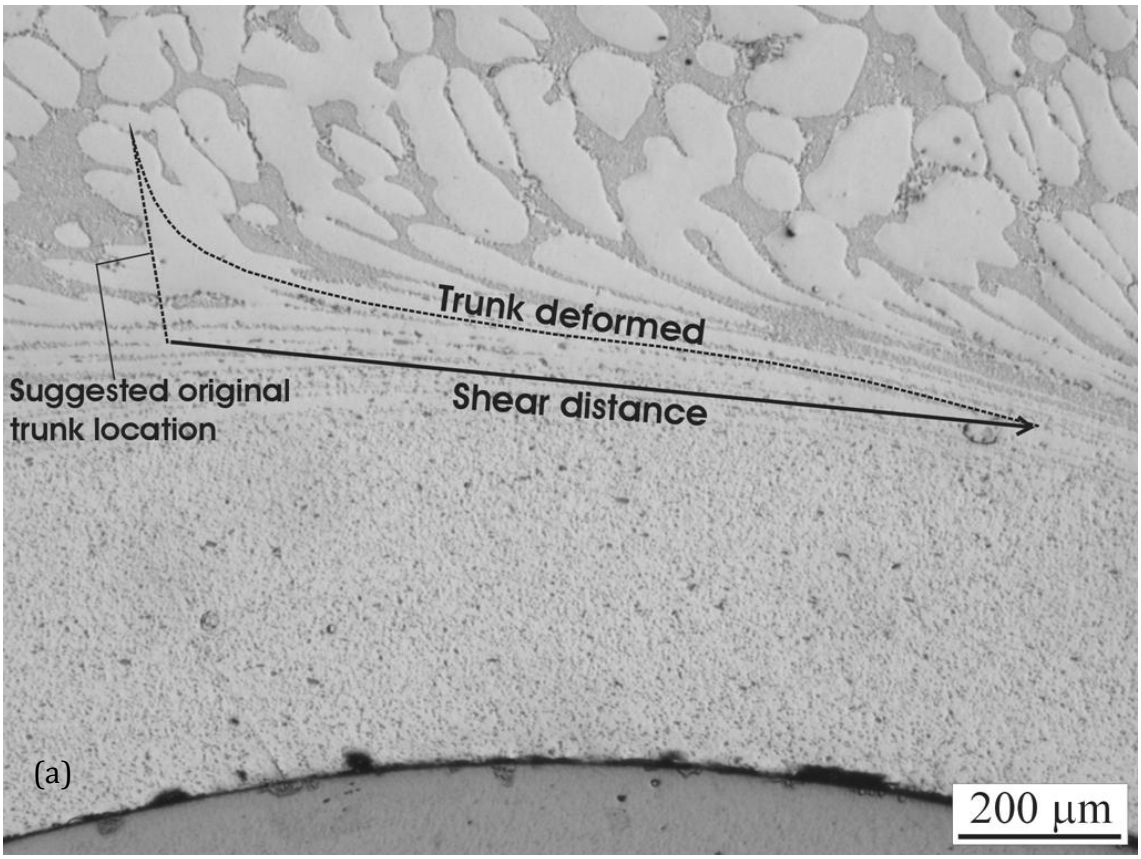

Figure 5-3. High magnification micrographs taken at locations (a) L, (b) R, (c) T, (d) A, and (e) T–A.

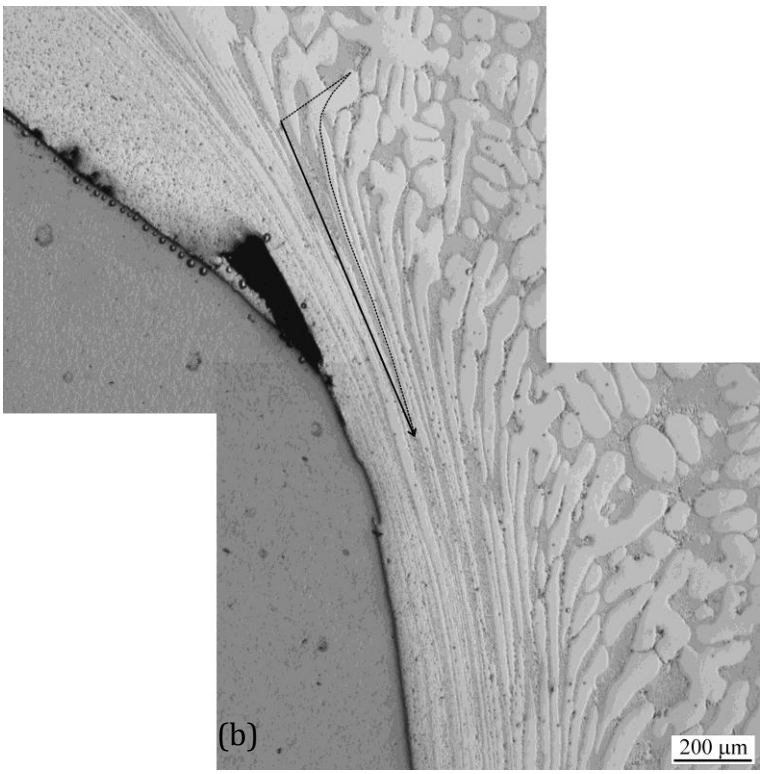

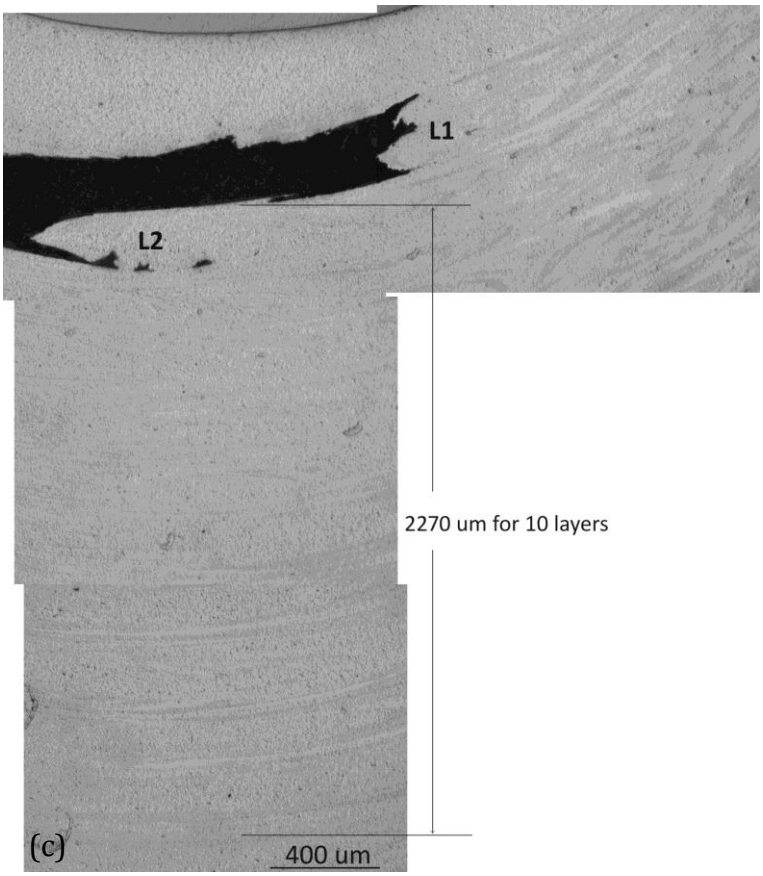

Figure 5-3. Continued.

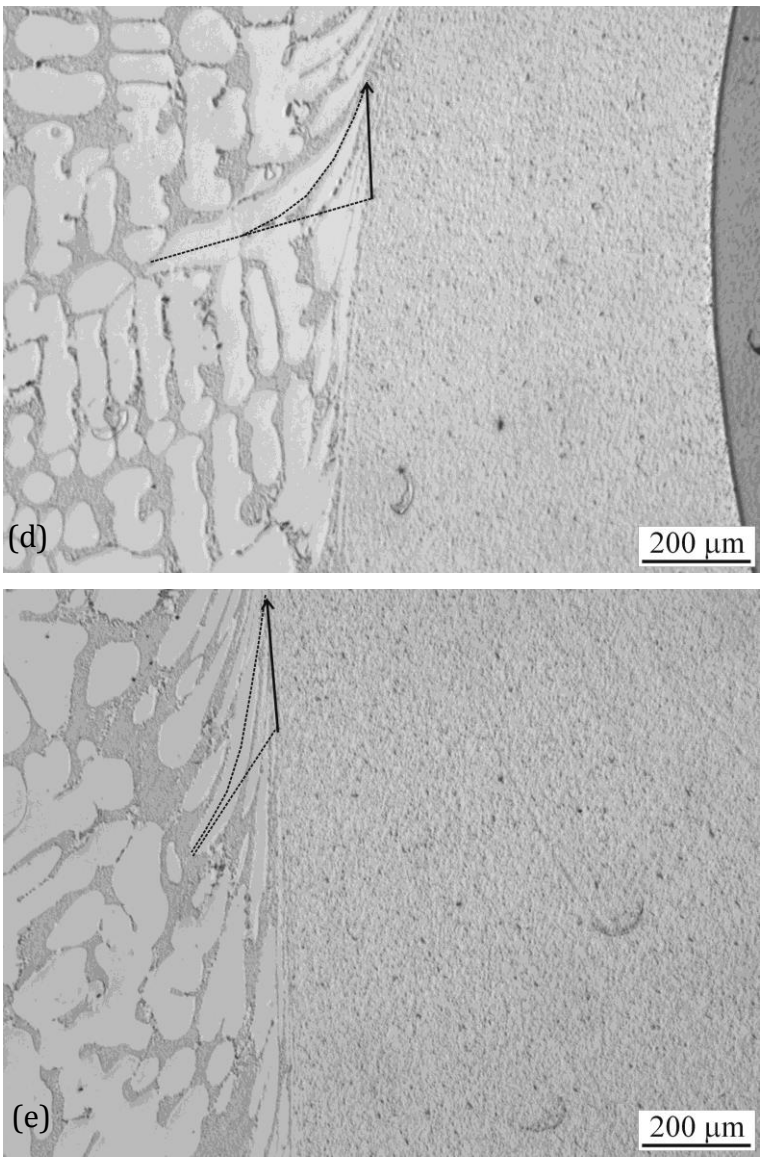

Figure 5-3. Continued.

In some micrographs, local material flow distances have been suggested in the transitional zone. To do this, a primary dendrite trunk or a secondary dendrite arm was traced and drawn as a curve (Figure 5-3a for a trunk). One end of this trunk is in the low deformation side of the transitional zone. Along the trunk, the amount of deformation increases, elongating (and curving) towards RSM. However, when the tracing approaches RSM, there is a region of 20–30 μm thick locally where dendrites have been deformed to such an extent that they appear as fine α(Al) layers wrapped around RSM. A dendrite trunk (or an arm) can be traced from the outside flowing into this most heavily deformed region but where it ends cannot be identified.

The orientation and length of the original trunk cannot be precisely determined but can be suggested judging by the low deformed portion of the trunk after FS (Figure 5-3a). Shear distance can then be estimated, as illustrated in Figure 5-3a, represented by an arrowed line. The heavily sheared distance is large when approaching RSM (> 800 μm in Figure 5-3a). The uncertainty in estimating the starting point of shear is unlikely to be more than 50 μm. Therefore the uncertainty only affects the suggested shear distances slightly. The suggested flow distances are not used to accurately construct a flow field. Rather, they were drawn to aid the interpretation of the characteristics of the deformed microstructure, and thus to aid the understanding of the flow characteristics around the pin.

In region L, in the area between 100–150 μm ahead of the RSM, shear deformation starts to sharply intensify, as can be seen in the horizontal plane in Figure 5-3a. This is consistent with the observation in the mid-thickness vertical plane, as shown in Figure 5-4a, where a sharp increase in the amount of compression can be seen starting from a distance of 100–150 μm ahead of the RSM. Within the region of 100–150 μm ahead of the RSM, a round (large radius) tip of a dendrite arm has become the shape of a knife edge, pointing to the shear direction. The round dendrite arm tips found in the as-cast state are the result of the coarsening of dendrites during solidification. The knife edge appearance is the result of an increasingly higher deformation strain.

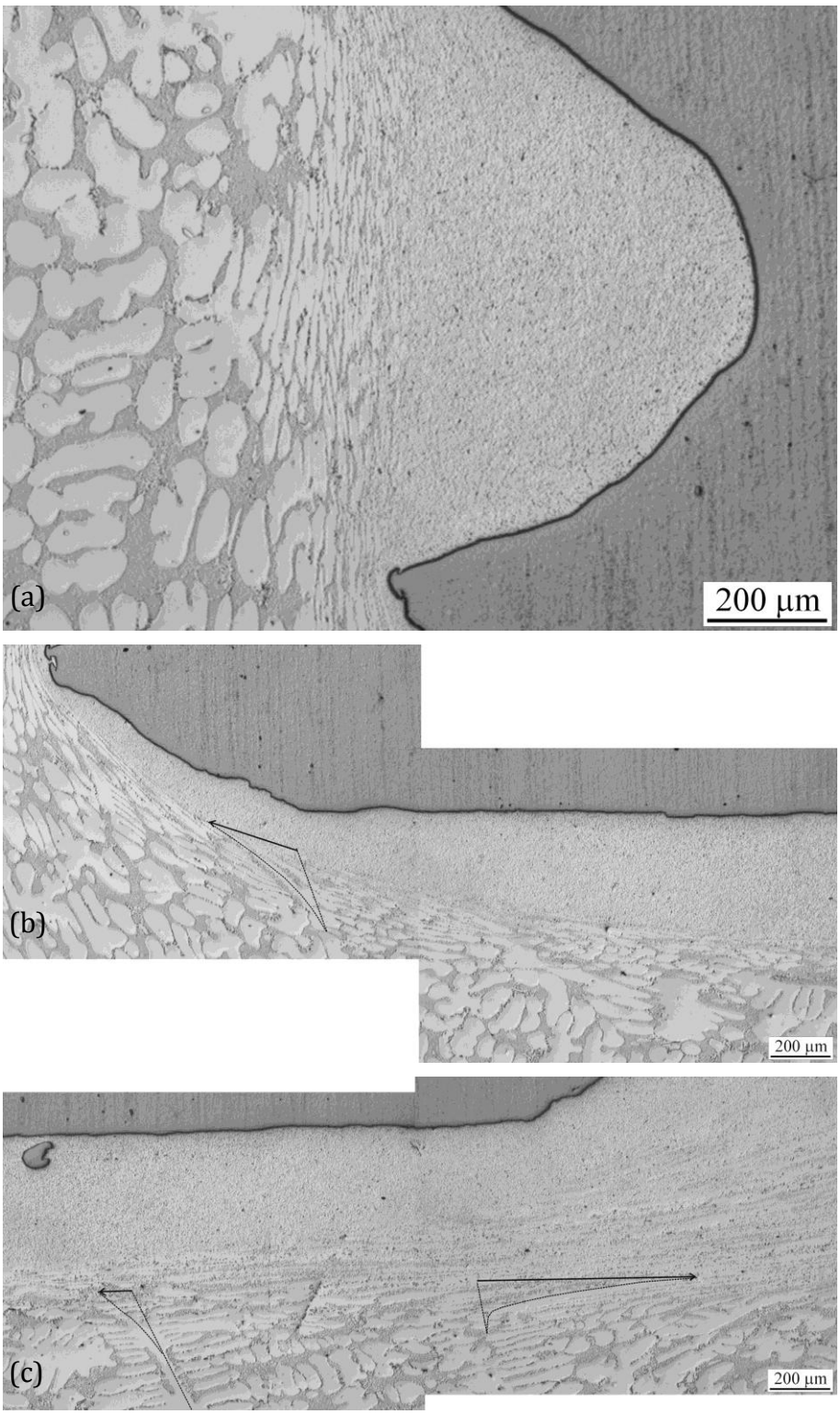

Figure 5-4. High magnification micrographs taken from the sample shown in Figure 5-1c, at locations (a) L, (b) F–B, (c) and (d) T–B.

Figure 5-4. Continued.

In the front part of region R, as shown in Figure 5-3b, a high gradient of shear deformation in the transitional zone can also be seen, in this case it is clearly indicated by a deformed and traced dendrite arm. On the other hand, as indicated in Figure 5-3d and e, the shear gradient at point A is considerably less than that in Figure 5-3b. Shear deformation increasingly intensifies after point A and towards region L. In the transitional zone beneath the pin/RSM (Figure 5-4b), the forward motion of the pin/RSM actually results in a forward shear flow direction in the front portion. In the rear portion, however, there must be a high rate of RSM detaching backward, thus resulting in a high amount of backwards shear flow (Figure 5-4c) in the transitional zone.

Although neither "Onion Rings" nor a clear banded structure are present in the nuggets in the present experiments, there is a weak periodicity associated with the material flow. This can be seen in Figure 5-3c. The separation of RSM flow from the adjacent rounding flow of less deformation occurs one by one (L2 and then L1) in the horizontal section. In the nugget zone, as the distance away from the pin increases, a pattern of repetition can be seen, though the spacing is non-constant. The average spacing is very close to v/ω and hence to the advance per revolution (λ), thus suggesting periodicity of flow. Weak periodic flow of RSM forming part of the nugget zone may also be seen in Figure 5-4d.

Two features of a threaded tool are periodic in nature. Firstly, for a single thread, material exit (RSM outflow) in the bottom part of the pin via the end of the thread should vary cyclically. This periodicity of RSM outflow is weakly apparent in Figure 5-4d. Secondly, in a horizontal plane, the workpiece material intersects with the

pin crest once in a cycle. This may also cyclically affect the rounding flow and may actually be the major cause of the periodic flow separation in region T–R (Figure 5-3c). Thus, considering the role of the pin (thread/crest) there must always be a periodicity of flow during FS. Flow periodicity alone is, however, not a sufficient condition for "Onion Rings" to form in the nugget.

5.3 Strain and Strain Rate Estimation

As illustrated above, during the identification of the flow mechanism for "Non Ring" flow, the deforming α-Al dendrites were used as markers to indicate the flow direction and features. In this section, the use of these dendrites markers provide a workable method based on which strain and strain rate can be estimated.

5.3.1 Tracing Deforming Dendrites

Two pin-embedded samples of FSP A356, performed under similar conditions, are presented below (Figure 5-5a and b), from which the deforming dendrite trunks can be easily identified in the leading transitional region. Since the deforming dendrites can be approximately traced, an attempt was made to determine the strain and strain rate experienced by the material in the transitional region. We only focus on the seemingly most severe deformation region of the workpiece.

Observing that region, a noticeable deformation appears to start at a distance (350–400 μm) ahead of the RSM. Thus a horizontal line (X axis) can be drawn, starting at a point where no obvious deformation can be identified (Figure 5-6). A vertical line (Y axis) can also be drawn pointing downward. This shows an increasing degree of deformation of the material before entering and being part of the RSM. This X–Y coordinate system and its superimposition on the micrograph shown in Figure 5-5a and b are given in Figure 5-6a and b respectively. Each X and Y unit is arbitrarily represented by the diameter of a small circle. One unit equals to 13.3 and 15.9 μm in Figure 5-6a and b respectively. In Figure 5-6a and b, the boundary between the transition zone and the RSM zone locates at Y = –30 units and Y = –26 units respectively.

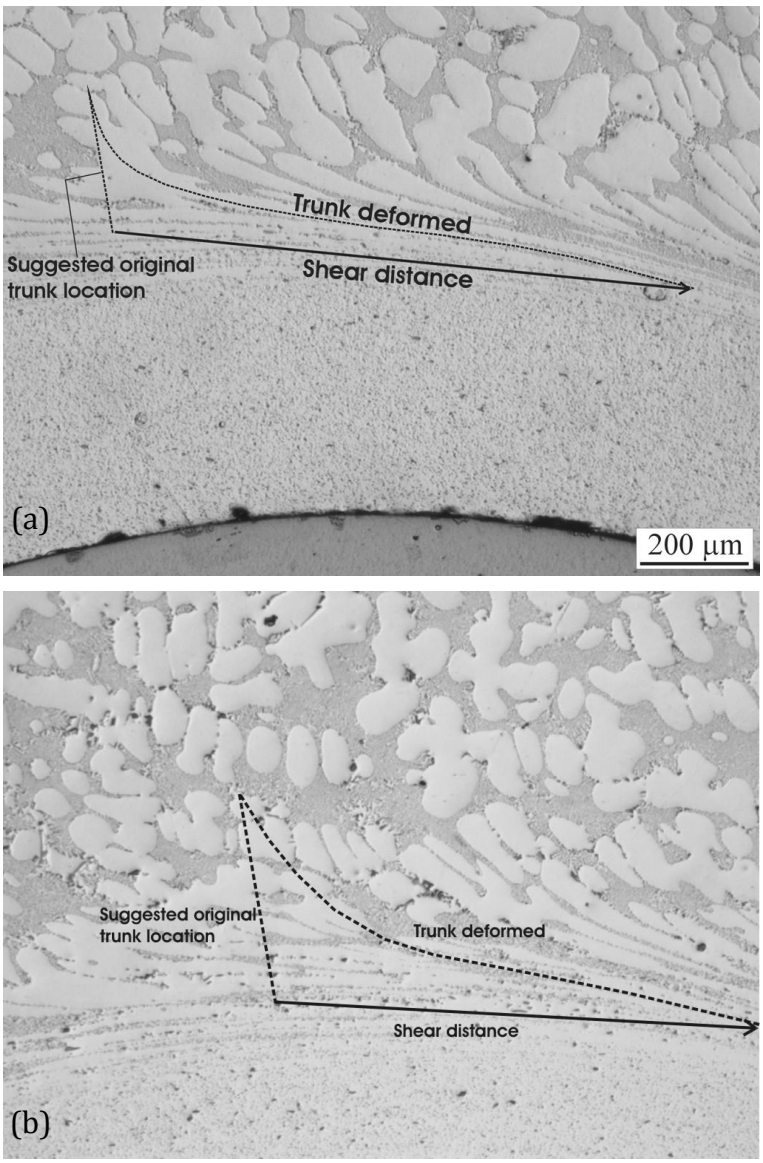

Figure 5-5. Tracing the deforming dendrite trunks in front of the broken pin embedded in A356 workpiece, (a) at v = 160 mm/min and ω = 710 rpm and (b) at v = 112 mm/min and ω = 710 rpm.

Curve 1 with six solid circles in Figure 5-6a was drawn by tracing the deforming dendrite trunk. The solid circles actually follow a regular increment in this case (the curve traces the deformed trunk well). For every 4.5 units increased in Y, the distance in X between two solid circles doubles from the previous distance. Curve 1 was drawn to X = 63 units and Y = –27 units, as beyond that the highly deformed portion of that trunk curves slightly following the periphery of the RSM. Curve 2 is part of Curve 1 for Y from 0 to –22 units, after being moved horizontally to the right. It is clear that Curve 2 traces the deformation of the two dendrite arms very

well, suggesting that Curve 1 is a very good trace of deformation in that transitional zone, except for the region very close (20–30 μm) to the RSM.

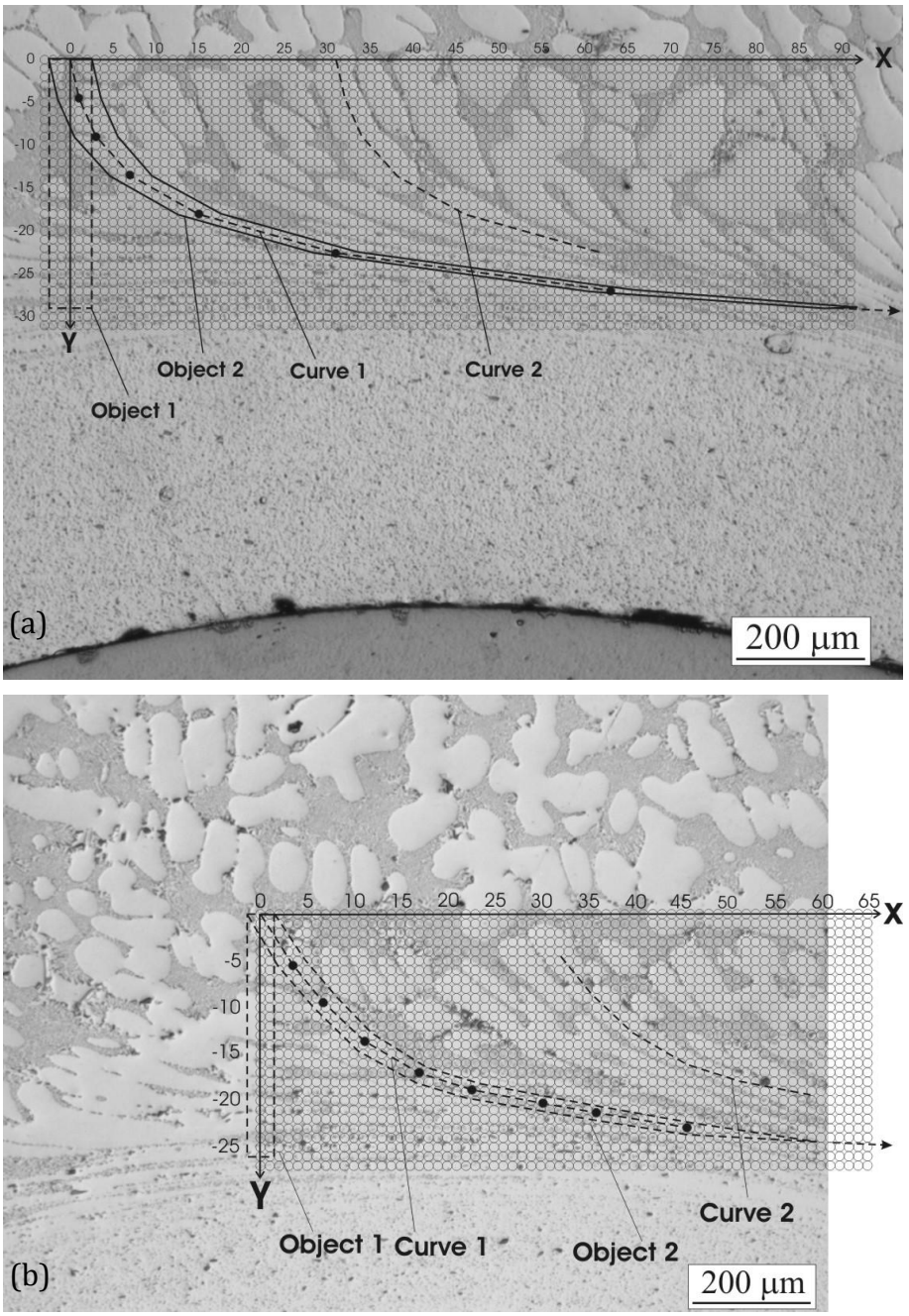

Figure 5-6. X–Y coordinates and illustration of various object tracings drawn on the micrograph as in Figure 5-5a and b. Curve 1 with solid circles represents the tracing of the dendrite trunk, Curve 2 is a portion of Curve 1 moved to the right, Object 1 represents an imaginary dendrite trunk and Object 2 represents Object 1 after shear deformation. One unit length (represented by the diameter of a circle) equals 13.3 and 15.9 μm in (a) and (b) respectively. The extrapolated ending point of Object 2 is (125, –30) and is (91.6, –26) respectively. However, due to the allowed space, this end has not been shown in the figure.

To further illustrate, Object 1 in Figure 5-6a was drawn to approximately suggest a particular dendrite trunk before deformation. After applying the same increments (doubling X increment for every 4.5 units in Y increment), we obtain Object 2 which describes the shape of the (real) deformed trunk well, although the tailing part (for X > 63 units) of the deformed trunk should curve slightly following the periphery of the RSM/pin.

It is important to point out that the original dendrites (Object 1) are assumed to be vertical, and consequently we have induced an uncertainty regarding to the original orientation of the dendrite. However, this uncertainty has a slight but insignificant influence on the final appearance of the deformed (heavy shear) shape (Object 2). This is due to the increasingly large shear within the short distance towards the RSM, dominating the final appearance. This uncertainty and its effects on the appearance of the tracing of the deformation (Object 2) will be discussed further in Section 5.3.4.

5.3.2 Strain and Strain Rate (160 mm/min)

The solid circles (points) of Curve 1 in Figure 5-6a were replotted and curve fitting was carried out (Equation 5-1), as shown in Figure 5-7. As mentioned previously, the tracing of the deformed dendrite ends at X = 63 units and Y = –27 units due to the fact that the deformed dendrite curves according to the periphery of the RSM zone. However, Equation 5-1 can be used to extrapolate Curve 1 further to Y = –30 units (where the boundary between transition zone and RSM zone locates), which yields X = 127 units.

$$Y = -\frac{0.015+5.9576X+0.3406X^2}{1+0.0614X+0.0002X^2} \qquad \textit{Equation 5-1}$$

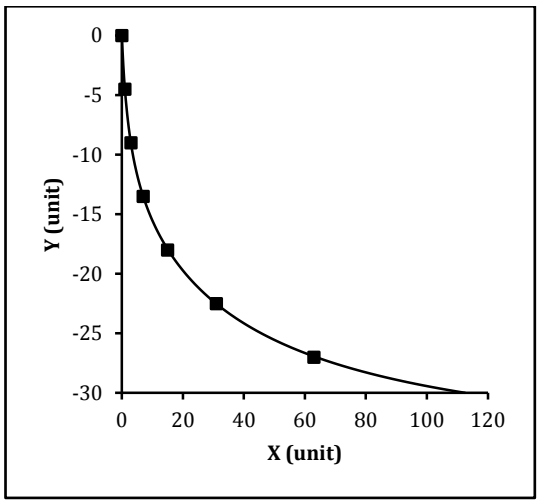

Figure 5-7. Traced points as illustrated in Figure 5-6a. At the boundary between transition zone and RSM zone (Y = 30 units), the shear distance is estimated to be X = 112.5 units. One unit represents 13.3 μm.

From this best-fit curve (Equation 5-1), local strain (depending on Y) can be determined by Equation 5-2.

$$\varepsilon = ln\left(\frac{\Delta l}{\Delta l_o}\right) = ln\left(\frac{\Delta\sqrt{\Delta x^2+\Delta y^2}}{\Delta y}\right) \qquad \textit{Equation 5-2}$$

Strain as a function of distance from the start of deformation is plotted in Figure 5-8a. Referring to Figure 5-6a, it may be reasonable to suggest that the material originally in location (0, –30), having a shear distance of (X =) 127 units into the retreating side, must have just entered the RSM region. Therefore, strain of 3.2 at Y = –30 units (shown in Figure 5-8a) should be the approximate maximum strain for the deforming material in the transition zone.

Knowing the strain and the feed rate ($v = \Delta y/\Delta t$), strain rate can also be estimated in that transition zone:

$$\dot{\varepsilon} = \frac{\Delta\varepsilon}{\Delta t} = \frac{\Delta\varepsilon}{\Delta y} \times \frac{\Delta y}{\Delta t} = \frac{\Delta\varepsilon}{13.3\frac{\mu m}{unit}\times\Delta y} \times 2.667\,\frac{\mu m}{s} \qquad \textit{Equation 5-3}$$

where 13.3 is the conversion factor from a Y unit into microns. Strain rate plotted as a function of the distance from the start of deformation is shown in Figure 5-8b. Similar to the reasoning before, strain rate increases rapidly towards the RSM region but the strain rate value at the time of entering the RSM zone should then be 69 s^{-1}.

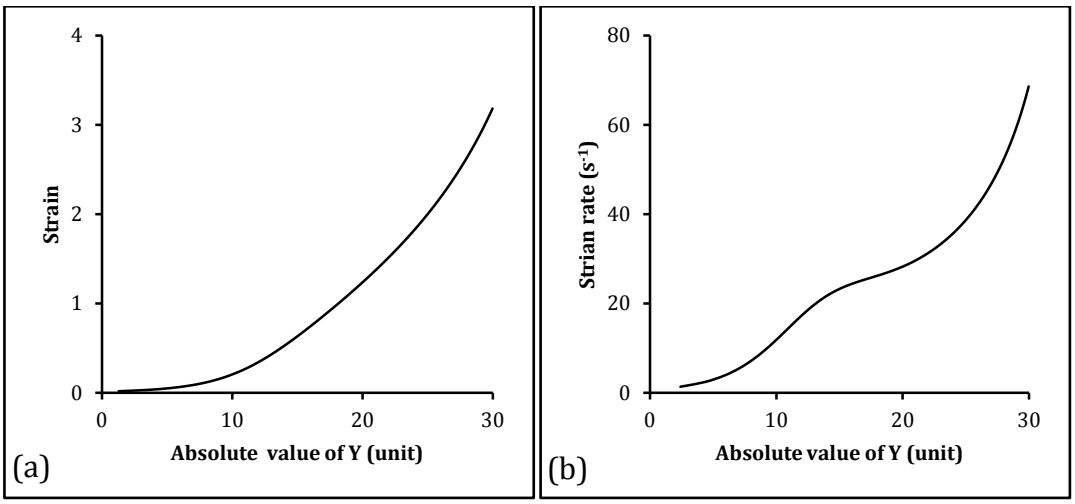

Figure 5-8. Strain and strain rate calculation based on Equation 5-1.

The further deformation strain of the material after entering into the RSM zone cannot be determined. However, as illustrated by Figure 5-5, there does not seem to be a reason for a further increase in strain after entering into the thread space in the present case. RSM, as it appears, may largely just rotate with the pin to be transported to detach behind and below the pin.

Furthermore, there is not a condition for the material to increase strain and strain rate towards the rear of the pin as the pressure is generally low towards the back of the pin. This low pressure has been reasoned and described by McQueen et al [122]. Our present work is slightly different but the illustration in Figure 5-3 is clear. RSM zone is quite separated from the rounding flow. In the trailing side these two flows separate from one another thus forming a stable cavity following the pin (Figure 5-3c). The existence of a cavity further indicates that there is not a normal force causing further shear of RSM in that region. Hence, it can be suggested that in the leading side, material experiencing a high strain entering the thread space and in the trailing side the additional strain of the material in the thread space is close to zero.

As little further strain is expected once the material has entered the thread space, consequently the strain rate would fall sharply. A rate of 69 s^{-1} may thus be the approximate maximum value in the present case.

5.3.3 Strain and Strain Rate (112 mm/min)

The same methodology can be used to estimate the strain and strain rate in another sample, conducted at v = 112 mm/min, and ω = 710 rpm (Figure 5-6b).

The traced points (seven in total) on the deformed dendrite and their best fit curve (Equation 5-4) has been given in Figure 5-9. The deforming dendrite can be very well traced between Y = 0 and Y = –20 units. As mentioned previously, the boundary between the transition zone and the RSM zone locates at Y = –26 units. Between –20 and –26 units, the deformed dendrite curves following the periphery of the RSM zone (Figure 5-5b), thus the actual shear distance cannot be determined by tracing the dendrite. However, Equation 5-4 can be used to determine the "actual" shear distance of the dendrite between –20 and –26 units. As can be seen from Figure 5-9, the curve extends to X = 91.6 units at Y = –26 units.

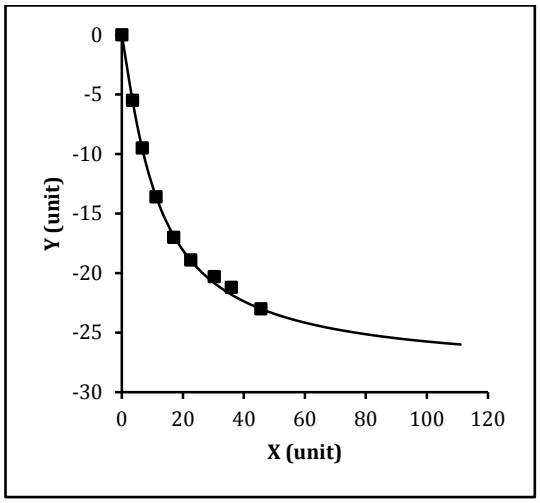

Figure 5-9. Traced points as illustrated in Figure 5-6b. At the boundary between transition zone and RSM zone (Y = 26 units), the shear distance is estimated to be X = 111.0 units. One unit represents 15.9 μm

$$Y = -\frac{0.0012+1.5120X+0.3892X^2}{1+0.1905X+0.0137X^2} \qquad \textit{Equation 5-4}$$

The calculated strain and strain rate are presented in Figure 5-10a and b respectively. The maximum strain experienced during the processing is about 3.9, and the maximum strain rate is around 97 s^{-1}. The maximum strain and strain rate are slightly and significantly higher than those of the FS conducted at a higher v (160 mm/min), which are 3.2 and 69 s^{-1} respectively. Referring back to

Mukherjee's study [41] (Section 1.4.4, which is a later study compared to the current study), by tracing the deformation pattern of the inserted marker, the maximum strain was estimated to be ~ 4.6. This value is higher than the current estimation (3.2–3.9). This slightly larger strain might be justified by the fact that a larger rotation speed was used in Mukherjee's study (1500 rpm), which might cause more intensive deformation. Furthermore, the strain rate estimated by Mukherjee (87 s^{-1}) was based on arbitrarily setting material flow velocity as 10% of the pin rotating velocity, which is physically inaccurate. However, the strain rate estimated in the current study is based on tracing the real-time material deformation, which is physically reasonable.

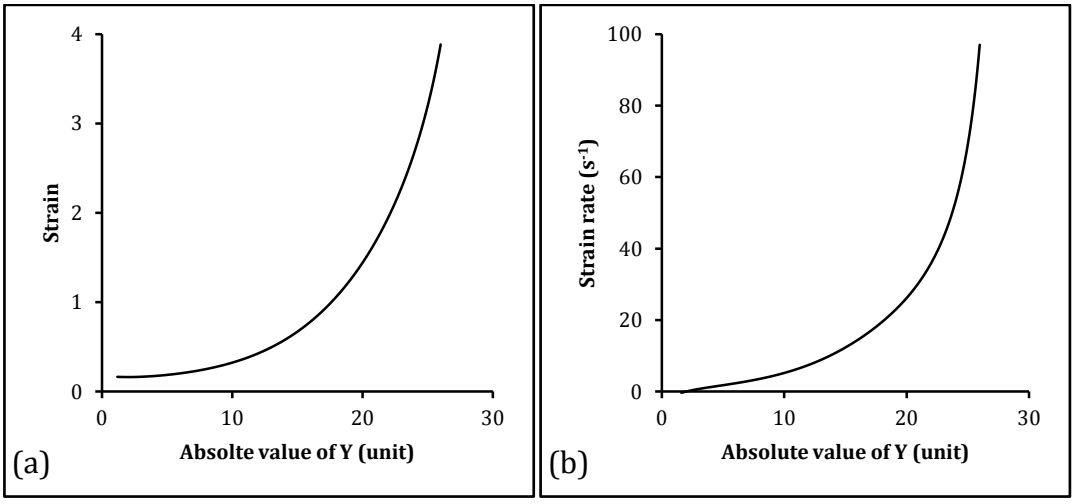

Figure 5-10. Strain (a) and strain rate (b) calculation based on Equation 5-4.

The decrease in linear velocity from 160 to 112 mm/min while keeping the rotation speed constant at 710 rpm should slightly intensify the deformation ahead of the pin as there will be more tool rotation per mm travelled by the tool. Therefore, it is reasonable to see increases in maximum strain (from 3.2 to 3.9) and maximum strain rate (from 69 to 97 s^{-1}).

5.3.4 Uncertainties Analysis

In the last section we have introduced a novel method of calculating the strain and strain rate experienced by the material ahead of the pin based on tracing a deforming dendrite. This is the first attempt of estimating strain and strain rate based on directly observing the real-time pin/workpiece interface. However,

several factors must be thoroughly considered in order to understand the uncertainties associated with the estimated values of strain and strain rate.

Referring to Figure 5-6, the deformed dendrite trunk (Object 2 and Curve 1) could be traced quite well. The non-deformed end of dendrite seems to suggest that the original dendrite is approximately parallel, thus slightly misaligned, with the tool travel direction. However, the actual misalignment cannot be determined, and therefore we have introduced an error by assuming the original dendrite is perfectly parallel with tool travel direction.

We will present an analysis of how this uncertainty would affect the strain and strain rate calculation in conjunction with Figure 5-11 below. Let's assume that trunk "A" has been "incorrectly" located, and trunk "A" in the figure was used for the estimation of strain and strain rate. Let's further assume that the correct orientation of the original trunk should have been placed as represented as "B" in Figure 5-11. It is important to note that the length of "B" in Y–direction is the same as that of "A". Due to the uncertainty of determining the orientation of the original trunk, we have introduced an error, resulting in placing "A" as the original trunk rather than placing correctly as "B". In the present case shown in the figure, this uncertain angle is 20 degrees. An uncertain angle of 20 degrees is not small.

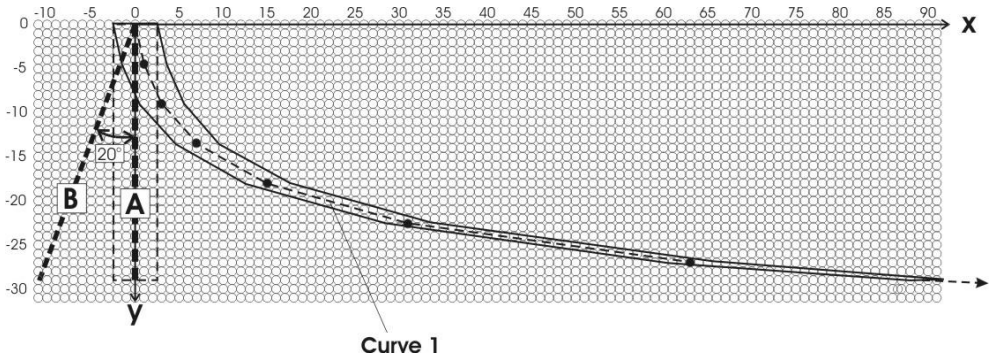

Figure 5-11. Illustration of the uncertainty involved in determining the original orientation of the dendrite, assuming Trunk "A" is incorrectly located and Trunk "B" is the corrected one.

After this correction, the length of (a portion of) the original dendrite (l_{ob} or Δl_{ob}) can be calculated as:

$$\Delta l_{ob} = \frac{\Delta l_{oa}}{cos\,20°} = \frac{\Delta y}{cos\,20°} \qquad \textit{Equation 5-5}$$

The local strain calculation for case "A" was given previously (Equation 5-2), and by following that, the strain for case "B" can be estimated as:

$$\varepsilon_b = \ln\left(\frac{\Delta l}{\Delta l_{ob}}\right) = \ln\left(\frac{\sqrt{\Delta x^2+\Delta y^2}}{\Delta y/\cos 20°}\right)$$
$$= \ln\left(\frac{\sqrt{\Delta x^2+\Delta y^2}}{\Delta y}\right) + \ln(\cos 20°) = \varepsilon_a - 0.06$$

Equation 5-6

Thus, the absolute error in the estimated strain is 0.06, a small value in comparison to the range of strain values estimated for the high deformed region (up to 3.2).

We now estimate strain rate for case "B":

$$\dot{\varepsilon}_b = \frac{\Delta\varepsilon_b}{\Delta t} = \frac{\Delta[\varepsilon_a+\ln(\cos 20°)]}{\Delta t} = \frac{\Delta\varepsilon_a}{\Delta t} = \dot{\varepsilon}_a$$

Equation 5-7

Thus, the estimation of strain rate is not affected by that uncertain angle. The reason for the estimated strain and strain rate within a short distance towards the thread space not being sensitive to the uncertainty of the original dendrite orientation, as explained in previous section, is due to the increasingly large shear within that short distance.

To briefly summarize: the segregation between RSM zone and the rest of nugget zone, as observed from the cross sections of FSP A356 samples produced with a wide range of speeds (Figure 4-2 and Figure 4-3), is related to the segregation in material depositions; the deposition of RSM occurs primarily at the trailing-advancing side of the pin, thus forming a portion of the nugget; the rest of the nugget is formed by the material which has been dragged by the depositing RSM, thus only experienced slight deformation. This explains the reason why a "Non Ring" nugget forms during FS of this alloy. The strain and strain rate in the transient flow zone (closely ahead of pin) can be estimated by tracing the deformation of the dendrites; under commonly used FSP conditions (710 rpm, 112–160 mm/min), the strain and strain rate are in the range of 3.2–3.9 and 69–97 s^{-1} respectively. These values and the process of evaluation, for the first time, have provided a more direct and insightful view of strain and strain rate during FS.

Chapter 6. Recrystallization and Texture Evolution during FSP A356 Alloy

In previous chapter, the macro-scale material flow and micro-scale material deformation (strain and strain rate) during FSP A356 have been examined. As detailed in Chapter 1, the transient microstructure development (closely ahead of pin) during FSP A356 (which contains non-deformable Si phase in a deformable α(Al) matrix) has not been well studied. This issue will be addressed in the current chapter. Specifically, the deformation induced recrystallization, the mechanical breakage and redistribution of Si particles, the subsequent texture evolution and its relationship with macro-scale material flow will be identified and characterized by examining the pin/workpiece sample using SEM and EBSD technique.

6.1 Grain Refinement ahead of Pin during FSP A356

A complete series of EBSD study was conducted on one of the "broken pin" samples (shown in Figure 5-5b) in order to reveal the details of microstructure and texture evolutions around the pin during FS A356. Locations examined under EBSD are summarized in Figure 6-1: with E2–E5 in the leading transition zone, E6 in the leading RSM zone, E7–E8 in the trailing advancing RSM zone, E9–E10 in the trailing advancing deposition zone, E11–E12 in the leading advancing RSM zone, E13–E14 in the retreating RSM zone, and E15 in the trailing deposition zone respectively. E1 locates far ahead of pin where no deformation has been introduced, and it is not included in Figure 6-1.

6.1.1 As-cast Structure

SEM image of the as-cast A356 is given in Figure 6-2a, where the highly segregated structure, i.e. Al-Si eutectic surrounded by α-Al dendrites, can be easily identified. The silicon particles are very coarse, some of which have length greater 20 μm. An EBSD scan (E1) has been obtained from this SEM image, and the Orientation Map (OM) and {111} Pole Figure (PF) of aluminium are given in Figure 6-2b and c

respectively. From this point onward, PF refers to the {111} PF of aluminium unless otherwise stated.

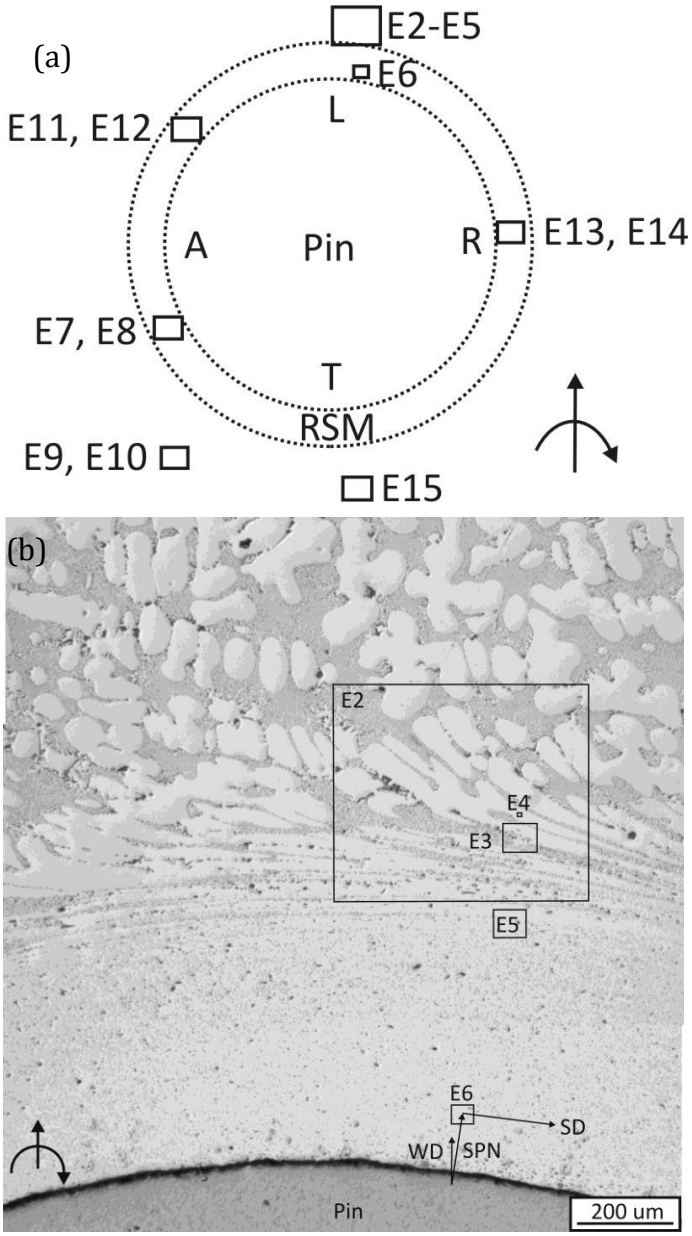

Figure 6-1. (a) Locations examined under EBSD with reference to the pin. Sample obtained using ω = 710 rpm, and v = 112 mm/min. Drawing not to scale. (b) Enlarged view of E2–E6, drawing to scale.

First of all, by comparing the OM to the SEM image, silicon particles are well outlined, although some shadows exist below silicon particles because they stand higher compared to α-Al dendrites. The OM has an overwhelming red-pink colour which demonstrates that the <100> axes of the Al dendrites are (close to) parallel to the direction of observation, which is the ND (refer to Figure 1-35c for sample

reference frame). Referring back to Figure 2-3, the heat flow direction (during casting of A356 ingot) is perpendicular to sectioned A356 plates. As introduced in Section 1.2.1, the dendrite growth direction of cube metal (e.g. Al) is along <100> directions, which have a tendency to align with the heat flow direction. Therefore, the <100> directions are perpendicular to the sectioned A356 plates. Thus, in Figure 6-2a, the <100> directions are parallel to the observation direction (ND), which explains the overwhelming red-pink colour in OM.

By comparing Figure 6-2c to Figure 1-36, the PF of as-cast A356 clearly demonstrates a "Cubic" texture ({100}<001>). This is because due to directional solidification, the <100> poles are parallel ND, which implies that {100} planes of the A356 are parallel to the equivalent shear plane of the FSP frame (Figure 1-35b). On the other hand, the directions of the silicon particles are relatively random, e.g. some silicon particles (green) in the upper part of Figure 6-2b have <110> axes parallel to eye sight, i.e. the normal direction (ND) of the sample; while a few large silicon particles (red) in the lower part of the figure have <100> axes parallel to eye sight.

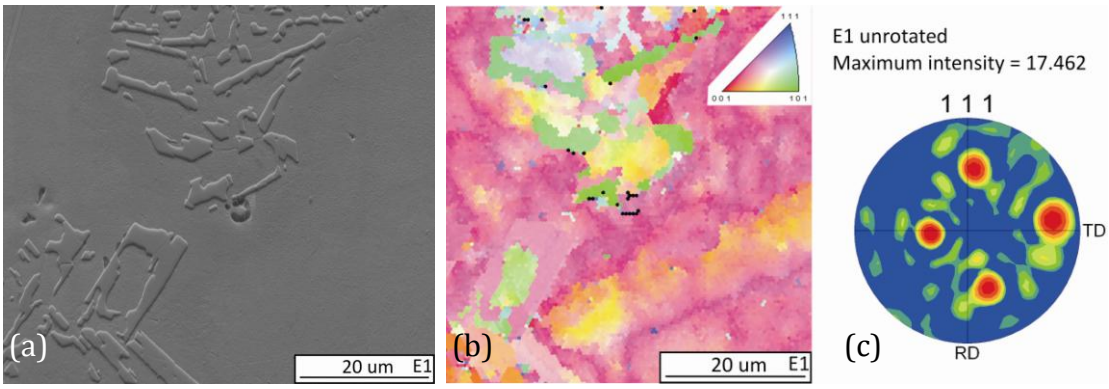

Figure 6-2. (a) A SEM image was taken from a location far away from pin where no deformation has been introduced. OM (scan step = 0.5 μm) and {111} pole figure (aluminium only, silicon not included) of that location are been given in (b) and (c) respectively.

6.1.2 Deforming Dendrites and Recrystallization

Figure 6-3 shows the OM of a relatively large area (up to 370 μm) in front of the RSM zone ahead of the pin. As can be seen, workpiece locates 58 μm from the RSM zone boundary has already completely recrystallized. Further away from the RSM

zone, the coarse α-Al dendrites are sheared towards the retreating side (right hand side) of the pin, and they become increasingly thinner (one example is indicated by the black arrows), which suggests a gradually intensifying shearing effect. However, the seemingly large shearing effect has not caused the dendrites to become fully recrystallized because the overall pink-red colour indicates that the as-cast orientation remains. On the other hand, the Al-Si eutectic which resides between dendrites displays a fully recrystallized morphology. This can be observed even at the top of Figure 6-3 where the dendrites have been only slightly deformed.

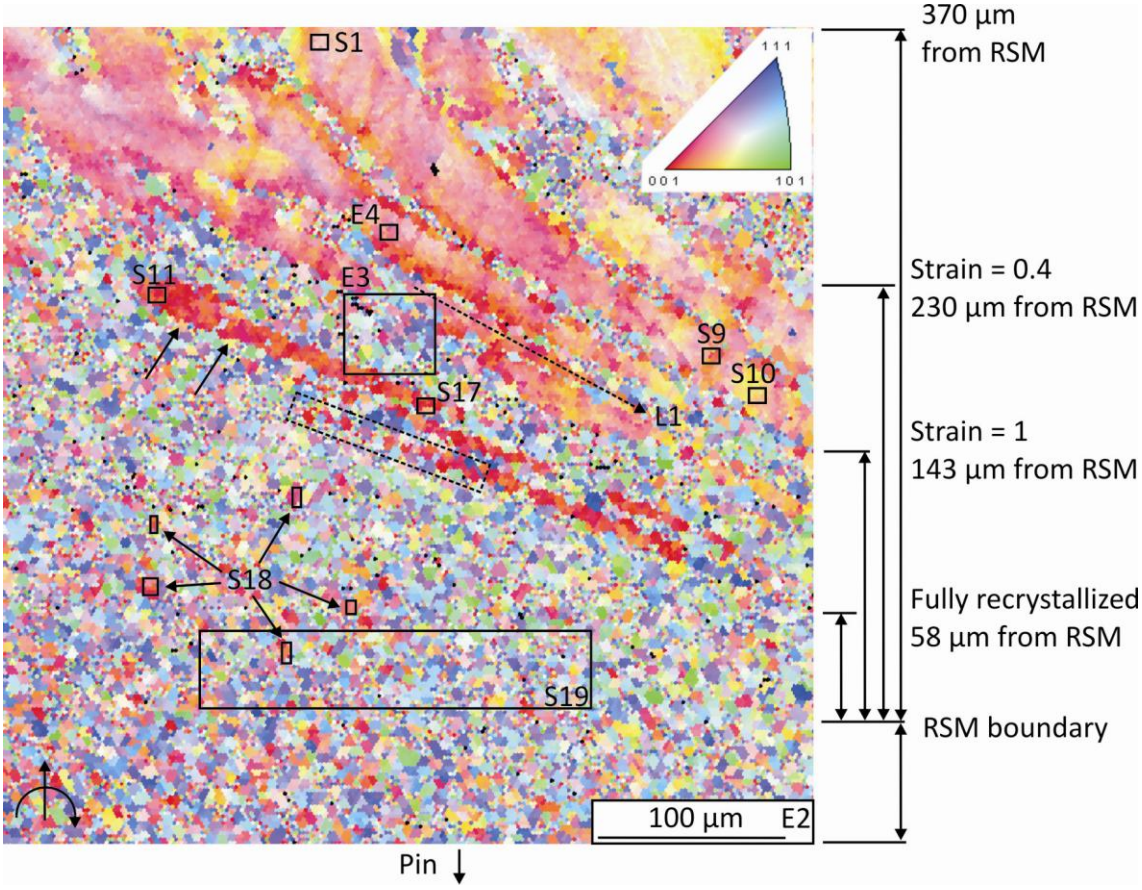

Figure 6-3. OM of position E2, which locates up to 370 µm from the boundary of RSM ahead of the pin. A scan step of 2 µm was used.

Let us take the location 143 µm ahead of the RSM zone boundary as an example: severe thinning of the dendrites and fully recrystallized fine grains between them can be clearly identified. Referring back to the strain and strain rate calculation (Figure 5-10), the macroscopic strain experienced by the dendrites is approximately 1 (Y = 17 units), and strain rate around 20 s^{-1}. However, aluminium

in the Al-Si eutectic region must have experienced much larger strain (>> 1.0) and strain rate (>> 20 s^{-1}) which causes recrystallization occurring much earlier compared to adjacent primary dendrites. This is due to the strain incompatibility between soft Al and hard Si particles, and will be discussed in more detail in the following paragraphs.

The thinner dendrites also tend to have more wavy boundaries compared to the thicker dendrites which are located relatively far away. The existence of wavy boundaries indicates that thermally activated grain boundary migration has occurred. The continuing thinning and elongation, due to geometrical constrains, may cause wavy boundaries impinging with each other once the distance between adjacent boundaries reach one subgrain size. This process thus generates fine equiaxed grains with HAGB. Such recrystallization phenomenon can be observed in the current study: several newly formed fine equiaxed grains (separated from the severely elongated dendrites) are included in the dashed black box (Figure 6-3). This strongly indicates that the grain refinement process of the coarse dendrites can be regarded as Geometrical Dynamic Recrystallization (GDRX). GDRX during hot deformation has been previously introduced, and it is the major recrystallization mechanism during FS AA2195 alloy [14]. Furthermore, it is clear that the elongated dendrite retains its as-cast orientation even though grain impingement has occurred on some portion of its boundaries. This retention of the original orientation is a common feature during GDRX.

The orientation of the deforming dendrites will be studied in more detail here. We first select a small portion of the deforming dendrite (position E4 as in Figure 6-3), where no recrystallization can be identified. OM and {111} PF of a position E4 are given in Figure 6-4a and b respectively. The as-cast coarse dendritic structure (with <100> axes parallel to observation direction) can be identified in Figure 6-4a, where subgrains (with their orientations slightly different from each other) can be easily observed. Correspondingly, a sharp “Cubic” texture is displayed in Figure 6-4b.

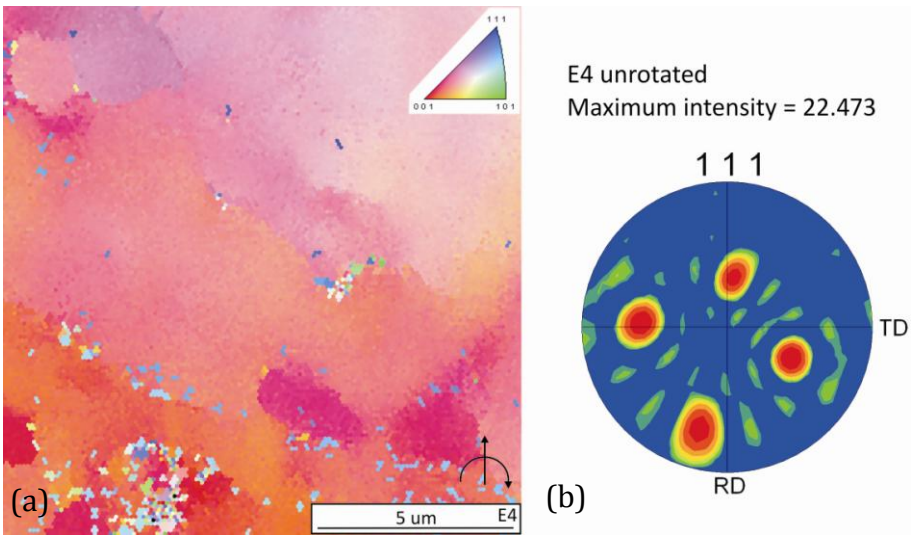

Figure 6-4. OM (a) and {111} PF (b) of a small portion of deforming dendrite (E4), as indicated in Figure 6-3. Scan step = 0.1 μm.

Let us further examine the PFs along two deforming dendrites. Ten small areas (S1–S10) were selected from a large dendrite relatively far away from the RSM zone, as indicated by Figure 6-3. S1 is located at the top portion of the dendrite where deformation is not apparent; while S10 is located at the lower end of that dendrite where fairly significant thinning has occurred. Only S1, S9 and S10 are indicated, areas S2 to S8 are located with equal spacing between S1 and S9. Similarly, 7 small areas (S11–S17) were selected from a dendrite which has been severely deformed. Area S17 marks the end of that dendrite, and fully recrystallized grains can be indentified to the right of S17. The PFs of S1, S9, S11, and S17 are given in Figure 6-5. In general, clear "Cubic" textures can be identified along the two deforming dendrites, indicating the change in strain level alone does not cause texture change. At area S17, the dendrite is thinned to an extent that the width reaches approximately one subgrain size. At this location, GDRX is about to occur or has just occurred. The corresponding texture still displays a fairly strong "Cubic" component, although the recrystallization surrounding S17 clearly dilutes the "Cubic" component. As such, the intensity of the PF drops significantly: from ~ 27 to ~ 21.

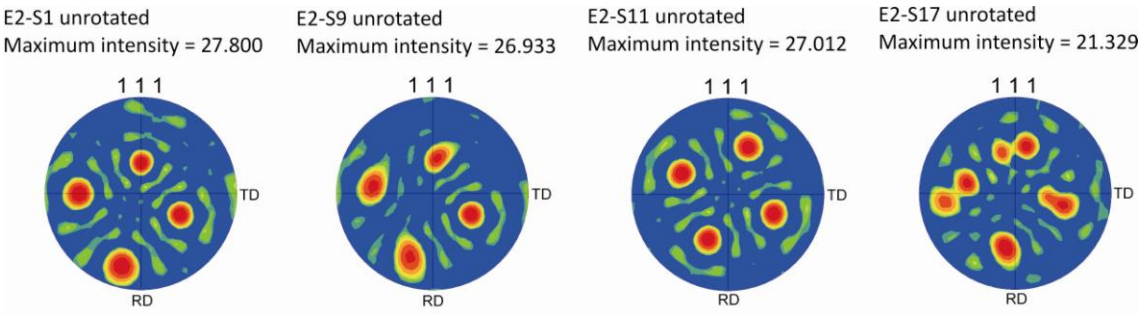

Figure 6-5. {111} PFs of selected areas S1, S9, S11 and S17 from two deforming dendrites in location E2 (Figure 6-3).

On the other hand, if CDRX was operational, it involves a gradual increase in misorientation due to subgrain rotation, which eventually develops HAGBs. A misorientation line scan (L1 in Figure 6-3) was conducted along a deforming dendrite. At the beginning of the dendrite, the macroscopic strain is approximately 0.4, and at the end of the dendrite, the strain is slightly less than 1. The increase in strain is justified by the reduction in the width of the dendrite. The end of L1 has gone slightly beyond the dendrite, thus entering into the fully recrystallized region. The recrystallized grains locating at the end of L1 are (likely) formed by GDRX mechanism.

Point-to-point and point-to-origin (accumulative) misorientation plots along L1 are given in Figure 6-6. As can be seen, along the dendrite (up to 100 μm), point to point misorientation is consistently small and therefore the accumulative misorientation from the start to the end of the dendrite is approximately 23°. Beyond 100 μm, thus entering into the recrystallized region, the point-to-point misorientation (and thus the accumulative misorientation) suddenly increases, indicating the existence of HAGBs. It is clear that the increase in point to point misorientation is far from being gradual. Furthermore, it is also clear that the increase in strain (from 0.4 to ~ 1) does not increase the point-to-point misorientation, which remains consistently low, along the deforming dendrite. These observations suggest that the deformation and subsequent recrystallization of the dendrites are not caused by CDRX but rather GDRX.

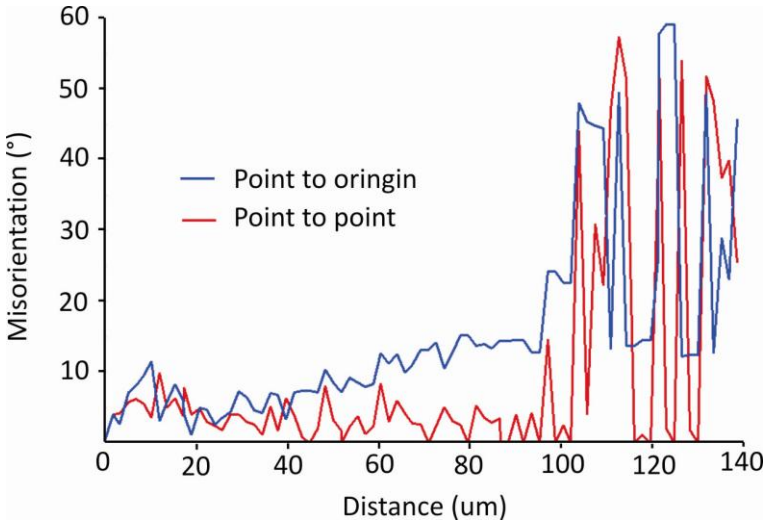

Figure 6-6. Misorientation plot of the line-scan (L1) performed on a deforming dendrite as indicated in Figure 6-3.

Referring back to Figure 6-3, the large dendrites are just thinned into strings of individual grains due to GDRX. It is apparent that some grains retain the as-cast orientation after GDRX, i.e. appear red/pink in the OM. These grains can also be found at regions very close to, or within, the RSM zone, where they mix thoroughly with recrystallized eutectic Al grains and broken down Si particles. A few of these grains were selected, indicated by S18, and their PF is given in Figure 6-7a. On the other hand, a large portion of the fully recrystallized region (very close to RSM zone) was also selected (S19) for examination. The PF of S19 is given in Figure 6-7b. It is clear that the grains, although recrystallized, with the as-cast appearance still display a very strong "Cubic" texture, i.e. the original texture. On the other hand, the region ahead of the RSM zone displays an overall "A" shear texture, which is commonly seen during hot torsion testing of Al alloys. It is important to note that the maximum intensity of area S19 (4.005) is significantly lower than that of area S18 (21.755). This is reasonable as S19 contains some grains which retain the as-cast texture and significantly more grains which have developed the "A" shear texture, thus resulting in an overall "A" texture with relatively low intensity. The development of the "A" texture will be discussed in more details in the next section.

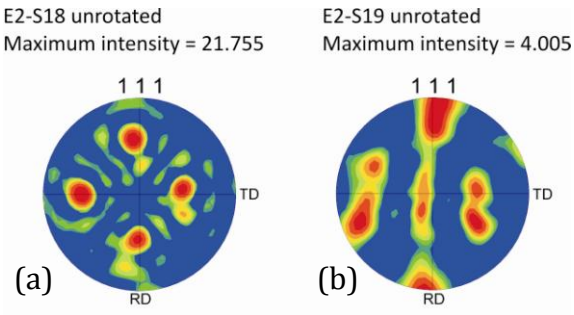

Figure 6-7. PFs of areas S18 (a) and S19 (b) in location E2, as indicated in Figure 6-3.

6.1.3 Deformation of Al-Si Eutectic

The deforming dendrites and Al-Si eutectic region (area E3 in Figure 6-3) will be examined in more detail and the corresponding OM and SEM are given in Figure 6-8 and Figure 6-9 respectively. In the OM, silicon particles are marked as black. Furthermore, the Grain Boundary Map (GBM) is given alongside the OM, where HAGBs and LAGBs are represented by black and grey lines respectively.

A number of features can be revealed by comparing the two figures. Firstly, Si particles reorientate to accompany the macroscopic shear flow direction. This is similar to the shear deformation of composite materials with non-deforming particles [123, 124].

Secondly, Si particles, particularly the large ones, are fragmented. An example of this is evident in a Si particle in the top left of Figure 6-9 which has broken into two (indicated by the arrow). This is also in common with the cracking of Si particles during plastic deformation of this alloy [125].

Thirdly, α-Al in the original eutectic regions is fully recrystallized while partially recrystallized/recovered in the deforming dendrites (indicated by the formation of subgrains). The formation of subgrains (with LAGBs which appear grey) within the large deforming dendrites can be clearly observed in the GBM, as indicated in Figure 6-8. Such observation has already been mentioned earlier. This is because, as Si particles are non-deforming, surrounding α-Al is needed to strain considerably more so that the total strain in that local eutectic region is the same as the strain in adjacent dendrites. This strain incompatibility between Al grains

and Si particles is commonly seen during equal channel angular pressing of A356 alloy [112].

Fourthly, looking closer at the Al-Si eutectic region where fine Si particles are rather closely packed, the fully recrystallized Al grains are 2–4 μm in size. However, slightly outside the eutectic region where fewer coarse Si particles are located far away from each other, the recrystallized Al grains are significantly coarser, mostly ranging from 5–10 μm. Thus it is clear that the grain size in the eutectic region is strongly influenced by the distribution of Si particles (which are very hard and non-deformable), i.e. closely located Si particles severely constrain the size of the recrystallized Al grains.

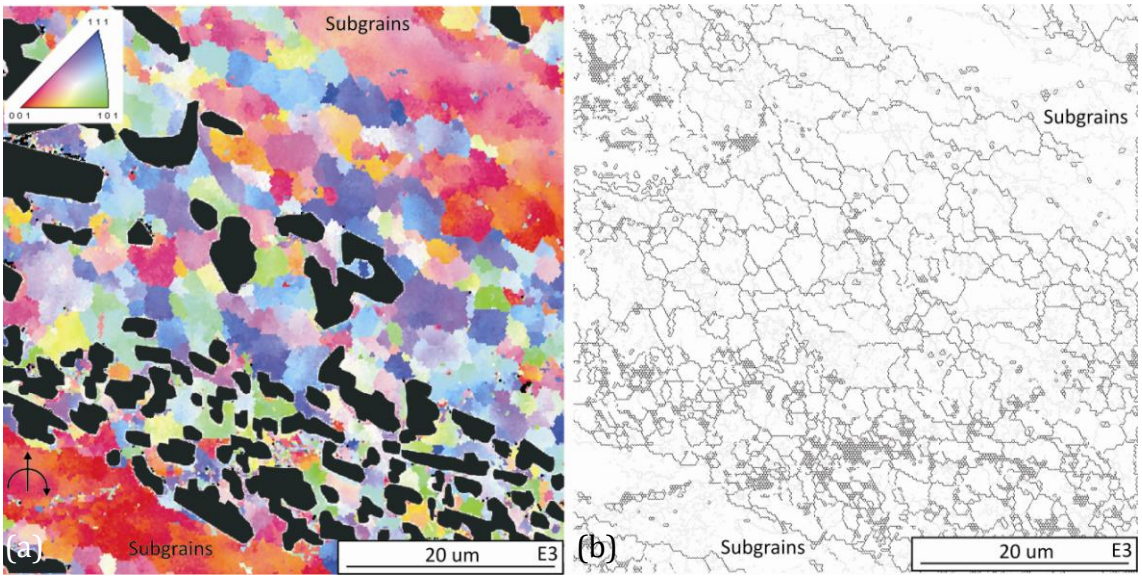

Figure 6-8. OM and GBM of position E3, which locates 0.7 mm ahead of pin. Silicon particles have been marked black in the OM, HAGBs are in solid black line, while LAGBs are in grey line. A scan step of 0.25 μm has been used.

The previous observation can be further illustrated by examining the {111} PFs of the deforming dendrites and Al-Si eutectic, as given in Figure 6-9. Three areas S1–S3 were selected, with S1 and S2 from deforming dendrites where no recrystallization can be identified, and S3 from eutectic α-Al where recrystallization seems to be intensive. The PFs of S1 and S2, as can be expected, demonstrate a strong "Cubic" texture (as-cast texture). However, the existence of non-deforming Si particles has greatly accelerated the deformation and subsequent recrystallization of Al in the eutectic region and thus the PF of S3

shows a fairly dominating “A” shear texture ({111}<110>). To obtain a standard “A” texture, the PF of area S3 must be rotated by (–5°, 0°, –10°) around (ND, TD, RD) respectively.

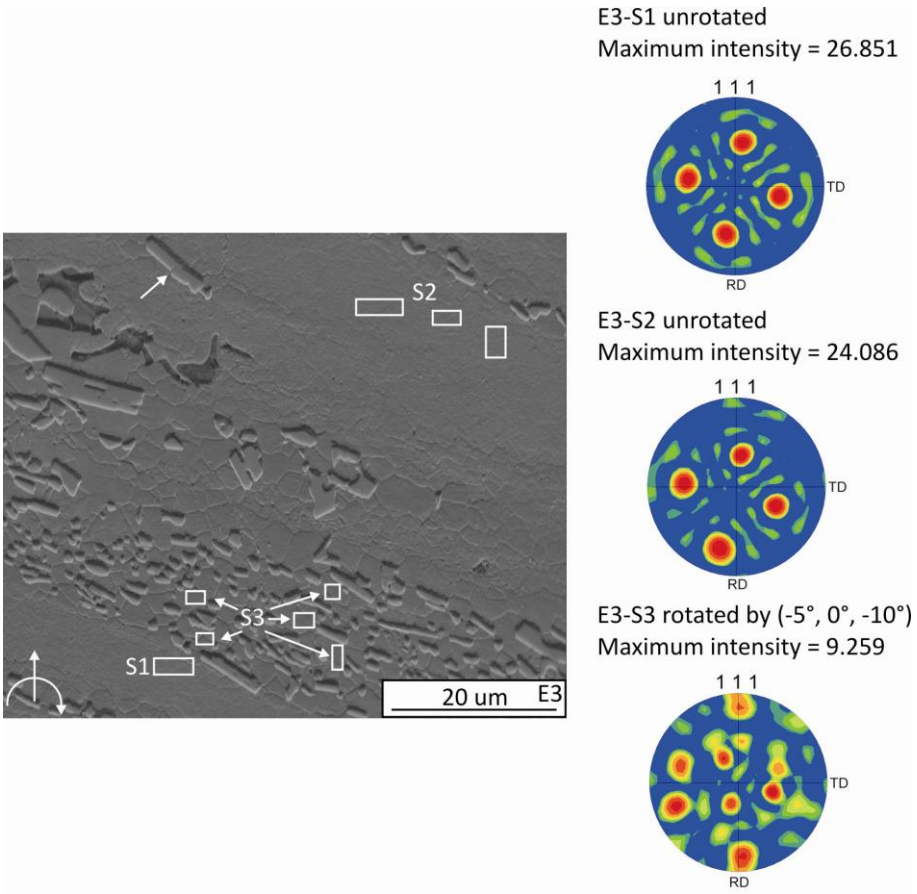

Figure 6-9. SEM image of position E3 (at L side of pin), with selected areas (S1–S3) examined under EBSD. Areas S1 and S2 are from Al dendrites, where no obvious recrystallization can be identified (as indicated by cubic texture). Area S3 is from deformed eutectic area, where Al has been extensively recrystallized (as indicated by “A” texture).

The “A” shear texture which is firstly developed in the Al-Si region, later becomes the dominant texture of the fully recrystallized region (S19). It is likely that as the recrystallized eutectic and dendrites become thoroughly mixed before entering the RSM zone, the former retains the “A” shear texture, while the later retains “Cubic” texture. Furthermore, the texture of the recrystallized dendrites Al grains (“Cubic”) could be influenced by adjacent eutectic Al grains (“A”), causing the texture transitioning from the “Cubic” texture to the “A” texture. Therefore the overall texture of the recrystallized region is dominated by the “A” component.

6.1.4 RSM Zone around Pin

The SEM images of a portion of newly formed RSM, which locates near the boundary between the transition zone and RSM zone (E5, as given in Figure 6-1b), and RSM around (very close to) the pin (E6, E8, E12, and E13) are given in Figure 6-10a to e respectively.

As illustrated above, at location E3, the effective strain (ε) was estimated to be slightly less than 1. The shear deformation gradually intensifies by moving closer to the pin. E5 (Figure 6-10a) locates at the boundary between the transition zone and the RSM zone, where the shear strain has increased to 3.2. It can be observed that the significant increase in strain causes intensive breaking up of Si particles (mostly 1–3 μm, with a few large ones up to ~ 10 μm). Therefore, Si particles at the boundary of the RSM zone (E5) tend to have lower aspect ratios, compared to those in the transition zone (E3). Furthermore, a high degree of mixing of recrystallized Al grains (mostly 3–5 μm) and Si particles with low aspect ratio is also resulted in E5.

In the transition zone, the size of the recrystallized grains is 2–4 μm and 5–10 μm inside and outside the eutectic region respectively (Figure 6-8 and Figure 6-9). It is thus likely that, after the thorough mixing of the eutectic regions with dendrites, the distance between adjacent Si particles is approximately uniform in the boundary of the RSM zone (E5). As such, the already recrystallized Al grains will experience further growth (increasing grain size) or deformation (reducing grain size) in order to accommodate the distribution of Si particles.

Further into the thread space (E6), the morphology of the RSM does not alter significantly, except the Al grains may have coarsened slightly and Si particles are more evenly distributed. Such observation is clearer by comparing the OMs and GBMs of locations E5 and E6 (Figure 6-11a and b). It has been previously suggested that once the material has entered the thread space and rotated around the pin, there seems to be no significant strain being further introduced. Such suggestion can be justified by the fact that the grains have coarsened at a location

closer to the pin (E6), which is likely due to static annealing effect. The removal of some HAGBs also indicates static recrystallization has occurred.

RSM locates at the leading advancing side (E12), and trailing advancing side (E8) of the pin display similar morphologies. Comparing E6, E8, and E12, it is apparent that the size of the recrystallized grains in these locations varies very little from one another. After the previous discussion, it is reasonable to state that the pin transportation of the RSM, through LA side (E12) and L side (E6) to TA side (E8), does not seem to alter the sizes of Al grains and Si particles to a noticeable extent.

However, the RSM zone locates on the retreating side of the pin (E13) displays some rather unique features. Firstly, the silicon particles seem to be smaller and have larger aspect ratios compared with those in other locations (E5, E6, E8, and E12). It seems that the small Si particles (1–3 μm) which are observed at those locations have reduced their width thus having a "short-needle" shaped morphology at location E13. Some of them are less than 1 μm long. The surfaces of the relatively large Si particles (5–10 μm) are "smoother" and "curvier" at E13, as opposed to the commonly observed rather straight boundaries. This feature is particularly clear at the ends of the Si particles. Furthermore, some of the large Si particles become hollow at the central regions.

It is possible that this small area of material (E13) sticks to the pin, thus it has rotated with the pin for several revolutions. As a result, this material has been exposed to high temperature for a relatively long period of time. Referring back to Table 4-1, the maximum temperature ahead of pin during a FSP performed under v = 112 mm/min and ω = 710 rpm is 534.0 °C, which is quite close to the equilibrium eutectic temperature of Al-Si alloy, which is 577 °C (Figure 1-3). As indicated in the Al-Si phase diagram, during non-equilibrium solidification, the Si solute level in the Al dendrites is below that of equilibrium condition. Hence, more eutectic Si particles are formed during non-equilibrium solidification compared to equilibrium solidification. It might be proposed that by exposing A356 (at E13) to high temperature for a relatively long period, part of the Si particles, especially the

outer portions, will diffuse into the Al matrix, resulting in the needle shaped Si particles.

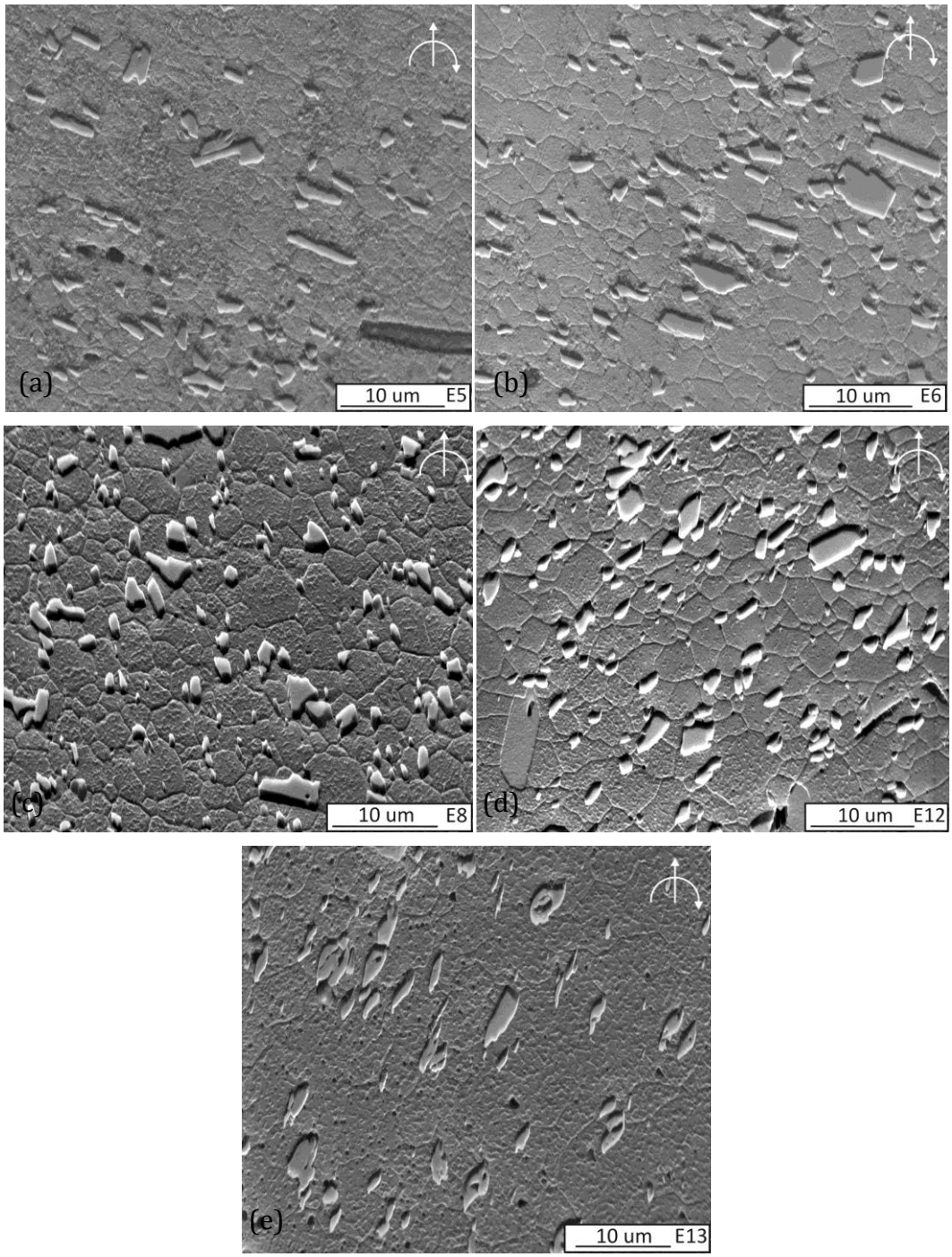

Figure 6-10. SEM images of locations (a) E5, (b) E6, (c) E8, (d) E12, and (e) E13.

On the other hand, the recrystallized Al grains are obviously larger (up to 10 μm in grain size) than those in other locations (3–5 μm in grain size), which is likely caused by significant static annealing effect during or after FSP. Such observation

is clearer in the OM and GBM taken from the location E13 (Figure 6-11e). It can be clearly seen that the size of recrystallized Al grains and the fraction of LAGBs (associated subgrains formation) has clearly increased.

The OMs, GBMs and PFs of E5, E6, E8, E12 and E13 are shown in Figure 6-11a to e respectively. All OMs and GBMs indicate that the aluminium is fully recrystallized, i.e. equiaxed grains with HABGs have been developed. PFs of the entire scan and selected areas (S1 in each scan) where no Si particles are included, which indicate that the recrystallized Al grains within thread spaces have a strong "A" shear texture ({111}<110>), except for the RSM on the retreating side, which displays a "Cubic" texture (the as-cast texture).

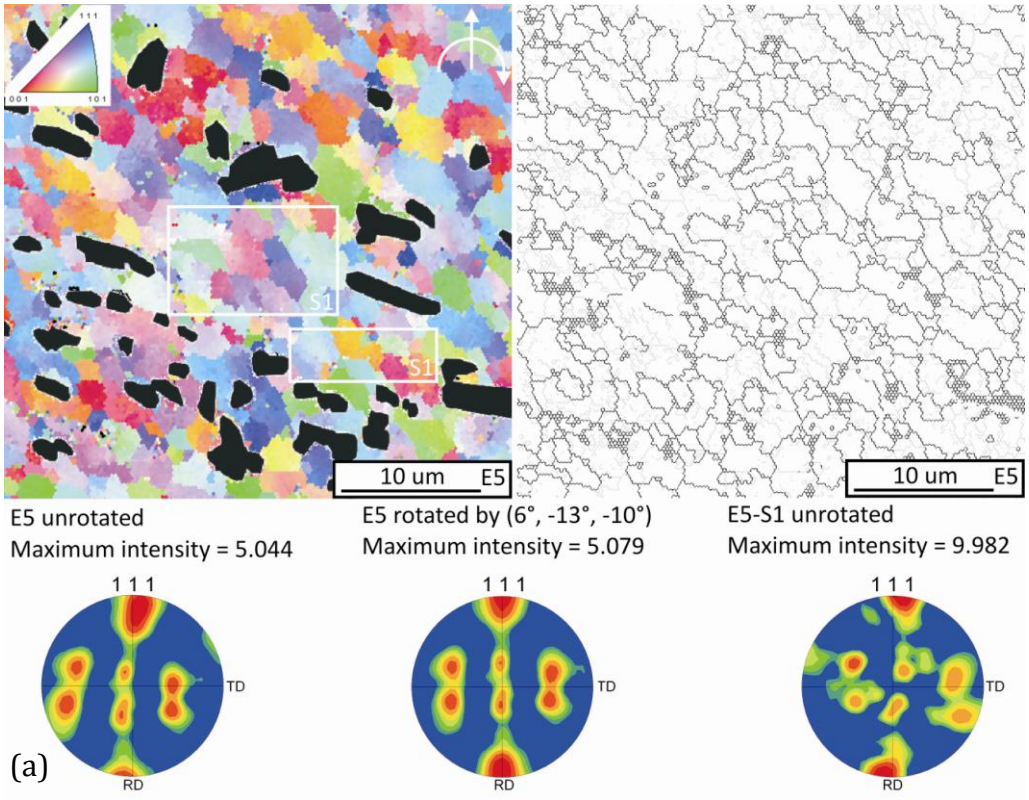

Figure 6-11. OMs , GBMs and PFs (both original and rotated) of locations (a) E5, (b) E6, (c) E8, (d) E12 and (e) E13. A scan step of 0.25 µm has been used for all EBSD scans. Silicon particles are marked black in OMs. Selected areas are denoted by "S".

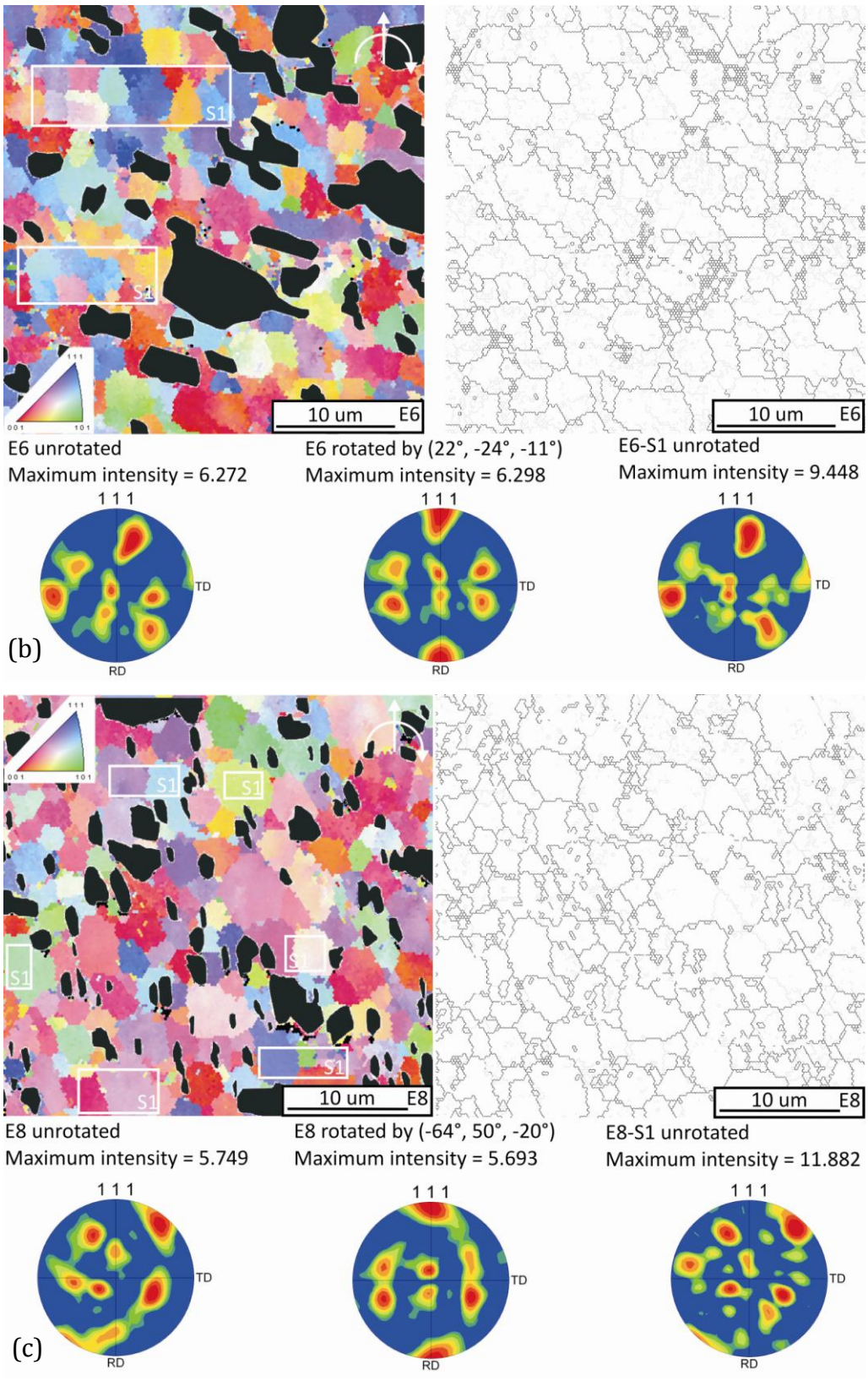

Figure 6-11. Continued.

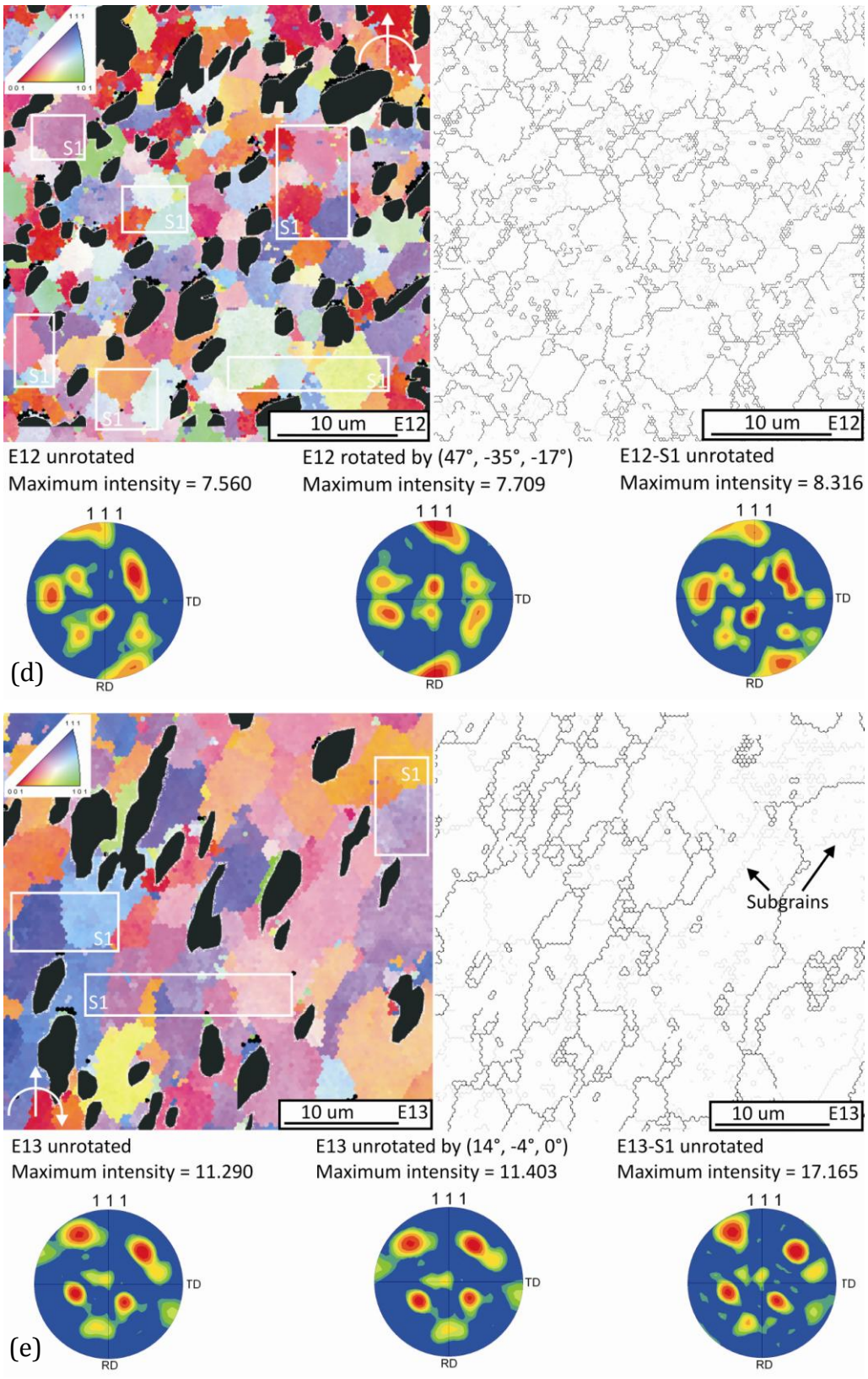

Figure 6-11. Continued.

Thus, it is clear that the “A” texture, which first appears in the transition zone ahead of pin, is stable after entering the RSM zone and being transported around the pin. The rotation flow around the pin does not seem to induce fundamental change to the deformation texture. In order to achieve a standard “A” texture, PFs of E5, E6, E8, and E12 must be rotated by (6°, –13°, –10°), (22°, –24°, –11°), (–64°, 50°, –20°), and (47°, –35°, –17°) around the (ND, TD, RD) respectively.

Suhuddin et al. [111] performed FSP experiments on 2 mm thick AA6016 alloy with rotation speed of 3000 rpm and linear speed of 2000 mm/min. Stop-action technique was used to obtain pin/workpiece couple during the experiment. It is observed that the “B” shear texture is the major deformation texture around the pin region. However, at the wake of the pin, they observed the transition from “B” texture to the “Cubic” texture, which is the (fully recrystallized) texture of the base material. It was suggested that the formation of “B” texture is associated with the deformation and subsequent recrystallization induced by pin flow. However, the shoulder flow, which is most intensive at the back of the pin, might cause the already recrystallized material undergoing further deformation, thus causing a transition in texture, i.e. from “B” to “Cubic”.

In the present case, however, the RSM locating on the retreating side of the pin (E13) does not seem to experience a different flow regime compared to the RSM locating at other locations (E6, E8, and E12) around the pin. Thus, it is expected the PF of E13 should also be an “A” texture. Hence, the transition from “A” texture to “Cubic” texture might be due to the excessive static annealing effect occurring at location E13, which is justified by the fact that the fine-recrystallized grains have grown substantially at E13. As discussed previously, the RSM region contains Al grains which retain the original “Cubic” texture and Al grains with the “A” shear texture (refer to Section 6.1.2 and location S18 and S19 in Figure 6-3). Therefore, it can be suggested that if significant static annealing has occurred, the “A” shear texture will be replaced by the more stable “Cubic” texture. The formation of “Cubic” texture due to static recrystallization of cubic alloys (Al, Cu and etc.) has been well established in literature [102, 103].

6.1.5 Deposited Material

As already illustrated in Figure 5-3c, a large portion of RSM detaches away from the pin, instead of continuously rotating with the pin, at the trailing advancing side (TA), due to the existence of a highly compressive zone ahead of the pin. Furthermore, the rest of RSM deposits on the trailing (T) and trailing retreating (TR) side of the pin. This portion of RSM also assists the as-cast material on the retreating side flowing towards the advancing side, causing a rounding flow. As already described in Section 5.1, material which has been dragged experiences overall less deformation compared to RSM, and thus the dendritic structure is still recognizable, especially on the TR side. Hence, the material on T and TR sides contains a mixture of the severely deformed RSM and the less deformed material which has been dragged by the depositing RSM.

The SEM images of the deposited material on TA (location E10) and TR (location E15) sides are given in Figure 6-12a and b respectively. Generally speaking, the morphology of the deposited RSM (E10) does not differ significantly with those around the pin (Figure 6-10). However, the recrystallized Al grains experience further static annealing, which is indicated by the overall growth in grain size: mostly ranging from 4–7 μm (compared to 3–5 μm at location E12 in Figure 6-10d), with some grains reaching 10 μm. On the TR side (Figure 6-12b), the mixing of RSM and the dragged (thus slightly deformed) as-cast structure is far from being thorough. The boundary between the deposited RSM (locates at the lower part of E15) and the dragged dendrites (locate at the centre of E15) can be clearly identified. Fully recrystallized Al with equiaxed morphology can be identified within the dragged dendrites region, despite the overall deformation caused by the drag flow is expected to be lower compared to the deformation experienced which leads to the formation of the RSM.

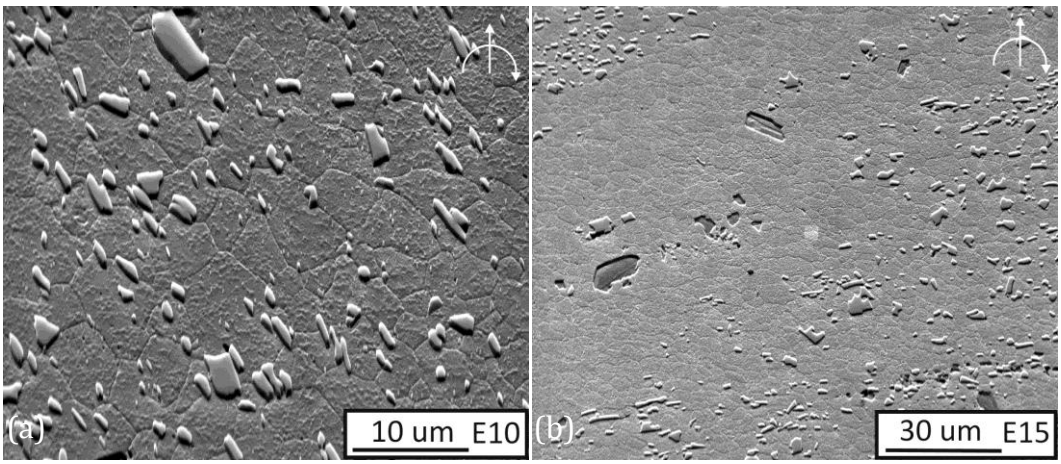

Figure 6-12. SEM image of locations E10 (a) and E15 (b).

OMs, GBMs and PFs of E10 and E15 are given in Figure 6-13a and b respectively. The OM and GBM of location E10 indicate that the deposited RSM on the TA side displays a fully recrystallized morphology, with high fraction of HAGBs. The deposited RSM on the TR side (upper and lower parts of E15) has similar morphologies. However, the recrystallized Al grains in the dragged dendrites region (central part of E15) display an overwhelming green colour which indicates that the <110> direction of the grains is parallel to the eye sight.

The PFs of the selected areas (marked by "S1") of E10 all show a very clear "A" shear texture. Furthermore, S1 and S2, which are chosen from the dragged dendrites region and deposited RSM region, also display a clear "A" shear texture. Thus, it can be suggested that the "A" shear texture, which is the dominating texture of the RSM zone around the pin, still persist after the deposition. The mild static annealing effect and the mixing of RSM and dragged material do not cause obvious change in the shear texture.

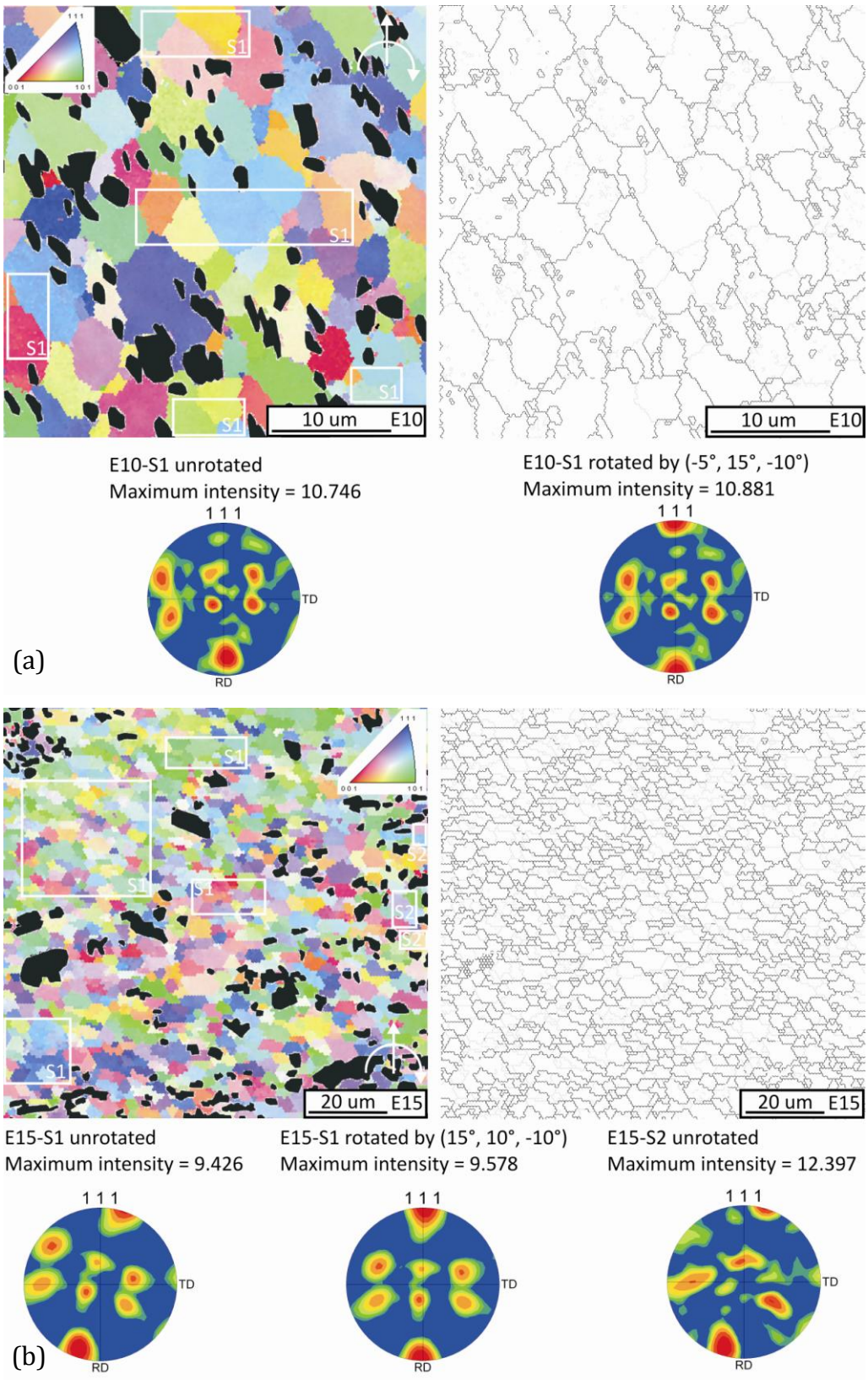

Figure 6-13. OM GBM and PFs of locations E10 (a) and E15 (b). Silicon particles are marked black in the OM. Selected area for examination is denoted by "S".

6.2 Texture Evolution

6.2.1 Texture Rotation and Material Flow

As previously discussed, "A" shear texture is first developed in the transition zone ahead of pin, it has remained stable after the material entering the thread space, rotating around the pin and depositing at the back. However, the "A" textures (with frame (r, θ, Z)) obtained at various locations must be rotated around the frame of the sample, i.e. (ND, TD, RD), by different amounts in order to obtain the standard "A" texture. This is because the shear frame, which is strongly dependent on the local pin shearing direction, misaligns with the sample frame, which is constant. Standard texture can only be obtained if the shear frame is rotated so that it completely aligns with the sample frame. In this section, the rotation of the shear texture, and how it is affected by the pin shear direction (thus the flow direction) will be addressed.

As introduced in the literature review, the rotating pin induces two major flow regimes: the simple shearing/extursion flow regime, and the screwing down flow regime. For a theoretical consideration: the shearing flow causes material to rotate around the ND, as illustrated in Figure 6-14a. If the material is located ahead of the pin centre (Figure 6-14b), the screwing down effect should only cause the rotation around TD; if the material is located on the advancing or the retreating side, the screwing down effect could only cause the rotation around RD (Figure 6-14c). Thus, the downward flow could cause rotations around both TD and RD if the material is located on the leading advancing side.

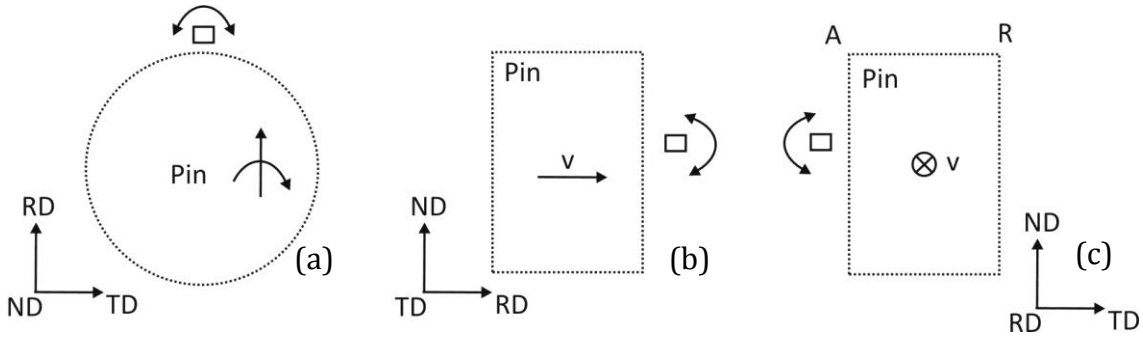

Figure 6-14. Schematic illustration of material rotation (a) due to pin shear effect, (b) and (c) due to pin screwing down effect.

The rotations required to obtain the standard textures at various locations around the pin are summarized in Table 6-1. Counter clockwise (CCW) rotation is positive while clockwise rotation (CW) is negative.

Table 6-1. Summary of rotations required to obtain standard textures at various locations around the pin.

Location	*ND*	*TD*	*RD*
E2–S1	–31	–16	–14
E2–S3	–31	–16	–12
E2–S5	–29	–16	–11
E2–S7	–29	–16	–11
E2–S9	–28	–13	–11
E2–S11	–22	0	0
E2–S12	–32	–7	–3
E2–S15	–36	–8	–3
E2–S17	–36	-8	–3
E5	6	–13	–10
E6	22	–24	–11
E8	–64	50	–20
E12	47	–35	–17

Deforming dendrites ahead of pin

Local PFs were examined at various locations (from E2–S1 to E2–S10, and from E2–S11 to E2–S17) along two deforming coarse dendrites, as indicated in Figure 6-3. The PFs of these locations are summarized in Figure 6-15, and all of them display a strong "Cubic" texture, i.e. the as-cast texture. In order to obtain the standard "Cubic" textures, the rotations around (ND, TD, RD) for S1, S9, S11 and S17 are (–31°, –16°, –14°), (–28°, –13°, –11°), (–22°, 0°, 0°), and (–36°, –8°, –3°) respectively (as summarized in Table 6-1).

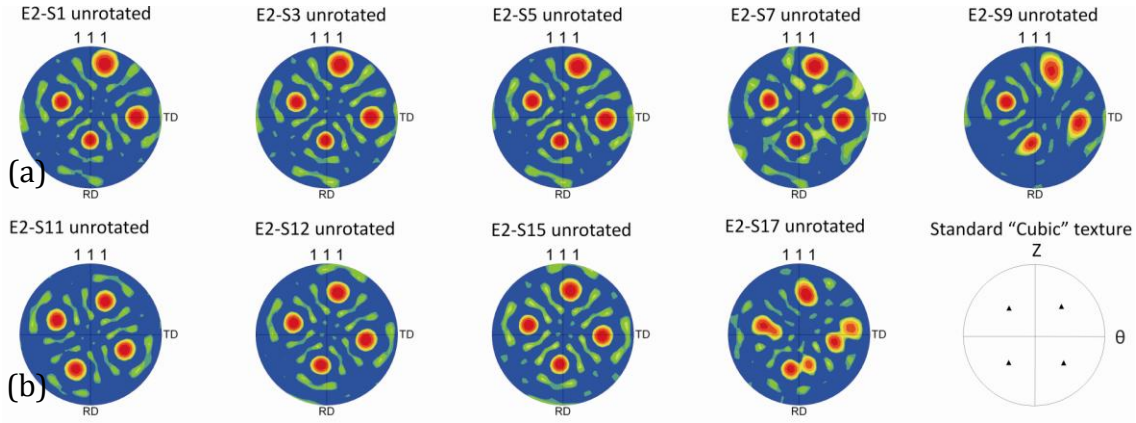

Figure 6-15. Selected unrotated PFs of locations (a) E2–S1 to E2–S10, and (b) E2–S11 to E2–S17. From S1 to S9, the PF has rotated around ND for 3° (CW); from S11 to S17, the PF has rotated around ND for 14° (CCW).

For the dendrite which is located further away from the pin, the rotation around ND at the beginning of the dendrite is –31° (E2–S1), and it has increased to –28° near the end of the dendrite (E2–S9). On the other hand, for the dendrite which is located closer to the pin, the rotation around ND has decreased from –22° (E2–S11) to –36° (E2–S17) from the beginning to the end of that dendrite. Hence, it can be suggested that from E2–S1 to E2–S9, rotation around ND increases by 3°, i.e. the orientation has rotated 3° CW from the beginning to the end of the dendrite. From E2–S11 to E2–S17, rotation around ND decreases by 14°, i.e. the orientation has rotated 14° CCW from the beginning to the end of the dendrite. These rotations can also be identified by comparing the PFs to the standard "Cubic" texture in Figure 6-15. It is clear that the dendrite closer to the pin experiences much more significant rotation around ND (14° along the dendrite) compared to the dendrite is located further away (3° along the dendrite). This is not surprising given that the shearing effect greatly intensifies as the pin approaches, which is the fundamental cause of rotation around ND.

As introduced in the literature review (Section 1.5.4) the rotation of a PF around ND is primarily dependent on the local pin shearing direction. Considering the two deforming dendrites ahead of the pin in the current case, the macroscopic shearing direction is the same, i.e. CW rotating pin results in shear towards the retreating side of the pin. Therefore, one should expect from the beginning (S1 and S11) to the end of the dendrites (S9 and S17), the PFs should gradually rotate CW around

ND. The CCW rotation around ND experienced by the dendrite nearer the pin might be explained as follows: the initial textures might have different susceptibility to the deformation, as previously described by Prangnell et al. [14], that despite the macroscopic shear direction is the same, subgrains/grains can rotate in opposite directions towards a stable orientation.

From Table 6-1, it is clear that from E2–S1 to E2–S9, and from E2–S11 to E2–S17, the rotations around TD and RD seem to be rather constant, except for the case of E2–S11. Specifically, for the dendrite which is located further away from the pin, the rotation around TD and RD range from –13° to –16°, and –11° to –14° respectively. As for the dendrite which is located closer to the pin, the rotation around TD ranges mainly from –7° to –8°, and rotation around RD is constant –3°. This is reasonable, as both dendrites are located relatively far ahead of the pin thread, where little downward flow is induced by the rotating pin. Hence, rotations around TD and RD, which are primarily influenced by the downward flow, have remained fairly constant along the deforming dendrites.

Rotating RSM around the pin

Now let us examine the rotations of PFs of the RSM around the pin (locations E5, E6, E8, and E12). These locations, and the suggested local shear directions (θ) and shear planes normal (Z) are given in Figure 6-16. In the current case, the theoretical shear direction (θ) is assumed to be tangential to the pin periphery. Therefore, θ is in line with RD on advancing and retreating sides of the pin, and it is in line with TD immediately ahead or behind the pin. Following this logic, it is expected that a location which is located at the middle (between advancing side and leading side) will have a PF in which the shear direction inclines 45° from the TD. Hence, a standard texture (of that location) can be obtained after a 45° rotation (clockwise) around the ND.

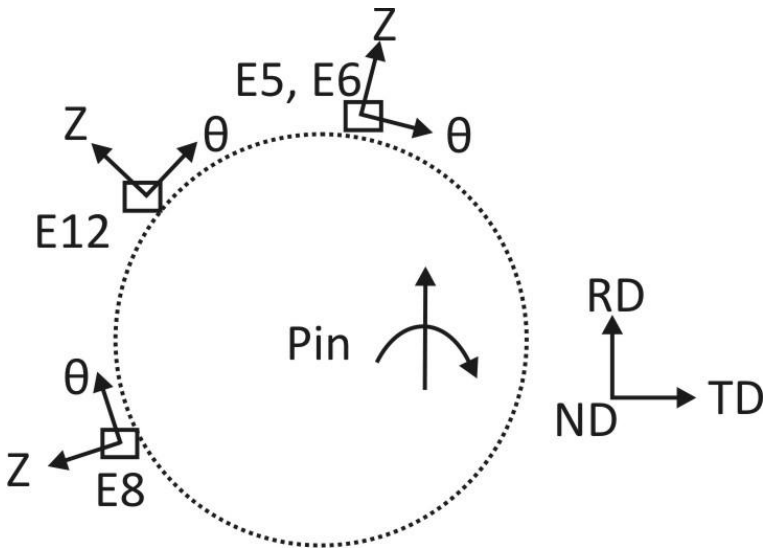

Figure 6-16. Suggested shear direction (θ) and shear plane normal (Z) at various locations around the pin.

Referring back to E5, E6, E8, and E12 (Figure 6-1): the incline angles between shear planes normal (Z) and RD, which are the same as those between shear direction (θ) and TD, of these three locations are 8.5°, 9.9°, 60.0°, and 52.4° respectively. Moreover, as summarised in Table 6-1, the PFs of these locations must be rotated by (6°, –13°, –10°), (22°, –24°, –11°), (–64°, 50°, –20°), and (47°, 35°, 17°) around the (ND, TD, RD) respectively to obtain standard "A" shear textures. It is clear the rotations around ND direction are closely related (however not equal) to the incline angles (between θ and TD) of these locations. Such observation is expected because at the pin/material contact interface, the shear direction is approximately tangential to the pin periphery.

Furthermore, the rotations around TD and RD of E8 and E12 are significantly higher than those of E6, the same rotations of which are further higher than those of E5. As illustrated earlier, rotations around TD and RD are primarily influenced by the screwing down effect induced by the rotating pin. Moreover, it has been demonstrated (in Section 5.1) that the downward flow of RSM is most severe on the advancing side. Hence, this more severe downward flow is likely to be responsible for the larger rotations around TD and RD of E8 and E12, compared to E6 and E5.

6.2.2 Texture Development

In the last section, how textures rotate with macroscopic material flow was discussed. This section investigates why "A" shear texture is the preferred texture in the current experiment.

Simulation of texture evolution

The creation of textures ({111} PFs) was simulated by rotating a 3D FCC unit cell, represented by a 3D Solidworks model, as indicated in Figure 6-17a. The frames of the unit cell are marked light green, and a stereo ball, with diameter equalling to the lattice parameter, is inside for the purpose of PF projection. In Figure 6-17b, the unit cell has a random orientation, and the eight {111} poles are represented by eight dashed green lines, and their interceptions with the stereo ball are marked by blue points. If the stereo ball is observed from the ND direction (in to the paper), only four of the eight interceptions which are located on the positive sphere are visible, as marked by "+" signs; and the other four which locate on the negative sphere are not visible, as marked by "–" signs. However, a texture system usually contains two components: e.g. to obtain the "A" shear texture, the shear plane normal and shear direction can be either $(1\bar{1}\bar{1})[110]$ or $(\bar{1}11)[\bar{1}\bar{1}0]$. As can be seen from Figure 6-17c, if $(1\bar{1}\bar{1})$ is the shear plane, while [110] is the shear direction: only five of the eight {111} poles which locate on the positive sphere can be seen, and they constitute the positive component of the "A" texture. In Figure 6-17d, if $(\bar{1}11)$ is the shear plane, while $[\bar{1}\bar{1}0]$ is the shear direction, the same five poles can be seen however their locations have rotated by 180 degrees around ND compared to those in Figure 6-17c, and they constitute the negative component of the "A" texture. By adding these two figures together, a standard "A" texture can be readily identified.

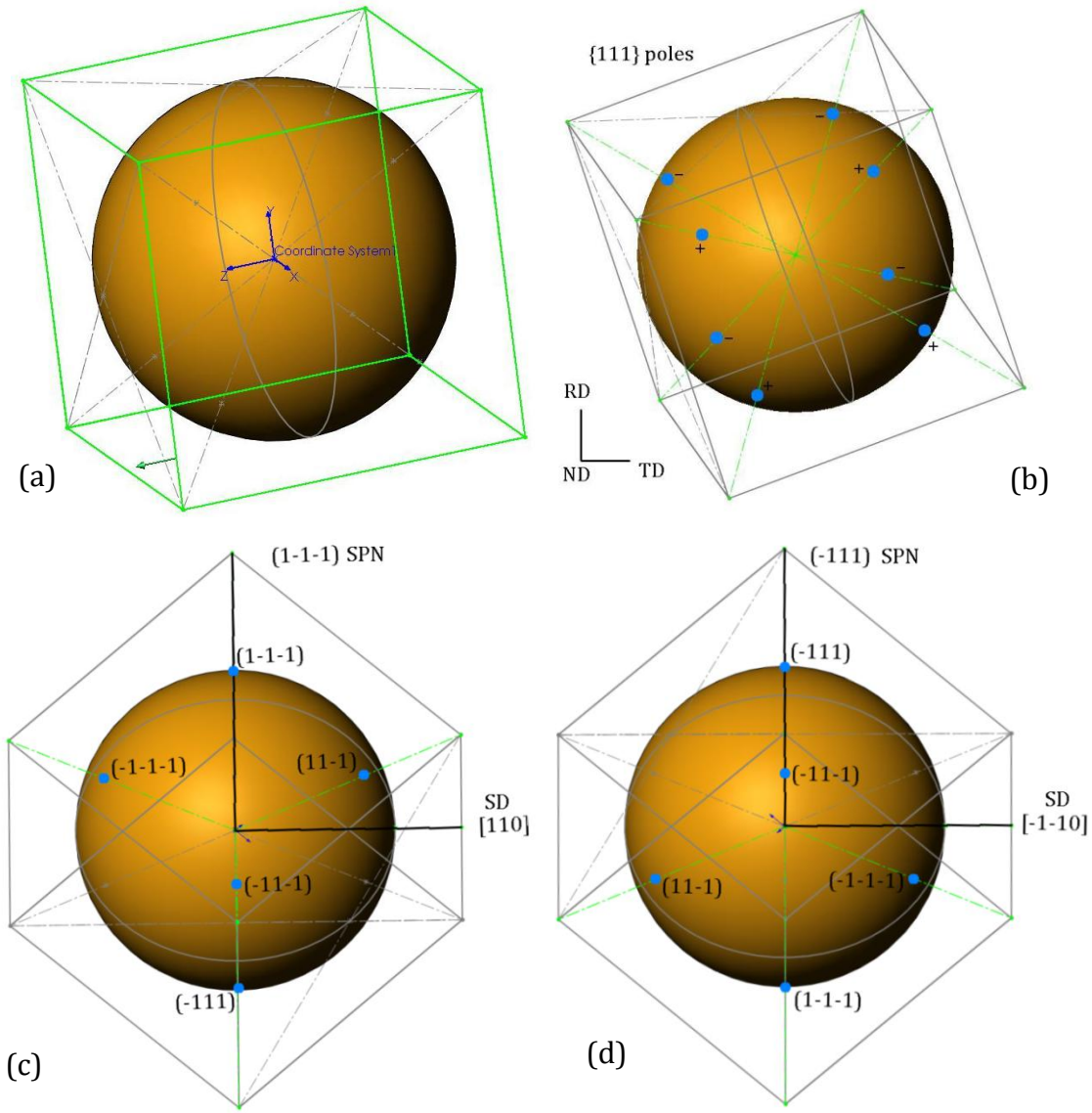

Figure 6-17. (a) A 3D Solidworks model which represents a unit cell, with a stereo ball inside for the purpose of pole figure projection; (b) {111} poles of the unit cell have been shown by the dashed green line, and the interceptions of the poles and the stereo ball have been marked by blue points; (c) the positive component: $(1\bar{1}\bar{1})[110]$ *of the "A" texture; (d) the negative component:* $(\bar{1}11)[\bar{1}\bar{1}0]$ *of the "A" texture.*

However, it is important to point out that to obtain a standard pole figure, the interceptions of the {111} poles with the reference sphere need to be projected onto a standard projection plane. As indicated in Figure 6-18, assume that line CP represents one of the {111} poles, and it intercepts with the sphere at point P. To obtain a standard PF, point P will need to be projected (starting from point B) on the projection plane, thus resulting point P'. Point P' represents one of the poles in a standard {111} PF (as indicated in Figure 1-36). However, the PFs obtained by

using the current Solidworks model are slightly different to the standard ones, as the interception points (e.g. point P) have not been projected on a standard plane (to obtain point P').

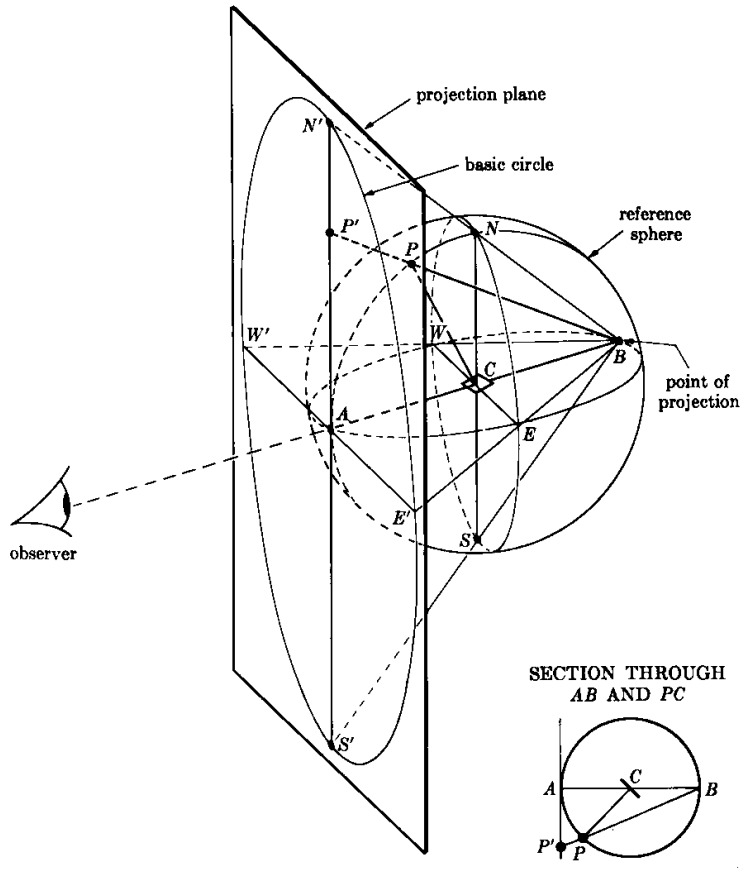

Figure 6-18. Schematic illustration of stereographic projection of a pole figure.

Rotations required to obtain different textures

The 3D model allows one to rotate the unit cell in any direction for any angle, thus simulating the development from the initial texture to the shear texture. As suggested by Fonda et al. [15] that orientations in shear deformation experience a continuous rigid rotation, a final stable orientation is never reached. Instead, the preferred texture components arise from the orientations that have the smallest rotation rates.

As can be seen from Figure 6-19a, a "Cubic" texture needs to rotate around ND for ±45°, then around TD for ±35.3°, ±54.7° and ±90° to obtain "A", "B" and "C" textures respectively. As far as the rotation rates are concerned, "A" texture should

be the preferred texture if the initial texture is “Cubic”, because the least rotation around TD is required.

If the initial texture is a “Goss” texture, as in a rolled sheet, one needs to rotate ±35.3° around RD, and then ±30° around ND to achieve “B” texture (Figure 6-19b); ±35.3° around ND and ±90° around RD to obtain “A” texture. Again, by considering the amount of rotation required, “B” texture should be the preferred texture because smaller rotations are required to obtain “B” compared to those of “A”.

Therefore, by purely considering the amount of rotation required, the “A” texture is easier to be obtained if the initial texture is “Cubic”; and the “B” texture is easier to be obtained if the initial texture is “Goss”. The aforementioned argument might be used to explain why “A” texture has been developed during FSP A356 in current study.

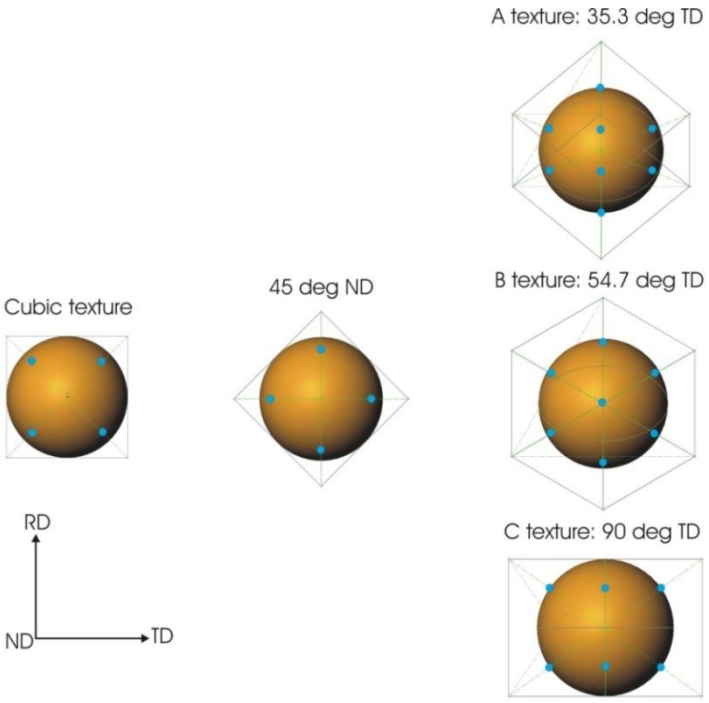

(a)

Figure 6-19. (a) developments from “Cubic” texture to “A” texture, “B” texture and “C” texture. “Cubic” texture needs to be rotated around ND for ±45°, and then rotated around TD for ±35.3°, ±54.7° and ±90° respectively to get “A”, “B” and “C” textures; (b) developments from “Goss” texture to “A” texture and “B” texture. “Goss” texture needs to be rotated around ND for ±35.3°, around RD for 90° to get “A” texture; and around RD for ±35.3° ND for ±30° to get “B” texture.

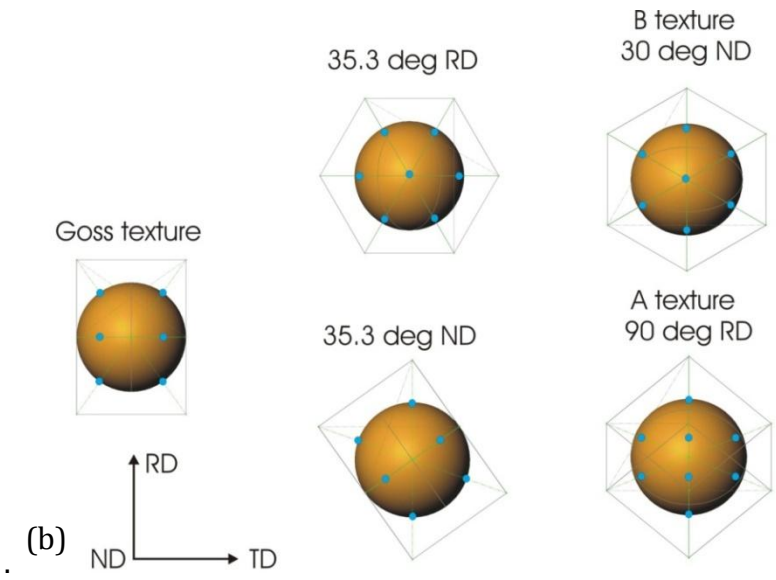

Figure 6-19 continued.

Texture Evolution due to Global Material Flow

It is important to make the distinction between individual unit cell rotation and overall texture rotation. If we consider an arbitrary situation that a grain, located closely ahead of pin, contains two Al unit cells which all together are experiencing shearing deformation. Both unit cells have a perfect "Cubic" texture (as-cast texture) to start with. In the current case, it is assumed a preferred texture exists (e.g. $(1\bar{1}\bar{1})[110]$ or $(\bar{1}11)[\bar{1}\bar{1}0]$). Let us make a further assumption that one of the unit cells deforms according to $(1\bar{1}\bar{1})[110]$, i.e. rotates 45° around ND and 35.3° around TD, and thus developing the positive component of the "A" texture (Figure 6-17c); and the other unit cell deforms according to $(\bar{1}11)[\bar{1}\bar{1}0]$, i.e. rotates –45° around ND and –35.3° around TD, and thus developing the negative component of the "A" texture (Figure 6-17d). Thus, the "A" texture will then be developed at certain stage during the deformation. However, as repeatedly introduced in previous sections, the obtained textures (around the pin) need to be further rotated around ND/RD/TD for various amounts to obtain the standard "A" texture. The overall texture rotation is due to the macro-scale material flow, rather than localized unit cell rotation. In a more vivid sense, this would mean that the two unit cells rotate together according to the overwhelming macro material flow; and thus the positive and negative components of the "A" texture rotate together. Therefore,

the “A” texture should persist throughout the deformation process as long as both unit cells rotate by the same amount.

To briefly summarize, the primary mechanism responsible for the recrystallization of Al dendrites (ahead of pin) is GDRX; the non-deformable Si particles accelerate the recrystallization of surrounding Al matrix; recrystallized Al grains, before and after deposition, display a dominating “A” shear texture; the texture rotation around ND is dependent on the local pin shear direction, and the rotation around RD and TD can be correlated to the downward flow induced by the pin threads; it is demonstrated that “A” shear texture is the preferred texture, if the original texture is “Cubic”, which is because the least amount of rotation of the unit cell is required as the texture transforms from “Cubic” to “A”.

Chapter 7. Removal of β-phase during FSP Mg-Al Alloys

In Section 1.5.6, it has been explained that the fundamental mechanism governing the removal of β-phase ($Mg_{17}Al_{12}$) during FSP Mg-Al alloys has not been well understood in current literature. In this chapter, this will be addressed. The microstructures of samples produced by FSP conducted on AZ91 and AM60 workpiece under common conditions will be characterized first. Secondly, the thermal histories experienced by the workpiece in the transient zone (ahead of pin) will be presented; and then the detailed investigation on the morphological change of $Mg_{17}Al_{12}$ using SEM, coupling with temperature data, will be given; and finally the volume fraction change of the $Mg_{17}Al_{12}$ will be discussed in a quantitative manner. It is important to point out that the investigation is primarily focused on FSP AZ91 alloy due to the fact that the volume fraction of the as-cast β-particles in AZ91 is significantly larger than that in AM60, which enables a clearer observation (detailed in Section 2.1).

7.1 General FSP Microstructures

FSP experiments were performed on AZ91 and AM60 cast ingots, using normal machine setups: ω = 1000 rpm, θ = 2.5°, and v = 160 and 112 mm/min for AZ91 and AM60 respectively. "Pin-breaking" and temperature measurement experiments, were also conducted under the conditions stated above, only that a zero tilt angle was used. The detailed experimental procedures were given in Section 2.2.4.

The initial microstructures and dimensions of the cast ingots were given in Section 2.2.3. The cross sections of FSP AZ91 and AM60 samples are given in Figure 7-1a and b respectively. FSP samples with no internal voids were obtained in both cases. Some commonly seen FSP features can be observed: in general, the nugget zones constitute most of the total stir zone, while only very thin shoulder flow zones can be observed on the top portion of the macrographs; furthermore, the banded structure ("onion-rings") is apparent in both cases. One important observation is

that the size of the nugget of FSP AM60 is much larger than that of FSP AZ91. This could be partially justified by the fact that a slightly lower linear speed was used during FSP AM60 (112 mm/min) than in FSP AZ91 (160 mm/min). As discussed in Section 4.2.1, a decrease in *v*, while keeping other FSP conditions the same, is likely to result in a larger nugget flow zone.

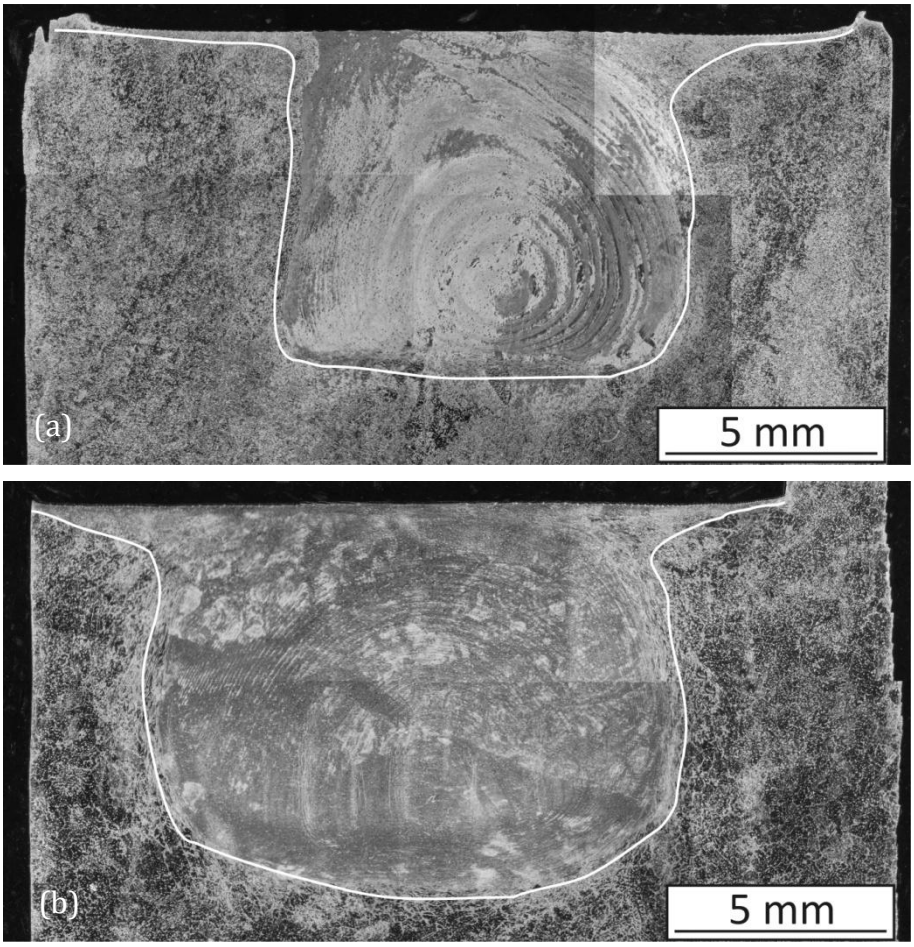

Figure 7-1. Macrographs of FSP AZ91(a) and AM60 (b). Advancing side is on the right. FSP conditions are: v = 160 and 112 mm/min for AZ91 and AM60 respectively, with constant ω at 1000 rpm, and θ at 2.5°.

Micrographs taken from centre of the nugget are given in Figure 7-2a and b respectively. Fully recrystallized grains can be clearly identified, most of which have a grain size of 10–15 μm. The as-cast microstructures of AZ91 and AM60 ingots, on which the current FSP experiments were performed, have previously been given in Figure 1-7a and b respectively. It is clear that FSP has led to a near complete removal of the β-phase in the nugget zone. However, the dissolution of

Al_8Mn_5 particles is insignificant. Hence these particles have remained in the nugget zone, with their original equiaxed morphology hardly changed.

Next, the fundamental thermomechanics and metallurgy responsible for the removal of the β-phase will be examined, which is the primary aim of the investigation on FS of Mg-Al alloys in the present work. The temperature experienced during FSP will be first presented.

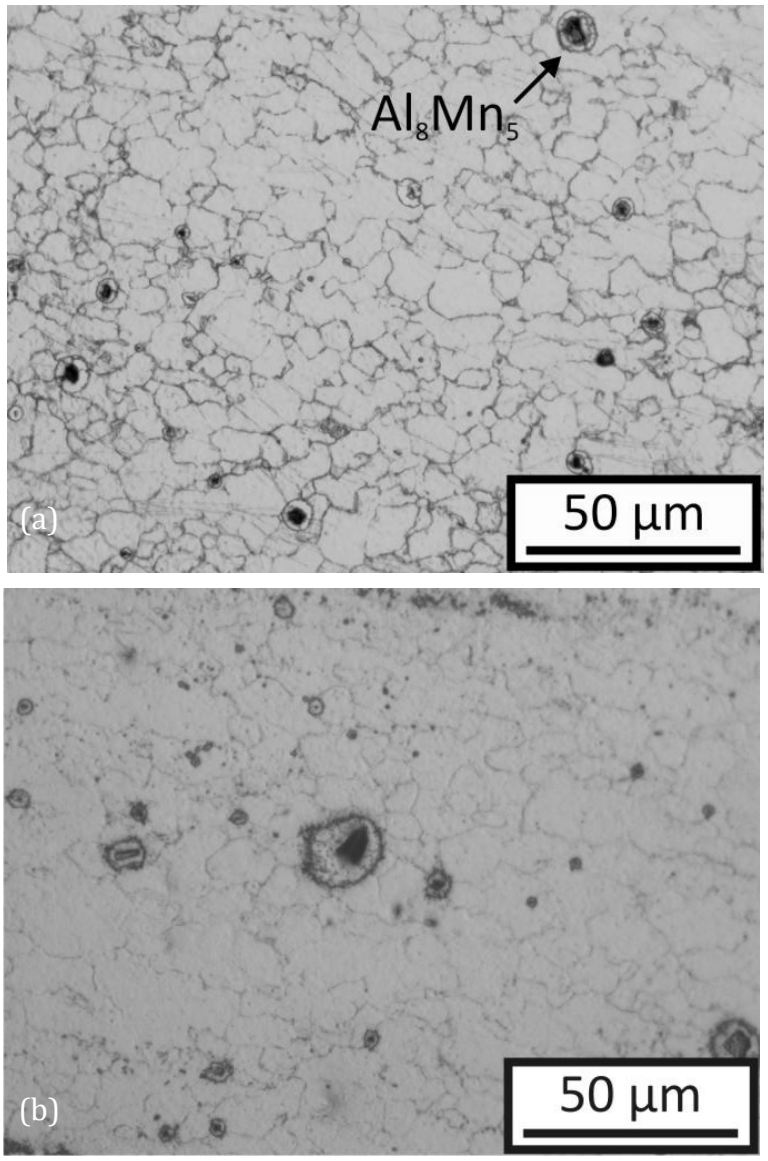

Figure 7-2. Micrographs taken from the nugget centre of FSP AZ91 (a) and FSP AM60 (b).

7.2 Thermal Histories

The temperature history experienced by the material during FSP is crucial for the understanding on the removal of the β-$Mg_{17}Al_{12}$ particles. Temperature measurements at various locations during FSP AZ91 and AM60 are shown in Figure 7-3a and b respectively. According to Mg-Al phase diagram (Figure 1-8), the binary equilibrium eutectic temperature ($T_{eutectic}$) is 437 °C. However, melting of the eutectic β-phase ($Mg_{17}Al_{12}$), formed during non-equilibrium solidification of AZ91 casting, can initiate at 426 °C [126]. $T_{eutectic}$ and the equilibrium solidus temperature ($T_{solidus}$ = 470 °C and 540 °C for AZ91 and AM60) are marked in Figure 7-3.

As illustrated in Section 2.2.4, temperature measurements during FSP AZ91/AM60 thick ingots include placing the thermocouples 4.5 mm from top surface, with thermocouple probe tip along pin centre, 1 mm away from the pin thread (5 mm from centre) on advancing side and 5 mm away from the pin thread (9 mm from centre) on advancing side. These three positions are thus denoted as 0 mm ahead, 5 mm and 9 mm respectively in Figure 7-3. As can be seen, the temperatures increase as pin gets closer to the thermocouples, and reaching their maximum levels when the pin is about to pass by the thermocouples. The time at this instance is denoted as "0". Thus, time is assigned negative as the pin travels towards the thermocouples; while positive as the pin has passed the thermocouples. As the pin travels further away, thus leaving the thermocouples behind it, the temperatures drop, as expected.

The two thermocouples placed in the last two locations have not been significantly moved by the rotating pin or the induced material flow. The thermocouple placed at the weld centreline (0 mm) was displaced from its position when it touched the pin threads (time 0). Pin movement should have caused the thermocouple probe to bend away from the pin (towards the advancing side). However, the thermocouple probes did not break due to the displacements, and temperature data were still recorded after the tool has travelled far ahead of the thermocouples. After the pin has passed by (thus time is positive), the exact positions to which these data points

correspond are, however, uncertain and these data points are indicated as "displaced" in the plots (0 mm).

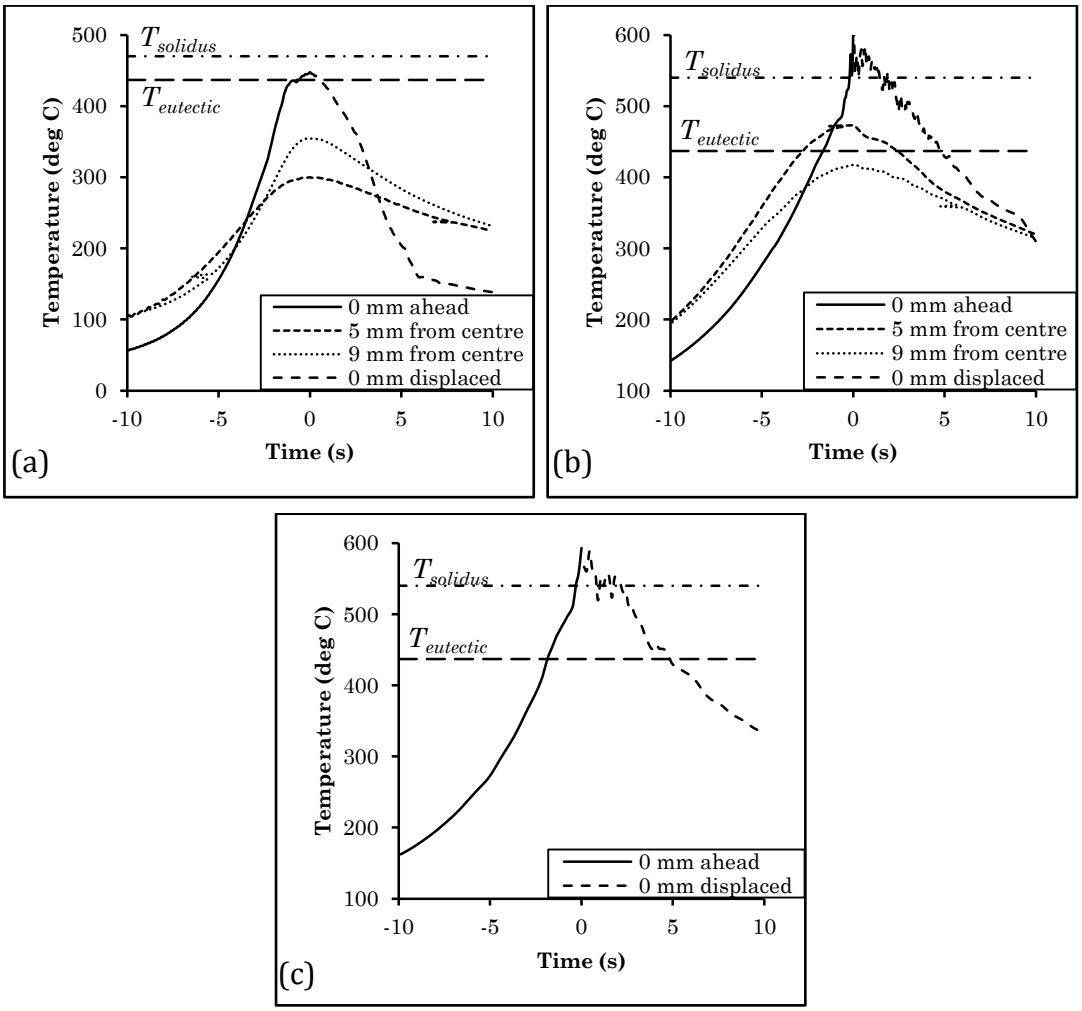

Figure 7-3. Measured temperature during (a) FSP AZ91 and (b) FSP AM60 thick ingot as a function of time. The locations of the thermocouple tips are illustrated in Figure 2-7. The thermocouple at 0 mm is displaced by the action of the tool during welding so the exact position for which displaced measurements is uncertain. (c) Temperature at pin centre during FSP AM60, under same conditions, has been measured again.

During FSP AZ91 and AM60, temperature (immediately) ahead of the pin centre exceeded $T_{eutectic}$, which strongly indicates that eutectic melting of the β-particles has occurred during FSP AZ91/AM60. $T_{eutectic}$ was first reached at –0.61 s and –1.65 s during FSP AZ91 and AM60 respectively, which correspond to 1.6 mm and 3.1 mm ahead of the pin. For FSP AM60, the temperature at a location 5 mm away from the pin centre (1 mm away from the pin threads) has also exceeded $T_{eutectic}$, which indicates the melting might have occurred even beyond the pin path.

The maximum temperature reached during FSP AZ91 is 447 °C, which is below (equilibrium) $T_{solidus}$ (470 °C). For FSP AM60, the maximum recorded temperature is 610 °C, which is significantly higher than the equilibrium solidus temperature (540 °C). Furthermore, the pin centre temperature has stayed above $T_{solidus}$ for about 1.62 s. However, it is generally believed that the maximum temperature during FS should not exceed $T_{solidus}$ of the workpiece. This is because once $T_{solidus}$ is reached during FSP, the matrix of the material (in the current case Mg and second phase) will start to melt. The liquid formed will considerably reduce the deformation/friction heating thus limiting the heat generation capacity of FSP. Therefore, it is widely accepted that the maximum attainable temperature during FSP is slightly below the equilibrium $T_{solidus}$ or $T_{eutectic}$ of the workpiece. Hence, the current temperature measurement is contradictory to this general belief. In order to confirm this rather surprising result, pin centre temperature was measured again using exactly the same experiment setup, except the temperature sampling rate was decreased by three times (from 0.045 s per data to 0.152 s per data), and the recorded temperature is given in Figure 7-3c. It can be seen that the temperature histories obtained from these two experiments are very similar to each other. Moreover, T_{max} has again well exceeded equilibrium $T_{solidus}$, and the temperature has stayed above equilibrium $T_{solidus}$ for about 2.43 s.

For a more detailed view, temperature readings above equilibrium $T_{solidus}$ during these two experiments have been presented again in Figure 7-4a and b. It is clear that the variations in temperature are quite significant once above equilibrium $T_{solidus}$. For example, the difference between the maximum and the second maximum temperatures is 32 °C in Figure 7-4a. Decreasing the sampling rate apparently reduces the variations in temperature measurement, and the difference between the maximum and the second maximum temperatures is smaller than 10 °C. However, the fact that T_{max} is significantly higher than equilibrium $T_{solidus}$ is not affected by the change in sampling rate. It is important to note that the thermocouples did not break and the temperature has been continuously monitored even after thermocouples have been bended. This strongly suggests the variations in temperature reading are not caused by thermocouple dysfunctioning.

Thus, it can be concluded that the measured temperatures represent the actual thermal condition experienced by the thermocouple probe during FSP.

The first possibility is that the pin threads have been shearing against the thermocouple probe and the friction between these two components, both of which are made in steel, can cause the instantaneous temperature at the pin/thermocouple interface reaching a fairly high level. Nonetheless, it is quite safe to state that T_{max} has exceeded the equilibrium solidus temperature (540 °C). This issue will be further discussed in Section 7.4.2.

As shown in Figure 7-3, it is clear that the average temperatures obtained (at various locations in the processing zone) during FSP AM60 are significantly higher than those of FSP AZ91. It is possible that the lower processing speed (112 mm/min) used during FSP AM60, as opposed to 160 mm/min during FSP AZ91, is partially responsible for the higher temperatures. However, this issue will be investigated further in Section 7.4.2 as the maximum achievable temperature is also closely related to microstructural evolution during FSP.

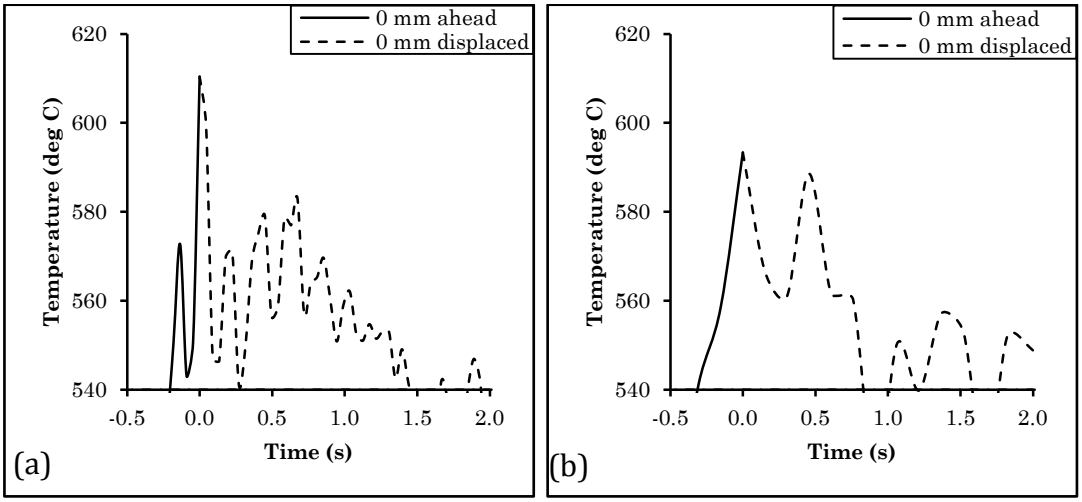

Figure 7-4. Enlarged view of the temperature readings (> equilibrium $T_{solidus}$ = 540 °C) during FSP AM60. (a) with a sampling rate of 0.045 s and (b) 0.152 s.

7.3 Melting and Re-solidification of β-phase

As indicated previously (Figure 7-2), the volume fraction of β-particles at the centre of the nugget of FSP AZ91 and AM60 is near zero. As explained in Section

1.5.6, the mechanism governing the removal of β-phase has been unclear. In the previous section, the temperatures ahead of the pin centre during FSP AZ91 and AM60 have (well) exceeded $T_{eutectic}$ which strongly suggested a (partial) melting of the β-phase during FSP. In this section, how the morphologies of the β-particles evolve ahead of the pin will be studied in detail by examining the pin/workpiece couples, to explain the phenomenon of (partial) melting and its relationship with the removal of β-phase.

7.3.1 Melting and Re-solidification of β-phase during FSP AZ91

Temperature Estimation

Let us consider the case of FSP AZ91, as the Al content (and thus volume fraction of β-phase) is higher than AM60, therefore enabling easier observation on the evolvement of β-particles. To study the change in β-eutectic morphology, a series of low magnification SEM images (Figure 7-5a) were taken from the leading side (up to 4.5 mm ahead) of the pin/workpiece couple. The top 4.5 mm of the sample was polished off, which leaves approximately half of the pin still embedded in the sample.

Re-examining temperature ahead of pin during FSP AZ91 (Figure 7-3a), the maximum temperature (448 °C) occurred when the pin touched the thermocouple probe, at time "0". Bearing mind the probe is 1 mm in diameter, therefore the recorded temperature should occur 0.5 mm ahead of the pin, which is marked as L1 in Figure 7-5a. A number of β-particles, P1–P7, were closely examined, and their morphologies are presented in Figure 7-6. Their location with reference to the pin is marked in Figure 7-5a.

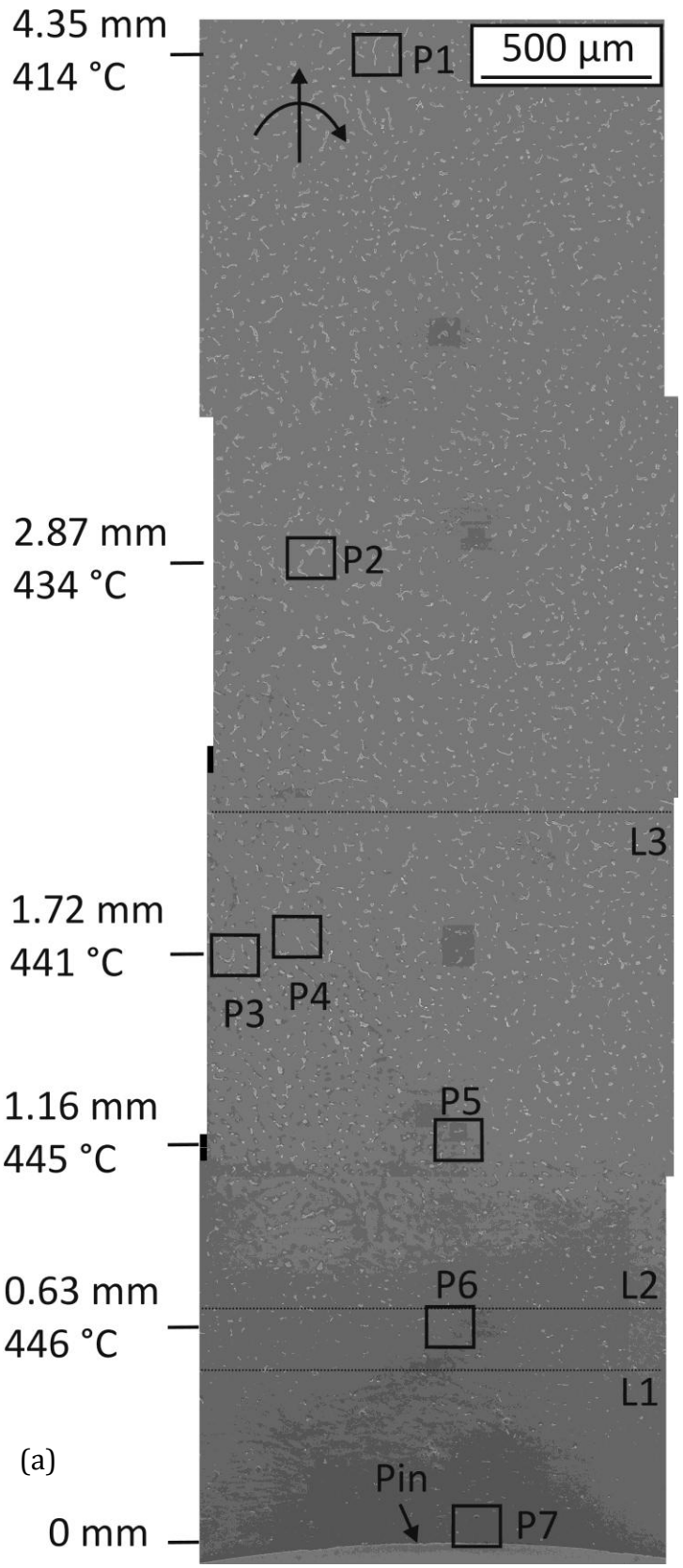

Figure 7-5. (a) Low magnification SEM image of the region locates up to 4.35 mm ahead of broken pin during FSP AZ91. (b) A higher magnification SEM shows the pin induced deformation became severe at ~ 0.68 mm ahead of the pin.

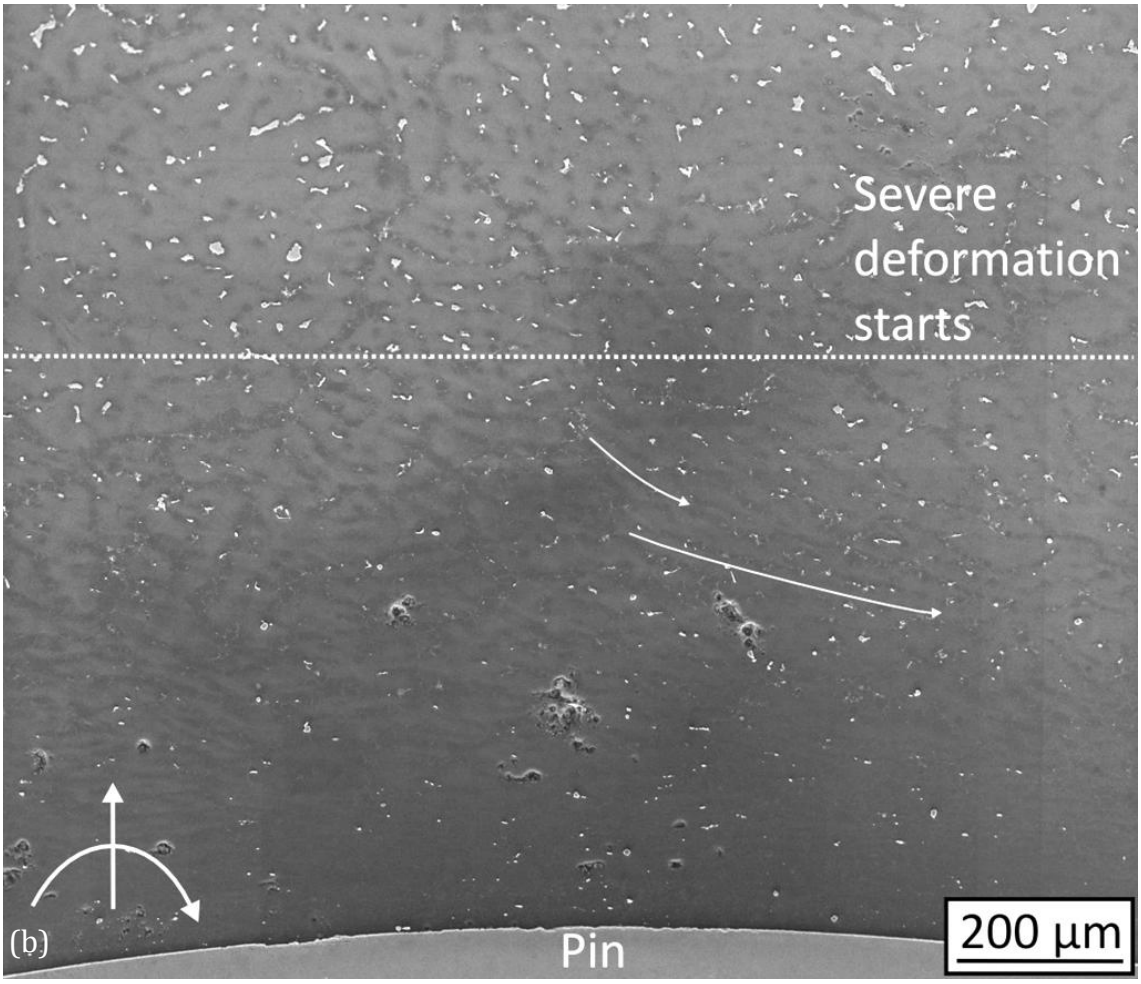

Figure 7-5. Continued.

The temperatures experienced by P1–P7 can be estimated by the following way. Firstly, it is assumed that stable FSP condition has been achieved in this experiment, so that the any location ahead of the pin centre experiences the same temperature history. This means that if the pin did not break, the temperature history of P1 would be the same as that of P7, which would be the same as which was measured in the current case (0 mm in Figure 7-3a). As indicated in Figure 7-5a, P1 locates 4.35 mm ahead of the pin, which corresponds to 3.85 mm (4.35 – 0.5) ahead of L1. Therefore, the temperature experienced by P1 should refer to the temperature data recorded at time –1.44s, i.e. time = 3.85 mm × 60s/160 mm min^{-1}. Referring to Figure 7-3a, this corresponds to 414 °C. By following the method stated above, the temperatures experienced by P2–P7 can also be estimated, and they are indicated in Figure 7-5a.

Furthermore, as given in Figure 7-3a, the temperature ahead of the pin reached $T_{eutectic}$ at –0.61 s. Hence, the centre of the thermocouple should locate 1.63 mm (= 0.61 s × 160/60 mm/s) ahead of L1 (Figure 7-5a), thus 2.13 mm ahead of the pin front. Hence, the location where $T_{eutectic}$ (437 °C) was reached is marked as L3 in Figure 7-5a.

A SEM image taken very close to the broken pin is given in Figure 7-5b. It can be seen that pin induced shear deformation is only severe ~ 0.68 mm ahead of the pin. Two deforming dendrites are traced by the white arrows. As such, L2 (Figure 7-5b) is drawn to indicate the beginning of observable deformation.

It is important to note that the "pin-breaking" and temperature measurement were performed in separate FSP experiments under exactly the same conditions. Therefore, it is reasonable to treat the temperature history during the "pin-breaking" experiment approximately the same as that obtained from the temperature test experiment.

Morphological Change of β-phase

Now let us examine closely the morphologies of the β-particles ahead of pin, which are given in Figure 7-6. In SEM, the β-particles appear grey with an irregular high aspect ratio shape, while the small Al_8Mn_5 appears bright grey with a spherical shape. It is important to clarify at this point, for the rest of discussion in this chapter, the morphology of Al_8Mn_5 particles does not change by moving from location P2 to P7.

P1 locates far ahead (~ 4.35 mm) of the pin, where the temperature (414 °C) is far below $T_{eutectic}$. The β-particles around P1, with irregular shapes, display the as-cast fully divorced eutectic morphologies.

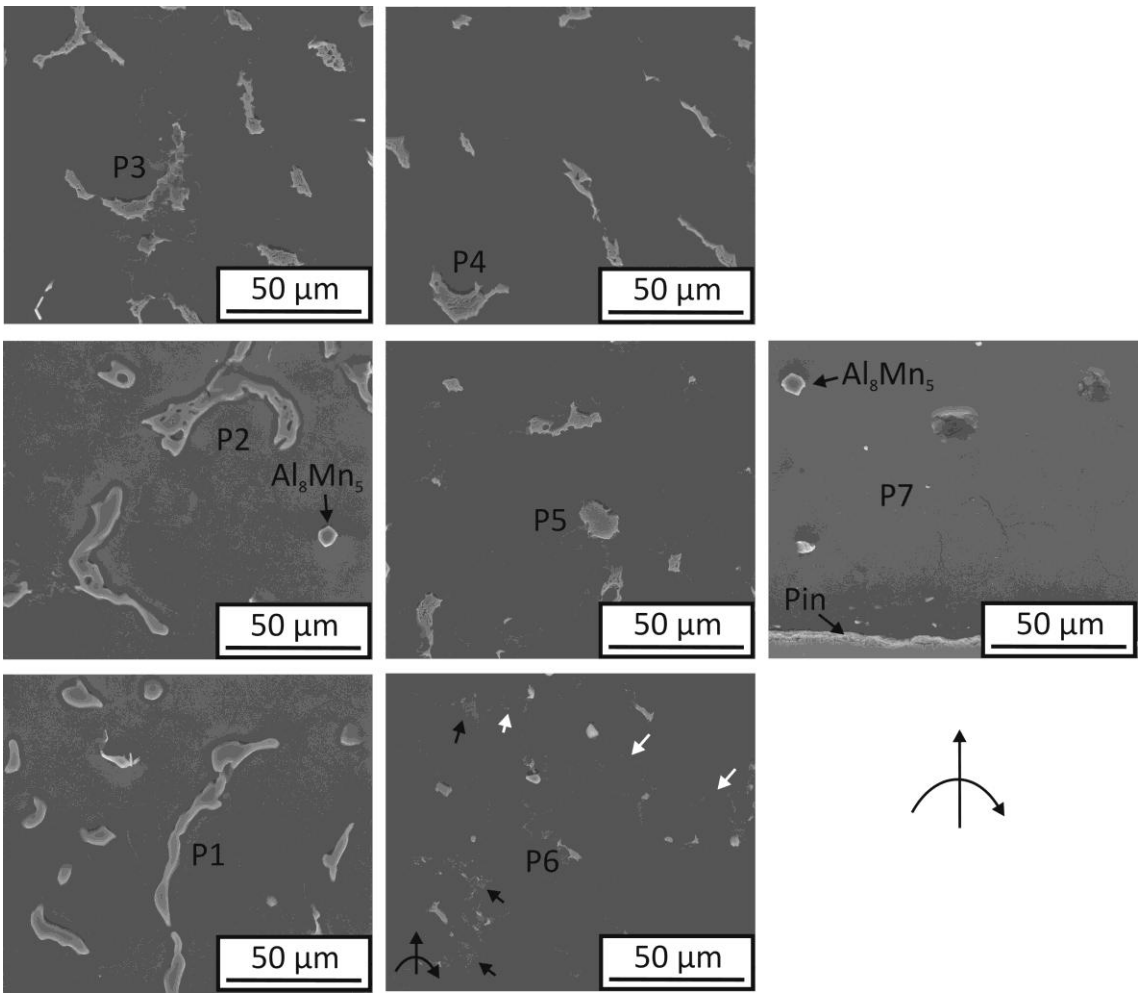

Figure 7-6. The change in morphology of β-particles as they approaches pin. Their locations with reference to pin are given in Figure 7-5a.

P2 locates 2.87 mm ahead of the pin, and a high magnification SEM image (Figure 7-7) indicates that P2 displays a seemingly partially divorced morphology, with islands of α-Mg inside. It is obvious that the morphology of P2 is slightly different to that of P1 (as-cast state). The temperature experienced by P2 is estimated to be approximately 434 °C, which is slightly below binary eutectic temperature ($T_{eutectic}$ = 437 °C). However, as mentioned previously, the eutectic melting of the β-particles in AZ91 can start at 426 °C, which is likely to be exceeded in the current case. Furthermore, it has been illustrated by Zhu et al. [126] that the melting initiates at the central portion of the β-particles, which is because the Al content is the lowest at that location, which corresponds to a lower eutectic melting temperature (see Figure 1-9). Bearing these in mind, it is quite likely that the morphological change of the β-particles is related to eutectic melting. To be

specific, the formation of islands of α-Mg inside β-particles is due to resolidification of molten β. The melting and resolidification sequence will be further discussed later in this section.

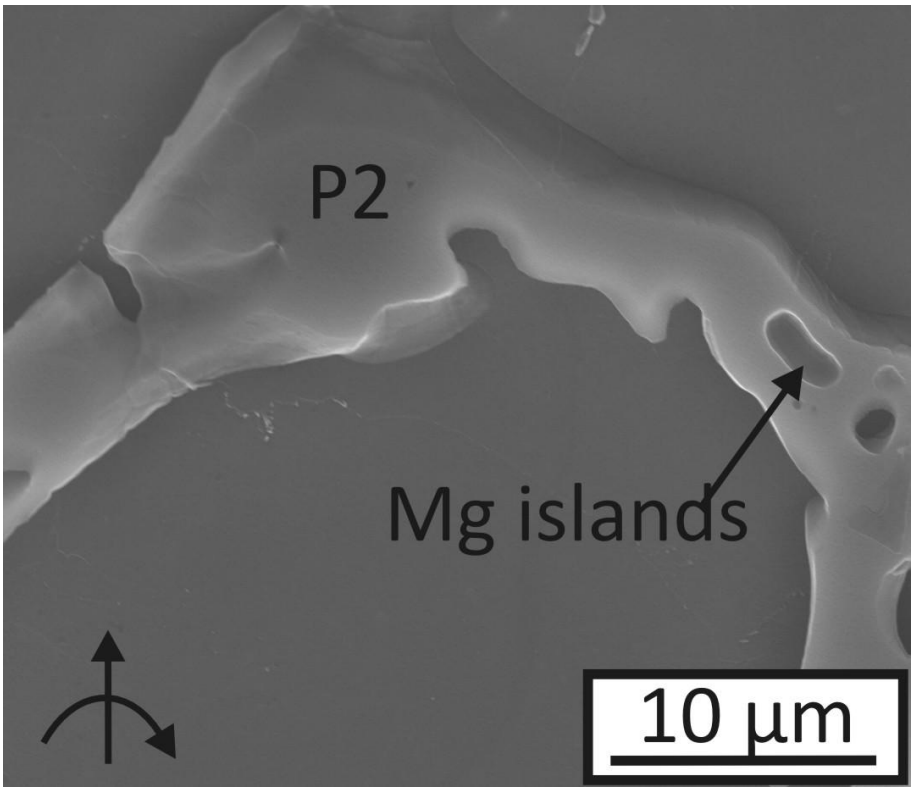

Figure 7-7. Enlarged view of P2 ahead of pin during FSP AZ91.

P3 and P4 are at a distance ~ 1.72 mm ahead of pin, where the estimated temperature is 441 °C, which is higher than $T_{eutectic}$. Therefore, it is almost definite that eutectic melting of β-phase has occurred around P3 and P4. It can be seen from Figure 7-6 that the size of β-particles has been reduced compared to P1 and P2. The enlarged view of P3 is given in Figure 7-8, which clearly demonstrates that the α/β interface becomes serrated, where as in the as-cast state the interface is rather smooth and clear (as indicated in Figure 7-6 near P1). Furthermore, fine islands of α-phase can be well observed within the β-particle, which appear as holes after being removed by etching. Hence, it can be suggested that the initial fully/partially divorced morphology of the β-phase has largely transformed into a two-phase morphology, i.e. fine islands of α-phase embedded within the β-particle. Moreover, this α + β structure is retained within the original β-particle.

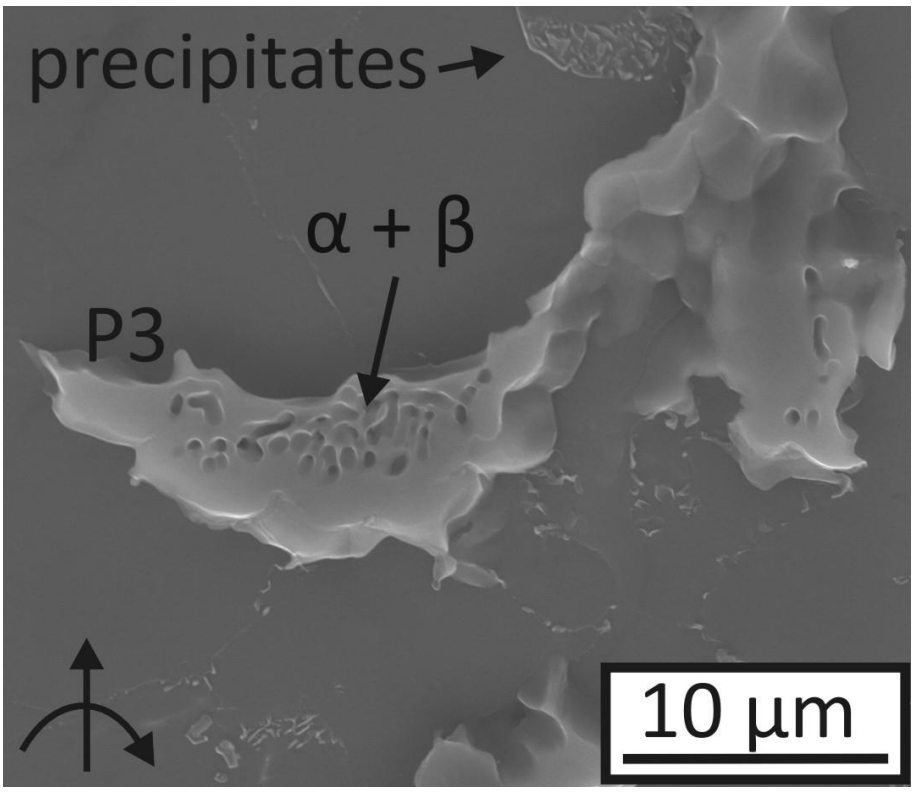

Figure 7-8. Enlarged view of P3 ahead of pin during FSP AZ91.

Such morphological transformation is very unlikely to be associated with α-phase precipitating inside the β-particle. Zhu et al. [126] have clearly shown that isothermal annealing of AZ91 samples at 420 °C (up to 30 mins) does not result in the two-phase microstructure inside the fully divorced β-particles. Therefore, it is clear that (near-full) melting and subsequent re-solidification of the β-particle is the mechanism responsible for the formation of the two-phase morphology.

Such a process can be explained by using the schematic given in Figure 7-9. The Mg-Al phase diagram is given in Figure 7-9a, while the initial state of fully divorced β-particle surrounded by α-Mg is represented by Figure 7-9b. As the temperature increases towards $T_{eutectic}$, the eutectic melting of the β-particle should start at the central portion of the particle, where the Al content is expected to be lower (refer to Figure 1-9).

As the temperature further increases to T_{P3}, which is 441 °C (> binary $T_{eutectic}$ = 437 °C) in the current case, it is expected that the β-particle is now fully melted. Furthermore, parts of the α-dendrites (which surround the β-particle), should also melt. This is because during non-equilibrium solidification, α-Mg dendrites

continue to grow at a temperature below $T_{eutectic}$ (see Figure 1-9). Hence, a mixture of fully melted β-particle surrounded by some melted α-dendrites is expected to exist. This mixture, and its composition, are schematically represented by Figure 7-9c.

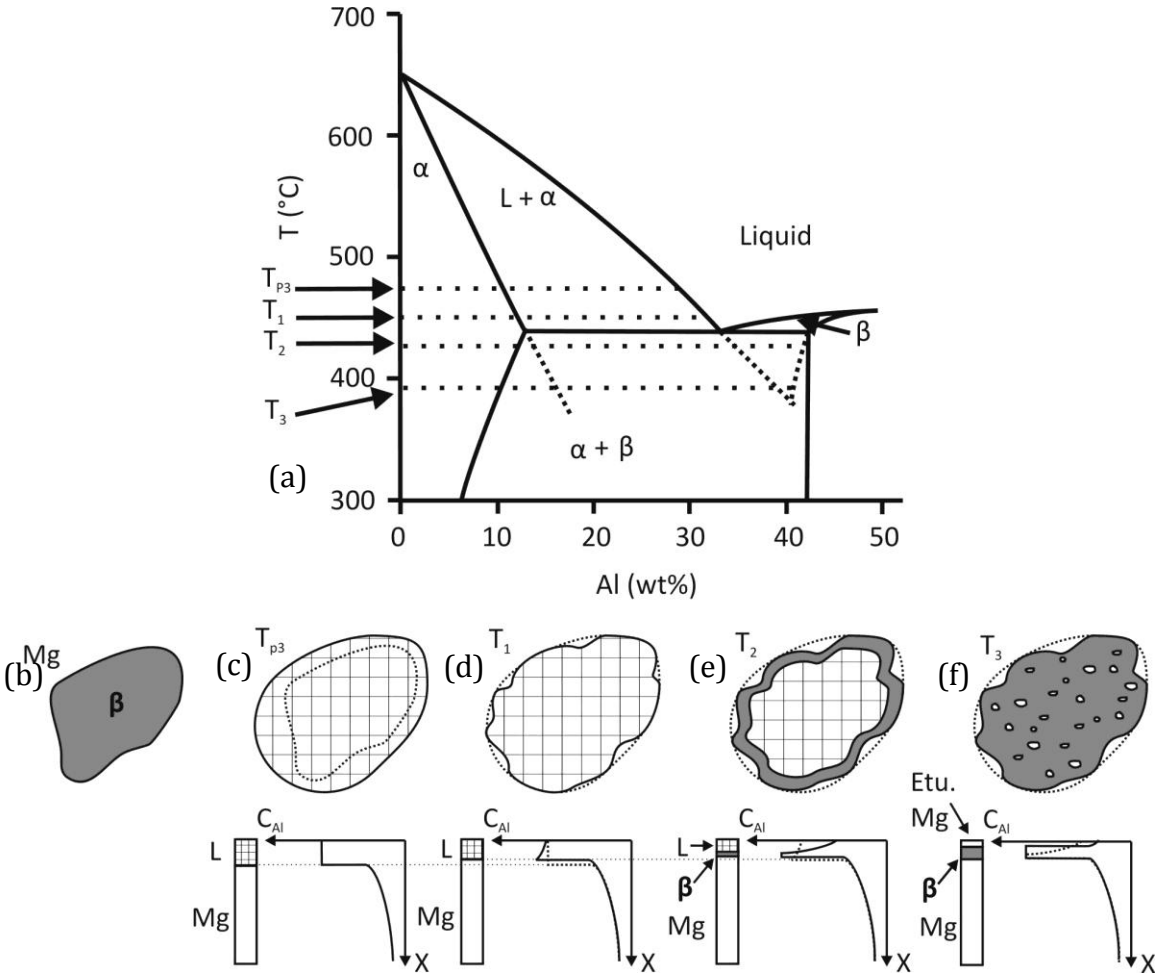

Figure 7-9. Schematic illustration depicting partial melting and the microstructures at various stages of re-solidification [51]. (a) binary Mg-Al phase diagram; (b) a fully divorced β-particle; (c) formation of liquid pool at temperature T_{P3}; (d) growth of Mg dendrites during cooling to T_1; (e) further growth of Mg and the initial formation of β-phase during cooling to T_2; (f) growth of β-phase and formation of Mg islands during cooling to T_3.

As soon as the pin broke, coolant was poured onto the AZ91 plate which resulted in a significant drop in temperature. During the temperature measurement experiment (conducted in a separate test however under the same condition as used in the pin-breaking experiment), coolant was also poured onto the plate as

soon as the pin touched the thermocouple tip. As can be estimated from Figure 7-3a, the temperature drop, from T_{max}, is around 53 °C/s.

As the temperature drops from T_{P3} to T_1, α-Mg grew with a cellular mode (Figure 7-9d), resulting in the reduction (or re-solidification) in the liquid mixture. This cellular growth is responsible for the formation of the serrated α/β interface, which can be clearly observed in Figure 7-8. The growth of α-Mg involves rejecting Al elements into the liquid, thus causing a rise in Al concentration at the α/β interface. This is schematically given in Figure 7-9d. However, β-phase cannot yet form at this stage because undercooling of the liquid is necessary.

Further cooling from T_1 to T_2, the α-Mg grows further, causing the α/β interface to become even more serrated (Figure 7-9e). The liquid is thus further enriched in Al, and the undercooling is sufficient to initiate the nucleation of the β-phase. Referring to Figure 7-9a, the undercooled liquid has passed the couple zone, which implies that the formation of β-phase is now leading the solidification process. It can be seen that the Al concentration of the β-phase (at T_2) is higher than that of the undercooled liquid. Hence, the formation of the β-phase must have caused the Al concentration in the remaining liquid to drop.

As the temperature further decreases to T_3, the formation of β-phase has completed. However, the growth of the β-phase has reduced to Al concentration in the remaining liquid to an extent that α-Mg islands can form within the re-solidified β-particle (Figure 7-9f). Very similar observation was made by Zhu et al. [126] by heating an AZ91 sample in furnace up to 440 °C and then air cooled. As can be seen from Figure 7-10, the fine α-Mg islands occupy a large portion of the re-solidified β-particle.

Referring back to Figure 7-7, the formation of α-Mg islands within P2 can also be explained following the previous arguments. However, it is likely that the eutectic melting has only begun to occur within P2 (given the temperature is ~ 434 °C), and no Mg dendrites have melted. During resolidification, the molten β nucleates reasonably easily, i.e. undercooling is very little, due to the existence of large non-melted β-particle surrounding it. Thus, the resolidified β-phase, onto the existing

β-particle, consumes the Al solute of the molten β, leaving fine α-Mg islands forming within P2.

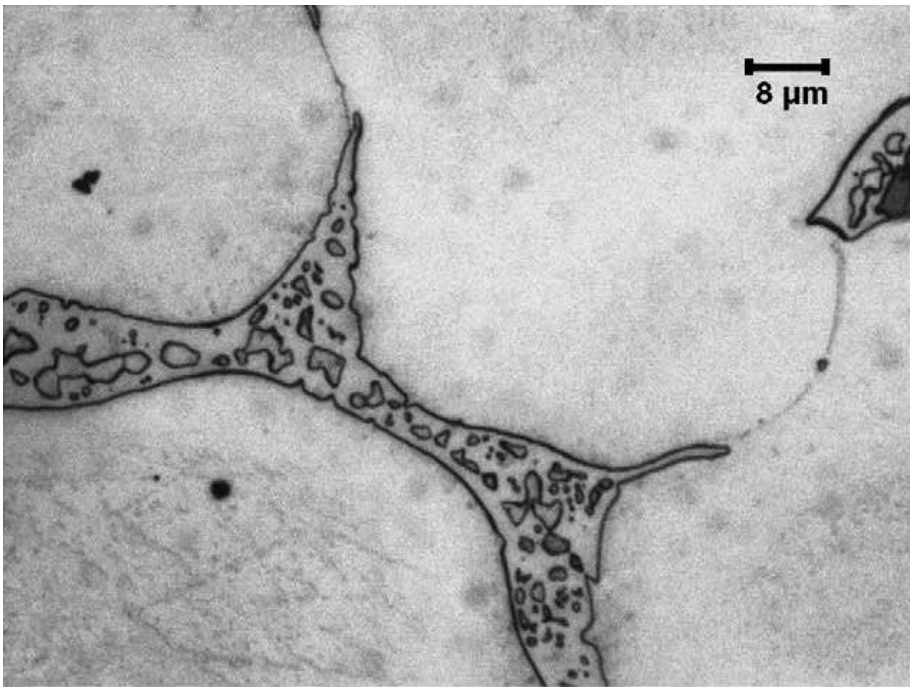

Figure 7-10. Morphologies of β-particles after furnace heating to 440 °C and air cooled [126].

Once P3 and parts of the surrounding dendrites have completely melted, the molten pool easily wets adjacent α-Mg grain boundaries. This is apparent in Figure 7-8, which shows extremely fine β-particles decorating the α-Mg grain boundaries, particularly near the large β-particle. The wetting effect leads to a very large surface area of liquid in contact with the surrounding α-Mg, which greatly accelerates the transfer of Al solute required for the α-Mg to grow into the liquid pool. Therefore, only very fine β-particles solidify along grain boundaries after quenching (Figure 7-8). One fundamental reason for the grain boundary wetting is that the transient zone ahead of pin is under highly compressive stress given the fact that the tool keeps moving ahead. The liquid pool cannot bear the pressure, thus the part of it must be "squeezed" into adjacent grain boundaries.

The wetting effect can be seen more clearly from a series of micrographs taken ahead of the pin, which are given in Figure 7-11a to d respectively. The distance ahead of pin is given in each micrograph. In Figure 7-11a, wetting of the grain boundaries can be clearly identified, as marked by the black arrows. The wetting

effect becomes increasingly severe nearer the pin (Figure 7-11b to d), meanwhile the size of the resolidified β-particles decreases continuously. This strongly suggests that the eutectic melting of the β-phase, and the subsequent wetting of the grain boundaries, is responsible for the removal of the β-phase during FSP; while the traditionally suggested breaking-up and solid-state diffusion of the β-phase is not supported by the current observation.

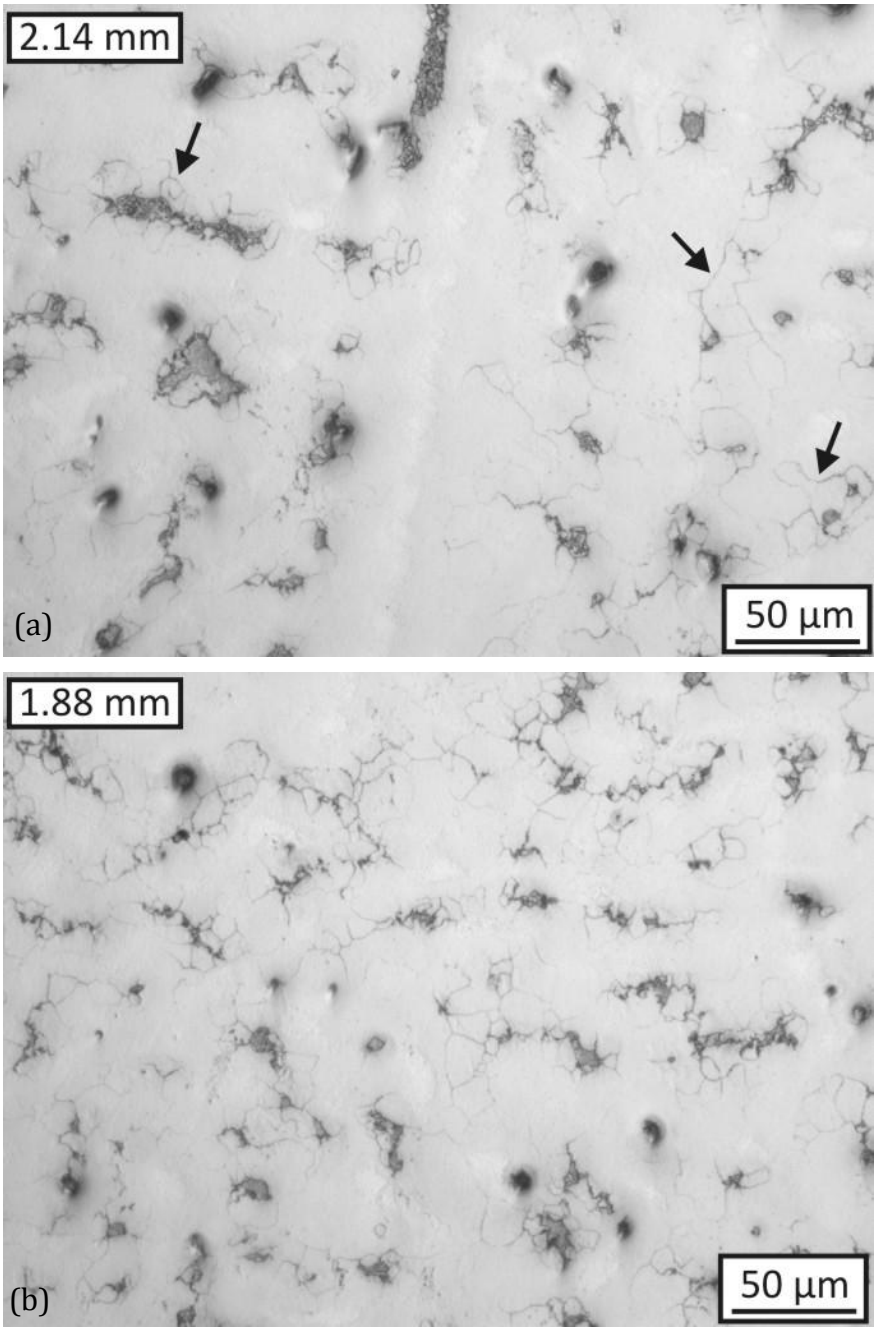

Figure 7-11. Micrographs taken at (a) 2.14 mm, (b) 1.88 mm, (c) 1.62 mm, (d) 1.38 mm ahead of the pin during FSP AZ91.

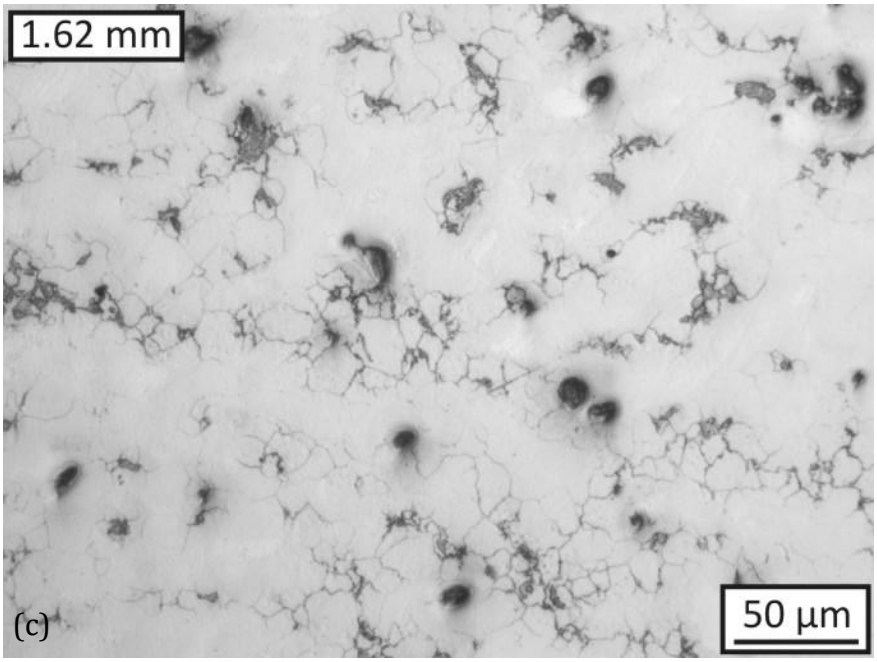

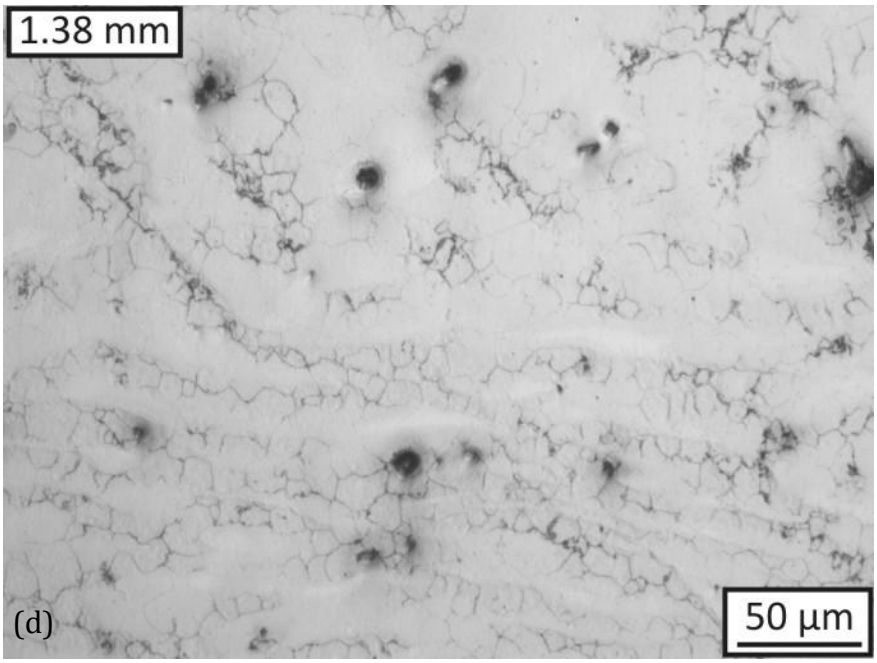

Figure 7-11. Continued.

The second important observation can be made from Figure 7-11a is that α-Mg, recrystallizes at a distance well ahead of the pin (> 2 mm). And this is especially so in α-Mg regions near the large β-particles. The recrystallized α-Mg grains are clearly outlined by the fine resolidified β-particles. As has been explained and illustrated in Figure 7-5, the pin induced deformation starts to become severe at a distance 0.68 mm ahead of pin, and the temperature at a location ~ 2 mm ahead of pin is expected to be slightly less than 440 °C. However, it is still expected the α-Mg

matrix 2 mm ahead of pin experiences a low strain deformation, due to the fact that there is inevitably a highly compressive zone ahead of the moving pin. Furthermore, it is quite likely the local strain experienced by α-Mg near the large β-particles is higher compared to the overall macro-scale compressive strain, due to the fact that brittle β-particles cannot be deformed (although which can fracture) which results in the α-Mg being deformed significantly more.

Nonetheless, it is clear that recrystallization of the matrix Mg occurs even when the overall deformation strain is quite low. It has been shown by Liu et al. [127] that under high temperature (400 °C) the matrix Mg can readily recrystallize at a strain between 0.1 and 0.2. Therefore, at a higher temperature (440 °C), it is expected the recrystallization to occur even with strain much less than 0.1. Thus, it is thermodynamically explainable that matrix Mg recrystallizes ~ 2 mm ahead of pin where the overall deformation strain is expected to be very low.

As can be seen from Figure 7-11b to d, as the distance to the pin decreases, the number of recrystallized α-Mg grains gradually increase, primarily due to the increase in pin induced deformation. Recrystallization naturally increases the grain boundary area, which would in turn encourage grain boundary wetting by the molten β-phase. The overall result is that the volume fraction of the β-phase continuously decreases as the pin approaches.

The third important observation can be made from Figure 7-8: that a cluster of fine β-particles form a lamellar structure near the as-cast β-particle (P3). In Mg-Al castings, the formation of this lamellar structure is usually associated with discontinuous precipitation (under relatively slow cooling condition). This lamellar structure usually grows from eutectic β-particles into the α-Mg dendrites, because the Al concentration is higher at the α/β boundaries [128].

P5 locates ~ 1.16 mm ahead of the pin, and the estimated temperature is about 448 °C. It can be seen from Figure 7-6 both the number and the size of the β-particles have been greatly reduced, due to a more intensive melting and subsequent grain boundary wetting effect. This can be confirmed by examining the micrograph shown Figure 7-11d, which locates 1.38 mm ahead of pin (very close

to where P5 locates), clearly showing the wetting of the grain boundaries is very significant. Furthermore, it can be seen from Figure 7-12, that the α + β structure fully occupies the β-particle, and the serrated α/β interface still exists. Such morphology does not differ from that of P3 and P4.

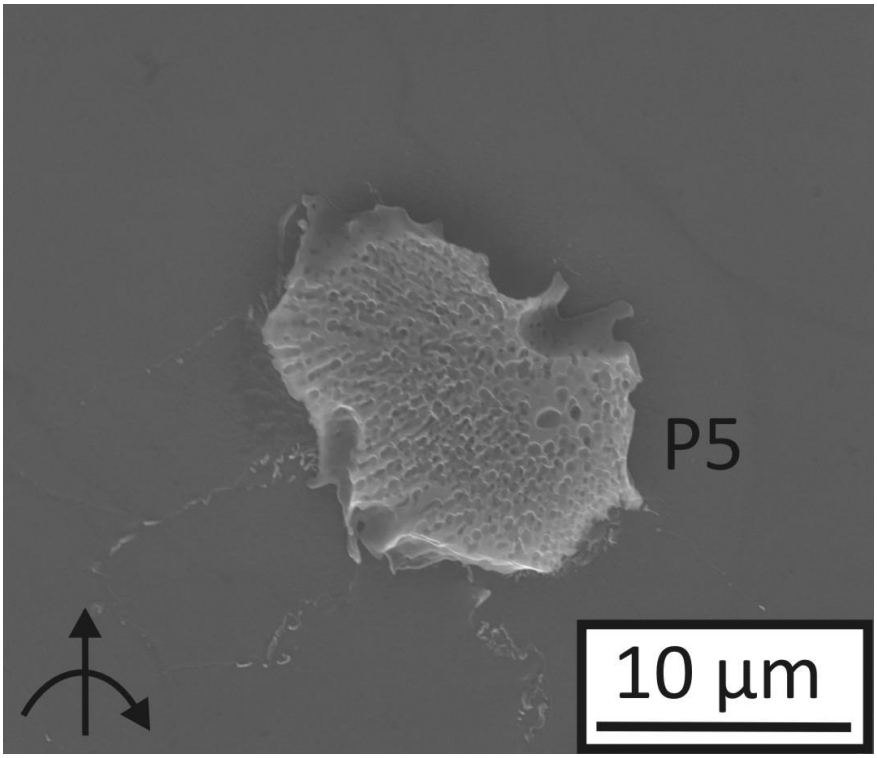

Figure 7-12. A high magnification SEM of P5.

The same reasoning can be used to explain the morphology of P6 (Figure 7-13) and P7 (Figure 7-14), which locate 0.63 mm from the pin and right ahead of the pin respectively. It can be seen from Figure 7-13 that only a few small β-particles can be identified at that location. Particles surrounding P6 have a length less than 10 μm, a very severe decrease in size compared to that of the as-cast particles (which can be longer than 1 mm). Very fine β-precipitates along grain boundaries become an obvious feature near P6, which are indicated by the white arrows in Figure 7-13. Furthermore, it is clear that extensive lamellar precipitates can be found adjacent to the left over β-particles, as marked by the black arrows. As a result of grain boundary wetting by the molten β and subsequent transferring of Al solute into the adjacent α-grains, Al concentration at the outer portion of the recrystallized grains should be relatively high. This high Al concentration tends to promote the formation of the discontinuous precipitation. Finally, at a location

immediately ahead of the pin, few original β-particles can be identified, which indicates that a (near) complete removal of the second phase has been achieved. This can be seen more clearly in Figure 7-14, that only the very fine β-particles along the recrystallized grain boundaries can be observed.

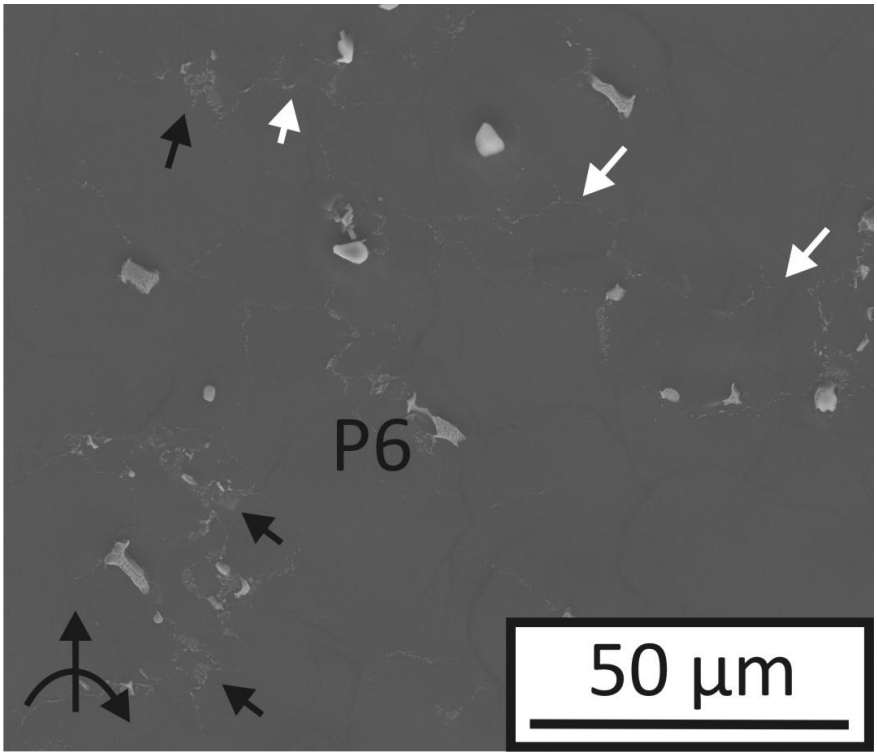

Figure 7-13. Enlarge view of P6. The black arrows indicate the discontinuous precipitates; the white arrows indicate fine of β-particles along grain boundaries.

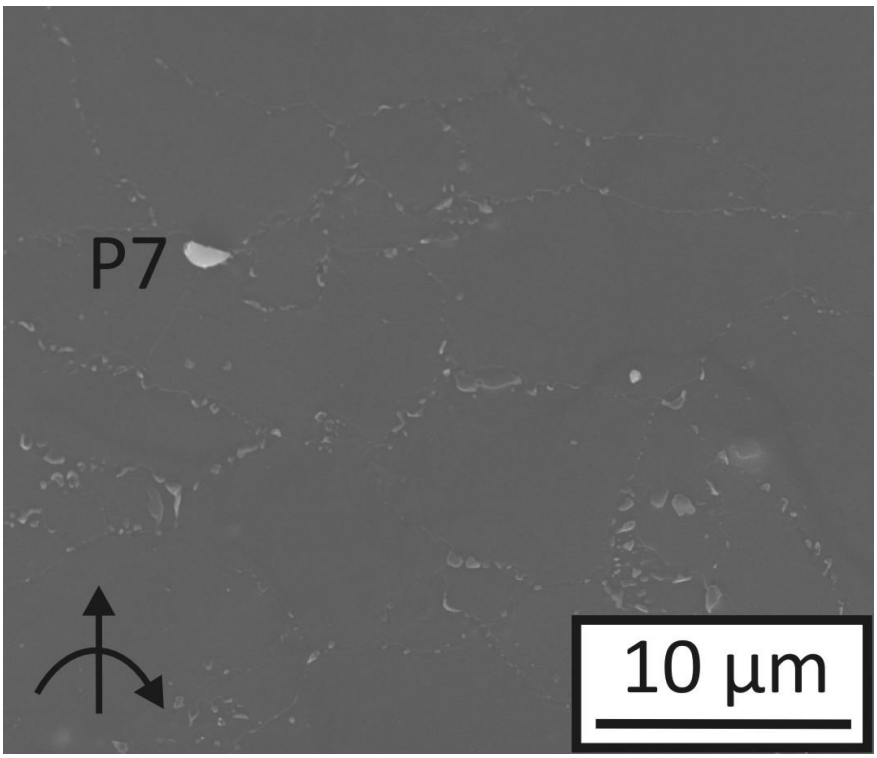

Figure 7-14. A high magnification SEM showing the microstructure right ahead of the pin during FSP AZ91.

7.3.2 Melting and Re-solidification of β-phase during FSP AM60

Up to this point, it is clear that eutectic melting of β-phase, and subsequent grain boundary wetting thus enabling great Al solute transferring into α-Mg matrix and the growth of α-Mg into liquid film, is the governing mechanism leading to the near-full removal β-phase during FSP AZ91. In this section, how β-phase evolves ahead of pin during FSP AM60 will be addressed, so that whether or not the previously mentioned mechanism is a common feature during FSP Mg-Al castings can be determined.

Figure 7-15 gives an overview of the microstructure ahead of pin during FSP AM60. Gradual disappearance of the β-phase (appears white) approaching the pin can be clearly identified. Severely deformed dendrites (appears dark grey) become clear from 0.78 mm ahead of pin.

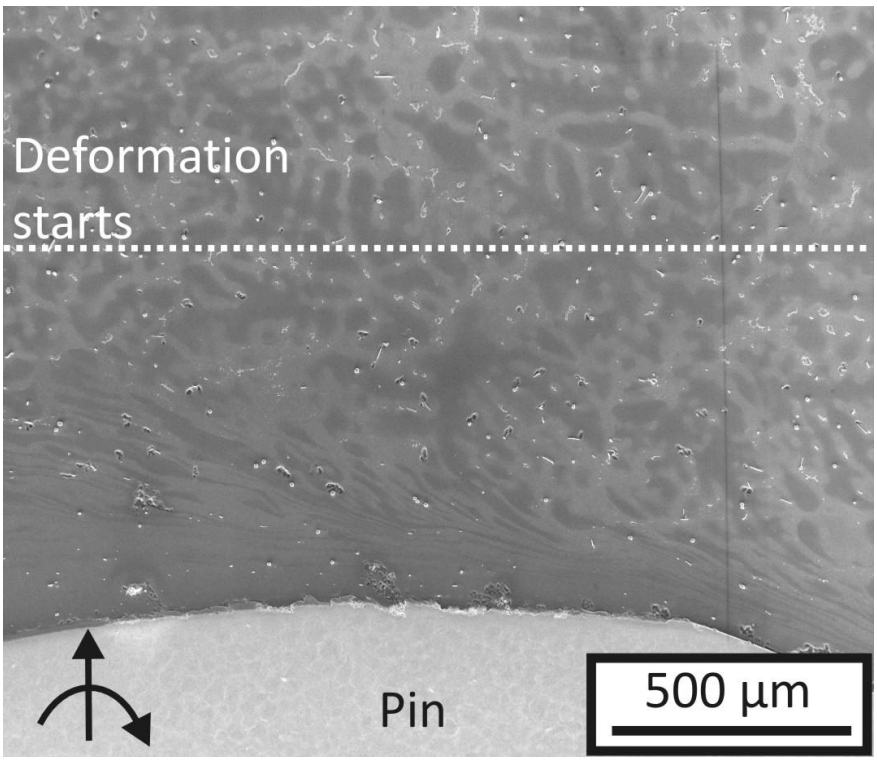

Figure 7-15. Low magnification SEM image showing the microstructure ahead of the pin during FSP AM60. Pin induced deformation became severe from 0.78 mm ahead of pin.

A SEM micrograph focusing on the material locates up to 400 µm ahead of the pin is given in Figure 7-16a. It is clear that manganese containing particles (Al_8Mn_5 and Al_4Mn), do not deform or dissolve as they approach the pin. Therefore their as-cast morphologies (equiaxed and fibrous respectively) are retained even within pin thread spaces (0.8 mm wide). A β-particle is outlined by the small black box, and it can be observed that these particles are hardly found close to the pin front, thus indicating a near total removal of the β-phase by FSP.

A higher magnification SEM image of the β-particle contained in the black box in Figure 7-16a is given in Figure 7-16b for a clearer view. In reference to the morphologies of the β-phase ahead of pin during FSP AZ91 (Figure 7-8 and Figure 7-13), a few common features can be observed, which include: although the macro-scale deformation induced by the pin is clear, the β-phase is not deformed and mechanically broken down as suggested in literature [47]; there is the existence of the two-phase inner structure within the β-particles; the α/β interfaces become very serrated; lamellar α + β structure, due to discontinuous precipitation, existing

adjacent to β-particles; and there are very fine β-precipitates decorating the recrystallized grain boundaries.

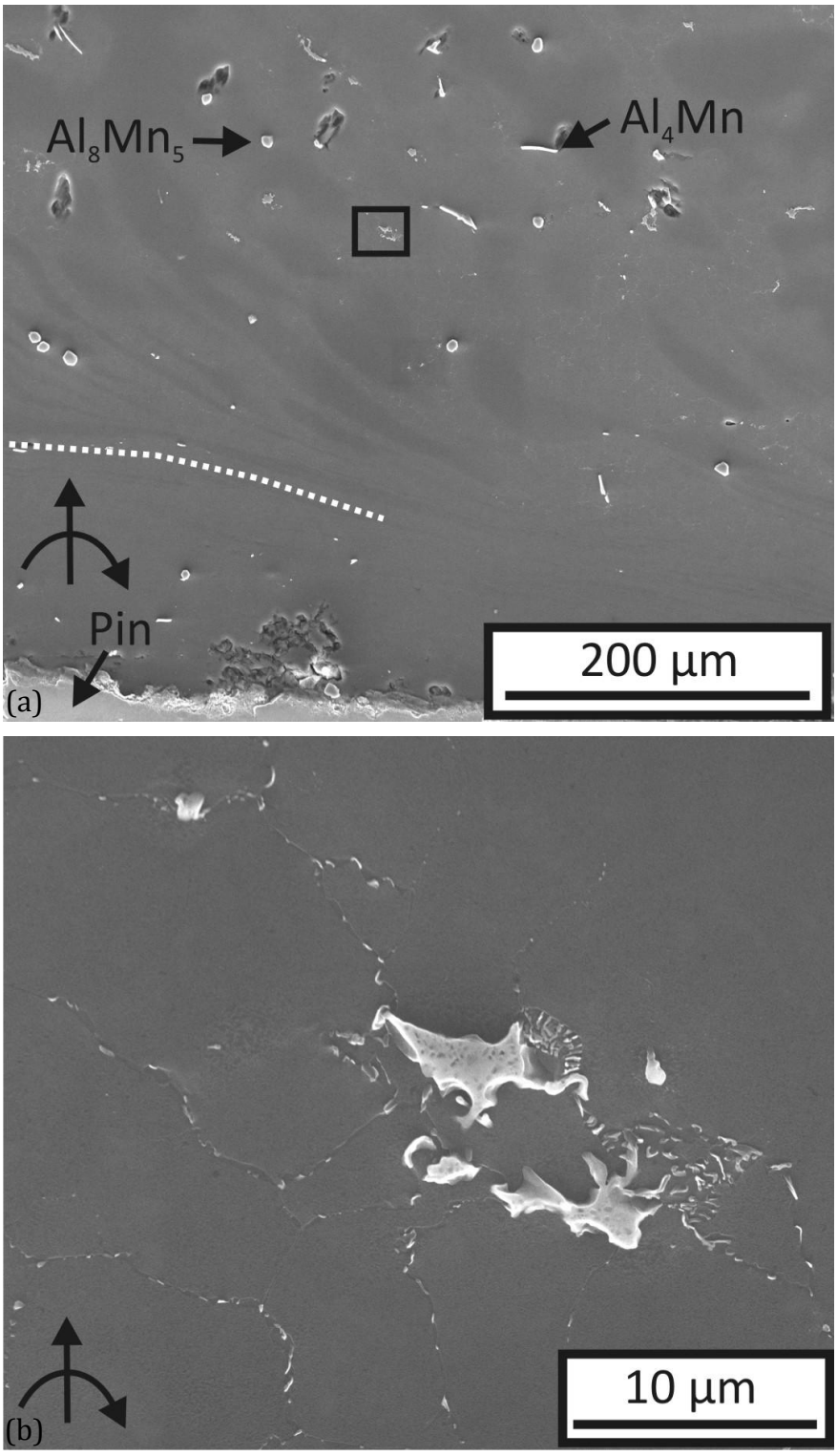

Figure 7-16. A SEM image focusing on the material locates up to 400 µm ahead of pin (a); and a dissolving β-particle contained in the square box in (a) is given in (b) for a clearer view. The white dashed line in (a) marks the outer thread periphery.

7.4 A More Detailed Discussion

The process by which β-phase is removed during FSP AZ91/AM60 was examined in the previous section, which is the primary objective of this chapter. However, two aspects will be further considered specifically in this section. Firstly, quantification of the volume fraction of the β-phase ahead of pin will be presented first, in order to describe the removal of β-phase from a quantitative manner. After that, a more integrated discussion on the eutectic melting, subsequent grain boundary wetting and re-solidification of the β-phase will be given, coupling with temperature data, pin induced deformation, and thermomechanical characteristics of AZ91 and AM60. Thus the fundamental thermomechanics and metallurgy associated with the evolution of β-phase during FSP Mg-Al ingot castings can be understood in a more integrated way.

7.4.1 Quantification on Volume Fraction of β-phase

The volume fractions of the β-phase ahead of the pin during FSP AZ91 and AM60 were determined by using ImageJ software, detailed in Section 2.5.2. Examples of β-phase identification in micrographs taken ahead of pin during FSP AZ91 and AM60 are given in Figure 7-17: (a), (c), (e) and (g) are original micrographs taken from 1687 μm, 0 μm ahead of the pin in FSP AZ91, and 1521 μm and 0 μm ahead of the pin in FSP AM60 respectively. Micrographs with the β-phase outlined by using ImageJ are given to the right to each of the original micrograph.

The volume fractions of β-phase ahead of the pin during FSP AZ91 and AM60 are given in Figure 7-18a and b respectively. The location where binary equilibrium eutectic temperature ($T_{eutectic}$) is reached, is marked. The volume fractions of β-phase of the as-cast AZ91 and AM60 microstructures are given to the right of each plot.

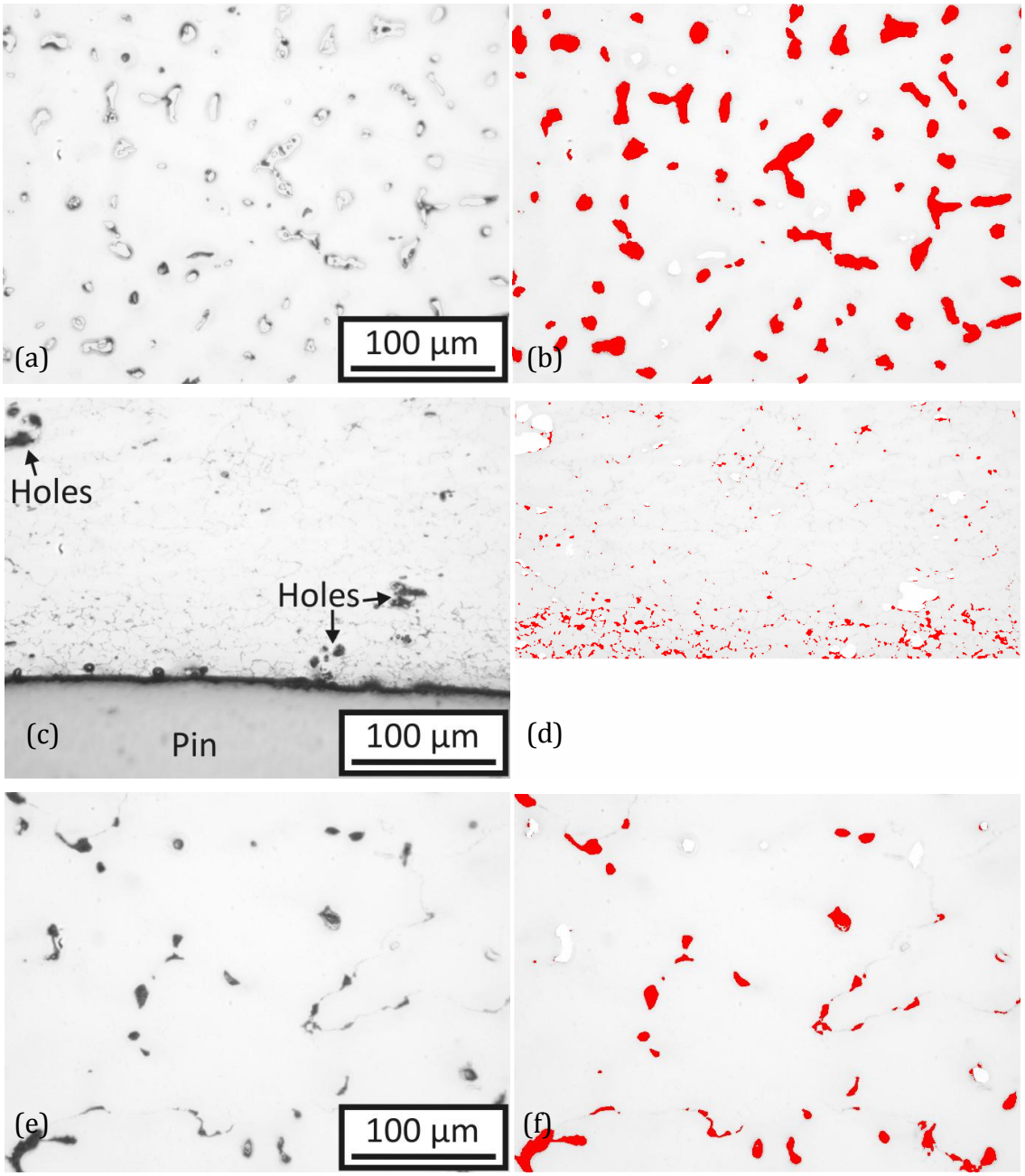

Figure 7-17. Original micrograph and micrograph with β-phase outlined, taken from 1687 µm (a-b), 0 µm (c-d) ahead of pin during FSP AZ91; and from 1521 µm (e-f), 0 µm (g-h) ahead of pin during FSP AM60.

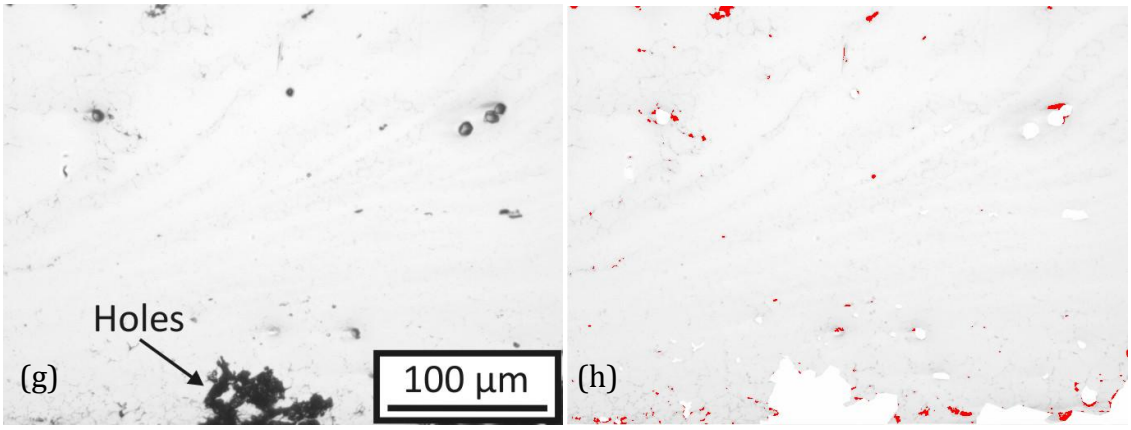

Figure 7-17. Continued.

It can be seen from Figure 7-18a that as $T_{eutectic}$ is reached, the faction of β-phase starts to decrease continuously from 8.5 to 0.6 vol%. The data suggests that the grain boundary wetting (and subsequent Al solute diffusion and resolidification) has been a rather continuous and steady process.

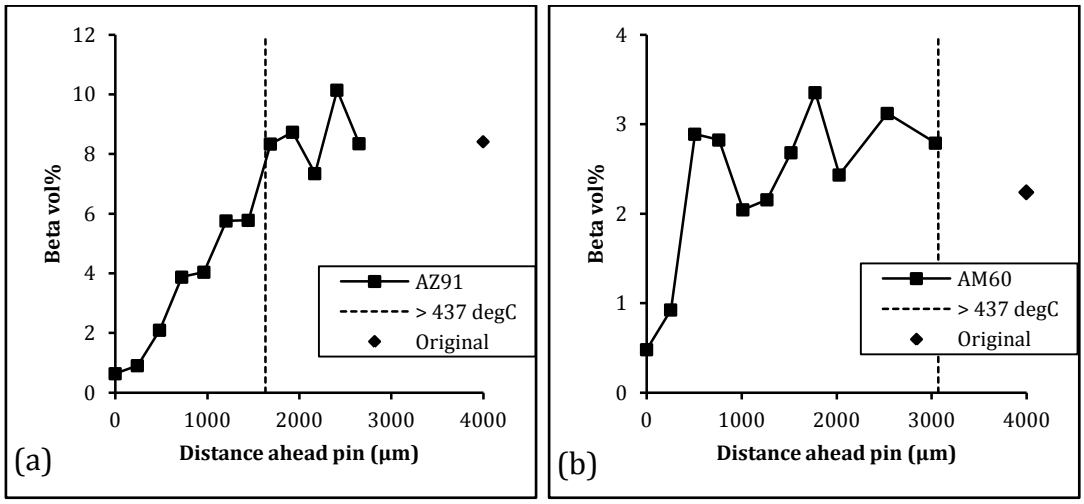

Figure 7-18. Volume fraction of β-phase as a function of distance ahead of pin during FSP AZ91 (a) and AM60 (b). "> 437 degC" denotes the location where temperature has reached $T_{eutectic}$, "original" denotes the fraction of β-phase of the as-cast AZ91 and AM60 microstructure.

A rather different observation can be made from Figure 7-18b. Although temperature has reached $T_{eutectic}$ since ~ 3 mm ahead of the pin, no obvious trend in the change in β-phase fraction can be recognized between 1–3 mm. The volume fraction obtained from a micrograph taken from the as-cast AM60 material is 2.2 vol%. In general, the volume fraction within approximately 1–3 mm ahead of pin has remained fairly close to the as-cast state.

That being said, eutectic melting of the β-phase does occur within this region, as can be seen from Figure 7-19a, which is taken from a location 3.16 mm ahead of the pin. As indicated, the α + β inner structure can be observed within most of the β-particles, indicating the occurrence of eutectic melting of the β-phase and resolidification. However, a few β-particles still display the as-cast fully divorced morphology. At a location 1.91 mm ahead of pin (Figure 7-19b), all β-particles have been melted and resolidified during quenching. However, little grain boundary wetting phenomenon can yet be observed at this stage. Such phenomenon finally becomes obvious at a location ~ 1 mm ahead of the pin, as indicated in Figure 7-19c and d.

In contrast, the grain boundary wetting during FSP AZ91 occurs at a much earlier stage: 1.72 mm ahead of pin, as indicated in Figure 7-8. Such observation has not yet been fully understood in the current study. However, it might be related to the fact that β-particles in as-cast AZ91 are larger and have much higher aspect ratio compared to these in as-cast AM60. This can be readily observed from Figure 2-4b and c. It has been previously discussed that material is located well ahead of pin (~ 2 mm ahead) experiences a slight macro-scale deformation during FSP AZ91. However, the existence of non-deformable β-particles causes the surrounding α-Mg to be locally deformed more intensively (Figure 7-11), thus causing recrystallization of the α-Mg. Following this logic, it is not surprising that during FSP AM60 the local recrystallization of α-Mg only occurs at a much later stage (~ 1 mm ahead pin) compared to FSP AZ91, due to the fact that less and smaller β-particles exist in AM60.

Therefore, although extensive melting of the β-phase occurs between 1–3 mm ahead of pin during FSP AM60, the fraction of the β-phase will not be significantly changed because the volume of the liquid pool has not been significantly reduced by grain boundary wetting, which is due to the recrystallization of α-Mg occurs at a much later stage. However, recrystallization and grain boundary effect will finally occur at a position very close to the pin, where the pin induced deformation becomes severe. This can be clearly observed in Figure 7-19c to f, which locate ~ 1 mm or less ahead of the pin. Hence, grain boundary wetting and subsequent Al

solute transfer into the Mg matrix can finally take place, leading to the removal of the β-phase.

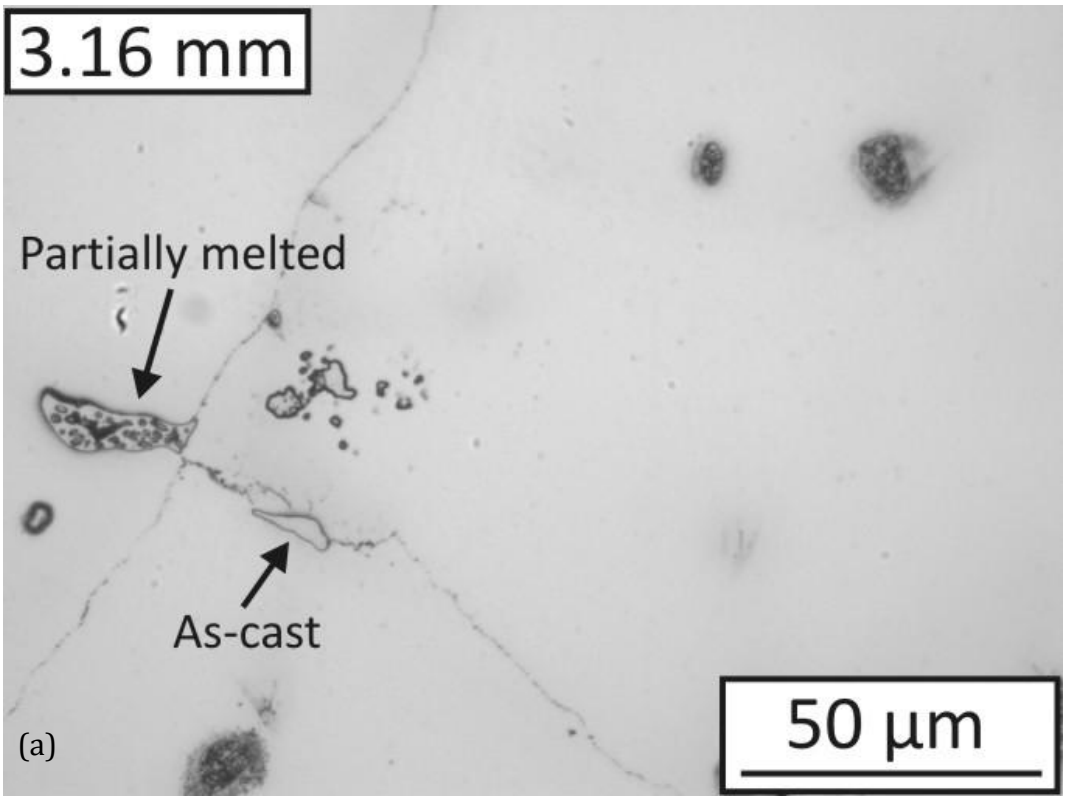

Figure 7-19. (a)–(f) Microstructures taken ahead of pin during FSP AM60, with distance ahead of pin given at the upper left of each micrograph.

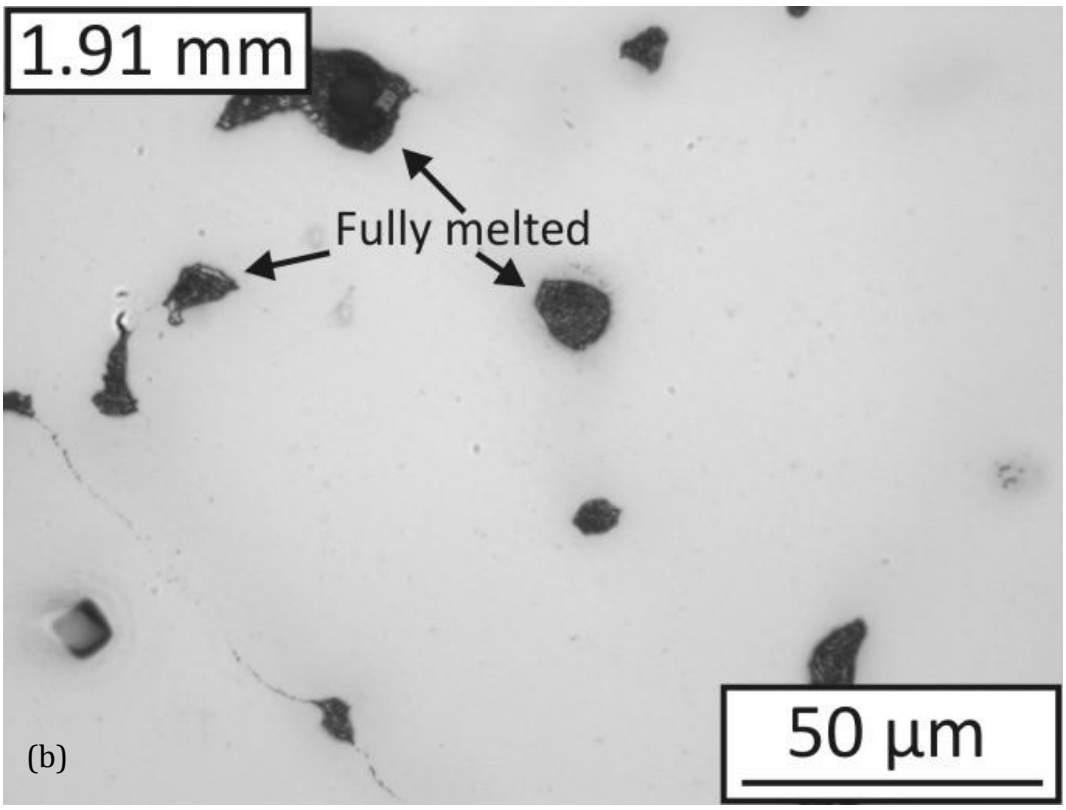

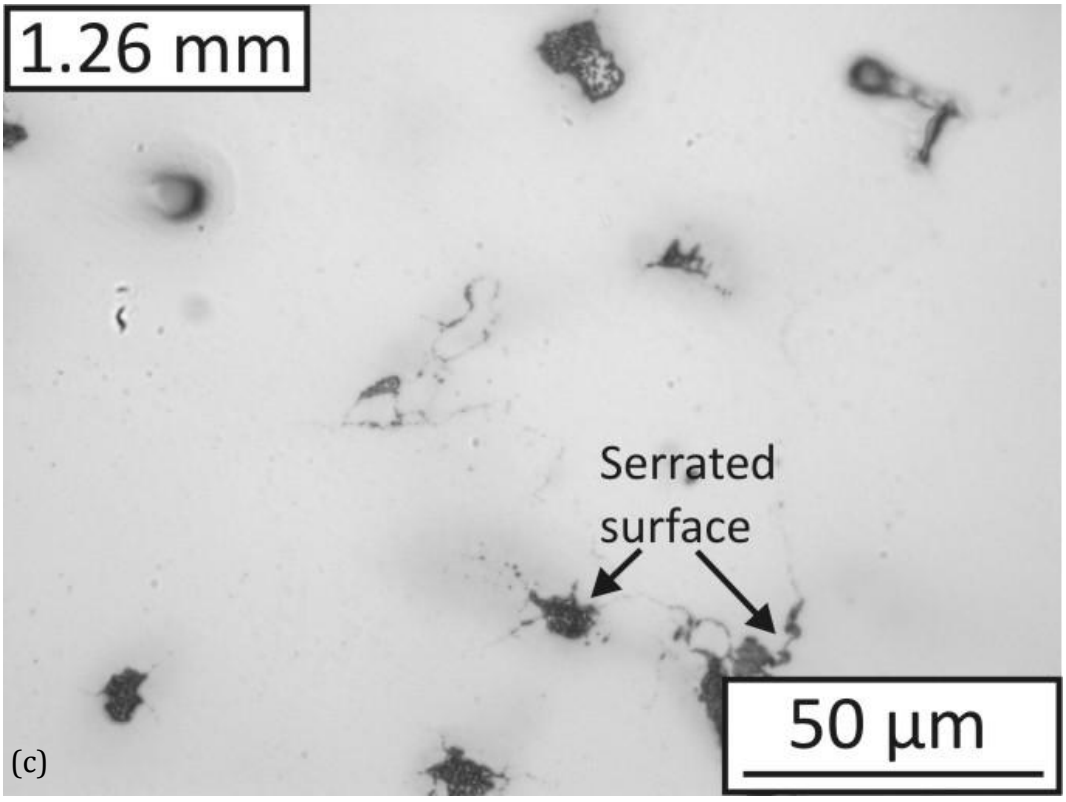

Figure 7-19. Continued.

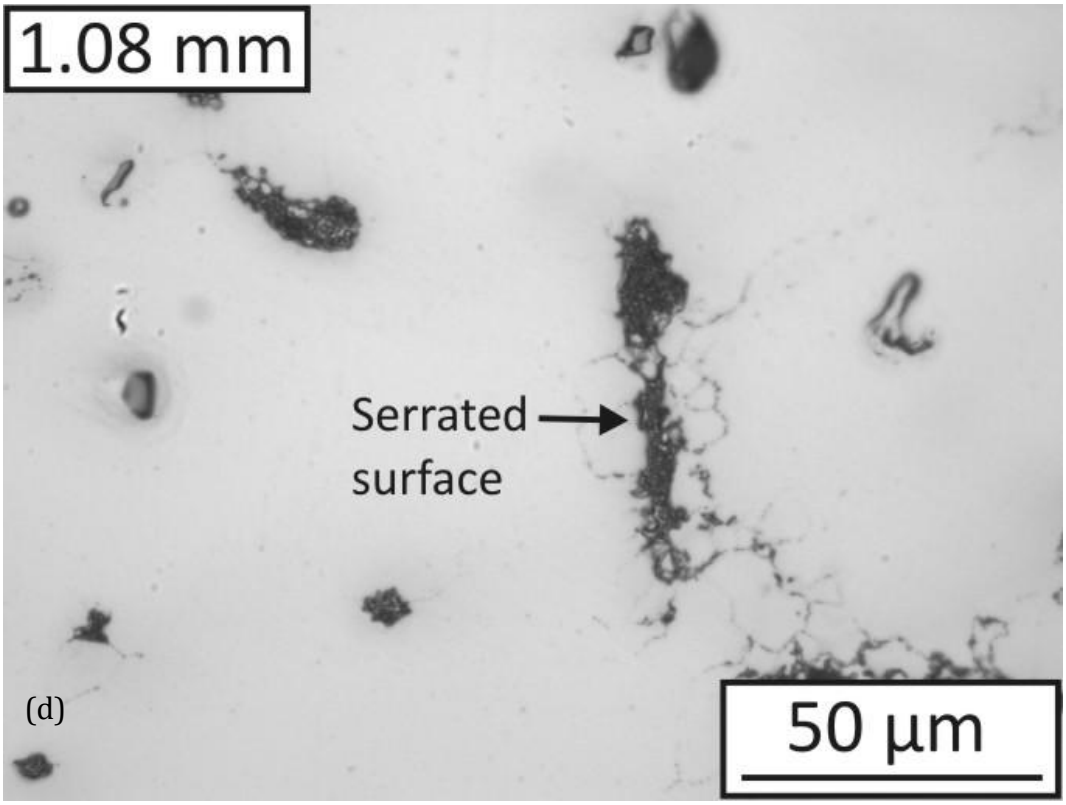

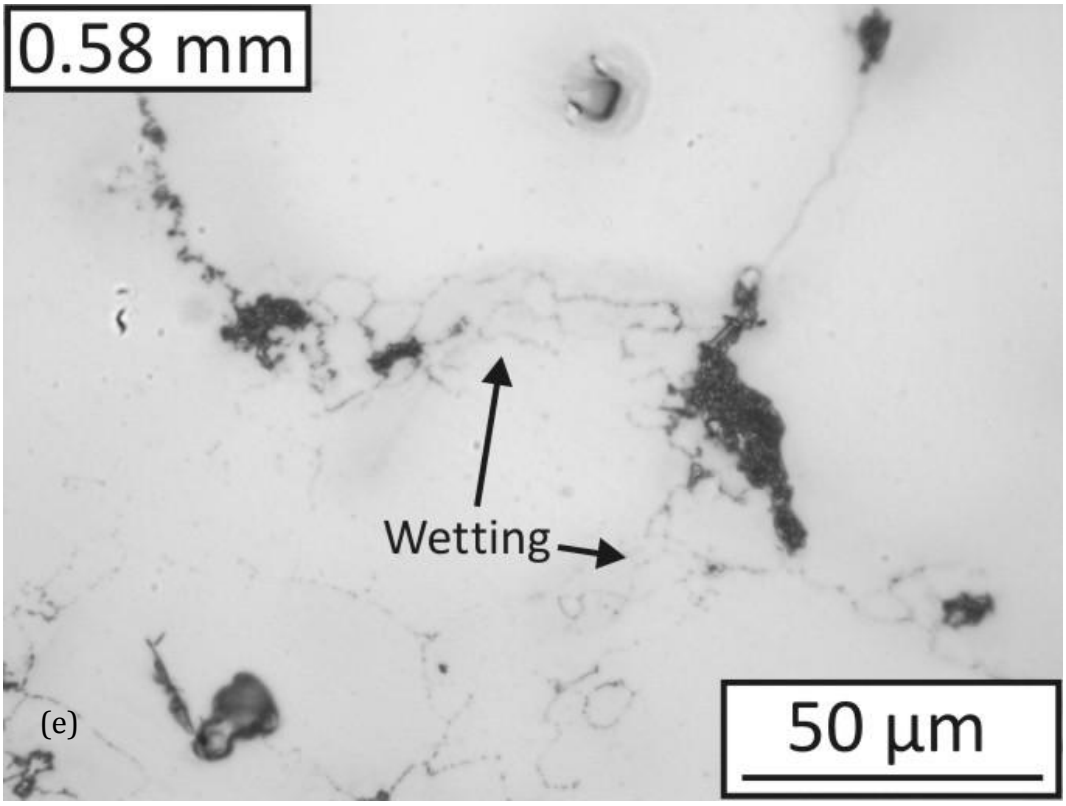

Figure 7-19. Continued.

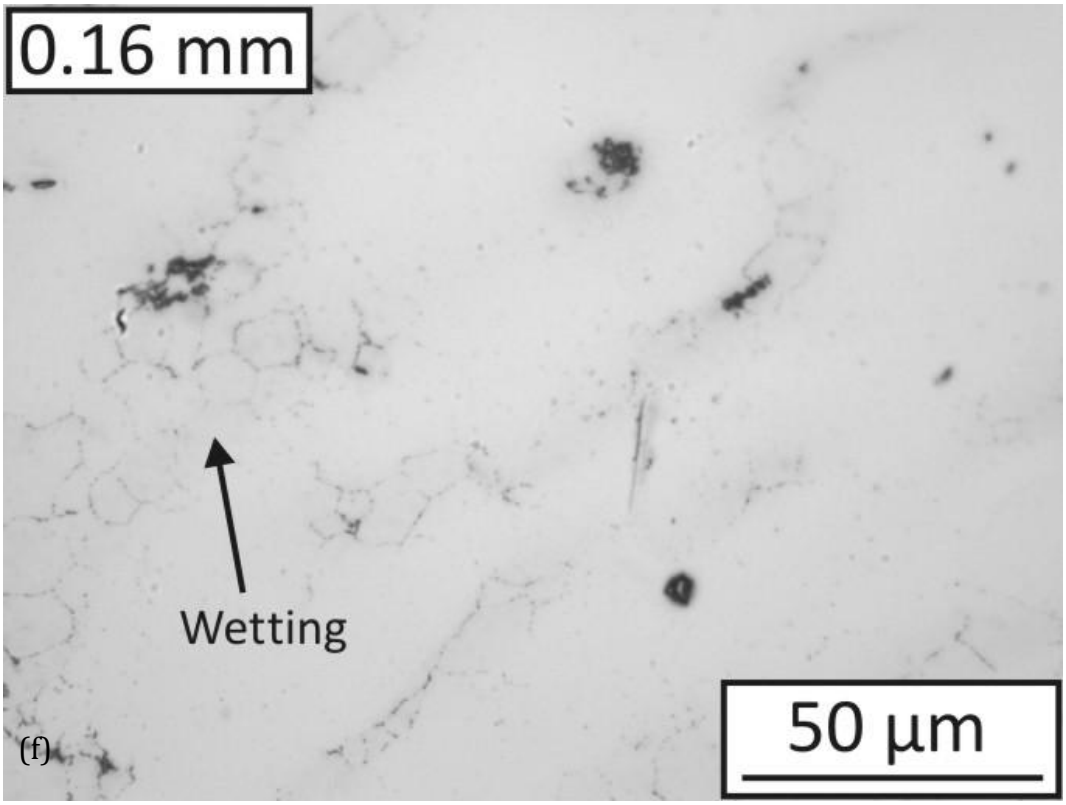

Figure 7-19. Continued.

7.4.2 Self-limiting Effect of FSP

After understanding the mechanism governing the melting and re-solidification of the β-phase during FSP Mg-Al castings, we can extend our analysis on the significant temperature difference between FSP AZ91 and AM60. Let us revisit the Mg-Al phase diagram again, as given in Figure 1-8. In general, Mg alloys with higher Al content corresponds to lower equilibrium solidus temperature. Under equilibrium condition, the solidus temperatures of AZ91 and AM60 are 470 and 540 °C respectively.

However, the solidification condition of AZ91 and AM60 is far from being equilibrium. As introduced in Section 1.2.1, during solidification of Mg-Al casting, Mg dendrites will solidify in such a way that Al content is the lowest at the centre of the dendrites; while it gradually increases towards the outer portion of the dendrites thus reaching the maximum at the α/β interface (Figure 7-20). As a result of this composition segregation, the non-equilibrium solidus temperature is highest at the centre of the dendrites, and it decreases towards the α/β interface.

On the other hand, the solute composition in wrought alloys is usually homogenized, and hence the equilibrium solidus temperature is meaningful.

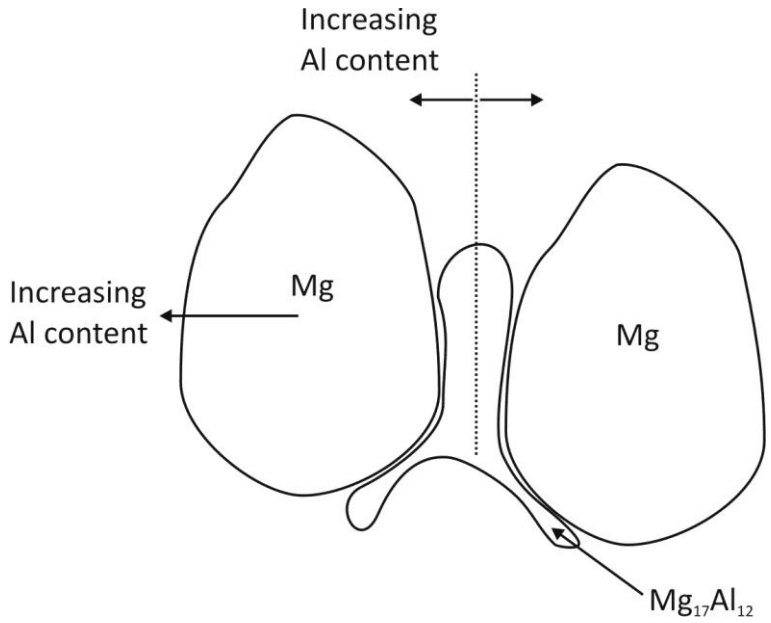

Figure 7-20. Schematic illustration of the Al distribution within Mg dendrites and $Mg_{17}Al_{12}$ particles.

FSP is a self-limiting process: heat is generated during FSP as the tool rotates and translates against the workpiece. Intrinsically, energy is positively influenced by the flow stress of the workpiece, which itself is temperature dependent. As the temperature increases due to the energy input, the flow stress of the material drops. If the material eventually melts, the existence of liquid would act as lubricant between tool and workpiece thus the heat generating ability during FSP will be substantially decreased. Hence, no gross material melting should occur during FSP of a single phase alloy. Therefore, during FSP wrought alloys (which are well homogenised), the maximum temperature during FSP is limited by the equilibrium solidus temperature of the workpiece. However, there are practically no equilibrium solidus temperatures in Mg-Al cast alloys due to Al solute segregation. Hence, during FSP Mg-Al cast alloys, even though a small (outer) portion of the dendrites and the β-phase melt during FSP, the inner portion of the dendrite is still in solid-state. Thus, the lubrication effect exists between tool and workpiece is expected to be small and hence further heat will be generated which will lead to further temperature rise.

Supporting this argument are studies of the compressive strength of partially molten AZ91 [129] demonstrating that there is no abrupt drop in flow stress at the eutectic temperature when melting begins. Indeed, even up to liquid fractions of 7.5%, the reported flow stress does not deviate from that expected had no melting occurred. However, the FSP process eventually will become self-limiting as the liquid pool reaches a certain fraction.

As illustrated in Figure 7-3a, the maximum recorded temperatures during FSP AZ91 and AM60 are 447 °C and > 560 °C respectively. As explained previously, the lower processing speed used during FSP AM60 is partially responsible for this temperature difference. However, following the self-limiting effect argument given above, it might be possible that the fraction of the melted β-phase is intrinsically higher during FSP AM60 than during FSP AZ91. Therefore, on average, more melting of the dendrites is allowed during FSP AM60 before FSP becomes self-limiting due to severe reduction in flow stress. Hence, a higher temperature can be obtained during FSP AM60. It is important to point out that more systematic investigation is required in order to clarify the relationship between the amount of melting and maximum attainable temperature during FSP Mg cast alloys.

7.5 Summary

To summarize this chapter, it has been clearly demonstrated that eutectic melting of the β-phase, and subsequent wetting of the recrystallized α-Mg grain boundaries, have occurred ahead of the pin during FSP Mg-Al cast alloys. The wetting effect greatly increases the interface between liquid pool and α-Mg grains, and thus the transfer of Al-solute into the α-matrix and the growth of α-Mg into the liquid film is significantly enhanced. It has been proposed that this mechanism is primarily responsible for the removal of the β-phase during FSP Mg-Al alloys, as opposed to the commonly suggested solid-state dissolution which involves mechanical-breakage of β-particles and unrealistic acceleration of diffusion coefficient. Furthermore, it has been proposed that higher temperature can be achieved during FSP AM60 than FSP AZ91 because less molten of β-phase exists ahead of

pin during FSP AM60 than FSP AZ91. Hence, the existence of liquid which limits the heat generation and temperature rise is less severe during FSP AM60 than FSP AZ91.

Chapter 8. Conclusions

The major conclusions of this thesis can be summarised as below:

a. Based on fitting the torque (M) data obtained from FSP A356 experiments covering wide ranges of rotation (ω) and linear speeds (v), the relationship between M and ω has been found to be well described by an exponential decay function: $M = M_o + M_f \exp(-n\omega)$. The influences of v on torque can be described reasonably well by linearly relating model parameters (M_o, M_f and n) to v. This model remains valid for any given ω and v value, as long as the process can still be characterized as FSP under those conditions.

   Using the model, a detailed evaluation of how strong the dependence of M on ω and v can be conducted. A dependence analysis has confirmed the general view that M is affected more by ω than by v, although this is not necessarily true at high ω values. The dependence of M on ω is a result of the change in material flow resistance. Thus, the physical meaning of M when ω approaches zero relates to the alloy strength at room temperature. The models allows for n and M_f to be adjusted to accommodate the alloying effect in the low ω range. M_o indicates high temperature strength of aluminium alloys during FSP at high ω range, where the alloy effect on material flow resistance has diminished.

   Models derived from the torque model relating tool power (P) and specific energy (E_s) to ω are also shown to extrapolate well for any ω. It has been found that over a wide range of commonly used ω, P increases only slightly when ω increases and E_s is not affected significantly by ω.

b. A method has been established in this study to quantify the cross section areas of shoulder and nugget flow zones ($A_{shoulder}$ and A_{nugget}). Based on these shoulder and nugget flow volumes generated per revolution (V_{S-rev} and V_{N-rev}) can be determined as the products of flow areas and v/ω (which is the tool advance distance per revolution).

Either increasing ω or decreasing v enhances pin shearing effect which results in an increase in A_{nugget} (and thus V_{N-rev}). In a confined space (i.e. cross section of the workpiece being constant), a larger nugget zone, which forms before the shoulder zone, results in a smaller $A_{shoulder}$ (and V_{S-rev}).

It has been observed that representing torque (M) as energy input per revolution is theoretically correct and meaningful in FSP study. It has been found V_{S-rev} is related to M, and this relationship is well described using an exponential rise function: $M = M_o + M_f[1 - \exp(-\gamma V_{S-rev})]$, where M_o and M_f are the same as in the torque model. V_{N-rev}, although being fairly large under low v and high ω condition, does not require a significant amount of energy input per revolution (M). This is because, geometrically, shoulder has a larger radius than the pin; hence to generate the same amount of material flow, a larger torque (which is positively related to radius) is required by the shoulder than by the pin. Thermomechanically, material flow resistance in the shoulder region is (overall) significantly higher than that in the nugget region, because temperature at shoulder zone is much lower than that at nugget zone, which is supported by thermocouple measurements in various locations in the stir zone during FSP A356. Thus more torque is required by the shoulder than by the pin to induce an equal amount of material flow, due to higher material flow resistance.

c. Under a normal condition (224 mm/min, 710 rpm, and 2.5° tilt), FSP A356 alloy yields highly segregated deformation regions in the nugget zone (on the cross section): with one region located on advancing side and lower mid-retreating side, characterized by refined Si particles evenly distributed among recrystallized Al grains (denoted as RSM); while the other region has only undergone mild deformation and thus the as-cast dendritic feature is still apparent. The flow segregation is a common feature under all FS conditions in current study, although the relative portions vary depending on the speeds.

It has been found that RSM occupies the entire thread space and rotates with the pin. At the back, a major portion of RSM was forced to deposit on

the advancing side due to a high pressure zone ahead of pin; a smaller portion deposits downward, due to pin screwing down effect, forming the lower mid-retreating side of the nugget. Shear flow material outside the thread spaces formed the rest of the nugget. This portion of the nugget has not experienced a sufficiently high amount of deformation so that the as-cast dendritic feature is still apparent, and an even distribution of Si particles has not been achieved.

A steep strain gradient in the transient zone (ahead of pin) was established. The deformed dendrites have acted as flow markers and this has enabled, for the first time, a realistic and a more direct estimation of strain and strain rate experienced by the workpiece during FSP. It has been estimated that in the transient flow zone, material deformed up to strains of 3.2–3.9, and strain rates of 69–97 s^{-1}, with ω = 710 rpm, v = 112 and 160 mm/min respectively.

d. Geometrical dynamic recrystallization (GDRX) has been found to be the primary mechanism governing the refinement of the Al dendrites, which involves gradual thinning of the dendrites thus eventually causing grain boundary impingement thus forming fine (3–5 μm) equiaxed grains. In the Al-Si eutectic region, non-deforming Si particles accelerate the recrystallization of adjacent Al matrix.

The as-cast Al dendrites display a “Cubic” texture. Recrystallized Al grains, regardless of location relative to the pin, display a dominating “A” shear texture. A small portion of material has stuck with the pin, and the recrystallized Al grains within which display a “Cubic” texture, which could be attributed to excessive static annealing effect.

Local textures, with frame (Z, θ, r), must be rotated around sample frame (ND, TD, RD) to obtain the standard texture because the former misaligns with the later. It has been found that the amount of rotation around ND is dependent on the incline angle between shear direction (tangential to pin thread) and the sample transverse direction (TD). Rotations around (TD,

RD) are related to the screwing down effect induced by the rotating thread. This downward flow is most severe on the advancing side of the thread space, thus large rotations (up to 50° and 20° around TD and RD) are required.

The overall texture rotation involves rotating a large amount of Al unit cells around (ND, RD, TD) for equal amounts. Therefore, the textures before and after the rotation remain the same. However, the evolution from one texture to another involves rotating equal amounts of Al unit cells for opposite amounts. It has been shown that a less amount of rotation is required to transform the as-cast "Cubic" texture to "A" texture compared to "B" texture. Hence, the "A" shear texture is the preferred texture as far as the amount of rotation is concerned, which is consistent with the dominant "A" texture found in the present FSP A356 sample.

e. The as-cast microstructures of AZ91 and AM60 ingots contain coarse dendritic α-Mg (~ 200 μm), with fully and partially divorced β-particles (~ 100 μm), alongside with small quantities of manganese containing particles (mostly Al_8Mn_5 and Al_4Mn). FSPs on AZ91 and AM60 resulted in fully recrystallized α-Mg (10–15 μm) occupying the nugget zone. Furthermore, the amount of as-cast β-phase has been significantly reduced while only fine β-particles (<< 1 μm) along grain boundaries can be observed. The manganese containing particles persist with their quantity and morphology hardly changed.

Detailed metallurgical analysis in this work has revealed that there is no evidence supporting that β-particles were mechanically broken up during FSP. It is clear that eutectic melting of the β-phase occurred well ahead of pin, and this is thermodynamically justified by the fact that the corresponding temperature was well above binary equilibrium $T_{eutectic}$ (437 °C). This implied that eutectic melting is the key step influencing the evolution of the β-phase during FSP.

Along with melting of β-phase in the region approaching the pin where plastic deformation have also started, the deformed α-Mg also started recrystallization and thus the amount of grain boundary also have started to increase. Recrystallization started in locations adjacent to β-phase particles, likely the result of the strain incompatibility between deformable α-Mg and non-deformable β-phase. As the material approached more to the pin and thus the amount of deformation increased and also temperature also increased, the amount of recrystallization increased.

Evidence has shown that liquid, formed due to eutectic melting, extensively wet the adjacent recrystallized grain boundaries, thus increasing considerably the liquid-solid interface. Thermodynamically, back diffusion of Al to the α-Mg interiors and the growth of α-Mg into the liquid (solidification) result in lowering the amount of Al rich liquid present. Kinetically, the considerable increase in the liquid-solid interfacial area must have accelerated that process of consuming that Al rich liquid. This is primarily the mechanism governing the β-phase removal during FSP of Mg-Al cast alloys.

References

1. R.S. Mishra and Z.Y. Ma, *Friction stir welding and processing.* Materials Science and Engineering R, 2005. **50**(1-2): p. 1-78.

2. R.S. Mishra, et al., *High strain rate superplasticity in a friction stir processed 7075 Al alloy.* Scripta Materialia, 1999. **42**(2): p. 163-168.

3. Z.Y. Ma, *Friction stir processing technology: A review.* Metallurgical and Materials Transactions A, 2008. **39**(3): p. 642-658.

4. Z.Y. Ma, et al., *Microstructural refinement and property enhancement of cast light alloys via friction stir processing.* Scripta Materialia, 2008. **58**(5): p. 361-366.

5. P. Cavaliere and P.P. De Marco, *Friction stir processing of AM60B magnesium alloy sheets.* Materials Science and Engineering: A, 2007. **462**(1-2): p. 393-397.

6. D.R. Ni, et al., *Enhancing the high-cycle fatigue strength of Mg-9Al-1Zn casting by friction stir processing.* Scripta Materialia, 2009. **61**(6): p. 568-571.

7. A.H. Feng and Z.Y. Ma, *Microstructural evolution of cast Mg-Al-Zn during friction stir processing and subsequent aging.* Acta Materialia, 2009. **57**(14): p. 4248-4260.

8. D. Zhang, M. Suzuki, and K. Maruyama, *Microstructural evolution of a heat-resistant magnesium alloy due to friction stir welding.* Scripta Materialia, 2005. **52**(9): p. 899-903.

9. Y.N. Wang, et al., *Texture and weak grain size dependence in friction stir processed Mg-Al-Zn alloy.* Scripta Materialia, 2006. **55**(7): p. 637-640.

10. R. Nandan, T. DebRoy, and H.K.D.H. Bhadeshia, *Recent advances in friction-stir welding - Process, weldment structure and properties.* Progress in Materials Science, 2008. **53**(6): p. 980-1023.

11. P.L. Threadgill, et al., *Friction stir welding of aluminium alloys.* International Materials Reviews 2009. **54**(2): p. 49-93.

12. R.W. Fonda, J.F. Bingert, and K.J. Colligan, *Development of grain structure during friction stir welding.* Scripta Materialia, 2004. **51**(3): p. 243-248.

13. U.F.H.R. Suhuddin, et al., *Grain structure evolution during friction-stir welding of AZ31 magnesium alloy.* Acta Materialia, 2009. **57**(18): p. 5406-5418.

14. P.B. Prangnell and C.P. Heason, *Grain structure formation during friction stir welding observed by the `stop action technique'.* Acta Materialia, 2005. **53**(11): p. 3179-3192.

15. R.W. Fonda, K.E. Knipling, and J.F. Bingert, *Microstructural evolution ahead of the tool in aluminum friction stir welds.* Scripta Materialia, 2008. **58**(5): p. 343-348.

16. T. Long, W. Tang, and A.P. Reynolds, *Process response parameter relationships in aluminium alloy friction stir welds.* Science & Technology of Welding & Joining, 2007. **12**(4): p. 311-317.

17. P.A. Colegrove and H.R. Shercliff, *Experimental and numerical analysis of aluminium alloy 7075-T7351 friction stir welds.* Science & Technology of Welding & Joining, 2003. **8**(5): p. 360-368.

18. P. Upadhyay and A.P. Reynolds, *Effects of thermal boundary conditions in friction stir welded AA7050-T7 sheets.* Materials Science and Engineering: A. **In Press, Corrected Proof**.

19. P. Kalya, et al. *Specific energy and temperature machanistic models for friction stir processing of Al-F357*. in *Friction Stir Welding and Processing IV*. 2007. Orlando, Florida, USA: TMS.

20. M. Peel, et al., *Dissimilar friction stir welds in AA5083-AA6082. Part I: Process parameter effects on thermal history and weld properties.* Metallurgical and Materials Transactions A, 2006. **37**(7): p. 2183-2193.

21. K.J. Colligan and R.S. Mishra, *A conceptual model for the process variables related to heat generation in friction stir welding of aluminum.* Scripta Materialia, 2008. **58**(5): p. 327-331.

22. J.W. Pew, T.W. Nelson, and C.D. Sorensen, *Torque based weld power model for friction stir welding.* Science & Technology of Welding & Joining, 2007. **12**(4): p. 341-347.

23. J.H. Yan, M.A. Sutton, and A.P. Reynolds, *Process-structure-property relationships for nugget and heat affected zone regions of AA2524-T351 friction stir welds.* Science & Technology of Welding & Joining, 2005. **10**(6): p. 725-736.

24. A.P. Reynolds, et al., *Relationships between weld parameters, hardness distribution and temperature history in alloy 7050 friction stir welds.* Science & Technology of Welding & Joining, 2005. **10**(2): p. 190-199.

25. W.J. Arbegast, *A flow-partitioned deformation zone model for defect formation during friction stir welding.* Scripta Materialia, 2008. **58**(5): p. 372-376.

26. S. Xu and X. Deng, *A study of texture patterns in friction stir welds.* Acta Materialia, 2008. **56**(6): p. 1326-1341.

27. S.R. Ren, Z.Y. Ma, and L.Q. Chen, *Effect of welding parameters on tensile properties and fracture behavior of friction stir welded Al-Mg-Si alloy.* Scripta Materialia, 2007. **56**(1): p. 69-72.

28. M. Peel, A. Steuwer, and P. Withers, *Dissimilar friction stir welds in AA5083-AA6082. Part II: Process parameter effects on microstructure.* Metallurgical and Materials Transactions A, 2006. **37**(7): p. 2195-2206.

29. J. Yan, M.A. Sutton, and A.P. Reynolds, *Process-structure-property relationships for nugget and heat affected zone regions of AA2524â€"T351 friction stir welds.* Science & Technology of Welding & Joining, 2005. **10**(6): p. 725-736.

30. F.C. Liu and Z.Y. Ma, *Influence of tool dimension and welding parameters on microstructure and mechanical properties of friction-stir-welded 6061-T651 aluminum alloy.* Metallurgical and Materials Transactions A, 2008. **39**(10): p. 2378-2388.

31. C.Y. Lee, et al., *Lap joint properties of FSWed dissimilar formed 5052 Al and 6061 Al alloys with different thickness.* Journal of Materials Science, 2008. **43**(9): p. 3296-3304.

32. B.C. Yang, et al., *Banded microstructure in AA2024-T351 and AA2524-T351 aluminum friction stir welds: Part I. Metallurgical studies.* Materials Science and Engineering A, 2004. **364**(1-2): p. 55-65.

33. Y.H. Zhao, et al., *Influence of pin geometry on material flow in friction stir welding process.* Materials Science and Technology, 2006. **22**(1): p. 45-50.

34. T.U. Seidel and A.P. Reynolds, *Visualization of the material flow in AA2195 friction-stir welds using a marker insert technique.* Metallurgical and Materials Transactions A, 2001. **32**(11): p. 2879-2884.

35. H.N.B. Schmidt, T.L. Dickerson, and J.H. Hattel, *Material flow in butt friction stir welds in AA2024-T3.* Acta Materialia, 2006. **54**(4): p. 1199-1209.

36. K. Colligan, *Material Flow Behavior during Friction Stir Welding of Aluminum.* Welding Journal, 1999. **78**: p. 229-237.

37. Z.W. Chen, T. Pasang, and Y. Qi, *Shear flow and formation of nugget zone during friction stir welding of aluminium alloy 5083-O.* Materials Science and Engineering A, 2008. **474**(1-2): p. 312-316.

38. Z.W. Chen and S. Cui, *On the forming mechanism of banded structures in aluminium alloy friction stir welds.* Scripta Materialia, 2008. **58**(5): p. 417-420.

39. U.F.H.R. Suhuddin, et al., *Grain structure and texture evolution during friction stir welding of thin 6016 aluminum alloy sheets.* Materials Science and Engineering: A. **527**(7-8): p. 1962-1969.

40. Z.W. Chen, et al., *Material flow and the shear layer in the upper weld zone during friction stir welding of aluminium alloys.* International Journal of the Society of Materials Engineering for Resources 2006. **20**: p. 4081-4086.

41. S. Mukherjee and A.K. Ghosh, *Flow visualization and estimation of strain and strain-rate during friction stir process.* Materials Science and Engineering: A, 2010. **527**(20): p. 5130-5135.

42. O. Frigaard, O. Grong, and O.T. Midling, *A process model for friction stir welding of age hardening aluminum alloys.* Metallurgical and Materials Transactions A, 2001. **32**(5): p. 1189-1200.

43. K. Masaki, et al., *Experimental simulation of recrystallized microstructure in friction stir welded Al alloy using a plane-strain compression test.* Scripta Materialia, 2008. **58**(5): p. 355-60.

44. G. Buffa, et al., *A continuum based fem model for friction stir welding-model development.* Material Science and Engineering A, 2006. **419**(1-2): p. 389-396.

45. A.P. Reynolds, *Flow visualization and simulation in FSW.* Scripta Materialia, 2008. **58**(5): p. 338-342.

46. A. Gerlich, G. Avramovic-Cingara, and T.H. North, *Stir zone microstructure and strain rate during Al 7075-T6 friction stir spot welding.* Metallurgical and Materials Transactions A, 2006. **37**(9): p. 2773-2786.

47. S. Kleiner, O. Beffort, and P.J. Uggowitzer, *Microstructure evolution during reheating of an extruded Mg-Al-Zn alloy into the semisolid state.* Scripta Materialia, 2004. **51**(5): p. 405-410.

48. R.E. Reed-Hill and R. Abbashian, *Physical Metallurgy Principles*. 1991, Boston: PWS Publishing Company.

49. Y. Lee, E. Chang, and C. Chieu, *Modeling of feeding behavior of solidifying Al-7Si-0.3Mg alloy plate casting.* Metallurgical and Materials Transactions B, 1990. **21**(4): p. 715-722.

50. D.J. Lloyd, *The solidification microstructure of particulate reinforced aluminium/SiC composites.* Composites Science and Technology, 1989. **35**(2): p. 159-179.

51. T.P. Zhu, *Mechanisms of partially melted zone microstructure formation during welding of magnesium AZ91 alloy*, in *Department of Chemical and Materials Engineering*. 2007, University of Auckland: Auckland.

52. A.K. Dahle, et al., *Development of the as-cast microstructure in magnesium-aluminium alloys.* Journal of Light Metals, 2001. **1**(1): p. 61-72.

53. S. Swaminathan, et al., *Peak Stir Zone Temperatures during Friction Stir Processing.* Metallurgical and Materials Transactions A.

54. K.J. Colligan. *A proposed conceptual model of the process variables related to heat generation in friction stir welding of aluminium*. in *Proceedings of the Seventh International Symposium of Friction Stir Welding*. 2008. Japan: TWI.

55. D. Rosenthal, *Mathematical theory of heat distribution during welding and cutting.* Welding Journal, 1941. **20**: p. 220-234.

56. A. Arora, et al., *Torque, power requirement and stir zone geometry in friction stir welding through modeling and experiments.* Scripta Materialia, 2009. **60**(1): p. 13-16.

57. Y.S. Sato, M. Urata, and H. Kokawa, *Parameters controlling microstructure and hardness during friction-stir welding of precipitation-hardenable aluminum alloy 6063.* Metallurgical and Materials Transactions A, 2002. **33**(3): p. 625-635.

58. P.A. Colegrove, H.R. Shercliff, and R. Zettler, *Model for predicting heat generation and temperature in friction stir welding from the material properties.* Science & Technology of Welding & Joining, 2007. **12**(4): p. 284-297.

59. A. Gerlich, M. Yamamoto, and T.H. North, *Strain rates and grain growth in Al 5754 and Al 6061 friction stir spot welds.* Metallurgical and Materials Transactions A, 2007. **38**(6): p. 1291-1302.

60. P. Su, et al., *Formation and retention of local melted films in AZ91 friction stir spot welds.* Journal of Materials Science, 2007. **42**(24): p. 9954-9965.

61. J.H. Record, et al., *A look at the statistical identification of critical process parameters in friction stir welding.* Welding Journal, 2007. **86**(4): p. 97-103.

62. A. Gerlich, M. Yamamoto, and T. North, *Local melting and tool slippage during friction stir spot welding of Al-alloys.* Journal of Materials Science, 2008. **43**(1): p. 2-11.

63. J. Ouyang and R. Kovacevic, *Material flow and microstructure in the friction stir butt welds of the same and dissimilar aluminum alloys.* Journal of Materials Engineering and Performance, 2002. **11**(1): p. 51-63.

64. M. Guerra, et al., *Flow patterns during friction stir welding.* Materials Characterization, 2002. **49**(2): p. 95-101.

65. K.N. Krishnan, *On the formation of onion rings in friction stir welds.* Materials of science and engineering, 2001. **A**(327): p. 246-251.

66. Z.Y. Ma, S.R. Sharma, and R.S. Mishra, *Effect of friction stir processing on the microstructure of cast A356 aluminum.* Materials Science and Engineering: A, 2006. **433**(1-2): p. 269-278.

67. Z.Y. Ma, S.R. Sharma, and R.S. Mishra, *Effect of multiple-pass friction stir processing on microstructure and tensile properties of a cast aluminum-silicon alloy.* Scripta Materialia, 2006. **54**(9): p. 1623-1626.

68. M. Jayaraman, R. Sivasubramanian, and V. Balasubramanian, *Establishing relationship between the base metal properties and friction stir welding process parameters of cast aluminium alloys.* Materials & Design. **31**(9): p. 4567-4576.

69. M. Amirizad, et al., *Evaluation of microstructure and mechanical properties in friction stir welded A356 + 15%SiCp cast composite.* Materials Letters, 2006. **60**(4): p. 565-568.

70. K. Nakata, et al., *Improvement of mechanical properties of aluminum die casting alloy by multi-pass friction stir processing.* Materials Science and Engineering: A, 2006. **437**(2): p. 274-280.

71. Y.G. Kim, et al., *Effect of welding parameters on microstructure in the stir zone of FSW joints of aluminum die casting alloy.* Materials Letters, 2006. **60**(29-30): p. 3830-3837.

72. Y.G. Kim, et al., *Three defect types in friction stir welding of aluminum die casting alloy.* Materials Science and Engineering A, 2006. **415**(1-2): p. 250-254.

73. T.S. Mahmoud, A.M. Gaafer, and T.A. Khalifa, *Effect of tool rotational and welding speeds on microstructural and mechanical characteristics of friction stir welded A319 cast Al alloy.* Materials Science & Technology, 2008. **24**(5): p. 553-559.

74. W. Woo, et al., *Microstructure, texture and residual stress in a friction-stir-processed AZ31B magnesium alloy.* Acta Materialia, 2008. **56**(8): p. 1701-1711.

75. G.M. Xie, et al., *Microstructural evolution and mechanical properties of friction stir welded Mg-Zn-Y-Zr alloy.* Materials Science and Engineering: A, 2007. **471**(1-2): p. 63-68.

76. J. Liao, N. Yamamoto, and K. Nakata, *Effect of Dispersed Intermetallic Particles on Microstructural Evolution in the Friction Stir Weld of a Fine-Grained Magnesium Alloy.* Metallurgical and Materials Transactions A, 2009. **40**(9): p. 2212-2219.

77. H. Zhang, et al., *Defects formation procedure and mathematic model for defect free friction stir welding of magnesium alloy.* Materials & Design, 2006. **27**(9): p. 805-809.

78. W.B. Lee, Y.M. Yeon, and S.B. Jung, *The improvement of mechanical properties of friction-stir-welded A356 Al alloy.* Materials Science and Engineering A, 2003. **355**(1-2): p. 154-159.

79. R.E. Avila, *A variational model for shear stress in friction stir welding based on the weld shape in transverse sections.* Modelling and Simulation in Materials Science and Engineering, 2006. **14**: p. 689-702.

80. X. Wang and K. Wang, *Microstructure and properties of friction stir butt-welded AZ31 magnesium alloy.* Materials Science and Engineering: A, 2006. **431**(1-2): p. 114-117.

81. G.M. Xie, Z.Y. Ma, and L. Geng, *Effect of microstructural evolution on mechanical properties of friction stir welded ZK60 alloy.* Materials Science and Engineering A, 2008. **486**(1-2): p. 49-55.

82. R.S. Mishra, *Preface to the Viewpoint Set on friction stir processing.* Scripta Materialia, 2008. **58**(5): p. 325-326.

83. Z.W. Chen and S. Cui. *Strain and strain rate during friction stir welding/processing of Al-7Si-0.3Mg alloy*. in *IOP Conf. Series: Materials Science and Engineering* 2009. Auckland, NZ.

84. P. Heurtier, C. Desrayaud, and F. Montheillet, *A thermomechanical analysis of the friction stir wedling process.* Materials Science Forum, 2002. **396-402**: p. 1537-1542.

85. T.R. McNelley, S. Swaminathan, and J.Q. Su, *Recrystallization mechanisms during friction stir welding/processing of aluminum alloys.* Scripta Materialia, 2008. **58**(5): p. 349-354.

86. K. Oh-Ishi, A. Zhilyaev, and T. McNelley, *A microtexture investigation of recrystallization during friction stir processing of as-cast NiAl bronze.* Metallurgical and Materials Transactions A, 2006. **37**(7): p. 2239-2251.

87. R.W. Fonda and J.F. Bingert, *Texture variations in an aluminum friction stir weld.* Scripta Materialia, 2007. **57**(11): p. 1052-1055.

88. J.Q. Su, T.W. Nelson, and C.J. Sterling, *Microstructure evolution during FSW/FSP of high strength aluminum alloys.* Materials Science and Engineering: A, 2005. **405**(1-2): p. 277-286.

89. J.Q. Su, T.W. Nelson, and C.J. Sterling, *Friction stir processing of large-area bulk UFG aluminum alloys.* Scripta Materialia, 2005. **52**(2): p. 135-140.

90. J.Q. Su, T.W. Nelson, and C.J. Sterling, *Grain refinement of aluminum alloys by friction stir processing.* Philosophical Magazine, 2006. **86**(1): p. 1 - 24.

91. F.J. Humphreys and M. Hatherly, *Recrystallization and related annealing phenomena*. 1996: Pergamo. 497.

92. R.D. Doherty, et al., *Current issues in recrystallization: a review.* Materials Science and Engineering A, 1997. **238**(2): p. 219-274.

93. S. Gourdet and F. Montheillet, *A model of continuous dynamic recrystallization.* Acta Materialia, 2003. **51**(9): p. 2685-2699.

94. M.R. Drury and F.J. Humphreys, *The development of microstructure in Al-5% Mg during high temperature deformation.* Acta Metallurgica, 1986. **34**(11): p. 2259-2271.

95. P.B. Prangnell, et al., *Continuous recrystallisation of lamellar deformation structures produced by severe deformation.* Acta Materialia, 2004. **52**(11): p. 3193-3206.

96. R.W. Fonda, et al., *Friction stir welding of single crystal aluminium.* Science & Technology of Welding & Joining, 2007. **12**(4): p. 304-310.

97. Y. Sato, et al., *Microtexture in the friction-stir weld of an aluminum alloy.* Metallurgical and Materials Transactions A, 2001. **32**(4): p. 941-948.

98. F. Montheillet, M. Cohen, and J.J. Jonas, *Axial stresses and texture development during the torsion testing of Al, Cu and [alpha]-Fe.* Acta Metallurgica, 1984. **32**(11): p. 2077-2089.

99. F. Montheillet, P. Gilormini, and J.J. Jonas, *Relation between axial stresses and texture development during torsion testing: A simplified theory.* Acta Metallurgica, 1985. **33**(4): p. 705-717.

100. G.R. Canova, U.F. Kocks, and J.J. Jonas, *Theory of torsion texture development.* Acta Metallurgica, 1984. **32**(2): p. 211-226.

101. J. Hirsch, E. Nes, and K. Lücke, *Rolling and recrystallization textures in directionally solidified aluminium.* Acta Metallurgica, 1987. **35**(2): p. 427-438.

102. I.L. Dillamore and H. Katoh, *The mechansims of recrystallization in cubic metals with particular reference to their orientation-dependence.* Metal Science, 1974. **8**: p. 73-83.

103. A.A. Ridha and W.B. Hutchinson, *Recrystallisation mechanisms and the origin of cube texture in copper.* Acta Metallurgica, 1982. **30**(10): p. 1929-1939.

104. Doherty, R.D., K. Kashyap, and S. Panchanadeeswaran, *Direct observation of the development of recrystallization texture in commercial purity aluminum.* Acta Metallurgica et Materialia, 1993. **41**(10): p. 3029-3053.

105. L.S. Toth, P. Gilormini, and J.J. Jonas, *Effect of rate sensitivity on the stability of torsion textures.* Acta Metallurgica, 1988. **36**(12): p. 3077-3091.

106. T. Pettersen and E. Nes, *On the origin of strain softening during deformation of aluminum in torsion to large strains.* Metallurgical and Materials Transactions A, 2003. **34**(12): p. 2727-2736.

107. R.W. Fonda and J.F. Bingert, *Precipitation and Grain Refinement in a 2195 Al Friction Stir Weld.* Metallurgical and Materials Transactions A, 2006. **37**(12): p. 3593-3604.

108. R.W. Fonda and J.F. Bingert, *Microstructural evolution in the heat affected zone of a friction stir weld.* Metallurgical and Materials Transactions A, 2004. **35**(5): p. 1487.

109. S.H. Kang, et al., *Microtexture analysis of friction stir welded Al 6061-T651 plates.* Materials Science Forum, 2005. **495-497**: p. 901.

110. M.M.Z. Ahmed, et al., *Quantifying crystallographic texture in the probe-dominated region of thick-section friction-stir-welded aluminium.* Scripta Materialia, 2008. **59**(5): p. 507-510.

111. U.F.H.R. Suhuddin, Y.S. Sato, and H. Kokawa, *Grain structure and texture evolution during friction stir welding of thin 6016 aluminum alloy sheets.* Materials Science and Engineering: A. **In Press, Accepted Manuscript**.

112. M. Moradi, et al., *Recrystallization behavior of ECAPed A356 alloy at semi-solid reheating temperature.* Materials Science and Engineering: A, 2010. **527**(16-17): p. 4113-4121.

113. C.I. Chang, C.J. Lee, and J.C. Huang, *Relationship between grain size and Zener-Holloman parameter during friction stir processing in AZ31 Mg alloys.* Scripta Materialia, 2004. **51**(6): p. 509-514.

114. J.Q. Su, et al., *Microstructural investigation of friction stir welded 7050-T651 aluminium.* Acta Materialia, 2003. **51**(3): p. 713-729.

115. Oxford Instruments. *Basics of EBSD*. 2005 [cited; Available from: http://www.ebsd.com/ebsd-explained/basicsofebsd1.htm.

116. B.D. Cullity, *Elements of X-ray diffraction*. 1959: Addison-Wesley Publishing Company.

117. H. Schmidt, J. Hattel, and J. Wert, *An analytical model for the heat generation in friction stir welding* Modeling and Simulation in Materials Science and Engineering 2004. **12**(1): p. 143-157.

118. P.A. Colegrove, *Comsol Friction Stir Welding Model User Manual*. 2006: University of Cambridge.

119. C.M. Estey, et al., *Constitutive behaviour of A356 during the quenching operation.* Materials Science and Engineering A, 2004. **383**(2): p. 245-251.

120. K.P. Solek, A. Lukaszek-Solek, and R. Kuziak, *Rheological properties of alloys near solidus point intended for thixoforming.* Archives of civil and mechanical engineering, 2009.

121. M. Haghshenas, et al., *Hot deformation behaviour of Thixocast A356 aluminum alloy during compression at elevated temperature.* International Journal of Material Forming, 2008. **1**(0): p. 1001-1005.

122. H.J. McQueen, M. Cabibbo, and E. Evangelista, *Piercing/extrusion and FSW nugget microstructure formation in Al alloys.* Materials Science and Technology, 2007. **23**(7): p. 803-809.

123. M. Yeh, et al., *Plastic flow behavior during the forging of a 6061 Al/10 vol pct Al2O3 (p) composite.* Metallurgical and Materials Transactions A, 2000. **31**(4): p. 1310-1313.

124. S.I. Hong and Y.S. Seo, *Effect of microstructure on wear behavior of Al-Mg-Si alloy matrix-10 vol.% Al2O3 composite.* Materials Science and Engineering: A, 1999. **265**: p. 29-41.

125. C.H. Caceres and J.R. Griffiths, *Damage by the cracking of silicon particles in an Al-7Si-0.4Mg casting alloy.* Acta Materialia, 1996. **44**(1): p. 25-33.

126. T. Zhu, Z.W. Chen, and W. Gao, *Incipient melting in partially melted zone during arc welding of AZ91D magnesium alloy.* Materials Science and Engineering: A, 2006. **416**(1-2): p. 246-252.

127. L. Liu and H. Ding, *Study of the plastic flow behaviors of AZ91 magnesium alloy during thermomechanical processes.* Journal of Alloys and Compounds, 2009. **484**: p. 949-956.

128. S. Kleiner, et al., *Microstructure and mechanical properties of squeeze cast and semi-solid cast Mg-Al alloys.* Journal of Light Metals, 2002. **2**(4): p. 277-280.

129. Y. Chino, et al., *An investigation of compressive deformation behaviour for AZ91 Mg alloy containing a small volume of liquid.* Acta Materialia, 2003. **51**(11): p. 3309-3318.